



Universitat de Girona

A STUDY OF THE BOND AND FLEXURAL BEHAVIOUR OF REINFORCED CONCRETE ELEMENTS STRENGTHENED WITH NEAR SURFACE MOUNTED (NSM) FRP REINFORCEMENT

Ibrahim ATTIA ABDELGAYED ABDELGAWAD SHARAKY

Dipòsit legal: Gi. 68-2014

<http://hdl.handle.net/10803/128331>



A study of the bond and flexural behaviour of reinforced concrete elements strengthened with near surface mounted (NSM) FRP reinforcement de Ibrahim Attia Abdelgayed Abdelgawad Sharaky està subjecta a una llicència de [Reconeixement 4.0 Internacional de Creative Commons](https://creativecommons.org/licenses/by/4.0/)

© 2014, Ibrahim Attia Abdelgayed Abdelgawad Sharaky



UNIVERSITAT DE GIRONA

PHD THESIS

A STUDY OF THE BOND AND FLEXURAL
BEHAVIOUR OF REINFORCED CONCRETE
ELEMENTS STRENGTHENED WITH NEAR
SURFACE MOUNTED (NSM) FRP
REINFORCEMENT

IBRAHIM ATTIA ABDELGAYED ABDELGAWAD SHARAKY

2013



UNIVERSITAT DE GIRONA

PHD THESIS

A STUDY OF THE BOND AND FLEXURAL
BEHAVIOUR OF REINFORCED CONCRETE
ELEMENTS STRENGTHENED WITH NEAR
SURFACE MOUNTED (NSM) FRP
REINFORCEMENT

IBRAHIM ATTIA ABDELGAYED ABDELGAWAD SHARAKY

2013

TECHNOLOGY DOCTORATE PROGRAMME

ADVISOR

DR. LLUÍS TORRES LLINÀS

University of Girona, Spain

A thesis submitted for the degree of Doctor of Philosophy by the
University of Girona

To whom it might concern,

Dr. Lluís Torres Llinàs, Professor at the *Universitat de Girona* of the Department of *Enginyeria Mecànica i de la Construcció Industrial*

CERTIFY that the study entitled *A study of the bond and flexural behaviour of reinforced concrete elements strengthened with near surface mounted (NSM) FRP reinforcement* has been carried out under their supervision by Ibrahim Attia Abdelgayed Abdelgawad Sharaky to apply for the doctoral degree with the European Mention. I also certify that Ibrahim Attia Abdelgayed Abdelgawad Sharaky was a full time graduate student at University of Girona, Girona, Spain, from January 2011 to present.

Dr. Lluís Torres Llinàs
University of Girona, Spain

IN THE NAME OF ALLAH

Acknowledgements

I would like to express my gratitude to my advisor, Dr. Lluís Torres Llinàs, for the indefatigable help and for the key contributions that have allowed the development of the present thesis. I also would like to thank the help received from Prof. Joaquim Barros during my short research stay in the University of Minho, Guimaraes, Portugal. I would like to thank also the help received from Dr. Albert Turon, Dr. Marta Baena, Dr. Cristina Miàs, Dr. Cristina Barris, and Mr. Irene Vilanova, who spent a lot of time making the work easy and clarified many things since the first day that I started to work with the research group AMADE on Monday 10th of January 2011.

Of course, I am grateful to all members of the research group AMADE of the University of Girona for the help and nice moments that I have received from each one.

I would also like to thank my family for the support they provided me through my entire life and in particular, I must acknowledge my parents, my wife Walaa and my sons Omer and Malek for their support and being without me for a long time throughout my stay in Girona. I have to do a special mention to my profs. in Egypt, Prof. Hossam Sallam and Prof. Mohamed Hassan seleem. I have to do a special mention to my friends Abdalla Kabeel and Mohammed Omran.

Funding

The period of research has been funded by the Comissionat per a Universitats i Recerca del Departament d'Innovació, Universitats i Empresa de la Generalitat de Catalunya, under a research grant FI pre-doctorate grant 2011FI.B 00003, started in April of 2011 until present.

Also, the present work has been partially funded by the Spanish Government through the Ministerio de Ciencia e Innovación under the Project BIA2010-20234-C03-02.

Part of the work has been carried out during during a three months research stay at the University of Minho, under the BE research stay grant 2011_BE1_00133, between September and December 2012.

Publications

The papers published and submitted during the development of this thesis are listed below:

1. **Sharaky I. A.**, Torres L., Baena M., Vilanova I. Effect of different material and construction details on the bond behaviour of NSM FRP bars in concrete. *Construction and Building Materials*, Vol. 38: pp. 890-902, 2013.
2. **Sharaky, I.A.**, Torres, L., Baena, M., Miàs, C., An experimental study of different factors affecting the bond of NSM FRP bars in concrete, *Composite Structures*, Vol. 99: pp. 350-365, 2013.
3. **Sharaky, I.A.**, Torres, L., Barros, J.A.O., Assessment of the bond behaviour of NSM FRP bars in concrete from numerical research *Cement and Concrete Composites*, Submitted April, 2013.
4. Torres, L., **Sharaky, I.A.**, Barris, C. Baena, M., Study of the influence of adhesive properties and bond length on the bond behaviour of NSM FRP bars in concrete. *Journal of Civil Engineering and Management*, Accepted September, 2013.
5. **Sharaky, I.A.**, L. Torres, J. Comas, C. Barris, Flexural response of reinforced concrete (RC) beams strengthened with near surface mounted (NSM) fibre reinforced polymer (FRP) bars, *Composite Structures*, Submitted September, 2013.

Contents

Summary	xxi
Resum	xxv
List of Figures	xxxvii
List of Tables	xl
1 Introduction and objectives	1
1.1 Introduction	1
1.2 Objectives	2
1.3 Thesis Layout	3
2 Literature Review	5
2.1 Introduction	5
2.2 FRP materials	5
2.2.1 Mechanical properties	6
2.3 Strengthening techniques	7
2.3.1 EB Technique	7
2.3.2 NSM Technique	9
2.4 Installation of NSM FRP reinforcement	10
2.5 Experimental research on NSM FRP bond tests	11
2.5.1 Direct pullout tests	11
2.5.2 Beam pullout tests	16
2.6 Bond models of NSM FRP reinforcement	17
2.6.1 Local bond slip laws	18

2.7	Flexural behaviour of strengthened RC beams	21
2.7.1	Laboratory works and tests setup	21
2.7.1.1	Strengthened beams with limited bonded lengths of NSM FRP reinforcement	21
2.7.1.2	Strengthened beams with partially bonded lengths of FRP reinforcement	27
2.8	Failure modes and mechanisms of NSM reinforcement	28
2.9	Conclusions of the literature review	30

I Study of bond behaviour of NSM FRP bars in concrete using the modified pullout test 33

3 Pullout test experimental programme 35

3.1	Introduction	35
3.2	Materials	36
3.2.1	Concrete	36
3.2.2	Epoxy	37
3.2.3	FRP bars and steel	38
3.3	Specimens preparation	39
3.3.1	Mould preparation, casting and curing procedure	39
3.3.2	Preparation of the grooves	39
3.3.3	Bonding of NSM bars	40
3.4	Specimen configurations	41
3.5	Test setup, instrumentation and test procedure	42
3.6	The pullout test arrangement	45
3.6.1	The first series	45
3.6.1.1	Overview	45
3.6.1.2	Test variables	46
3.6.2	The second series	47
3.6.2.1	Overview	47
3.6.2.2	Test variables	48
3.6.3	The third series	50
3.6.3.1	Overview	50

3.6.3.2	Test variables	50
3.7	Analysis of measurements	53
4	Pullout test experimental results	55
4.1	Introduction	55
4.2	Results and discussion of the first series	55
4.2.1	Specimens with CFRP bars	56
4.2.1.1	Failure modes and loads	56
4.2.1.2	Average bond stress slip curves	58
4.2.1.3	Longitudinal strain distribution along the bond length	60
4.2.2	Specimens with GFRP bars	62
4.2.2.1	Failure modes and loads	62
4.2.2.2	Average bond stress slip curves	66
4.2.2.3	Effect of the confinement of the inside concrete part on the transverse strain	69
4.2.3	Effect of FRP properties on the failure load and bond behaviour	71
4.2.4	Conclusions	72
4.3	Results and discussion of the second series	75
4.3.1	Specimens with CFRP bars	75
4.3.1.1	Failure modes and load slip response	75
4.3.1.2	Effect of bar type on transverse strain distribution in epoxy and concrete	79
4.3.2	Specimens with GFRP bars	80
4.3.2.1	Failure modes and load slip response	80
4.3.2.2	Transverse strain distribution in epoxy and concrete	86
4.3.3	Discussion of the effect of different parameters on behaviour and failure load	90
4.3.3.1	Groove dimensions, groove geometry and bar size . .	90
4.3.3.2	Adhesive type and concrete strength	94
4.3.4	Conclusions	97
4.4	Results and discussion of the third series	100
4.4.1	NSM CFRP results	100
4.4.1.1	Bond behaviour in the longitudinal direction	100

4.4.1.2	Transverse strain	104
4.4.2	NSM GFRP results	109
4.4.2.1	Bond behaviour in the longitudinal direction	109
4.4.2.2	Transverse strain	113
4.5	Comparison and discussion of results	117
4.5.1	Conclusions	119
5	Pullout test numerical analysis	123
5.1	Overview	123
5.2	Experimental programme	124
5.3	Experimental results	124
5.4	Numerical analysis	128
5.4.1	FEM model	128
5.5	Numerical results and comparison	132
5.5.1	Inverse analysis	132
5.6	Discussion of the numerical results	134
5.6.1	Specimens with CFRP bars	134
5.6.2	Specimens with GFRP bars	137
5.6.3	Strain distribution	140
5.6.4	Detailed comparisons of the numerical results for specimens with CFRP and GFRP bars	144
5.7	Conclusions	149
II	Study of the flexural behaviour of RC beams strengthened using NSM FRP bars/strips	151
6	Flexural test experimental programme	153
6.1	Introduction	153
6.2	Test specimens preparation	153
6.2.1	RC beams and internal reinforcement	154
6.2.2	Specimen casting and curing	154
6.2.3	Groove preparation and bonding of the NSM reinforcement	157
6.3	Test setup	160

6.4	Instrumentation	160
6.4.1	Deflections at different locations of the beam	161
6.4.2	Rotations and mean curvatures in the central zone	161
6.4.3	Concrete strains on the mid-span section surface	162
6.4.4	Concrete and epoxy strains on the bottom of the beam	163
6.4.5	Strains along the NSM FRP reinforcement	163
6.5	Strengthening of RC beams	164
6.5.1	Overview	164
6.5.2	The first series	165
6.5.3	The second series	166
6.5.4	The third series	171
6.6	Material Properties	172
6.6.1	Concrete	174
6.6.1.1	Compressive strength	174
6.6.1.2	Modulus of elasticity	175
6.6.1.3	Tensile strength	176
6.6.2	Steel reinforcement	176
6.6.3	FRP bars, strips and sheets	176
6.6.4	Epoxy	177
7	Flexural test experimental results	179
7.1	Introduction	179
7.2	Results and discussion of the first series	179
7.2.1	Beams strengthened with NSM CFRP bars	180
7.2.1.1	Load deflection curves and mode of failure	180
7.2.1.2	Load end slip curves	182
7.2.1.3	Strain distribution along the CFRP bars	183
7.2.1.4	Sectional strain profile	185
7.2.1.5	Transverse strain	185
7.2.1.6	Deflection and stiffness	187
7.2.2	Beams strengthened with NSM GFRP bars	188
7.2.2.1	Load deflection curves and mode of failure	188
7.2.2.2	Load end slip curves	190

7.2.2.3	Strain distribution along the GFRP bars	191
7.2.2.4	Sectional strain profile	193
7.2.2.5	Transverse strain	193
7.2.2.6	Deflection and stiffness	194
7.2.3	Comparison and discussion of results	195
7.2.4	Conclusions	198
7.3	Results and discussion of the second series	200
7.3.1	Mode of failure and load deflection curves	200
7.3.1.1	Effect of NSM shape, dimensions and area	200
7.3.1.2	Effect of NSM material and arrangement	202
7.3.1.3	Effect of mechanical interlocking with shear connectors and transverse wrapping	203
7.3.2	Effect of NSM FRP reinforcement (FRPR) on the stiffness of the beams	205
7.3.3	Strain distribution along the FRP reinforcement	206
7.3.4	Compressive strain in concrete	209
7.3.5	Deflection distribution and stiffness	212
7.3.6	Conclusions	214
7.4	Results and discussion of the third series	216
7.4.1	Load deflection curves and mode of failure	216
7.4.1.1	Effect of bond length	216
7.4.1.2	Effect of end anchorage and transverse wrapping	218
7.4.2	Strains in the NSM FRP reinforcement	219
7.4.3	Compressive strain in concrete	222
7.4.4	Deflection and stiffness	223
7.4.5	Global comparison	227
7.4.6	Conclusions	229

III Conclusions and Future Work 231

8	Conclusions and future work	233
8.1	Summary	233
8.2	Bond behaviour	233

<i>CONTENTS</i>	xix
8.2.1 Experimental research	233
8.2.2 Numerical analysis	235
8.3 flexural behaviour	236
8.4 Future work	239
Bibliography	239
IV Appendix	253
A EMPIRICAL CALIBRATIONS FOR INVERSE ANALYSIS	255

Summary

In the past, externally bonded (EB) systems have shown their effectiveness in strengthening reinforced concrete (RC) structures. The use of bonded steel plates and rebars for the strengthening and rehabilitation of reinforced concrete structures has been popular for years. Recently, the use of externally bonded fibre reinforced polymer (EB FRP) laminates has been one of the most attractive methods for strengthening RC structures and a large number of research and practical projects have been undertaken. More recently, the use of near surface mounted (NSM) FRP bars has become an attractive novel method for strengthening RC members and masonry, thus increasing both flexural and shear strength. Over the last few years, a number of research studies concerning the use of NSM FRP for strengthening RC structures, either in shear or flexure, have been carried out. The use of the NSM FRP technique presents many advantages over the EB FRP technique (surface preparation, protection, bond and aesthetics). Many factors involved in the interaction between FRP reinforcement, adhesive and concrete can affect the bond behaviour and failure load of the NSM strengthening system. Due to limited experimental research into the NSM technique compared to the EB technique, there is no general formulation to predict the failure load of NSM FRP joints. Although the previous studies have made significant contributions to the understanding of the bond behaviour between NSM FRP and concrete, the large number of factors involved makes it necessary to carry out further experimental work to have additional available data with the aim of arriving at a better understanding of the role of the different parameters influencing the design of this system.

The main objective of this thesis is to study the bond behaviour of the NSM FRP strengthening technique and to investigate the effectiveness of strengthening RC beams with NSM FRP rods and strips. With this aim an extensive programme

of experimental tests complemented with numerical analysis has been performed to study the effect of the variables affecting this technique.

In the first part of the thesis a study of the bond behaviour is carried out by means of the modified pullout test. In the first series of pullout tests it is studied the effect of groove surface (preformed and saw cut), groove geometry (dimensions and shapes), FRP bar type (material and surface treatment), bond length; and also of the incorporation, in the groove-concrete system, of different construction details that modify the NSM-concrete interaction (transverse interlocking with or without shear connectors, covering plate with shear connectors and confinement of surrounding concrete). The second series of pullout tests is carried out to study the effects of adhesive properties, bar type, bar size, FRP properties, groove geometry and the use of mechanical interlocking on the capacity and bond behaviour of a NSM joint. In the second series, the concrete strength is lower than that used for casting the specimens in the first series. A comparison between the results of the two previous series was carried out to study the effect of concrete properties on the NSM bond behaviour. Finally a third series of pullout tests was carried out to study in detail the effect of adhesive properties and bond length on the bond behaviour of NSM bars in longitudinal and transverse directions.

Due to the variety of factors affecting the behaviour of NSM FRP strengthening systems, mechanical models able to incorporate the influencing variables acquire major importance for the correct prediction of the load capacity and the contribution of the different parameters. Therefore, for a reliable numerical simulation of NSM FRP pullout tests, numerical models capable of simulating the fracture initiation and propagation of the cement based structure surrounding the NSM FRP elements should be used. To perform the numerical study the Finite Element Analysis (FEM) model was used to assess the influence of the main parameters affecting the bond behaviour between reinforcement and concrete on the local bond slip law: geometric and mechanical properties of FRP and adhesive, bond length, and concrete strength. A Finite Element Analysis (programme FEMIX V4) has been carried out to perform several trials to fit as much as possible (inverse analysis) the force versus loaded end slip response obtained experimentally in direct pullout tests. The model is capable of simulating the FRP-concrete interaction, as well as the crack initiation and propagation in the surrounding concrete. Using the inverse analysis, the bond

stress, radial and tangential stresses in interface elements and concrete and the strain distribution along the bond length are obtained.

In the second part of this thesis an experimental programme of flexural tests on RC beams strengthened with NSM FRP has been carried out to study the effect on the flexural behaviour of some of the previous variables studied in the first part. Thus, in this part the influence of the following parameters has been considered: FRP bar type (material and surface treatment), bond length, and the incorporation of different construction details that modify the NSM-concrete interaction, using different FRP elements (bars and strips) and adhesive properties. The flexural tests have been performed in three series. In the first series, the effect of material type (carbon and glass), epoxy properties, bars size and the number bars were studied. The tested beams were strengthened with a limited bond length in order to imitate work-place real conditions as the grooves could only be cut up to the faces of the supporting columns with difficulty. In the second series, the beams were strengthened with FRP bars and strips. The effect of transverse wrapping and construction details on the flexural behaviour has been studied. In the third series the beams were strengthened with partially bonded FRP bars and strips. The effect of bond length, transverse wrapping and end anchorage on the flexural behaviour has also been studied. Finally, a detailed comparison between the experimental results of the three series has been performed

Resum

L'ús d'elements encolats com a reforç extern ha demostrat ser un sistema efectiu per a la rehabilitació, reparació i augment de la capacitat resistent de les estructures de formigó armat. Les xapes i barres d'acer encolades per al reforç i rehabilitació s'han emprat amb èxit durant anys. En els últims temps, la utilització de laminats de polímers reforçats amb fibres (en anglès *fibre reinforced polymer*, FRP) com a reforç extern ha mostrat ser un mètode molt atractiu per al reforç d'estructures de formigó armat i això ha comportat que s'hagin portat a terme un gran nombre de projectes de recerca i aplicacions pràctiques en aquest camp. Més recentment, la utilització d'FRP inserits en el recobriment (en anglès *near surface mounted*), NSM) ha esdevingut un nou mètode per al reforç d'estructures de formigó i obra de fàbrica tant per a l'augment de la resistència a flexió com a tallant. En el decurs dels últims anys s'han realitzat diversos estudis sobre la utilització de la metodologia NSM FRP per al reforç d'estructures de formigó. L'ús de la tècnica NSM FRP presenta diversos avantatges respecte dels sistemes de reforç extern amb FRP (preparació de la superfície, protecció, adherència, estètica). La interacció entre el reforç d'FRP, l'adhesiu i el formigó es pot veure afectada per diferents factors que tenen incidència en el comportament adherent i en la càrrega que pot suportar el sistema de reforç amb NSM FRP. Com a conseqüència d'una recerca més limitada en comparació amb els sistemes de reforç extern, no hi ha una d'una formulació general per a la predicció de la càrrega que pot resistir el reforç d'estructures de formigó amb NSM. Malgrat que els estudis previs han fet aportacions significatives per a la comprensió del comportament adherent entre reforç i formigó, el gran nombre de factors implicats fa que sigui necessari plantejar nous treballs experimentals per tal de disposar de més dades per a una millor explicació del paper dels diferents paràmetres que incideixen en el disseny reforç.

L'objectiu principal d'aquesta tesi és l'estudi del comportament adherent de la tècnica de reforç NSM FRP i investigar l'eficàcia del reforç de bigues de formigó armat amb barres i tires de NSM FRP. D'aquesta manera s'ha realitzat un extens programa d'assajos experimentals complementat amb anàlisis numèriques per tal d'estudiar les variables que incideixen en aquesta tècnica.

En la primera part de la tesi es fa un estudi de l'adherència emprant l'assaig de pullout modificat. En la primera sèrie d'assajos s'estudia l'efecte de la superfície de la ranura (preformada o tallada amb disc), de la geometria de la ranura (dimensions i forma), tipus de barra FRP (material i acabat superficial), de la longitud d'adherència, i de la incorporació de diferents detalls constructius per tal de modificar la interacció entre NSM FRP i formigó (introducció de traves transversals amb i sense connectors de tallant, xapes de recobriment amb connectors i confinament del formigó circumdant).

La segona sèrie d'assajos de pullout s'ha portat terme per tal d'estudiar els efectes de les propietats de l'adhesiu, de tipus de barra, de la mida de la barra, propietats de l'FRP, de la geometria de la ranura i de la utilització de traves mecàniques. En la segona sèrie s'ha emprat un formigó amb una resistència menor que en la primera i això ha permès estudiar l'efecte de les propietats del formigó en el comportament adherent. Finalment s'ha portat a terme una tercera sèrie d'assajos per tal d'estudiar amb més detall l'efecte de les propietats de l'adhesiu i la longitud d'adherència de les barres en el comportament adherent, tant en la direcció longitudinal com transversal.

A causa de la quantitat de factors que incideixen en el comportament del sistema de reforç NSM FRP, adquireixen una importància fonamental els models numèrics capaços de predir correctament la capacitat resistent i la contribució dels diferents paràmetres, de manera que per a una simulació numèrica fiable s'han d'emprar models capaços de simular l'inici i propagació de la fractura en la base de ciment que envolta l'element NSM FRP. D'aquesta manera s'ha portat a terme un estudi numèric amb el mètode dels elements finits (MEF) per tal de valorar la influència dels principals paràmetres que afecten el comportament adherent entre el reforç NSM FRP i el formigó a nivell de la llei adherència-lliscament local: propietats mecàniques i geomètriques del reforç i adhesiu, longitud d'adherència i resistència del formigó.

S'ha realitzat una anàlisi amb el MEF (programa FEMIX V4) per tal de fer diverses proves per ajustar amb la màxima precisió possible (anàlisi inversa) la resposta força-lliscament de l'extrem carregat de la barra obtinguda experimentalment en els assajos de pullout. El model és capaç de simular la interacció entre FRP i formigó, així com la iniciació i propagació de fissures en el formigó circumdant. Mitjançant l'anàlisi inversa s'obtenen les tensions d'adherència, les tensions radial i tangencial als elements d'interfície i al formigó i la distribució de deformacions unitàries al llarg de la barra.

A la segona part de la tesi s'ha portat a terme un programa d'assajos a flexió d'elements de formigó armat reforçats amb NSM FRP per tal d'estudiar l'efecte d'algunes de les variables analitzades en la primera part. D'aquesta manera, en aquesta part s'ha considerat la influència dels següents paràmetres: tipus de barra FRP (material i acabat superficial), longitud d'adherència, i incorporació de diversos detalls constructius que modifiquen la interacció entre NSM i formigó, emprant diferents formats d'FRP (barres i tires) i propietats de l'adhesiu. Els assajos de flexió s'han realitzat en tres sèrie.

En la primera s'ha estudiat l'efecte del tipus de material (fibra de carboni i vidre), de les propietats de la resina epoxídica, de la mida de la barra i del número de barres. Les bigues s'han reforçat amb longitud d'adherència limitada per tal de simular una situació que es pot donar a la pràctica a causa de la dificultat d'execució de les ranures fins a les cares de les columnes. A la segona sèrie, les bigues s'han reforçat amb barres i tires d'FRP i s'ha estudiat l'efecte de diferents detalls constructius i del confinament amb teixit d'FRP disposat transversalment. A la tercera sèrie les bigues s'han reforçat també amb barres i tires d'FRP però amb adherència parcial i s'ha estudiat la influència de la longitud d'ancoratge, del confinament amb teixit d'FRP, així com de l'ancoratge al final de les barres. Finalment s'ha realitzat un estudi comparatiu dels resultats de les tres sèries.

List of Figures

2.1	Surface treatment of some available FRP bars.	6
2.2	A comparison of the tensile properties of FRP and steel bars [44]. . .	8
2.3	Strengthening techniques.	10
2.4	Test setup for direct and beam pullout tests [42].	11
2.5	Test specimen configuration of the modified pullout test [68].	12
2.6	Test specimen configuration of the modified pullout test [69].	14
2.7	Test specimen configuration and setup of the single shear test [71]. . .	15
2.8	Test specimen configuration and setup [76].	16
2.9	Test specimen configuration and setup of beam pullout test [77]. . . .	17
2.10	Beam pullout test setup [78].	18
2.11	Typical bond slip curves of NSM FRP reinforcement [15].	20
2.12	Plan view of the NSM strengthening with mechanical interlocking grooves [90].	24
2.13	Details and setup of the tested beams [27].	25
2.14	Details of the tested beams [21].	26
2.15	Failure mode of the tested beams [21].	27
2.16	Bond failure modes of NSM systems observed in bond tests [38]. . . .	29
2.17	Failure modes observed in strengthened RC beams with NSM rein- forcement [33].	30
3.1	Pullout tests arrangements.	36
3.2	Surface treatment of the FRP bars.	39
3.3	Mould preparation and casting.	40
3.4	Bonding of NSM bars.	41
3.5	Specimen details and test setup.	43

3.6	Strain gauges details.	44
3.7	NSM configurations (dimensions in mm).	49
4.1	Failure modes of specimens with CFRP bars.	59
4.2	Average bond stress slip curves of NSM CFRP bars.	61
4.3	Effect of the inside concrete part confinement and groove geometry on the behaviour of specimens with NSM C1 bars.	62
4.4	Longitudinal strain distributions along the bond length of NSM C1 bars.	63
4.5	Modes of failure of specimens with GFRP bars.	67
4.6	Average bond stress slip curves of NSM GFRP bars.	68
4.7	Effect of the inside concrete part confinement on the behaviour of specimens with NSM G2 bars.	69
4.8	Effect of bond length on the behaviour of specimens with NSM G2 bars.	70
4.9	Effect of the inside concrete part confinement on the transverse strain.	71
4.10	Behaviour of specimen with different FRP bars.	72
4.11	Failure modes of specimens with NSM CFRP bars.	77
4.12	Load slip curves of specimens with NSM CFRP bars bonded with epoxy type A.	78
4.13	Load slip curves of specimens with NSM CFRP bars bonded with epoxy type B.	79
4.14	Transverse strain distribution for specimen L1616AC1.	80
4.15	Transverse strain distribution for specimen L1515AC2.	81
4.16	Failure mode of specimens with NSM GFRP bars bonded with adhe- sive type A.	83
4.17	Failure mode of specimens with NSM GFRP bars bonded with adhe- sive types B, C and D.	84
4.18	Load slip curves of specimens with NSM GFRP bars bonded using epoxy type A.	85
4.19	Load slip curves of specimens with NSM GFRP bars bonded using epoxy types B,C and D.	86
4.20	Transverse strain distribution for specimen L1616AG1.	87
4.21	Transverse strain distribution for specimen L1620AG1T.	88

4.22	Transverse strain distribution for specimen L1916AG1U.	88
4.23	Transverse strain distribution for specimen L1616AG1I.	89
4.24	Transverse strain distribution for specimen L1818AG2.	89
4.25	Transverse strain distribution for specimen L1616BG1.	90
4.26	Transverse strain distribution for specimen L1616CG1.	90
4.27	Effect of groove dimensions, geometry and bar size on behaviour of specimens with NSM CFRP bars.	91
4.28	Effect of groove width, shape and FRP bar size on behaviour of specimens with NSM GFRP bars.	92
4.29	Effect of groove dimensions and bond length on the capacity of specimens reported in [68–70, 72], ($K = d/d_b$; $w =$ groove width; $n = L_b/d_b$; $L_b =$ bond length).	93
4.30	Effect of adhesive properties on the behaviour of tested specimens. . .	95
4.31	Effect of adhesive types on the failure load of tested specimens reported in [[68–70]], ($K = d/d_b$; $n = L_b/d_b$).	96
4.32	Transverse strain distribution for specimens L1616AG1 and L1616BG1.	97
4.33	Transverse strain distribution for specimens L1616AG1 and L1616CG1.	97
4.34	Failure mode of specimens with CFRP bars.	102
4.35	Average bond stress slip curves for specimens with CFRP bars bonded with epoxy A.	103
4.36	Average bond stress slip curves for specimens with CFRP bars bonded with epoxy B.	104
4.37	Average bond stress slip curves for specimens with CFRP bars bonded with epoxy D.	105
4.38	Transverse strain distribution on epoxy paste for specimens with CFRP bars bonded with epoxy A.	106
4.39	Transverse strain distribution on concrete for specimens with CFRP bars bonded with epoxy A.	107
4.40	Transverse strain distribution for specimens with CFRP bars bonded with epoxy B (L16BC-b).	108
4.41	Transverse strain distribution on epoxy for specimens with CFRP bars bonded with epoxy D.	108

4.42	Transverse strain distribution on concrete for specimens with CFRP bars bonded with epoxy D.	109
4.43	Failure mode of specimens with GFRP bars.	111
4.44	Average bond stress slip curves for specimens with GFRP bars bonded with epoxy A.	112
4.45	Average bond stress slip curves for specimens with GFRP bars bonded with epoxy B.	112
4.46	Average bond stress slip curves for specimens with GFRP bars bonded with epoxy D.	113
4.47	Transverse strain distribution on epoxy for specimens with GFRP bars bonded with epoxy A.	114
4.48	Transverse strain distribution on concrete for specimens with GFRP bars bonded with epoxy A.	114
4.49	Transverse strain distribution on epoxy for specimens with GFRP bars bonded with epoxy B.	115
4.50	Transverse strain distribution on concrete for specimens with GFRP bars bonded with epoxy B.	116
4.51	Transverse strain distribution for specimens with GFRP bars bonded with epoxy D (S16DG-a).	116
4.52	Effect of epoxy type and bond length for specimens with CFRP bars on: (a) $\tau_{max,av}$ and (b) $\%F_{max,av} / F_u$; ($n = L_b/d_b$).	117
4.53	Effect of epoxy type and bond length for specimens with GFRP bars on: (a) $\tau_{max,av}$ and (b) $\%F_{max,av} / F_u$; ($n = L_b/d_b$).	118
4.54	Effect of epoxy type and bond length on the transverse strain of NSM CFRP bars.	119
4.55	Effect of epoxy type and bond length on the transverse strain of NSM GFRP bars.	119
5.1	Failure mode of the tested specimens.	127
5.2	Finite element mesh of half of specimen: (a) complete mesh and (b) details of the model.	129
5.3	Trilinear stress strain diagram to simulate the fracture mode I crack propagation ($\sigma_{n,2}^{cr} = \alpha_1 \sigma_{n,1}^{cr}$, $\sigma_{n,3}^{cr} = \alpha_2 \sigma_{n,1}^{cr}$, $\varepsilon_{n,2}^{cr} = \xi_1 \varepsilon_{n,u}^{cr}$, $\varepsilon_{n,3}^{cr} = \xi_2 \varepsilon_{n,u}^{cr}$).	131

5.4	(a) local bond stress slip relationship and (b) qualitative correlation between $\tau - s$ and $F-d$ relationships in a bond test [101].	131
5.5	Experimental and numerical calibration curves of specimen L16A1C1-1.	133
5.6	Experimental and numerical $F-d$ curves of specimens with CFRP bars (concrete 1).	136
5.7	Experimental and numerical $F-d$ curves of specimens with CFRP bars (concrete 2).	137
5.8	Comparisons of the $\tau - s$ curves of specimens with CFRP bars: a) influence of the bar size and adhesive properties; b) influence of the concrete strength and groove size.	138
5.9	Experimental and numerical $F-d$ curves of specimens with GFRP bars.	139
5.10	Comparisons of the $\tau - s$ curves of specimens with GFRP bars: (a) influence of the bar size and adhesive properties and (b) influence of the concrete strength.	140
5.11	Numerical and experimental comparisons: (a) tensile strain and (b) bond shear stress distribution for specimen L12A2C1.	141
5.12	Effect of FRP type on the: (a) strain distribution and (b) bond stress distribution.	142
5.13	Effect of bar size on the: (a) strain distribution and (b) bond stress distribution.	143
5.14	Effect of adhesive type on the: (a) strain distribution and (b) bond stress distribution.	144
5.15	Effect of bond length on the: (a) strain distribution and (b) bond stress distribution.	145
5.16	Longitudinal bond stress distributions along the bond length for specimens of NSM FRP bars: (a) L16A1C1-1 and (b) L16A1G1-1.	146
5.17	Scheme for the calculation of tensile stress in the concrete in the transverse plane.	146
5.18	Distribution of bond shear stress in the first interface element and tensile stress in the first concrete element at the loaded end: (a) L16A1C1-1 and (b) L16A1G1-1.	147

5.19	Theoretical distribution of normalized tensile stresses in the concrete: (a) L16A1C1-1 and (b) L16A1G1-1.	147
5.20	Distribution of σ_{ct} along the bonded length ($F = 0.75F_{max}$ at 1st interface element): (a) L16A1C1-1 and (b) L16A1G1-1.	148
5.21	FEMIX output (drawmesh) of σ_{ct} along the bonded length ($F =$ $0.75F_{max}$ at 1st interface element): (a) L16A1C1-1 and (b) L16A1G1-1.	148
6.1	Dimensions and reinforcement details of the RC beam.	155
6.2	Appearance of the mould and reinforcement.	155
6.3	Procedure of casting and curing for beams and cylinders.	156
6.4	Formation of the grooves in the tension side of beams.	157
6.5	Full details and locations of the grooves for the strengthened beams. .	158
6.6	Steps of NSM installation in the grooves of the RC beams.	159
6.7	Flexural test setup.	160
6.8	Sketch of the tested beams instrumentation.	161
6.9	Arrangement of the vertical transducers and inclinometers.	162
6.10	Arrangement of the concrete strain gauges in the mid-span top section.	163
6.11	Strain gauges on the NSM bars.	164
6.12	Surface treatment of the FRP reinforcement used in the flexural test.	166
6.13	Strengthening scheme of the beams in the first series.	167
6.14	Strengthening scheme of the beams in the second series.	169
6.15	Strengthening scheme of the beams with T and IS.	170
6.16	Details of the sections of the beams with T and IS.	171
6.17	Strengthening scheme of the beams in the third series.	173
6.18	Preparation of specimens with ES and T.	174
7.1	Load deflection curve of beams strengthened with NSM CFRP bars. .	181
7.2	Failure modes of beams strengthened with NSM CFRP bars.	182
7.3	Free end slip curves of beams strengthened with CFRP bars.	183
7.4	Strain distribution along half of the NSM CFRP bars.	184
7.5	Strain profile of beams strengthened with NSM CFRP bars.	186
7.6	Transverse strain distribution on epoxy for beams strengthened with NSM CFRP bars.	187
7.7	Deflection of beams strengthened with NSM CFRP bars.	188

7.8	Load deflection curve of beams strengthened with NSM GFRP bars.	189
7.9	Failure modes of beams strengthened with NSM GFRP bars.	190
7.10	Free end slip curves of beams strengthened with GFRP bars.	191
7.11	Strain distribution along half of the NSM GFRP bars.	192
7.12	Strain profile of beams strengthened with NSM GFRP bars.	194
7.13	Transverse strain distribution on epoxy for beams strengthened with NSM GFRP bars.	195
7.14	Deflection of beams strengthened with NSM GFRP bars.	196
7.15	Comparison of the load capacity and the corresponding deflection of strengthened beams.	197
7.16	Comparison of stiffness of strengthened beams at service load and at yielding load of the CB.	197
7.17	Modes failure of the tested RC beams.	201
7.18	Effect of NSM shape, dimensions and area on the load deflection curve of the strengthened beams.	202
7.19	Effect of NSM material and arrangement on the load deflection curve of the strengthened beams.	203
7.20	Effect of mechanical interlocking with shear connectors and transverse wrapping on the load deflection curve of the strengthened beams with CFRP bars.	204
7.21	Effect of mechanical interlocking with shear connectors and transverse wrapping on the load deflection curve of the strengthened beams with GFRP bars.	205
7.22	Comparison of stiffness of strengthened beams at service load and at yielding load of the CB.	206
7.23	Strain distribution along half of the CFRP reinforcement.	207
7.24	Strain distribution along half of the FRP reinforcement.	208
7.25	Strain distribution along half of the GFRP bars.	209
7.26	Compressive strain in concrete for beams with CFRP reinforcement.	210
7.27	Compressive strain in concrete for beams with combined FRPR.	211
7.28	Compressive strain in concrete for beams with GFRP bars.	211
7.29	Defection of beams strengthened with combined NSM FRP reinforce- ment.	212

7.30	Deflection of beams strengthened with NSM CFRP reinforcement.	213
7.31	Deflection of beams strengthened with NSM GFRP bars.	214
7.32	Effect of bond length on the load deflection curve of the strengthened beams: (a) C1 bars, (b) S1 strips, (c) G1 bars and (d) G2 bars.	217
7.33	Modes of failure of the tested RC beams.	218
7.34	Effect of end anchorage of the NSM bars and transverse wrapping on the load deflection curve of the strengthened beams: (a) C1 bars and (b) G2 bars.	219
7.35	Strain in the NSM CFRP bars.	220
7.36	Strain in the NSM CFRP strips.	221
7.37	Strain in the NSM G1 bars.	221
7.38	Strain in the NSM G2 bars.	222
7.39	Compressive strain in concrete for beams with NSM CFRP bars.	223
7.40	Compressive strain in concrete for beams with NSM CFRP strips.	224
7.41	Compressive strain in concrete for beams with NSM GFRP G1 bars.	224
7.42	Compressive strain in concrete for beams with NSM GFRP G2 bars.	225
7.43	Deflection of beams strengthened with NSM CFRP bars.	226
7.44	Deflection of beams strengthened with NSM CFRP strips.	226
7.45	Deflection of beams strengthened with NSM GFRP G1 bars.	227
7.46	Deflection of beams strengthened with NSM GFRP G2 bars.	228
7.47	Effect of NSM reinforcement on the load efficiency of the strengthened RC beams: (a) at yield load and (b) at ultimate load.	229
A.1	Calibration curves for specimen L16A1C1-2.	256
A.2	Calibration curves for specimen L16B1C1-1.	256
A.3	Calibration curves for specimen L16B1C1-2.	257
A.4	Calibration curves for specimen T16B1C1-1.	257
A.5	Calibration curves for specimen T16B1C1-2.	258
A.6	Calibration curves for specimen L15A1C2-1.	258
A.7	Calibration curves for specimen L15A1C2-2.	259
A.8	Calibration curves for specimen L16A2C1-1.	259
A.9	Calibration curves for specimen L15A2C2-1.	260
A.10	Calibration curves for specimen L12A2C1-1.	260
A.11	Calibration curves for specimen L16A1G1-1.	261

A.12 Calibration curves for specimen L16B1G1-1. 261
A.13 Calibration curves for specimen L16B1G1-2. 262
A.14 Calibration curves for specimen L16B1G1-3. 262
A.15 Calibration curves for specimen L16C1G1-1. 263
A.16 Calibration curves for specimen L16C1G1-2. 263
A.17 Calibration curves for specimen L16C1G1-3. 264
A.18 Calibration curves for specimen L16D1G1-1. 264

List of Tables

2.1	Mechanical properties of FRP and steel materials [4].	7
3.1	Concrete 1 composition in kg.	37
3.2	Concrete 2 composition in kg.	37
3.3	Adhesive properties.	38
3.4	FRP properties.	38
3.5	Configurations of the tested specimens (first series).	48
3.6	Configurations of the tested specimens (second series).	51
3.7	Configurations of the tested specimens (third series).	52
4.1	Results of the tested CFRP NSM bars (first series).	56
4.2	Results of the tested GFRP NSM bars (first series).	64
4.3	Results of the tested CFRP NSM bars (second series).	76
4.4	Results of the tested GFRP NSM bars (second series).	82
4.5	Results of the tested CFRP NSM bars (third series).	101
4.6	Results of the tested GFRP NSM bars (third series).	110
5.1	Main experimental data and results from the pullout test for specimens with CFRP bars.	125
5.2	Main experimental data and results from the pullout test for specimens with GFRP bars.	126
5.3	Values of the parameters of the concrete constitutive model [102]. . .	132
5.4	Empirical calibrations of the parameters defining the $\tau-s$ relationship (specimen L16AC1-1).	133
5.5	Empirical calibrations of parameters define the $\tau-s$ relationship (series L16AC1).	134

5.6	Values of the bond law parameters assessed by inverse analysis. . . .	135
6.1	FRP properties.	165
6.2	Test specimens' configuration of the first series.	168
6.3	Test specimens' configuration of the second series.	171
6.4	Test specimens' configuration of the third series.	172
6.5	Concrete composition for the tested beams in kg.	175
6.6	Properties of concrete for each series.	175
7.1	Results of the tested RC beams (first series).	180
7.2	Results of the tested RC beams (second series).	200
7.3	Results of the tested RC beams (third series).	216

Chapter 1

Introduction and objectives

1.1 Introduction

Reinforced concrete (RC) structures have a limited service life. Damage of reinforced structures may be the result of insufficient reinforcement, large deflections, poor concrete quality, and corrosion of steel reinforcement or insufficient capacity [1, 2]. The bonding of steel plates for the strengthening and rehabilitation of reinforced concrete structures was a popular strengthening method in the past [3]. However, corrosion of steel under certain environments can lead to deterioration of structural elements, deriving to large repair and rehabilitation costs. In order to prevent these high expenses, construction industry has tried several approaches to inhibit the corrosion of steel, but they normally appear to be either expensive or ineffective [4]. Therefore, the use of advanced composite materials for rehabilitation of deteriorated infrastructure has been embraced worldwide. Many new techniques have used the light weight, high strength and the corrosion resistance of fibre reinforced polymers (FRP) laminates for repair and retrofit applications [5, 6].

The cost of rehabilitation and repair in most cases is far less than the cost of replacement. Furthermore, repair and rehabilitation usually take less time than replacement and thus reducing service interruption time [6]. The superior mechanical and physical properties of fibre reinforced plastics (FRP) make them excellent candidates for repairing and retrofitting structures. FRPs are made of high-strength filaments such as glass, carbon, and aramid placed in a resin matrix. Glass-based composites have been readily available and fairly inexpensive. They have been used

in applications involving concrete and masonry structures. The low-tensile modulus of these composites made them ineffective for retrofitting steel structures [7].

In the past, externally bonded (EB) systems have shown their effectiveness in strengthening RC structures. The use of bonded steel plates and bars for the strengthening and rehabilitation of RC structures has been popular for years [3, 8]. Recently, several new techniques have made use of the properties of FRP laminates for repairing and retrofitting applications [2, 5, 6]. The use of externally bonded fibre reinforced polymer (EB FRP) laminates has been one of the most attractive methods for strengthening RC structures and a large number of research and practical projects have been undertaken [3, 9]. More recently, the use of near surface mounted (NSM) FRP bars has become an attractive method for strengthening RC members and masonry, thus increasing both flexural and shear strength. Over the last few years, a number of research studies concerning the use of NSM FRP for strengthening RC structures, either in shear or flexural, have been carried out [10–36].

The use of the NSM FRP technique presents several advantages over the EB FRP technique, as indicated elsewhere [20, 37, 38]. The most noteworthy advantages are that the application of NSM reinforcement does not require any surface preparation work except grooving; once the NSM reinforcement is protected by the concrete cover, it is then suitable to strengthen the negative moment regions of beams and slabs; NSM reinforcement is less prone to debonding from the concrete substrate; and furthermore, the aesthetics of a strengthened structure with NSM reinforcement are virtually unchanged.

1.2 Objectives

Since the available studies on NSM strengthening technique are still limited, the need of further experimental researches are essential to deeply understand the bond behaviour between the NSM reinforcement and concrete. Moreover the effectiveness of the NSM strengthening system on the flexural and shear behaviour of RC beams also still needs to be supported on rigorous studies able to provide reliable data to be used to propose design and prediction methods. The main objective of the present thesis is to study the bond behaviour of the NSM FRP strengthening technique and

to investigate the effectiveness of strengthening RC beams with NSM FRP rods and strips. . In order to achieve this aim, the following tasks were undertaken:

1. Review the literature focused on the bond behaviour of NSM FRP reinforcement in concrete through both pullout and flexural tests, so that the roles of the different variables involved in the bond behaviour are identified.
2. Experimentally investigate the main parameters that affect the bond behaviour of NSM reinforcement in concrete using the modified pullout test: bar diameter, type of fibers, surface configuration, adhesive properties, construction details and concrete compressive strength. Based on experimental results, the influence of the different variables on both bond behaviour and bond failure mode of specimens with NSM FRP reinforcement using the modified pullout tests should be defined and compared with previous results in the literature.
3. Using finite element analysis to study the parameter affecting the bond behaviour of NSM FRP reinforcement in concrete in dependence on the previous experimental results.
4. Experimentally investigate the flexural behaviour of RC beams strengthened with GFRP and CFRP bars/strips. The experimental programme was carried out to study the effect of FRP materials (carbon, and glass), number and area of bars, bond length, epoxy properties, and strengthening arrangement on the flexural response of RC beams strengthened with limited bond length of NSM FRP reinforcement. Modifications to enhance the capacities and to prevent the undesired modes of failure of the strengthened RC beams were also tested and discussed. According to the objectives previously described, the thesis is structured as follows:

1.3 Thesis Layout

In Chapter 2 a detailed review of the works on the study of bond behaviour of NSM reinforcement in concrete members available in the bibliography is given. First, a complete review of experimental and numerical programmes on pullout tests is presented. A special attention is given to the influence on the bond behaviour of

the main variables involved (concrete strength, bar diameter, surface configuration, adhesive properties and fibre material). Moreover, the available analytical works describing bond slip relationships that define the local bond behaviour are also presented. In a second part of the chapter, a review on the available experimental programmes on strengthened RC beams with EB and NSM is reported. Furthermore, a complete review of numerical programmes on flexural tests of RC beams is presented. Based on the analysis done in Chapter 2, this thesis is divided in two main parts. In Part I the modified pullout test is used to study the bond behaviour of NSM FRP bars in concrete. The experimental programme is described in detail in Chapter 3. The test setup and specimen dimensions, groove shapes are indicated. The instrumentation and the test variable are also explained. The material properties of the FRP bars, epoxy paste and concrete are obtained from laboratory tests. In Chapter 4, the significant experimental results of the modified pullout tests are presented and discussed. In Chapter 5 a numerical analysis of the bond behaviour based on results of the previous chapter is carried out. Analysis using the Finite Element Method (FEM) is performed using the programme FEMIX V4 which main features are firstly described. A FEM based smeared crack model is used to assess, by inverse analysis, the influence of the following parameters on the bond behaviour of the NSM FRP systems: epoxy properties, bar type, bar diameter, bond length and concrete strength. This assessment is executed by modelling a series of pullout tests in which the effect of different geometric and mechanical properties are investigated experimentally in Chapter 3. All the numerical calibrations on bond slip and force displacement curves are included in Appendix A.

The objective of Part II is to study the flexural behaviour of RC beams strengthened with NSM FRP reinforcement. In Chapter 6, the details of the flexural test to study the behaviour of RC beams strengthened with NSM reinforcement is reported. In addition details on the materials properties, test setup, test variables and configuration of beams are also given. In Chapter 7, the significant experimental results of the flexural tests are presented and discussed. Finally, in Chapter 8 conclusions are drawn and topics for future work are suggested.

Chapter 2

Literature Review

2.1 Introduction

There is an increasing demand for rehabilitation and strengthening of existing reinforced concrete (RC) structures due to deterioration, damage or need of higher structural capacity. This chapter presents a survey of the previous literature on the basic techniques used for repairing and strengthening of RC, masonry and timber structures. An overview on the relevant aspects of the externally bonded (EB) and near surface mounted (NSM) strengthening techniques is reported. Advantages of using NSM technique over the EB technique and the properties of composite materials such as fibre reinforced polymer (FRP) and other materials used in strengthening of reinforced concrete structures are investigated. A detailed review of the previous bond tests performed to study the bond behaviour of NSM FRP reinforcement in concrete are reported. Another detailed review of strengthened members is discussed focusing on the flexural strengthening of RC structures using NSM FRP reinforcement. The details of the previous analytical and numerical studies are also explained.

2.2 FRP materials

The use of the composite materials presents several advantages, such as the easier and speed installation, the smaller weight and higher durability than conventional steel reinforcements. The main disadvantage is their high initial costs. The fibre

reinforced polymer is the most widely composite material used. Fibre reinforced polymer consist of different types of fibres (carbon, glass and aramid) embedded in a polymer matrix, which usually is epoxy resin.

On the other hand, fibers from polyethylene terephthalate (PET) bottles was also used to increase the ductility of the concrete [39, 40]. The fibres were obtained by cutting the bottles. This kind of fibre was used as discrete reinforcement of small beams instead of steel bars or added to the concrete mix. Other researches were performed to assess the behaviour of concrete specimens reinforced with rheoplastic mortars [41].

Unlike steel bars, the tensile strength of FRP bars is not constant and depend on the cross sectional area. When a FRP bar is pulled in tension through the surface, a differential movement between the core and the surface fibers may occur and results a non-uniform distribution of normal stresses through the cross section of the bar [42]. FRP bars are also manufactured with several surface treatments that affect greatly their bond behaviour when used as NSM reinforcement [43]. Fig. 2.1 shows surface treatment of some available FRP bars.

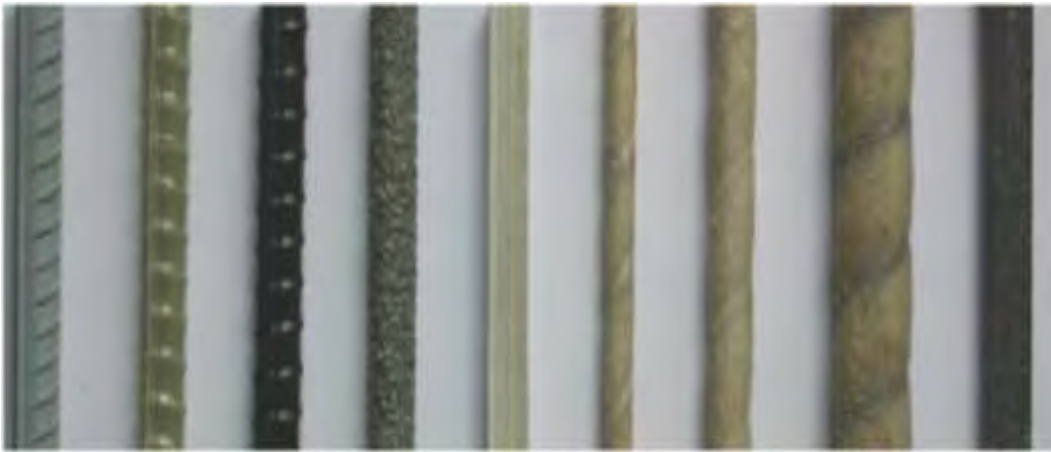


Figure 2.1: Surface treatment of some available FRP bars.

2.2.1 Mechanical properties

The Young's modulus of FRP bars are generally lower than that of steel and remain practically constant up to the failure point (elastic brittle behaviour) unlike

steel bars, for which a ductile behaviour is expected and therefore considered in design codes. Due to the lower values of modulus of elasticity, deformations expected in FRP reinforced concrete structures are larger than that of steel reinforced concrete structures. These two differences in mechanical properties will affect bond behaviour and therefore it is important to have them into consideration when developing design codes. Glass fibre reinforced polymer (GFRP) bars (having the lowest value of modulus of elasticity) are cheaper than the other types of FRP bars [4].

The tensile strength of FRP bars is higher than that of steel bars. For example, the tensile strength of GFRP bars can be more than twice the tensile strength of steel bars, whereas carbon fibre reinforced polymer (CFRP) and aramid fibre reinforced polymer (AFRP) bars can develop more than threefold, depending on the nature of fibers and matrix. A comparison of the tensile properties of FRP and steel bars is shown in Table 2.1 [4] and Fig. 2.2 [44].

Table 2.1: Mechanical properties of FRP and steel materials [4].

FRP types	Unit	GFRP	CFRP	AFRP	Steel
Fibre content	wt%	50-80	65-75	60-70	-
Density	kg/m ³	1600-2000	1600-1900	1050-1250	7850
Tensile modulus	GPa	25-55	120-250	40-125	200
Tensile strength	MPa	400-1800	1200-2250	1000-1800	400

2.3 Strengthening techniques

The main strengthening techniques of RC structures using FRP materials are the EB reinforcement and NSM reinforcement (see Fig. 2.3). The two techniques are explained in the following:

2.3.1 EB Technique

The EB technique is the method of bonding FRP sheets to the tension-side surface of concrete for reinforcing the existing RC slabs and beams. In the past, externally bonded systems have shown their effectiveness in strengthening RC structures.

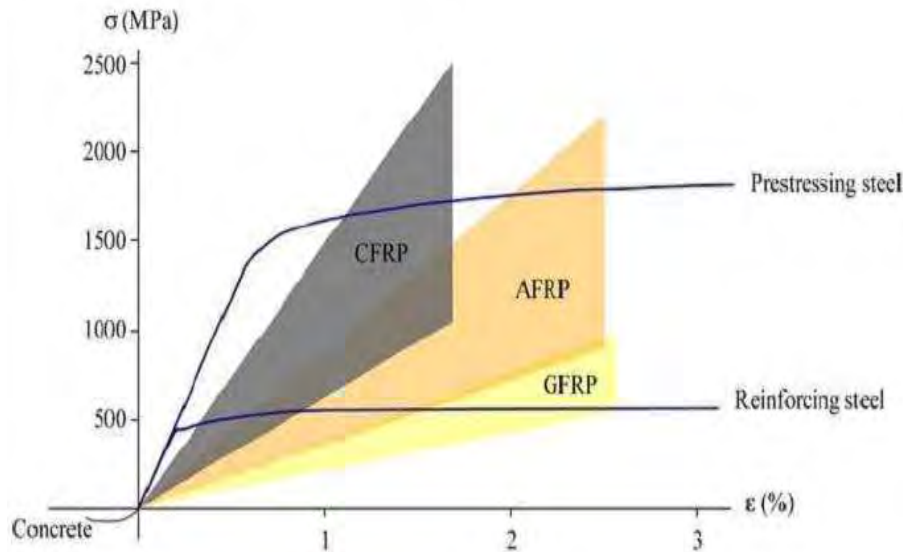


Figure 2.2: A comparison of the tensile properties of FRP and steel bars [44].

The use of bonded steel plates and bars for the strengthening and rehabilitation of reinforced concrete structures has been popular for years [3, 8]. Recently, several new techniques have used the light weight, high strength, corrosion resistant FRP laminates for repairing and retrofitting applications [2, 5, 6]

The use of EB FRP laminates has been one of the most attractive methods for strengthening RC structures and a large number of research and practical projects have been undertaken [3, 9]. Adhesively bonding FRP CFRP plates to the surfaces of RC structures is now a well-established form of retrofitting with advanced design rules and mathematical models that quantify the debonding mechanisms. However, externally bonded plates tend to debond at low strains which limit the effectiveness of this retrofitting technique [45].

The performance of the FRP-to-concrete interface in providing an effective stress transfer is an important issue. Indeed, a number of failure modes in FRP strengthened RC members are directly caused by interfacial debonding between the FRP and the concrete. One of the failure modes, referred to as intermediate crack induced debonding (IC debonding), involves debonding which initiates at a major crack and propagates along the FRP-concrete interface. The research on IC debonding of EB FRP plates has reached the stage where fundamental governing mathematical

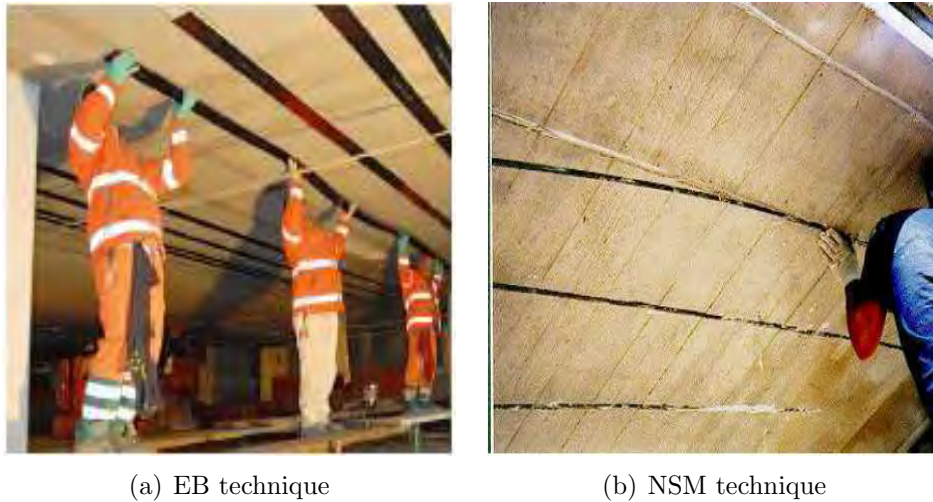
models have been established and which have both identified and quantified the major parameters governing IC debonding [46–53]. Also increasing the shear capacity of reinforced concrete (RC) beams by adhesively bonding FRP to the sides of the beam, where the fibers are in the transverse or vertical direction is now a convenient, inexpensive and well-known procedure [54–56].

2.3.2 NSM Technique

The NSM FRP has become an attractive method for strengthening RC members and masonry increasing their flexural and shear strength. In this technique, the FRP reinforcement is bonded into grooves cut into the concrete cover. The NSM FRP technique has been used in many applications and it presents several advantages over the EB FRP technique in strengthening concrete structures and masonry walls [20, 37, 38, 57–61].

The most noteworthy advantages are that the application of NSM reinforcement does not require any surface preparation work except grooving; once the NSM reinforcement is protected by the concrete cover, it is then suitable to strengthen the negative moment regions of beams and slabs; a significant decrease of harm resulting from fire, mechanical damages and other effects, NSM reinforcement is less prone to debonding from the concrete substrate, and furthermore, the aesthetics of a strengthened structure with NSM reinforcement are virtually unchanged [20, 37, 38].

Although the bond performance is greatly improved as compared with the EB system, it is still the key factor in the design of NSM FRP strengthened elements. There are two interfaces in this technique, the bar-epoxy and the concrete-epoxy, in which the bond is affected by factors which include FRP properties, FRP surface treatment, bar size, groove surface, groove geometry, adhesive, test setup and concrete properties [38]. ACI Committee 440 [1] is presently a revision of the document titled: "Guide for the Design and Construction of Externally Bonded FRP Systems for Strengthening Concrete Structures (ACI 440.2R-02)," to include such technology [20]. Based on previous studies the committee recommends the use of debonding strain of the NSM FRP reinforcement $\varepsilon_{fd} = 0.7\varepsilon_{fu}$, ε_{fu} is the ultimate tensile strain in the FRP.



(a) EB technique

(b) NSM technique

Figure 2.3: Strengthening techniques.

2.4 Installation of NSM FRP reinforcement

Details of the procedure of installation of NSM FRP laminates and bars to concrete members can be found elsewhere [18, 21, 25, 38, 62–65]. Two methods are used to form the grooves. The application of NSM laminates in concrete using the first method was discussed in detail by Barros and Fortes [21] as follows:

1- slits were cut in the concrete cover on the tension face of the beam using a diamond cutter, 2- the compressed air were used to clean the slits; 3- the CFRP laminates were cleaned by acetone, 3- the slits were filled with the epoxy adhesive, 4- the epoxy adhesive was applied on the faces of the CFRP laminates, and 5- the CFRP laminates were introduced into the slits and the excess epoxy adhesive was removed. The second method is an easy method to make grooves [62]. Before concrete casting, plastic strips with the dimensions of the needed grooves are installed at the bottom of the wooden mould in the positions needed. After concrete curing, the plastic strips were removed and the grooves are left at the bottom surface of the beam. The NSM bars or strips are applied as discussed before [21]. To applying prestressing FRP reinforcement as NSM, the NSM FRP reinforcements are pre-stressed prior to bonding [66].

2.5 Experimental research on NSM FRP bond tests

Several test methods have been proposed to study the bond of NSM FRP reinforcement. The direct and the beam pullout tests are considered the most common tests used to study the bond. Different test setups have been proposed for each of the two bond tests [42].

Fig. 2.4 shows two test setups for direct and beam pullout tests. As the NSM technique is a recent strengthening technique, few experimental researches concerning the bond behaviour are available. These researches are discussed in the following according to the test method.

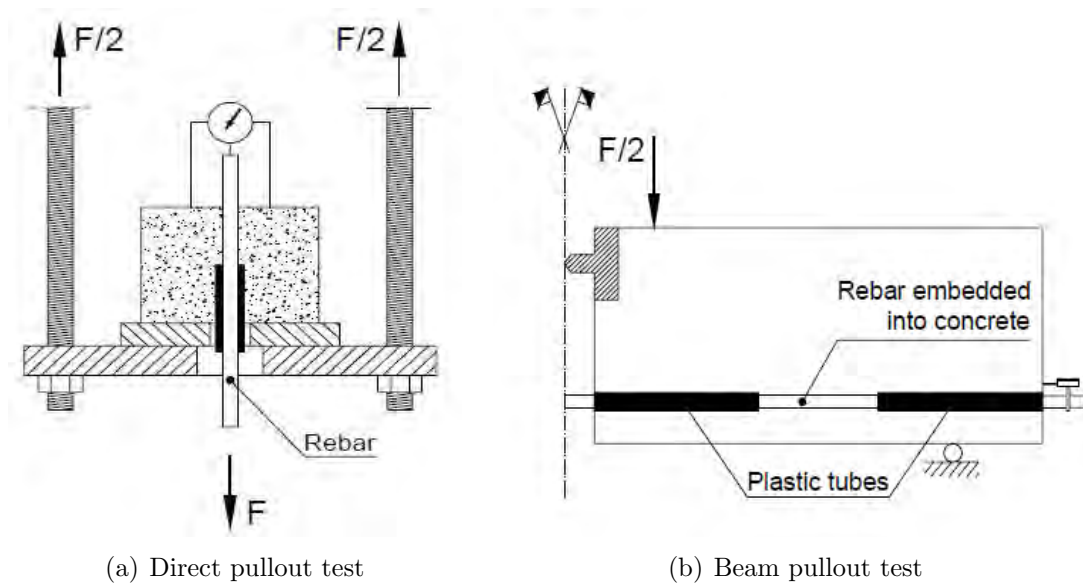


Figure 2.4: Test setup for direct and beam pullout tests [42].

2.5.1 Direct pullout tests

In recent years, a number of studies have used the pullout test [67–72] to examine NSM bond behaviour. The direct pullout test assumes several configurations, depending on the aim of the study. Due to its simplicity the modified pullout test, such as that reported in [68, 70] has been among the various setups used.

De Lorenzis et al. [68] used the modified pullout test to investigate the effect of test variables on the bond performance of NSM bars in concrete. The specimen consisted of a C-shaped concrete block with a groove in the middle for embedment of the NSM reinforcement as shown in Fig. 2.5. Two types of FRP bars (spirally wound and ribbed rods with nominal diameter of 7.5 and 9.5 mm, respectively) are used. Epoxy paste and cement mortar were used for the embedment of the NSM FRP bars. The results of the test indicated that for smooth groove surfaces, concrete-epoxy interface failure was the critical failure mechanism in NSM FRP reinforcement.

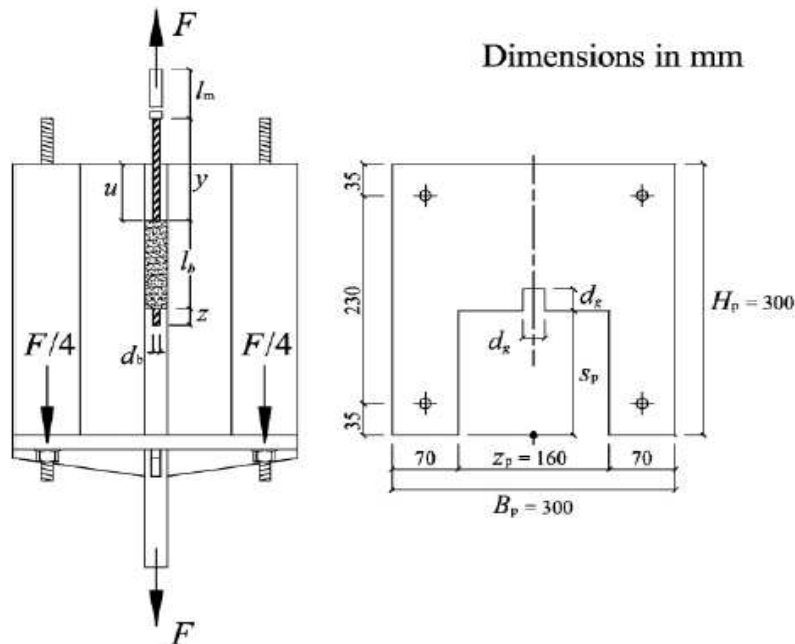


Figure 2.5: Test specimen configuration of the modified pullout test [68].

Soliman et al. [70] used the same previous configuration to study the bond behaviour of NSM bars in concrete. Bond length, type and size of FRP bars, groove width, type of adhesive and environmental conditions (normal room temperature and 200 freeze/thaw cycles) were the investigated parameters. The results showed that the main mode of failure for most of the specimens tested was concrete tension failure, with the increase in groove size not having a significant effect on the failure load. The failure load decreased as the environmental conditions changed.

The effect of construction details including groove depth and width-to-depth ratio, the distance of the groove from the edge of the member, the mechanical properties of the groove-filling epoxy, and the use of transverse FRP sheets for confinement of the joint were all studied in [69]. The specimens tested in this investigation consisted of two concrete blocks of $1000 \times 500 \times 300 \text{ mm}^3$ (Fig. 2.6). Grooves with various depths and widths were cut on these blocks. One CFRP spirally-wound and sand-coated bar (7.5 mm in diameter) was embedded in each groove as shown in Fig. 2.6. The results indicated that increasing the groove dimensions or the groove width (at a constant depth) increased the local bond strength of the NSM joint. They also showed that increasing the modulus of elasticity and the tensile strength of the adhesive increased the failure load of the NSM joints [69].

Another test setup known as the "single shear test" was also used to study the bond behaviour. This setup was used to study the bond efficiency of EBR and NSM FRP systems in the strengthening of concrete elements using various types of FRP strips and bars [71]. The specimen dimensions and test setup are shown the Fig. 2.7. The results indicated that the tensile strength of the FRP materials was better exploited by the NSM technique, with utilization factors (ratio of the tensile stresses of NSM reinforcements at the failure load to the tensile strength of FRP reinforcement) of approximately 15 % higher than those attained in EB systems.

Yan et al. [73] performed bond tests using a specimen consisting of concrete blocks $152 \times 152 \times 203 \text{ mm}^3$. The grooves were cut on two opposite faces and epoxy paste was used for the embedment of sandblasted CFRP NSM bars. The main failure mode of specimens with long length were pullout while specimens with shorter bond lengths failed by rupture of the concrete at the edge of the block.

D. Novidis et al. [72] studied experimentally the bond behaviour of NSM bars; two failure modes were observed: concrete-epoxy interface failure and bar-epoxy interface failure. The test results indicated that, increasing the groove size, increased average bond strength when failure is controlled by the interface between bar and epoxy paste. In addition, increasing the bonded length, for a given groove size, increased the load capacity of the joint.

Al-Mahmoud et al. [74], developed an experimental programme to investigate the effects of concrete strength, filling material, groove dimensions, and groove surface preparation for the CFRP rods used in the NSM technique. The pullout and the

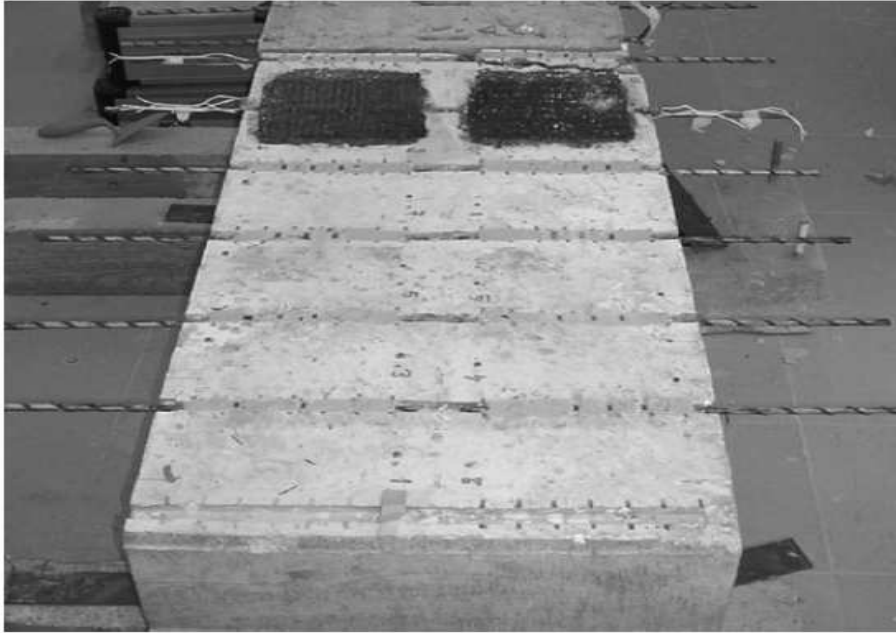


Figure 2.6: Test specimen configuration of the modified pullout test [69].

tension member tests were used to characterize the anchoring capacity of the CFRP rod and the bond between the CFRP rod and concrete in cracked RC beams. The results of the pullout test indicated that, when the mortar was the bonding material the ultimate load was always about half that obtained when the resin was used. The ultimate load increased by 15 % when sandblasting for the concrete surface was applied. The results also indicated that the optimal groove width ranged between 1.7 and 2.5 the nominal rod diameter.

Sena-Cruz et al. [75] studied the bond behaviour between glulam and GFRP rods, applied according to the NSM technique. Failure modes included glulam shear failure, interfacial failure (glulam-adhesive), interfacial failure (FRP-adhesive) and adhesive splitting. On the other hand, the maximum pullout force and the loaded and free end slips increased with bond length, while the bond strength decreased. A rougher external surface of the rod provided a better bond performance, as well as a deeper installation of the GFRP into the groove.

Seracino et al. [76] conducted a series of push-pull direct bond tests to study the influence of bond length, dimensions of the strips and concrete strength on the bond behaviour of NSM FRP strips in concrete and to develop an appropriate bond

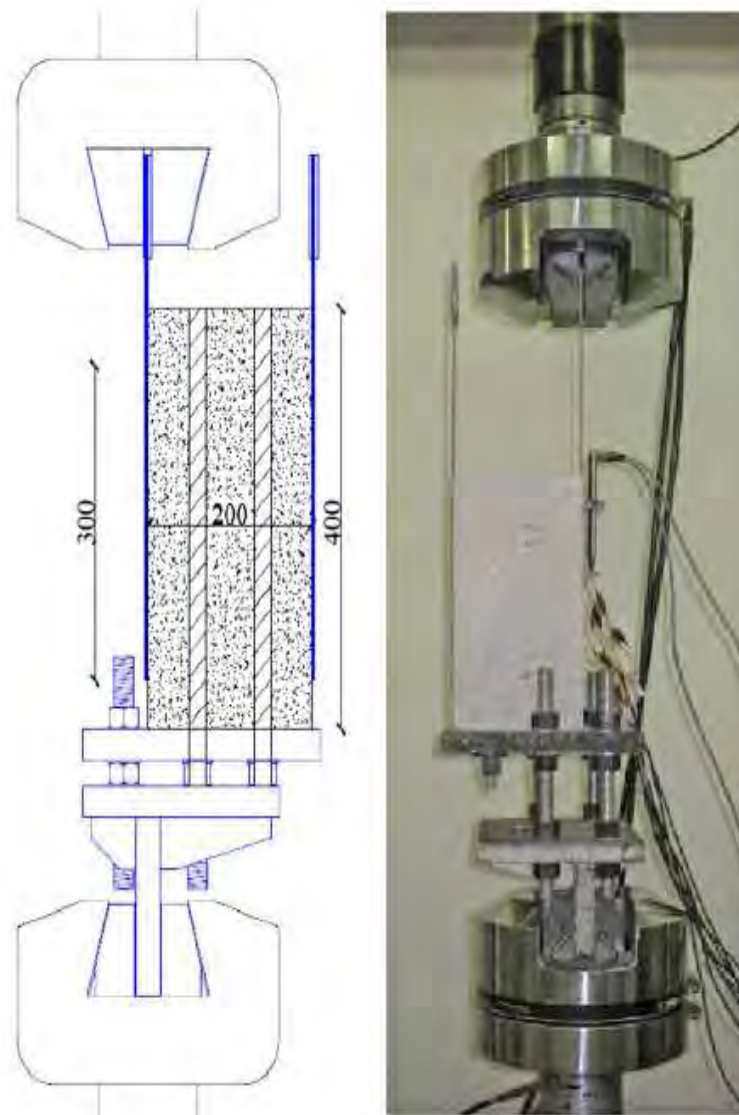


Figure 2.7: Test specimen configuration and setup of the single shear test [71].

model. The specimen dimensions and setup is shown in Fig. 2.8 the results of the test showed that the bond strength increased as the dimensions of strips increased. On the other hand, concrete strength had insignificant effect on the bond strength as the modes of failure of the tested specimens were FRP rupture, concrete- adhesive interface failure and adhesive splitting.

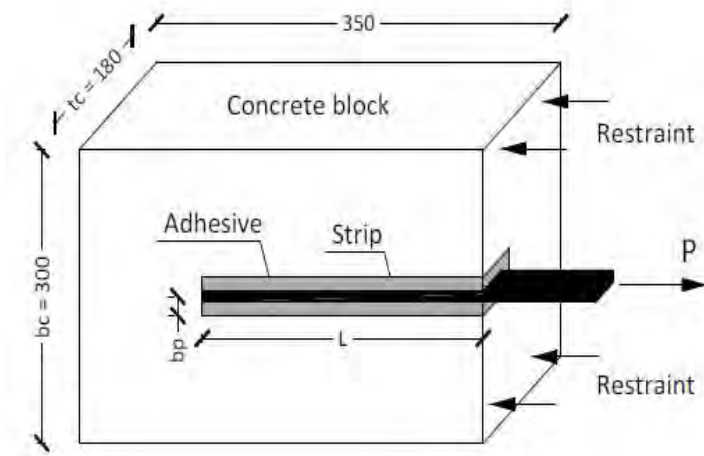


Figure 2.8: Test specimen configuration and setup [76].

2.5.2 Beam pullout tests

De Lorenzis [77] performed a beam pullout tests with inverted T-shape cross section, reinforced with GFRP and CFRP bars. The beam had a steel hinge at the top and a saw cut at bottom located at mid-span as shown in Fig. 2.9. The test variables were bond length and groove size. The vertical deflection of the beam and the end slip of the NSM bars were measured using linear variable displacement transducer (LVDTs). The test results indicated that the pullout load increased as the bond length increased. On the other hand the ribbed bars experienced higher average bond strengths than that of the sandblasted bars. The modes of failure were splitting of the epoxy cover, cracking of the concrete surrounding the groove and pullout of FRP bar.

Sena-Cruz and Barros [78] performed pullout bending tests to study the influence of bond length and concrete strength on bond behaviour of NSM CFRP strips to

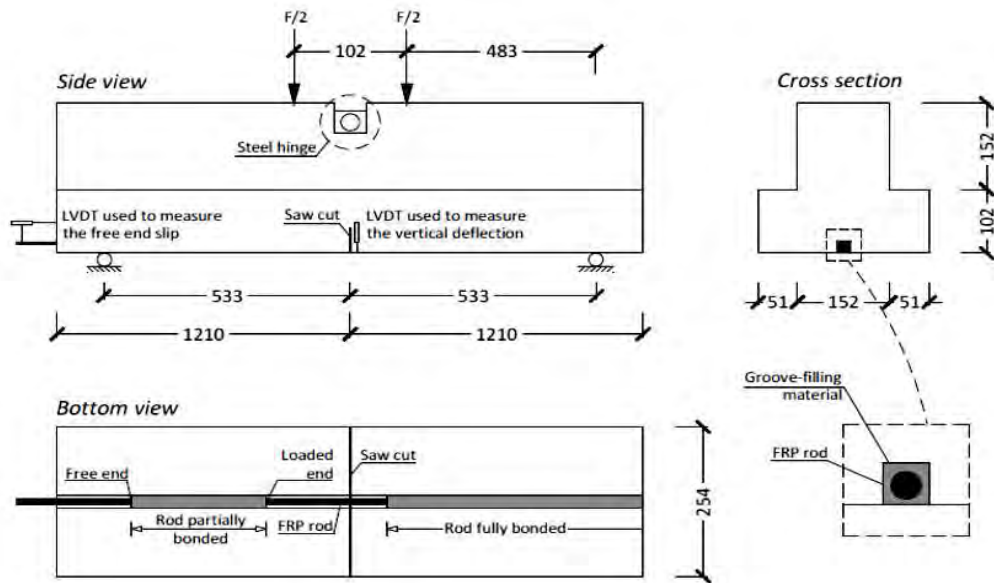


Figure 2.9: Test specimen configuration and setup of beam pullout test [77].

concrete. The specimen dimensions and test setup are shown in Fig. 2.10. The bond length and the concrete strength were the test variables. The test results indicated that the failure load increased as the bond length increased while concrete strength had marginal effects on the bond behaviour. Failure occurred at concrete-adhesive and adhesive-laminate interfaces, with the formation of cracks in epoxy paste. Other beam pullout tests with NSM square CFRP bars were also performed [79].

2.6 Bond models of NSM FRP reinforcement

Many reported studies have tried to model NSM bond behaviour using several methods. De Lorenzis et al. [68] modeled the NSM bond behaviour based on local bond slip curves derived empirically from experimental bond tests. A closed form analytical solution was proposed to predict the interfacial shear stresses [14]. The model was validated using experimental test results and nonlinear Finite Element (FE) analysis. Another model based on equilibrium and displacement compatibility using FE analysis was also reported by Hassan and Rizkalla [19].

Furthermore, an analytical bond stress slip relationship was obtained by Cruz and Barros [78] using the experimental results of the pullout-bending tests and

$$\tau(s) = \begin{cases} \tau_{max}(\frac{s}{s_{max}})^\alpha = Cs^\alpha, & 0 \leq s \leq s_{max} \\ \tau_{max}(\frac{s}{s_{max}})^{\alpha'} = C's^{\alpha'}, & s > s_{max} \end{cases} \quad (2.1)$$

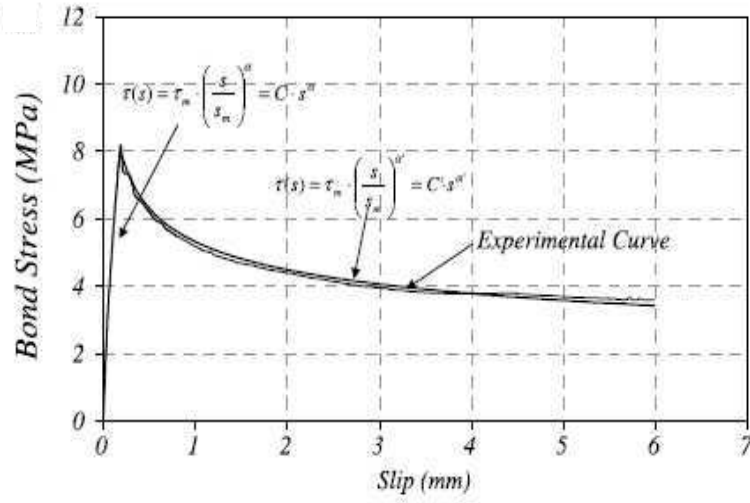
where τ is the local bond stress, s is the local slip, τ_{max} and s_{max} are bond stress and slip at the peak point, α is a parameter that varies between 0 and 1 and α' is a parameter varies between -1 and 0 and C and C' are constant. Parameters τ_{max} , s_{max} , α and α' are calibrated by best fitting of the experimental results.

Some bond tests were carried out on FRP NSM bars [15, 68] and others on NSM strips [78, 83]. Using the data derived from these tests, the local bond slip (τ - s) relations were deduced. Three types of local bond slip behaviour are reported in [15] depended mainly on the mode of failure of joints. When the bond failure occurs at the interfaces or by cover splitting, the equation (Eq. 2.1) seems to reproduce rather accurately experimental curves with a gradual decrease of local bond stress after the peak (Fig. 2.11a). The equation proposed by Sena-Cruz and Barros [78] has the same form as Eq.2.1. The second type of local bond behaviour (type II, Eq. 2.2) was observed when the failure occurred in concrete (Fig. 2.11b). The third type (for sand-blasted round bars) could be seen as a special case of the second type. In this type the decay from the maximum bond stress to the frictional bond stress is a linearly decreasing branch. Once the analytical τ - s relation is known, it can be used to analytically solve all problems related to bond behaviour [68].

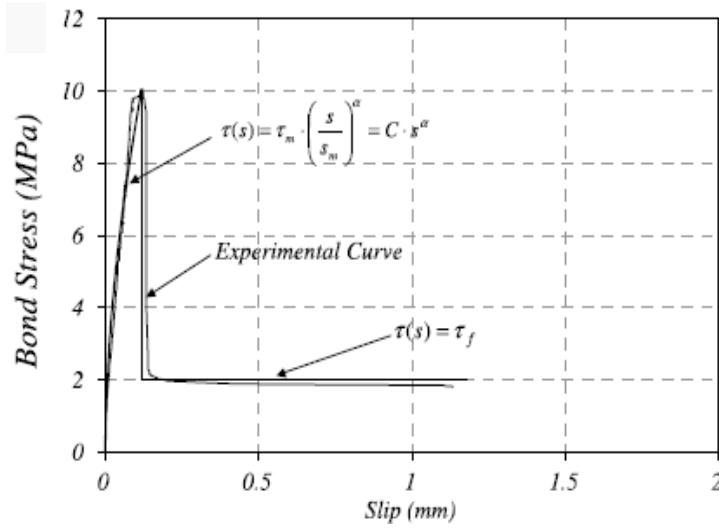
$$\tau(s) = \begin{cases} \tau_{max}(\frac{s}{s_{max}})^\alpha = Cs^\alpha, & 0 \leq s \leq s_{max} \\ \tau_f, & s > s_{max} \end{cases} \quad (2.2)$$

The bond behaviour of the NSM round deformed bars is strongly dependent on the splitting tensile stresses in the epoxy cover and in the surrounding concrete. De Lorenzis [77] and Hassan and Rizkalla [14] modeled the bond behaviour in the plane perpendicular to the bar axis using the approach proposed by Tepfers [84]. The following two assumptions are considered: - The frictional coefficient(μ) relating bond shear stress and internal splitting pressures is constant. - The radial pressure distribution is considered uniform.

Hassan and Rizkalla [19] proposed a model for cover splitting failure, based on elastic FE methods, which leads to the following two formulas:



(a) Type I



(b) Type II

Figure 2.11: Typical bond slip curves of NSM FRP reinforcement [15].

$$\tau_{max \text{ epoxy-concrete}} = \frac{f_{at}\mu}{G_1} \quad (2.3)$$

$$\tau_{max \text{ bar-epoxy}} = \frac{f_{at}\mu}{G_2} \quad (2.4)$$

where f_{at} is the tensile strength of epoxy, f_{ct} is the axial tensile strength of

concrete, and G1 and G2 are coefficients that were evaluated by FE analysis and are dependent on the groove depth-to-bar diameter and groove width-to-bar diameter ratios.

The use of strips in the NSM FRP technique is a very advantageous choice to increase the bearing capacity of concrete columns or beams. Several pullout bond tests were carried out to study the behaviour of NSM strips in concrete. The approach proposed by Blaschko [83] is given by:

$$\tau_{max} = 0.2\sqrt[4]{a_e} \cdot \tau_{af}, \quad a_e \leq 150mm \quad (2.5)$$

where τ_{af} is the shear strength of the epoxy.

On the other hand Hassan and Rizkalla's formula is given by:

$$\tau_{max} = \frac{f_c f_{ct}}{f_c + f_{ct}} \quad (2.6)$$

where f_c and f_{ct} are the compressive and tensile strengths of concrete, respectively. The main difference between the previous formulas is discussed in detail in [38].

2.7 Flexural behaviour of strengthened RC beams

2.7.1 Laboratory works and tests setup

This section deals with the laboratory work performed to study the flexural behaviour of RC beams strengthened using NSM reinforcement. The details of the tested beams, test setup, test variable and the obtained results are reported and discussed. The installation of NSM FRP reinforcement to concrete elements was already discussed in section 2.4

2.7.1.1 Strengthened beams with limited bonded lengths of NSM FRP reinforcement

De Lorenzis and Teng [38] provided a detailed and critical review of existing research on the flexural behaviour of concrete structures strengthened with NSM FRP reinforcement. From this review it was concluded that the existing work is

still limited in both scope and depth, and many questions remain to be answered before the technique can be widely accepted by practicing engineers.

De Lorenzis et al. [85] performed an experimental programme to study the flexural and shear strengthening of reinforced concrete structures with near surface mounted FRP rods. Four full-scale RC beams with a T-shaped cross-section and a total length of 4.5 m were tested in flexural. The beams were loaded under four-point bending with a shear span of 1830 mm, and were instrumented to record deflections along the beam span, and strains in concrete, steel reinforcement and NSM bars. The test results indicated that increasing the amount of the NSM reinforcement (doubled) does not produce a significant gain in capacity (11 %).

Tang et al. [62] performed an experimental work to study the effect of type of concrete (lightweight polystyrene aggregate concrete and normal concrete), type of reinforcing bars (GFRP and steel), and type of adhesive on the flexural behaviour of RC members strengthened with NSM GFRP bars. The beams experienced an increase in ultimate moment ranging from 23 % to 53 % the un-strengthened beams. On the other hand epoxy type controlled the moment-deflection response up to the peak moment.

De Lorenzis et al. [86] performed an experimental test to investigate the effect of changing the ratio of internal steel reinforcement and the ratio of FRP superficial reinforcement on the flexural behaviour of RC beams strengthened with NSM bars reinforcement. The test results confirmed that NSM FRP rods significantly increase the flexural capacity of RC elements. In the tested beams, an increase in the ultimate load ranging from 21.3 % to 60.6 % was achieved. The failure mode was concrete crushing after yielding of the steel longitudinal reinforcement for the beams with the higher steel reinforcement ratio, and splitting of the concrete cover of the steel longitudinal reinforcement accompanied by debonding of the NSM rods for the other beams.

Hassan and Rizkalla [19] studied the bond mechanism of NSM FRP bars for flexural strengthening of concrete structures. The test results suggested that the development length of NSM CFRP bars with the given groove dimensions and material properties used in this programme should not be less than 80 times the diameter of the bars. Changing the type of epoxy adhesive had a negligible effect on ultimate load capacity of the strengthened beams.

The results of the experimental tests carried out by De Lorenzis et al. [87, 88] illustrated that the ultimate load increased as the bond length of the rod increased and the resistance to splitting increased as the groove size increases (i.e. the epoxy cover increased).

Three specimens were used to study the flexural behaviour of RC beams reinforced with NSM AFRP rods [89]. The axial stiffness (EA) of reinforcing material was varied by changing the FRP bar size. The tested beams reached the ultimate state with AFRP rod debonding failure mode. Other tests were performed to study experimentally the strengthening of concrete structures with square NSM CFRP bars [59]

El-Hacha and Rizkalla [18] studied experimentally the FRP reinforcement for flexure strengthening of RC structures. CFRP bars were used as NSM reinforcement while the CFRP and GFRP strips were used either as NSM or EB. The results showed that using the same CFRP strips as NSM increased the strength of strengthened beams by approximately 4.8 times that obtained using externally bonded CFRP strips.

Jung et al. [90] studied the flexural behaviour of RC beams strengthened by EB and NSM FRP reinforcement. Eight beams were casted and tested. One unstrengthened denoted as control beam, two beams were strengthened with EB strips, two with NSM strips, one with an NSM rod, and two with NSM reinforcement with mechanical interlocking grooves Fig. 2.12. The beams strengthened with NSM strips experienced higher moment capacity than that with EB strips. The same observation was reported by Taljsten and Nordin [91]. On the other hand, the mechanical interlocking grooves prevented the premature debonding of the FRP and improved the efficiency of NSM systems.

Al-Mahmoud et al. [27] studied experimentally and analytically the strengthening of RC members with NSM CFRP rods. The dimensions, reinforcement details and test setup of the beams are shown in Fig. 2.13. In this study the effect of CFRP length, filling type, CFRP section and concrete compressive strength on the behaviour of strengthened beams were studied.

The beam strengthened by CFRP rods and bonded with mortar showed a debonding of the mortar from the groove. On the other hand, when the failure was NSM system failure (i.e. epoxy failure, FRP rupture and failure at bar-epoxy and concrete-

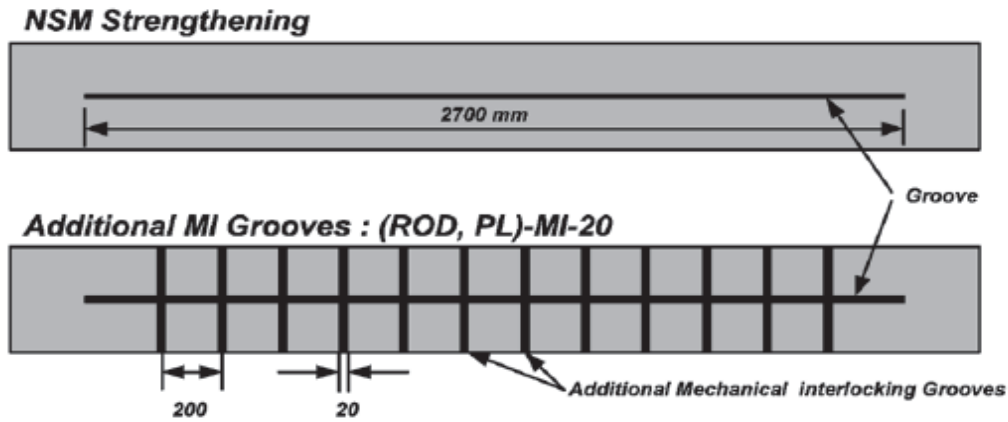


Figure 2.12: Plan view of the NSM strengthening with mechanical interlocking grooves [90].

epoxy interfaces), the concrete strength had insignificant effect on load carrying capacity of the strengthened beam.

The behaviour of RC beams strengthened using high performance CFRP bars with a trapezoidal cross section as NSM was experimentally studied in [24]. The results of the tested beams showed that, the increase in load carrying capacity of strengthened beams ranged between 14.2 % and 55.1 % over that of the control beam depending mainly on the strengthening methodology. On the other hand, using the CFRP trapezoidal bars in the concrete groove in combination with bolted U-type metal fittings achieved the best composite action.

Al-Mahmoud et al.[28] studied experimentally the strengthening of concrete structural members with NSM CFRP rods. Analytical and FE models were also performed to predict the peeling-off failure mode. The factors studied were the bond length and the type of loading. The test results showed that, the failure mode is pullout of CFRP rods if the strengthening length is sufficient to avoid the intersection between the shear cracks initiated by a bending crack and the CFRP rods end otherwise the failure was concrete peel-off. On the other hand cantilever strengthened beams experienced the same failure modes as the beams tested in four point flexure without any effect of strengthening outward pressure.

Wahab et al. [92] studied the bond behaviour of concrete beams strengthened with NSM non-prestressed and prestressed CFRP rods. The failure mode for the

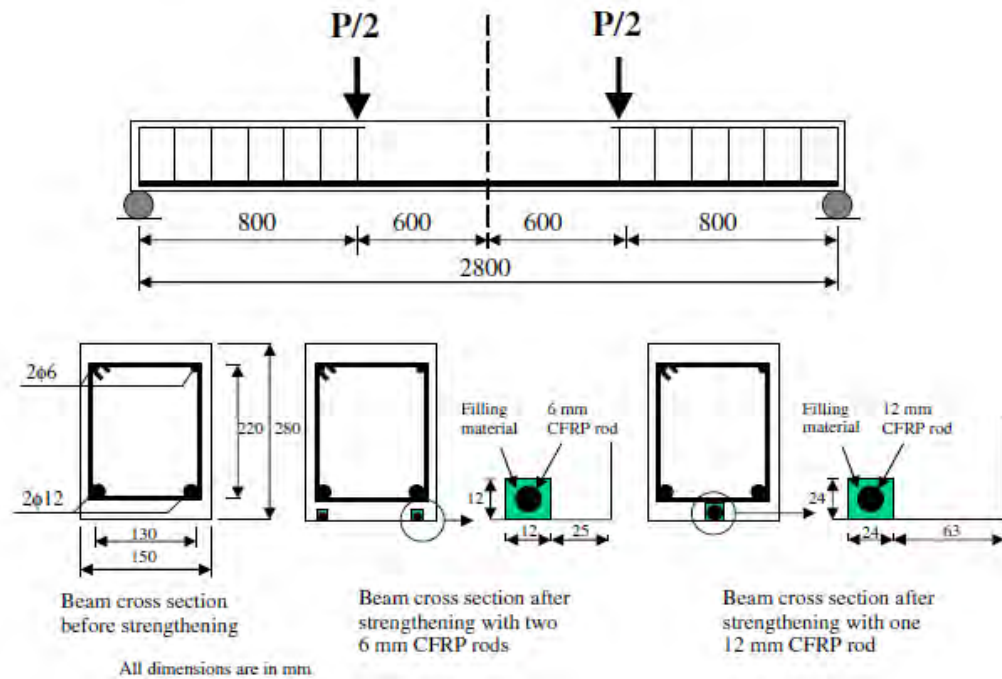


Figure 2.13: Details and setup of the tested beams [27].

non-prestressed beams was caused by CFRP rod pullout while the failure mode of the prestressed strengthened beams depended on the type of rod used.

Kalayci et al.[32] carried out an experimental programme to identify the effects of groove size tolerance on NSM FRP systems. The results indicated that the groove size tolerances within the range studied did not affect the response of the strengthened beams with either NSM strips or bars. The main failure modes were epoxy splitting and concrete splitting for specimens with small and large grooves respectively.

A total of nine concrete T-beams were fabricated to study the effect of changing the number and spacing of NSM strips, and the number and the width of EBR CFRP strips in [65]. The test results indicated that strengthening with NSM CFRP reinforcements did not contribute to increase the stiffness and strength in the elastic range. However, after cracking the NSM CFRP strips increased the flexural stiffness and strength of the beams. Failure of the beam reinforced with NSM and EBR strips is initiated by debonding of EBR strips attached on the bottom face then partial separation of NSM strips along the longitudinal direction occurred.

Barros and Fortes [21] studied experimentally the flexural strengthening of concrete beams with CFRP laminates bonded into slits. The test specimen's details are shown in Fig. 2.14. The results of the tested beams showed that this strengthening technique (designated as NSM) assured an average increase of 91 % on the ultimate load of the tested RC beams. On the other hand, the main failure mode of the strengthened beams was characterized by the detachment of a layer of concrete at bottom of the beam (see Fig.2.15).

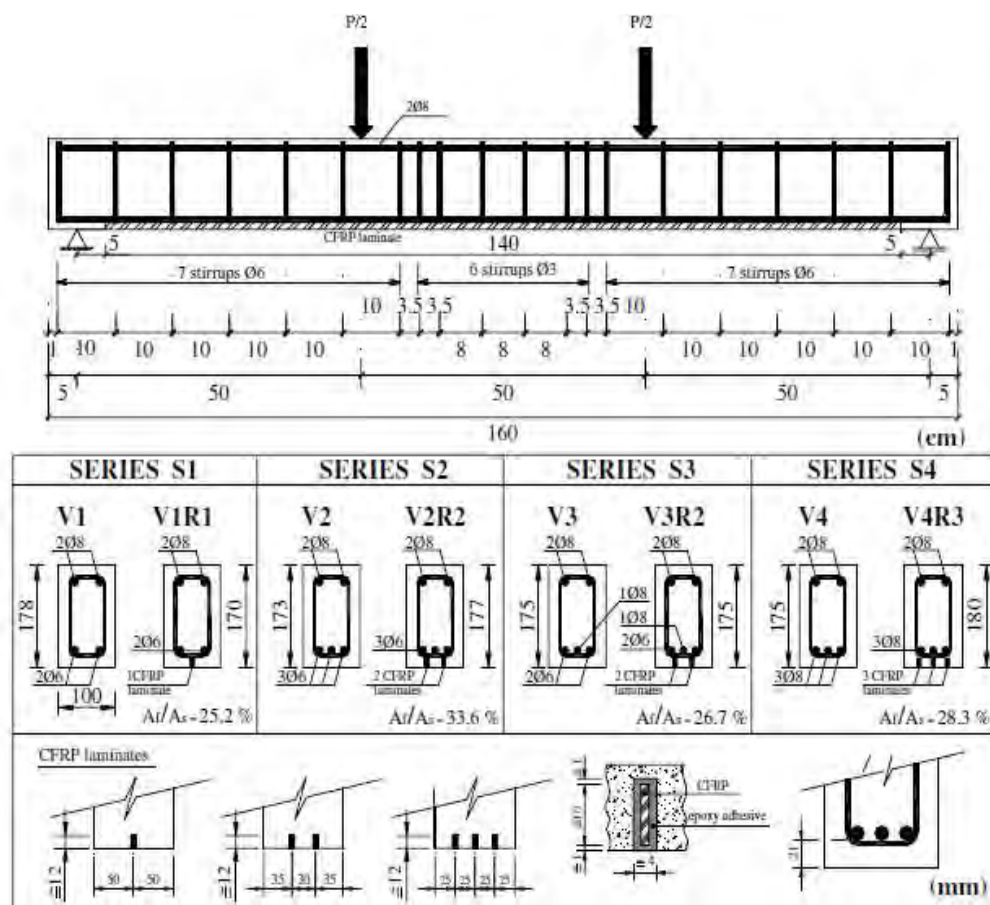


Figure 2.14: Details of the tested beams [21].

The influence of cutting the bottom arm of steel stirrups to install NSM strips for the flexural strengthening of RC beams was studied in [30]. The test results showed that, cutting the bottom arm of the steel stirrups for the installation of CFRP strips led to a decrease in the beam load carrying capacity of less than 10 %, compared to the reference beam (with intact steel stirrups).



Figure 2.15: Failure mode of the tested beams [21].

The load capacity of the beam strengthened with NSM CFRP strips increased by 50 % (the bottom arm of the steel stirrups cut for the installation of CFRP strips). Other researches were performed the study the flexural behaviour of strengthened beams with NSM FRP strips or laminates [14, 23, 58, 80, 81, 93–95]

2.7.1.2 Strengthened beams with partially bonded lengths of FRP reinforcement

Choi et al.[33] studied experimentally the behaviour of RC beams with partially bonded strengthening reinforcement utilizing NSM CFRP bars with the specific objective of improving deformability. The results of the tested beams indicated that the stiffness of the beams at the post-yielding stage decreased as the unbounded length increased. The deformability of the partially bonded beams increased as the load increased after yielding. The ultimate load capacity slightly decreased as the unbounded length increased while the ultimate deflection in the partially bonded beams at failure had a slight increase compared to the fully bonded beam.

Soliman et al.[31] studied experimentally the effect of the internal steel reinforcement ratio, type of NSM FRP bars, FRP bar diameter, bond length, and groove size on the flexural behaviour of concrete beams strengthened with NSM FRP bars. The ratios of the internal reinforcement were 0.4 %, 0.8 % and 1.6 %. The results showed that increasing the bond length from $24d_b$ to $48d_b$ (d_b is the diameter of CFRP rod) increased the ultimate capacity by 29% while the ultimate capacity increased by 3%

only increasing as the bond length increased from $48 d_b$ to $60 d_b$ (i.e. A bonded length of 48 times the bar diameter was indicated as a limit beyond which there was no increase in the load capacity of the strengthened RC beams with increasing the bonded length). Using small groove size increased the distance between NSM FRP bar and steel reinforcement achieving higher capacities. On the other hand, GFRP bars increased the ductility compared to CFRP bars, with nearly similar increase in capacity. The main mode of failure for the strengthened beams was debonding in the form of concrete cover splitting.

2.8 Failure modes and mechanisms of NSM reinforcement

In this section the observed modes of failure of the NSM FRP system (Figs. 2.16 and 2.17) have been discussed. several modes of failure can be obtained when testing the bond behaviour of FRP NSM systems as shown in (Fig. 2.16). The bond failure at the bar-epoxy interface may occur as either pure interfacial failure (BE-I), or as cohesive shear failure in the groove filler (BE-C). On the other hand, bond failure at the epoxy-concrete interface may occur as pure interfacial failure (EC-I), or as cohesive shear failure in the concrete (EC-C). The failure caused by splitting of the epoxy cover is observed as the critical failure mode for deformed (i.e. ribbed and spirally wound) round bars. Detailed analysis of the above modes of failure is reported in [38].

In addition to the aforementioned modes of failure, Concrete crushing and FRP rupture may also occur in RC beams strengthened by NSM reinforcement (see Fig. 2.17). The concrete crushing failure occurs when the concrete reaches its crushing strain before the FRP NSM reinforcement fails. The FRP rupture takes place when concrete crushing and the debonding failure are prevented. The existing researches indicate that FRP rupture is more likely for the NSM strips than for NSM bars.

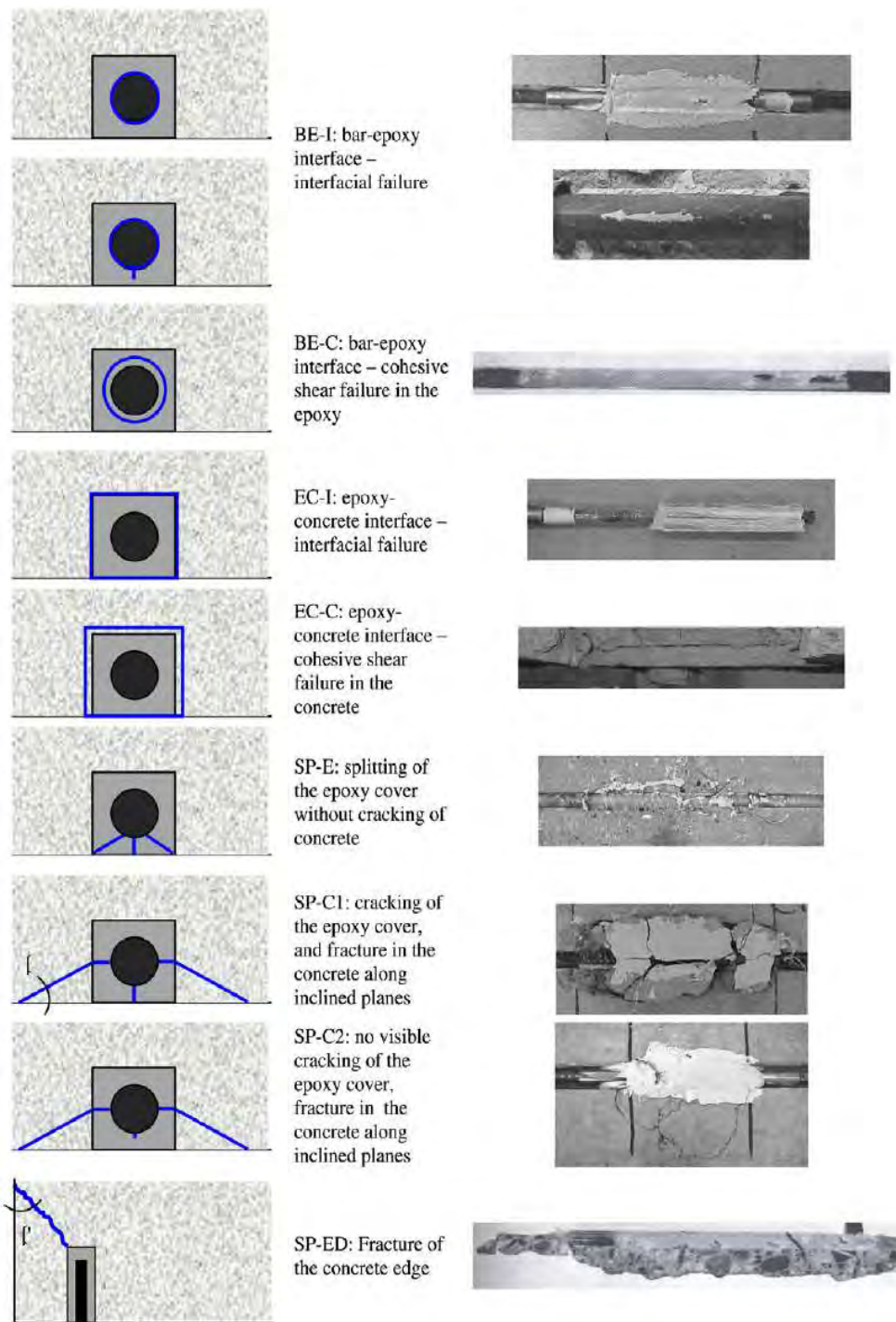


Figure 2.16: Bond failure modes of NSM systems observed in bond tests [38].

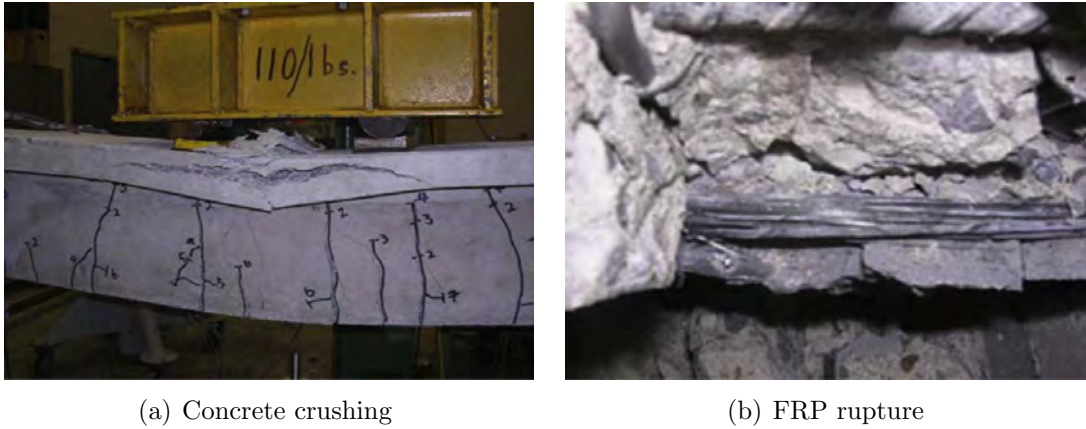


Figure 2.17: Failure modes observed in strengthened RC beams with NSM reinforcement [33].

2.9 Conclusions of the literature review

From the analysis of the previous literature review the following main conclusions can be drawn:

1. The use of NSM FRP rods/strips is an effective technique to enhance the stiffness and flexural capacity of RC beams. The development length of the NSM FRP reinforcement is highly dependent on the dimensions of the bars, concrete, adhesive properties, reinforcement configurations and groove width. On the other hand, the bond characteristics have a great effect on the performance of the NSM technique.
2. When controls the failure, increasing the amount of the NSM reinforcement does not produce a significant gain in the load capacity of the joint. On the other hand, when the failure is NSM system failure (bar-epoxy or concrete-epoxy interface failure and bar rupture), the concrete strength has no effect on the load capacity of the strengthened beam. Moreover, high strength concrete increases the resistance to concrete splitting failure. Moreover, when the failure is governed by damage on concrete or epoxy, the use of high modulus FRP have insignificant influence in the load capacity of the RC strengthened beams.
3. Increasing the bonded length increases the load capacity of the strengthened RC beams. A bonded length of 48 % times the bar diameter was indicated

as a limit beyond which there was no increase in the load capacity of the strengthened RC beams with increasing the bonded length [31]. In contrast, the test results reported in [19] suggested that the development length of NSM CFRP bars with the given groove dimensions and material properties used in this programme should not be less than 80 times the diameter of the bars. Further work is needed to discuss the limit of the development length.

4. When small groove sizes are used, the distance between the NSM bar and the internal steel reinforcement increases, which delays the concrete cover splitting and increases the load capacity of the strengthened RC beams. A minimum clear spacing of twice and four times the diameter were proposed between two adjacent grooves and from the edge of the beam respectively.
5. There is no effect of the loading type for beams strengthened by CFRP rods which had the same failure modes without any effect of the strengthening outward pressure. On the other hand, the partially bonded beams experienced a slight increase in the ultimate deflection compared to the fully bonded beams with slight decrease in the ultimate load carrying capacity as the bonded length decreases.
6. Although the NSM FRP methodology presents some advantages over the EB FRP technique (improved bond, protection, aesthetics), concrete beams strengthened with NSM GFRP, NSM AFRP or NSM CFRP may present relatively low values of the strength efficiency when the failure of the strengthened beams is due to pullout or concrete cover separation.
7. Due to limited experimental research into the NSM technique compared to the EB technique, there is no general formulation to predict the failure load of NSM joints. Although the previously mentioned studies have made significant contributions to the understanding of the bond behaviour of NSM FRP and concrete, the large number of factors involved makes it necessary to carry out further experimental work to have more data available to arrive to a better understanding of the different parameters influencing the design of this system.

Part I

Study of bond behaviour of NSM FRP bars in concrete using the modified pullout test

Chapter 3

Pullout test experimental programme

In this chapter a detailed description of the pullout test programme was reported. Three series of experimental tests have been performed to investigate the bond behaviour of near surface mounted (NSM) fibre reinforced polymer (FRP) in concrete. The choice of the study parameters, the mechanical properties of the materials used, the specimen preparation, the experimental setup, instrumentation and the testing procedure are presented.

3.1 Introduction

The use of the near surface mounted (NSM) technique has become a popular method for strengthening reinforced concrete (RC) members and masonry, thereby increasing both flexural and shear strength [20]. Although bond performance is greatly improved as compared with the externally bonded (EB) system, it is still the key factor in the design of NSM fibre reinforced polymer (FRP) strengthened elements. There are two interfaces in this technique, the bar-epoxy and the concrete-epoxy, in which the bond is affected by FRP properties, FRP surface treatment, bar size, groove surface, groove geometry, adhesive, test setup and concrete properties [38]. In recent years, a number of studies have used the pullout test [67–71, 76] to examine NSM FRP bond behaviour. Due to its simplicity the modified pullout test setup, such as that reported in ([68, 70], Fig. 3.1), has been widely used.

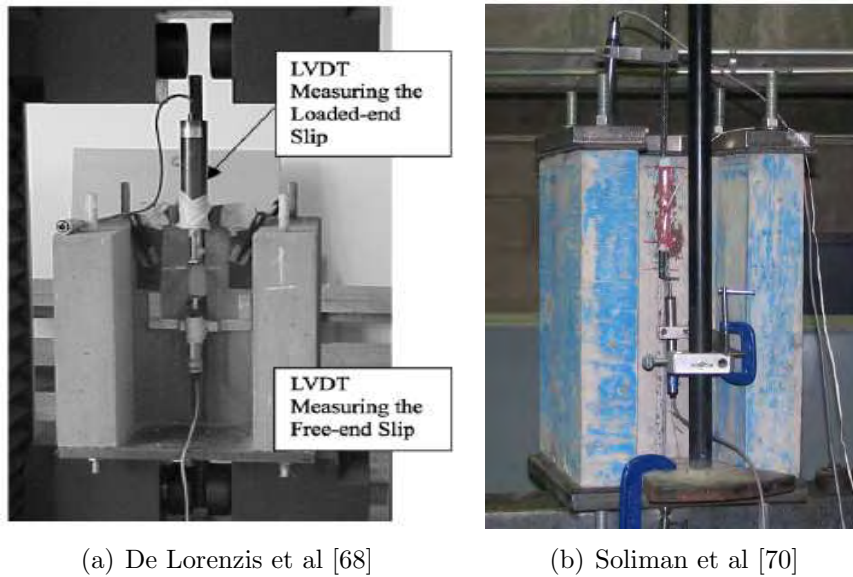


Figure 3.1: Pullout tests arrangements.

3.2 Materials

3.2.1 Concrete

All the test specimens were cast using ready mixed concrete. Two different concrete strengths, concrete 1 and concrete 2, were used. The composition of delivered concrete is given in Tables 3.1 and 3.2 for concrete strengths 1 and 2 respectively. The specimens were cast in separate batches of six specimens per batch. For each batch of concrete, standard control samples ($150 \times 300 \text{ mm}^2$ cylinders) were cast and cured under the same conditions as the specimens. The control samples were tested in direct compression (three standard specimens) to determine the concrete strength in compression. Others (two standard specimens) were tested under splitting test to determine the tensile strength. For concrete 1, the average compressive strength of the different batches ranged between 22 and 25 MPa, while the average tensile strength ranged between 2.2 and 2.5 MPa. On the other hand, for concrete 2, the average compressive strength of the different batches ranged between 35.2 and 42.2 MPa, while the average tensile strength ranged between 2.9 and 3.2 MPa.

Table 3.1: Concrete 1 composition in kg.

Component	Quantity
Water	120
Cement I52.5	260
Sand 0/4	641
Sand 0/4	200
Gravel 15/25	500
SIKAMENT 390	1.20% weight of cement

Table 3.2: Concrete 2 composition in kg.

Component	Quantity
Water	$\leq 0.6\%$ weight of cement
Cement	280
Course aggregate	1060
Course aggregate 20 mm	660
Course aggregate 15 mm	120
SIKAMENT 90P	1.20% weight of cement
SIKAMENT 500	0.5% weight of cement

3.2.2 Epoxy

Two main types of epoxy resins were used for the embedding of the NSM bars, which resulted in four different types of adhesive, as explained below. The first type (A), MBRACE ADHESIVE HT (BASF), consisted of primer and epoxy paste. According to the manufacturer, a first layer of fluid "primer" must be applied to assure good bonding between the epoxy and the concrete, followed by the application of the epoxy between 90 minutes and 48 hours after the primer, with a curing time of approximately 3 days. The second type of resin was POLYFIXER EP (ROBERLO). The properties of this resin were modified by adding a special additive (Polypropylene glycol diglycidyl ether, Grilonit® F 704) with two different percentages (1.88%, 3.76%) in order to obtain resins with different properties, in such a way that finally three more types of adhesive were obtained: the non-modified resin (B), and two modified resins (C, D). Table 3.3 indicates the material properties for the four adhesives obtained from the experimental tests.

Table 3.3: Adhesive properties.

Epoxy ID	Product	Additive (%)	$E_{r,c}$ (MPa)	$f_{ru,c}$ (MPa)	$\varepsilon_{ru,c}$ (-)	$f_{ru,t}$ (MPa)	$\varepsilon_{ru,t}$ (-)
A	BASF	-	5761	70.15	0.00199	18.8	0.0045
B	ROBERLO	-	8000	95.5	0.0244	23.0	0.0051
C	ROBERLO	1.88	7163	85.3	0.0231	22.3	0.0062
D	ROBERLO	3.76	6900	84.3	0.0227	21.0	0.0081

$E_{r,c}$ = compressive modulus ; $f_{ru,c}$ = compressive strength; $\varepsilon_{ru,c}$ = ultimate compressive strain; $f_{ru,t}$ = tensile strength; $\varepsilon_{ru,t}$ = ultimate tensile strain.

3.2.3 FRP bars and steel

GFRP and CFRP bars were used. Table 3.4 indicates the characteristics and average mechanical properties of the four types of FRP bars used (MBRACE, ASLAN, G1 and COMBAR). The surface texture of the FRP bars is also illustrated in Fig. 3.2. Steel plates ($192 \times 50 \times 1.6 \text{ mm}^2$ and $54 \times 16 \times 1.6 \text{ mm}^2$) and threaded steel rods (6 mm in diameter and 80 mm long) were used to add shear transmission capacity and confinement to the bonded zone.

Table 3.4: FRP properties.

FRP ID	FRP material	d_b (mm)	f_{fu} (MPa)	E_f (GPa)	Surface treatment
C1	CFRP	8	2350	170	SST
C2	CFRP	9	2010	134	ST
G1'	GFRP	9.28	765	41	SC, HW
G1, G2	GFRP	8, 12	1350	64	GR

SC=sand coating, SST=smooth surface texture, ST=surface texture, HW=helical wrapping, GR=grooves.

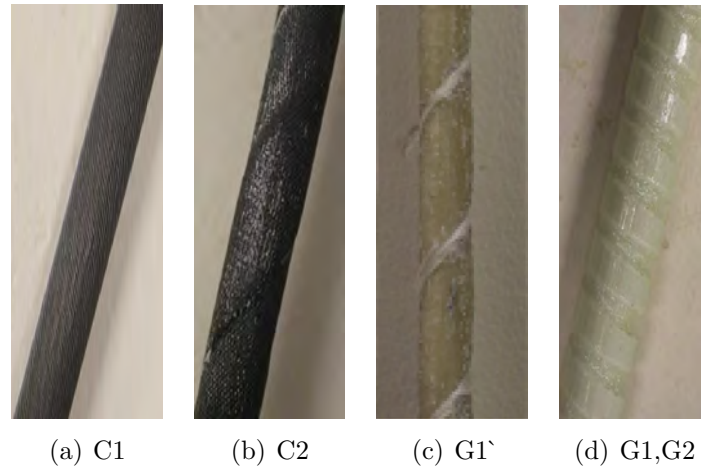


Figure 3.2: Surface treatment of the FRP bars.

3.3 Specimens preparation

3.3.1 Mould preparation, casting and curing procedure

The moulds used for casting C-shaped concrete specimens were made of metal shown in Fig. 3.3. Before each casting, the inside of the mould was coated with a thin film of oil to make easier the demoulding of concrete specimens (see Fig. 3.3). After moulding, specimens were kept in the mould for 24h. Thereafter, the concrete specimens were demoulded and covered using wet fabric and plastics for three weeks then the specimens were marked and kept in the lab temperature until testing.

3.3.2 Preparation of the grooves

In this study, two types of grooved surfaces were studied. The first type was formed using a piece of wood attached to the concrete mould before casting. The other type was formed by making two saw cuts and using a manual hammer to complete the groove formation. Before bonding the NSM bars to the pre-formed grooves, an abrasion tool was used to remove 1 mm (weak cement layer) from each groove side. The grooves were cleaned using compressed air. In first series, the two types of grooved surfaces were studied while only the saw cut grooves were studied in other series (second and third series).



Figure 3.3: Mould preparation and casting.

3.3.3 Bonding of NSM bars

To bond the bars to the concrete specimens using adhesive MBRACE (BASF), the grooves were painted using the first component of the adhesive system (primer). According to the manufacturer a first layer of fluid (primer) must be applied to assure good bond between epoxy and concrete, and the epoxy resin must be applied between 90 minutes and 48 hours after the primer, having a curing time of approximately 3 days. In this study the epoxy resin to bond the NSM FRP bars was applied 24 hour after the primer, and in all cases testing was performed 3 or 4 days after the application of the main part of the adhesive. The other type of adhesive (Roberrlo) was used directing to bond the FRP bar. Steel tubes bonded

to the loaded ends of the bars were used to grip the FRP to the testing machine. The lengths of the bonded steel anchors had been tested previously to prevent the slip of the FRP bars from the gripping system prior to FRP rupture. The procedure of the bonding process is explained in Fig. 3.4

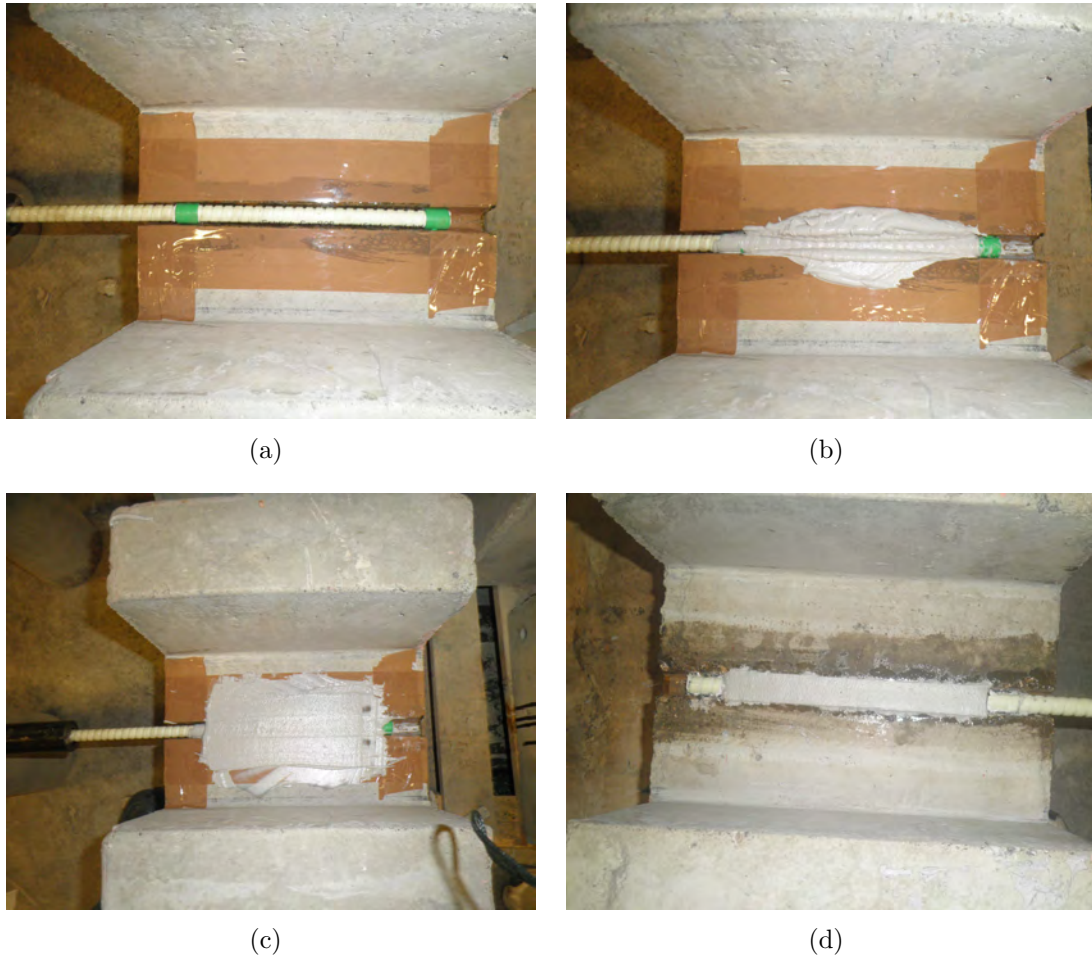


Figure 3.4: Bonding of NSM bars.

3.4 Specimen configurations

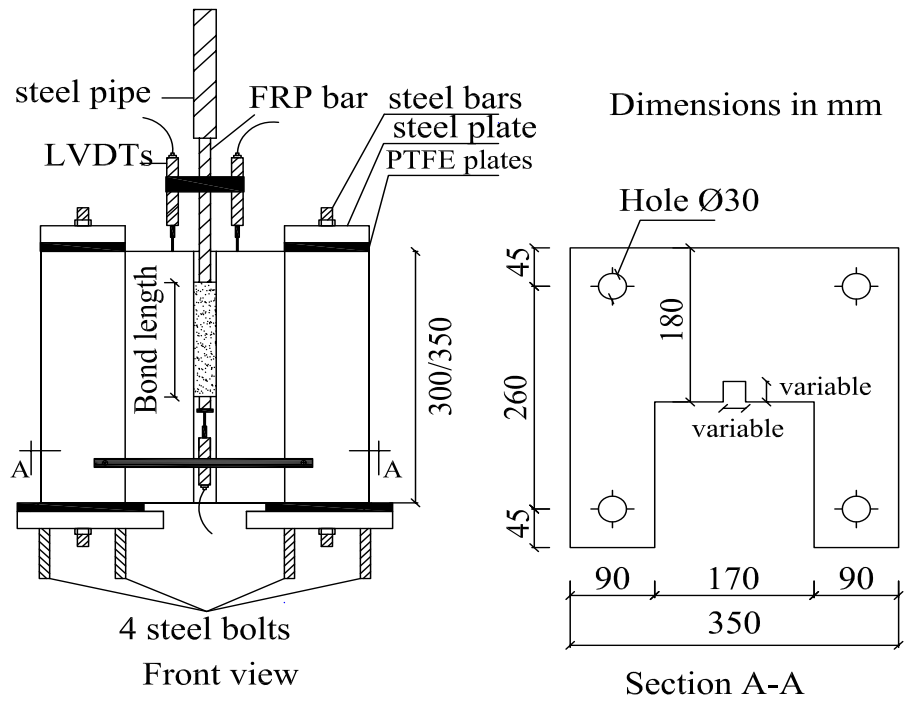
In this experimental campaign the specimens were tested using the configuration of the modified pullout test described in [68, 70], shown in Fig. 3.5a. C-shaped concrete blocks of $350 \times 350 \text{ mm}^2$ outside dimensions, $170 \times 180 \text{ mm}^2$ inside dimensions, and with a height of 300 mm height were used.

The C-shaped specimen presents the advantages of the direct pullout type of test like specimen manageability size and easiness of measurements, as well as that it does not requires the use of additional bonded lengths of FRP rod for reaction, thus minimizing eccentricity problems [68] .

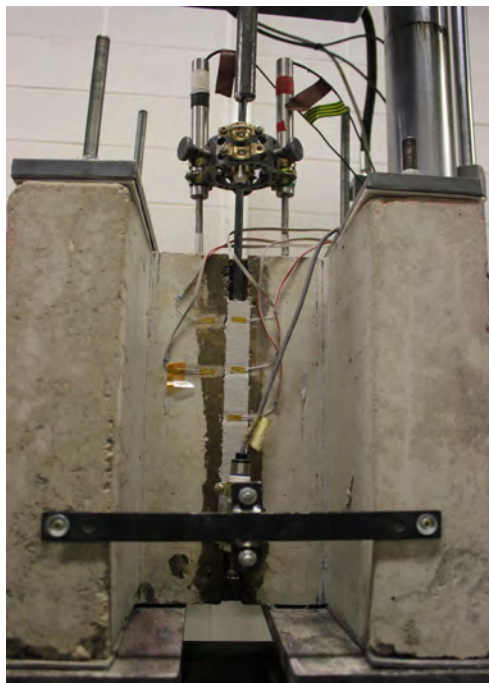
3.5 Test setup, instrumentation and test procedure

The specimens were tested in pullout using a servo-hydraulic testing machine with a displacement controlled rate of 0.003 mm/s up to failure. The specimens were attached to the testing machine using four steel bars inserted into previously formed holes in the corners (see Fig. 3.5a). Two separate steel plates ($350 \times 90 \times 20$ mm³) were used to distribute the anchoring forces exerted by the steel bars on the top surface of the test specimen. Polytetrafluoroethylene (PTFE)plates were placed on the upper and bottom surfaces of the tested specimen, between the concrete and the supporting system.

Two displacement transducers (LVDTs) were used to measure the loaded end slip, while another measured the free end slip (see Fig. 3.5b). Electrical resistance strain gauges (EGs) with a gauge length of 6.0 mm were mounted on the outer surface of the FRP bars to measure the strain distribution along the bond length. Fig. 3.6a shows the stain gauges (strain 1 to strain 5) instrumented for specimens with bond length equal to 192 mm ; for bond lengths equal to 40 mm only one strain gauge was mounted at the center of the bonded length. Transverse strain gauges were mounted on the top surfaces of the epoxy paste filling the grooves (strain 1e, strain 2e and strain 3e) and concrete (strain 1c and strain 2c) to measure the transverse strains of specimens with bond lengths 192 mm and 240 mm. For specimens with bond length 96 mm, transverse strain gauges were mounted on the top surfaces of the epoxy paste (strain 1e and strain 2e) and concrete (strain 1c and strain 2c) while only one strain gauges was mounted on the top surfaces of the epoxy paste and another one on concrete (strain 1c) for specimens with bond length equal to 48 mm. Number and arrangement of strain gauges for each bond length are illustrated in Fig. 3.6b. An automatic data acquisition system was used to record the data.

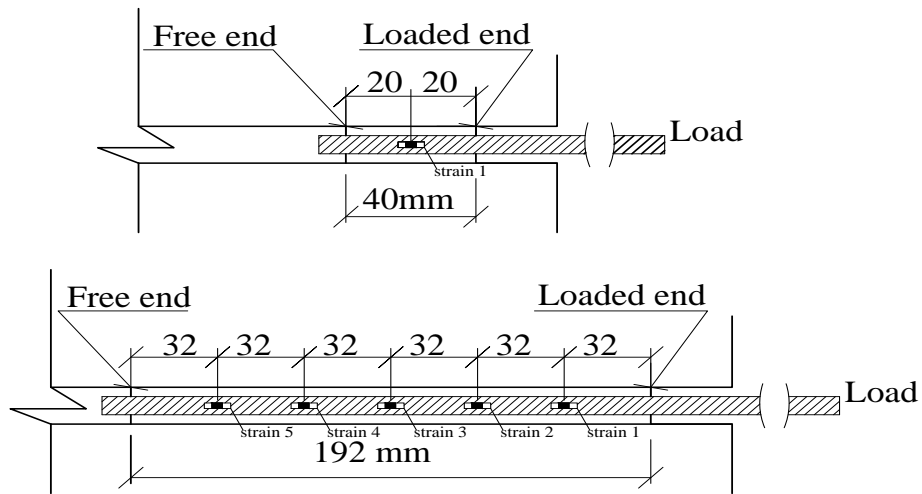


(a) Specimen details

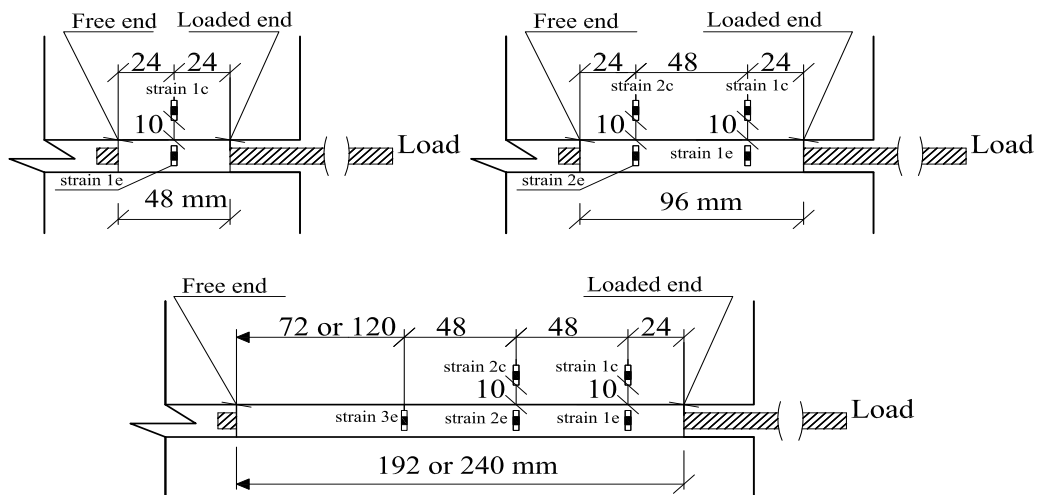


(b) Test setup

Figure 3.5: Specimen details and test setup.



(a) Longitudinal strain gauges on FRP bars



(b) Transverse strain gauges on concrete (c) and epoxy (e) surfaces

Figure 3.6: Strain gauges details.

3.6 The pullout test arrangement

In this study the experimental pullout test was performed in three series. In the first series the effect of different material and construction details on the bond behaviour of NSM FRP bars in concrete was discussed. In this series four types of FRP bars were tested. The bars were bonded using one kind of adhesive. In the second series, the effect of adhesive properties, bar type, bar size, FRP properties, groove geometry, and the use of mechanical interlocking on the capacity and bond behaviour of NSM joints were studied and discussed. Low concrete strength, constant bond length, four types of epoxy and two types of FRP materials (carbon and glass) with different bar sizes were used in the tests.

In the third series an experimental programme was performed to study the effect of epoxy properties on the bond behaviour of NSM bars in longitudinal and transverse direction. Three epoxy types, two FRP materials and four bond length were used. Finally a total of ninety six specimens were tested, forty three specimens with CFRP bars and fifty three specimens with GFRP bars. The three series are discussed in detail in the following:

3.6.1 The first series

3.6.1.1 Overview

In this series a total of twenty six specimens were tested, twelve specimens with CFRP bars and fourteen specimens with GFRP bars. The effect of groove surface (preformed and saw cut), groove geometry (dimensions and shapes), FRP bar type (material and surface treatment), bond length; and also of the incorporation, in the groove-concrete system, of different construction details that modify the NSM-concrete interaction (transverse interlocking with or without shear connectors, covering plate with shear connectors and confinement of surrounding concrete) was studied.

All specimens of this series was casted using concrete 2 defined in section 3.2.1. Two types of CFRP bars (8 and 9 mm in diameter) and Two types of CFRP bars (9.38 and 12 mm in diameter) (see Table 3.4) were used . One type of epoxy (MBRACE, BASF) was used to bond the FRP bars.

3.6.1.2 Test variables

The test variables are groove surface (pre-formed and saw cut), groove geometry (dimensions and shapes), FRP type (carbon and glass), bar diameter, modulus of elasticity, bond length, and the incorporation of different modifications in the NSM-concrete interaction (transverse interlocking with or without shear connectors, covering plate with shear connectors and confinement of surrounding concrete). The details of the tested specimens are indicated in Table 3.5. The identification of the specimens in the first column is as follows: the first letter indicates the way the grooves were formed (P = pre-formed grooves, S = saw cut grooves); the following four digits indicate groove dimensions in mm (the first two the depth, and the second two the width); the next letter indicates the bond length (short S = 40mm for CFRP or 48 mm for GFRP, medium M = 88 mm and long L = 192 mm); the subsequent two characters indicate the type of bar (C = carbon, G = glass, 1 = type 1, 2 = type 2). Finally, the last characters (when applicable) indicate the groove form and the modification of the NSM-concrete interaction introduced (U = U-shaped groove, W = stepped groove, I = groove with mechanical interlocking, IS = groove with mechanical interlocking and shear connectors, C=covering plate, and * = unconfined). For instance, P1212LC1 represents specimen reinforced with carbon fibre type 1 (C1) installed into a pre -formed groove(P) with size of $12 \times 12 \text{ mm}^2$ and bonded along a bond length of 192 mm (L).

For specimens with a U-shaped groove (Fig. 3.7a), an initial rectangular groove with constant width(b) and depth(h) was cut and thereafter the semi-circular part with radius ($r = b/2$) was formed manually tilting the cutting edge of the circular saw. The circular groove was thought to avoid stress concentrations that may result at the corners of a rectangular groove. The width b and the maximum depth ($d = (h + u)$) for this groove are reported in Table 3.5. For specimens with a stepped groove (Fig. 3.7b), a groove of $1.5d_b$ (18 mm) wide followed by another groove of $2.5d_b$ (30 mm) wide was formed. The groove had a constant depth equal to $1.5d_b$. The bond lengths extend 60 mm and 132 mm in the two groove sizes ($1.5d_b \times 1.5d_b$ and $1.5d_b \times 2.5d_b$) respectively. This stepped groove may prevent slip at the epoxy- concrete interface and, additionally, exert compressive stresses on the concrete surrounding the narrower groove through the perpendicular faces to the FRP bar alignment formed at the width change.

Figs. 3.7c and d illustrate the details of grooves with mechanical interlocking and mechanical interlocking with shear connectors, respectively. For specimens with connectors, threaded steel rods (6 mm in diameter and 80 mm long) were bonded to drilled holes in the concrete specimen using epoxy paste and, after the placement of the NSM FRP bars, steel plates ($54 \times 16 \times 1.6 \text{ mm}^3$) were bonded to the top surface of the epoxy paste. After 24 hours, the plates were attached to the steel bars. For specimens with a covering plate, a steel plate ($192 \times 50 \times 1.6 \text{ mm}^3$) was bonded to the epoxy paste filling the groove and connected to the concrete specimen core using threaded steel anchors. The steel bars collaborate in transferring the stresses from the steel plate to the concrete core in order to reduce the average bond stress on groove sides and surrounding concrete and additionally restrain the transverse strains originated when pulling the bar in both epoxy and concrete. To study the effect of the supporting system on the confinement inside part ($170 \times 180 \text{ mm}^2$) of the test specimen, two narrow grooves (5 mm wide \times 30 mm deep) were cut at a distance of 15 mm from the two supporting parts ($90 \times 350 \text{ mm}^2$).

3.6.2 The second series

3.6.2.1 Overview

In this series, a total of thirty two specimens were tested, twelve specimens with CFRP bars and twenty specimens with GFRP bars. The effect of adhesive properties, bar type, bar size, FRP properties, groove geometry, and the use of mechanical interlocking on the capacity and bond behaviour of NSM joints are studied and discussed. Low concrete strength (concrete 1) defined in section 3.2.1. The grooves were formed by cutting. Two types of epoxy were used. The properties of the second type of epoxy were modified by adding a special additive as discussed before in section 3.2.2 in such a way that finally three more types of adhesive were obtained: the non-modified resin (B), and two modified resins (C, D).

The grooves were formed by cutting. Two types of CFRP bars (8 and 9 mm in diameter) and one GFRP bar two sizes (8 and 12 mm in diameter) as shown in Table 3.4) were used.

Table 3.5: Configurations of the tested specimens (first series).

Specimen ID	d (mm)	b (mm)	d_b (mm)	$K = d/d_b$	L_b (mm)	Test variable
Specimens	with	CFRP	bars			
P1212SC1	12	12	8.0	1.5	40	Groove
S1212SC1	12	12	8.0	1.5	40	surface
P1212MC1	12	12	8.0	1.5	88	and
S1212MC1	12	12	8.0	1.5	88	bond length
P1212LC1	12	12	8.0	1.5	192	"
S1212LC1	12	12	8.0	1.5	192	"
S1616LC1	16	16	8.0	2.0	192	Groove size
S1616LC1U	16	16	8.0	Fig. 3.7a	192	Groove shape
S1616LC1*	16	16	8.0	2.0	192	Confinement
S1313LC1	13	13	8.0	-	192	Bar type
S1515MC2	15	15	9.0	-	192	and
S1515LC2	15	15	9.0	-	192	bond length
Specimens	with	GFRP	bars			
S1515LG1	15	15	9.28	-	192	Bar type
S2020LG1	20	20	9.28	-	192	Groove size
S1818LG2	18	18	12.0	1.5	192	Bar type
S1830LG2	18	30	12.0	1.5	192	Groove width
S1830LG2W	18	Fig. 3.7b	12.0	1.5	192	Stepped groove
S1818LG2I	18	Fig. 3.7c	12.0	1.5	192	MI
S1818LG2IS	18	Fig. 3.7d	12.0	1.5	192	MI and SC
S1818LG2C	18	18	12.0	1.5	192	Covering plate
S1818LG2*	18	18	12.0	1.5	192	Confinement
S1830LG2*	18	18	12.0	1.5	192	"
S1830LG2W*	18	Fig. 3.7b	12.0	1.5	192	"
S1818LG2I*	13	Fig. 3.7c	12.0	1.5	192	"
S2218LG2U	21.8	18	12.0	Fig. 3.7a	192	Groove shape
S1818SG2	18	18	12.0	1.5	192	Bond length

d = groove depth, b = groove width, MI = mechanical interlocking and SC = shear connectors.

3.6.2.2 Test variables

The variables considered in this experimental campaign were groove geometry (dimensions and shapes), FRP type (carbon and glass), bar diameter ($d_b = 8, 9, 12$ mm), modulus of elasticity (64, 134, 170 GPa), adhesive type, bond length and

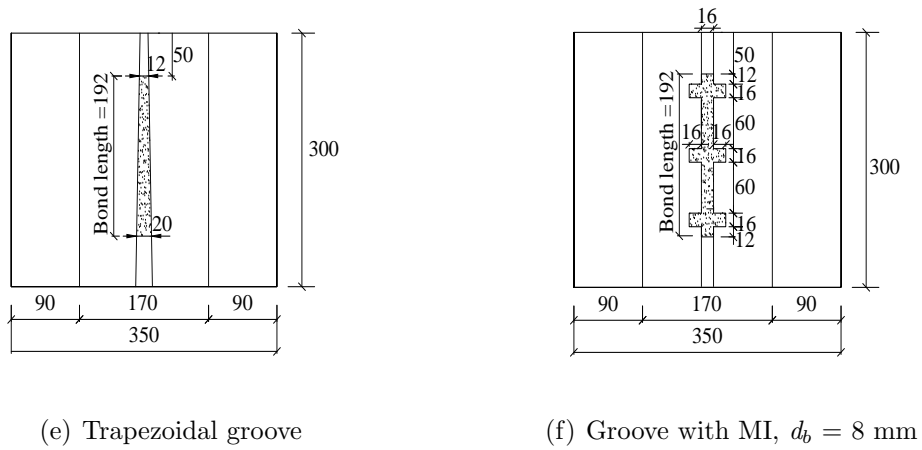
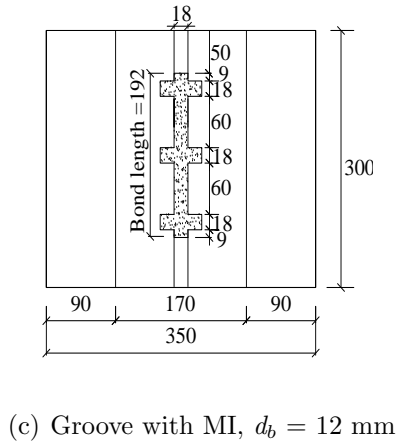
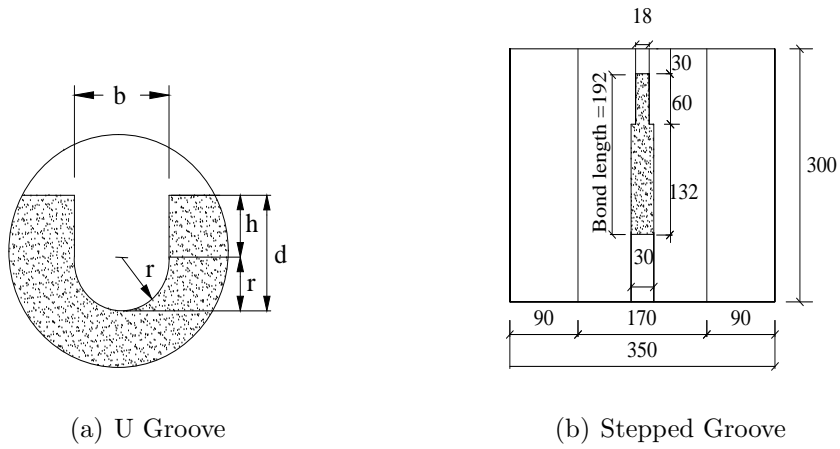


Figure 3.7: NSM configurations (dimensions in mm).

the use of transverse mechanical interlocking. The specific details and identification of the specimens are indicated in Table 3.6. The specimens in the first column are identified as follows: the first letter indicates bond length ($L = 192$ mm and $T = 240$ mm); the following four digits indicate groove dimensions (first two the depth, second two the width); the sixth character indicates the adhesive type (A, B, C or D), and the following two characters indicate the type of bar (C = carbon, G = glass, 1 = type 1, 2 = type 2). Finally, the last character (when it appears) indicates the groove form and the modification of NSM-concrete interaction introduced (U = U groove, T = Trapezoidal groove and I = groove with mechanical interlocking), followed by the specimen number (-1, -2, -3).

Figs. 3.7a and 3.7e illustrate specimens with U groove and a trapezoidal groove respectively, while Fig. 3.7f illustrates the details of specimens with mechanical interlocking. For specimens with a U groove (Fig. 3.7a), the U groove was formed as illustrated in section 3.6.1.2. The width (b) and the maximum depth ($d = h + r$) for this groove are reported in Table 3.6. For specimens with trapezoidal grooves (Fig. 3.7e), the groove had a width of $1.5d_b$ (12 mm) at the loaded end and increased linearly to reach $2.5d_b$ (20 mm) at the free end of the bond length, at a constant depth of $2d_b$ (16 mm).

3.6.3 The third series

3.6.3.1 Overview

In this series, a total of thirty six specimens were tested, nineteen specimens with CFRP bars and nineteen specimens with GFRP bars. A detailed study on the effect of epoxy properties on the bond behaviour of NSM bars in longitudinal and transverse direction was performed. Low concrete strength (concrete 1) defined in section 3.2.1, three types of epoxy (A, B, D) were used (see Table 3.3). The grooves were formed by cutting. CFRP and GFRP bars with one size (8 mm in diameter) (see Table 3.4) were used. Moreover, four bond lengths were studied.

3.6.3.2 Test variables

Adhesive type, FRP material and bond length are the main variable of the test. The details of the tested specimens are indicated in Table 3.7.

Table 3.6: Configurations of the tested specimens (second series).

Specimen ID	d (mm)	b (mm)	d_b (mm)	$K =$ d/d_b	L_b (mm)	Test variable
Specimens with CFRP bars						
L1612AC1-1	16	12	8.0	1.5	A	Reference
L1612AC1-2	16	12	8.0	1.5	A	"
L1616AC1-1	16	12	8.0	2.0	A	Groove width
L1616AC1-1	16	12	8.0	2.0	A	Groove width
L1620AC1T-1	16	variable	8.0	2.0	A	Groove shape
L1620AC1T-2	16	variable	8.0	2.0	A	Groove shape
L1515AC2-1	15	15	9.0	1.62	A	FRP type
L1515AC2-2	15	15	9.0	1.62	A	"
L1616BC1-1	16	16	8.0	2.0	B	Adhesive type
L1616BC1-2	16	16	8.0	2.0	B	Adhesive type
T1616BC1-1	16	16	8.0	2.0	B	Bond length
T1616BC1-2	16	16	8.0	2.0	B	Bond length
Specimens with GFRP bars						
L1612AG1-1	16	12	8.0	1.5	A	FRP type
L1612AG1-2	16	12	8.0	1.5	A	"
L1616AG1-1	16	12	8.0	2.0	A	Groove width
L1616AG1-2	16	12	8.0	2.0	A	Groove width
L1620AG1T-1	16	variable	8.0	2.0	A	Groove shape
L1620AG1T-2	16	variable	8.0	2.0	A	Groove shape
L1916AG1U-1	19.4	16	8.0	variable	A	"
L1916AG1U-2	19.4	16	8.0	variable	A	"
L1616AG1I-1	16	16	8.0	2.0	A	MI
L1616AG1I-2	16	16	8.0	2.0	A	"
L1818AG2-1	18	18	12.0	1.5	A	Bar size
L1818AG2-2	18	18	12.0	1.5	A	"
L1616BG1-1	16	16	8.0	2.0	B	Adhesive type
L1616BG1-2	16	16	8.0	2.0	B	Adhesive type
L1616BG1-3	16	16	8.0	2.0	B	"
L1616CG1-1	16	16	8.0	2.0	C	"
L1616CG1-2	16	16	8.0	2.0	C	"
L1616CG1-3	16	16	8.0	2.0	C	"
L1616DG1-1	16	16	8.0	2.0	D	"
L1616DG1-1	16	16	8.0	2.0	D	"

All specimens had the same groove size (square groove $16 \times 16 \text{ mm}^2$). One size of FRP bars, 8 mm diameter, was used. The identification of the specimens in the first and second columns is as follows: the first letter indicates bond length (S = 48, M = 96 mm, L = 192 mm and T = 240mm); the following two digits indicated the size of the grooves (square groove $16 \times 16 \text{ mm}^2$), the following character indicates the adhesive type (A, B and D), the following character indicates the type of bar (C = carbon, G = glass). Finally the last characters indicate the specimen number (-a, -b, -c).

Table 3.7: Configurations of the tested specimens (third series).

Specimen with CFRP	Specimen with GFRP	adhesive type	Bond length
M16AC-a	M16AG-a	A	$12d_b$
M16AC-b	M16AG-b	A	$12d_b$
L16AC-a	L16AG-a	A	$24d_b$
L16AC-b	L16AG-b	A	$24d_b$
T16AC-a	---	A	$30d_b$
T16AC-b	---	A	$30d_b$
---	S16AG-a	B	$6d_b$
---	S16AG-b	B	$6d_b$
M16BC-a	M16BG-a	B	$12d_b$
M16BC-b	M16BG-b	B	$12d_b$
L16BC-a	L16BG-a	B	$24d_b$
L16BC-b	L16BG-b	B	$24d_b$
---	L16BG-b	B	$24d_b$
T16BC-a	T16BG-a	B	$30d_b$
T16BC-b	T16BG-b	B	$30d_b$
---	S16DG-a	D	$6d_b$
---	S16DG-b	D	$6d_b$
M16DC-a	M16DG-a	D	$12d_b$
M16DC-b	M16DG-b	D	$12d_b$
L16DC-a	L16DG-a	D	$24d_b$
L16DC-b	L16DG-b	D	$24d_b$
L16DC-c	---	D	$24d_b$
T16DC-a	---	D	$30d_b$
T16DC-a	---	D	$30d_b$

3.7 Analysis of measurements

Data recorded during the tests were used to reproduce the average bond stress slip relationship for each specimen. The average bond stress at bar-epoxy interface any stage in the test was the recorded pullout load on the bar divided by the nominal surface area of the embedment length of the bar.

The free end slip was directly obtained from the bottom LVDT. However, the two top LVDTs measured not only the slip of the rebar relative to concrete but also the elastic elongation of the portion of the bar from the transducer support point to the level of the bonded bar. Therefore, the loaded end slip s_{le} was obtained as the difference of the average measured slip s_t and the slip correction s_c (Eq. 4.2). The slip correction s_c represents the elongation of the bar between the actual loaded end of the embedment length and the attachment point of the LVDTs, and could be computed using Eq.3.1.

$$s_{le} = s_t - s_c \quad (3.1)$$

$$s_c = \frac{FL}{A_f E_f} \quad (3.2)$$

where F is the applied force, L is the length between the top surface of bonded length and the average point of attachment of the LVDTs on the bar, E_f is the modulus of elasticity of the bar and A_f is the cross-sectional area.

Chapter 4

Pullout test experimental results

4.1 Introduction

The experimental results obtained from the pullout tests described in the previous chapter are presented in this chapter. From the experimental data, an examination of the mode of bond failure of the near surface mounted (NSM) fibre reinforced polymer (FRP) bars and of the various parameters that influence bond behaviour and load capacity of tested specimens has been performed. In this study, three series of pullout test specimens were tested to analyze bond behaviour of NSM FRP bars. The analysis was performed in relation to different types of FRP bars and various influencing parameters as discussed in the previous chapter. The results of each series are discussed in detail in the following:

4.2 Results and discussion of the first series

The results of the tested specimens in this series are discussed in terms of failure load, failure mode, average shear stress at the two interfaces (bar-epoxy interface and epoxy-concrete interface), and slip recorded at the two NSM ends (loaded end and free end). The results are reported in Tables 4.1 and 4.2 for CFRP and GFRP FRP bars respectively. Where P_f is the maximum load of the NSM joint, P_{max} is the ultimate tensile load of the FRP bars, P_f/P_{max} is the load efficiency factor and τ_{av1} , τ_{av2} , S_{le} and S_{fe} , are the average bond stress at the bar-epoxy interface, the average bond stress at the concrete-epoxy interface, the loaded end slip and the free

end slip at maximum load of the NSM joint, respectively. τ_{av1} , τ_{av2} are calculated using the equations Eq.4.1 and 4.2 respectively [68].

$$\tau_{av1} = \frac{P_f}{\pi d_b L_b} \quad (4.1)$$

$$\tau_{av2} = \frac{P_f}{\Sigma A_c} \quad (4.2)$$

where P_f , d_b , L_b and $\Sigma(A_c)$ are the tensile load (N), the FRP bar diameter (mm), bond length (mm) and concrete-epoxy interface area subjected to bond stress (mm^2) respectively.

Table 4.1: Results of the tested CFRP NSM bars (first series).

Specimen ID	P_f (kN)	P_f/P_{max} (%)	τ_{av1} (MPa)	τ_{av2} (MPa)	S_{le} (mm)	S_{fe} (mm)	Failure mode
P1212SC1	12.75	10.79	12.43	8.60	0.270	0.0526	B-E
S1212SC1	10.37	8.78	10.12	6.40	0.170	0.0511	B-E
P1212MC1	30.41	25.74	14.31	9.33	0.616	0.1752	LC+B-E
S1212MC1	26.49	22.42	12.46	8.75	0.454	0.0713	LC+B-E
P1212LC1	27.17	23.00	5.60	3.93	0.613	0.1599	LC+B-E
S1212LC1	36.59	30.95	7.58	5.15	0.593	0.0404	LC+B-E
S1616LC1	42.02	35.57	8.70	4.56	0.662	0.0824	B-E
S1616LC1U	38.91	32.94	8.06	4.93	0.741	0.0776	LC+B-E
S1616LC1*	40.05	33.90	8.30	4.28	0.871	0.1087	LC+B-E
S1313LC1	35.10	29.71	7.13	4.68	0.603	0.0680	B-E
S1515MC2	25.64	19.83	10.25	6.33	0.333	0.0243	LC+B-E
S1515LC2	47.00	35.35	8.61	5.32	0.623	0.0873	ES

B-E = bar-epoxy interface failure; ES = epoxy splitting; and LC = longitudinal cracking of the epoxy.

4.2.1 Specimens with CFRP bars

4.2.1.1 Failure modes and loads

Six specimens of carbon fibre reinforced polymer (CFRP) NSM bars (P1212SC1, S1212SC1, P1212MC1, S1212MC1, P1212LC1 and S1212LC1) were tested to study the effect of groove surface and bonded length on NSM bond behaviour. The test

results indicated that the main mode of failure of these specimens was pullout of the FRP bar. This mode of failure depends mainly on the bond between bar and epoxy. The test results revealed that the groove surface had no effect on the failure load when the failure was at the bar-epoxy interface. On the other hand, the failure load increased with the increase of bond length. By contrast, specimen P1212LC1 had a lower failure load than specimen P1212MC1 due to the failure of the epoxy paste at the positions of the strain gauges mounted on the top surface of the FRP bars as shown in Fig. 4.1a. Specimens with short bond lengths failed at the bar-epoxy interface with no visible cracks either in the epoxy paste or in the concrete surface. For specimens with medium bond lengths, two inclined cracks (at approximately 45°) formed in the epoxy paste near the loaded end and propagated longitudinally towards the free end of the bonded bar as the applied load increased. At the moment the longitudinal crack reached the free end, a sudden failure occurred at the bar-epoxy interface with an immediate large slip at this interface. On the other hand, the failure of specimen S1212LC1, with a long bond length, initiated with the formation of cracks in the epoxy paste at the positions of the strain gauges instrumented on the top surface of the bonded bars. The epoxy split at the strain gauge located near the free end was followed by a bar-epoxy interface failure with large slip of the FRP bar; specimen P1212LC1 failed due to splitting of the epoxy paste at the positions of all mounted strain gauges at a lower load capacity than specimen S1212LC1, having the same bond length.

Specimens S1616LC1 and S1616LC1U, characterized by larger groove sizes than specimen S1212LC1, failed at the bar -epoxy interface and attained load capacities slightly higher than this specimen. This means that increasing the groove size from $1.5d_b$ to $2d_b$ delayed the bar-epoxy interface failure and increased the failure load by approximately 14.8 % this results agree with the results reported in [69]. Specimen S1616LC1 failed with no visible cracks either in epoxy or in concrete, while, in the case of specimen S1616LC1U, failure initiated with the formation of a longitudinal crack that started near the loaded end and propagated towards the free end of the bonded bar. When the crack reached the free end, failure occurred at the bar-epoxy interface without the formation of a crack in the concrete. A very thin layer of epoxy was observed along the bonded length of the bar after failure indicating that the interfacial failure occurred due to cohesive shear failure in the epoxy.

Similar observations were reported by Galati and De Lorenzis [69]. On the other hand, the groove shape had no evident effect on the failure load when this was due to bar-epoxy interface failure. Unlike the failure of specimen S1616LC1, the failure of the un-confined specimen S1616LC1* was initiated by the formation of a longitudinal crack in the epoxy paste which started at the loaded end and propagated towards the free end of the bonded bar. Once the longitudinal crack reached the free end, a failure with large slip at the bar-epoxy interface occurred at a load capacity slightly lower than that of specimen S1616LC1. This means that the un-confinement of the inside part of the specimen allowed the epoxy transverse strain to increase, forming a longitudinal crack in the epoxy paste.

Specimen S1515MC2, with medium bond length, also failed at the bar-epoxy interface. The failure was initiated by the formation of a longitudinal crack in the epoxy paste. The crack propagated with the load increase until it reached the free end of the bonded bar, when bar-epoxy interface failure occurred. For specimen S1515LC2, with long bond length, the failure was initiated by the splitting of the epoxy cover and extended to cause damage to the surrounding concrete (Fig. 4.1b). Specimen S1313LC1 failed at the bar-epoxy interface with no visible cracks either in the epoxy or the concrete. Although specimens S1313LC1 and S1515LC2 had nearly the same groove perimeter to diameter ratios, specimen S1515LC2 had a maximum load capacity higher than that of specimen S1313LC1 (approximately 134 %). The results from the previous three specimens indicated that increasing the FRP bar diameter and/or enhancing the surface texture of the FRP bar, increase the failure load and/or changes the mode of failure. Furthermore, the increase of bond length from medium (88 mm) to longer (192 mm) increased the maximum load of the NSM joints from 25.64 kN to 47.00 kN (approximately 183%) and changed the mode of failure from bar-epoxy interface failure to splitting of the epoxy cover with a portion of concrete surrounding the grooves.

4.2.1.2 Average bond stress slip curves

Effect of groove surface, bonded length and bar type. Fig. 4.2 illustrates the average bond stress slip curves of specimens with a CFRP bar. For specimens with short bond lengths the groove surface had no effect on the average bond stress slip relation due to the occurrence of slip at the bar-epoxy interface.

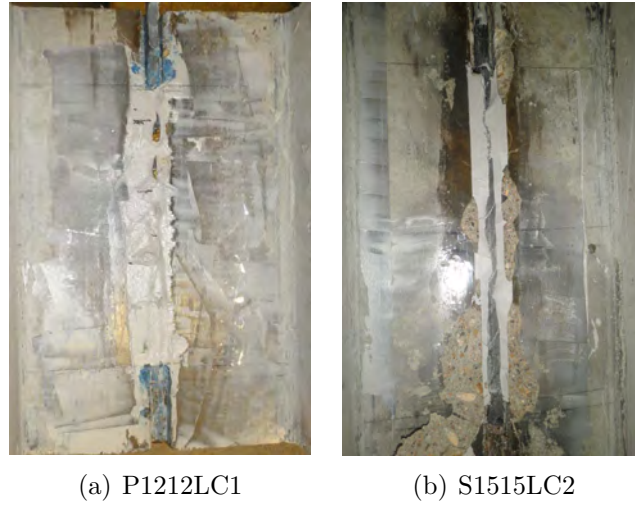


Figure 4.1: Failure modes of specimens with CFRP bars.

The two curves corresponding to S1212SC1 and P1212SC1 (Fig. 4.2a) show elastic behaviour until loads equal to 40 % of their failure loads followed by a sudden small slip at those loads; their load capacities then increased again until failure. After attaining the maximum load, the two curves have sharp descending average bond stress slip relations.

The specimens with long bond lengths, S1212LC1 and P1212LC1 (Fig. 4.2a), present different average bond stress slip relations due to the failure of the epoxy paste at the positions of the strain gauges, as discussed above, without being affected by the groove surface. At the failure load, specimen S1212LC1 had a sharp descending average bond stress slip relation while specimen P1212LC1 had a horizontal one. The previous specimens followed similar average bond stress slip behaviour at the free end (Fig. 4.2b).

On the other hand, the bond length of the NSM bars had a great effect on the average bond stress slip relations. As reviewed before [68, 69] the longer the bond length of the NSM bars, the lower the average bond stress distribution along this length due to the non-uniform distribution of the bond stresses along the bond length. This effect was clear in the case of specimens with short and long bond lengths (Fig. 4.2c). By contrast, test results reported in Table 4.1 and illustrated in Fig 4.2c shows that specimens with medium bond lengths attained higher average bond stresses than those with short and long bond lengths. This means that the

specimens with medium bond lengths accomplished the best average bond stress distribution along their bond lengths.

In the case of specimens with C2 bars (Fig. 4.2d), the shorter the bond length the higher the average bond stress. The specimens with a medium bond length had a linear average bond stress slip relation until the failure load, followed by a descending branch with bar-epoxy interface failure. The specimen with a long bond length presented an approximate linear average bond stress slip relation until a load of 42 % of its failure load, followed by another linear relation until the failure load. After the failure load, a descending branch was observed until epoxy splitting occurred. On the other hand, specimens S1313LC1 and S1515LC2 (Fig. 4.2d) showed a similar average bond stress slip trend but with higher average bond strength in the case of C2 bars. This difference in the average bond strength may be due to the effect of the FRP bar surface texture which enhanced the bond between the bars and the surrounding epoxy.

Effect of groove size, shape and specimen confinement. Fig. 4.3a illustrates the effect of groove size, shape and confinement on the average bond slip relations at the loaded end of the bond length. All the specimens had long bond length (L) and bar type (C1). The average bond stress increases with the increase in groove size. The specimen with U-shaped groove had an average bond stress lower than that of specimen S1616LC1 and higher than that of specimen S1212LC1. Specimen S1616LC1* with an entire un-confined part had lower average bond stress than the ordinary specimen with the same groove size. The surrounding concrete decreased the transverse strain on the epoxy paste, resisted the formation of longitudinal cracks and delayed the bar-epoxy interface failure. The previous specimens followed the same average bond stress slip relation at the free end with unpronounced difference in the slip (Fig. 4.3b).

4.2.1.3 Longitudinal strain distribution along the bond length

Fig. 4.4 illustrates the longitudinal strain distribution along the bond length for specimens S1212LC1, P1212LC1 and S1212SC1. The strain gauges are numbered from 1 to 5, starting from the loaded end side (see Fig. 3.6a). The strains increased with the load increase, having different values depending on their locations.

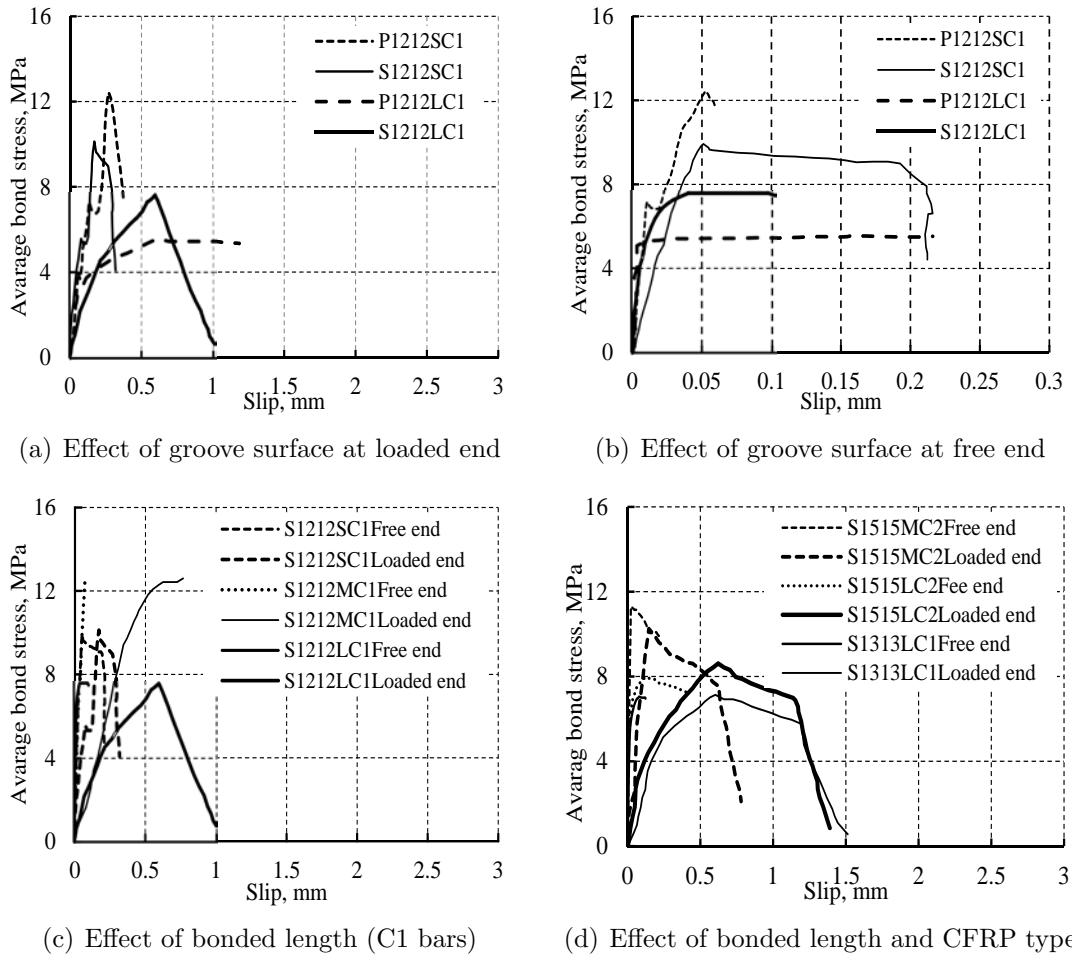


Figure 4.2: Average bond stress slip curves of NSM CFRP bars.

The strain gauge closest to the loaded end (strain 1) recorded the highest strain values. The recorded strain increased rapidly when the epoxy cover split at the strain gauge location. Figs. 4.4a and b show that recorded strains for specimen P1212LC1 started to increase rapidly at a load of 20 kN for the strain gauges located near the loaded end (strain 1 and strain 2) and at a load of 24.4 kN for the strain gauge located near the free end (strain 5) due to epoxy cover splitting at the location of the strain gauges. On the other hand, recorded strains for specimen S1212LC1 increased without sudden changes as the load increased until a load of 35 kN (just before failure). By contrast, the recorded strain for the specimen with a short bond length (one strain gauge located in the middle of the bond length) increased with the applied load increase until failure (Fig. 4.4c).

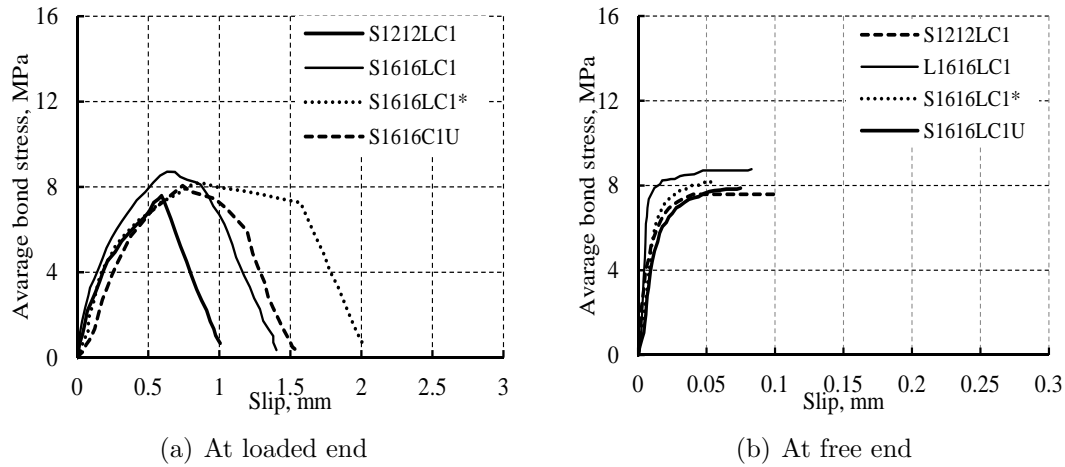


Figure 4.3: Effect of the inside concrete part confinement and groove geometry on the behaviour of specimens with NSM C1 bars.

4.2.2 Specimens with GFRP bars

4.2.2.1 Failure modes and loads

A total number of 14 pullout specimens with two types of glass fibre reinforced polymer (GFRP) bars (G1 and G2) were tested. The tested specimens had several modes of failure: concrete splitting, epoxy splitting, concrete tensile failure and concrete-epoxy interface failures. The results of all the tested specimens are reported in Table 4.2 and are discussed below. Specimens S1515LG1' and S2020LG1', with long bond lengths and a NSM glass bar (G1'), failed with a sudden epoxy cover splitting which extended to cause concrete splitting (Fig. 4.5a). During the test, small diagonal cracks were visible on the top surface of the epoxy paste and the cracks propagated with the applied load increase until failure. The two specimens had load efficiency factors of 82.16 % and 67.65 % respectively. During the loading of specimen S2020LG1 a grip problem occurred, the machine was stopped at a load of 30 kN and was then loaded again until failure; which may be the reason for its lower capacity than specimen S1515LG1'.

The specimens described next had long bond lengths and NSM bars (G2). Specimen S1818LG2 failed at the epoxy-concrete interface with considerable damage to the epoxy, which extended to cause concrete splitting at a load of 58.68 kN. Small diagonal cracks were visible on the top surface of the epoxy paste near the loaded

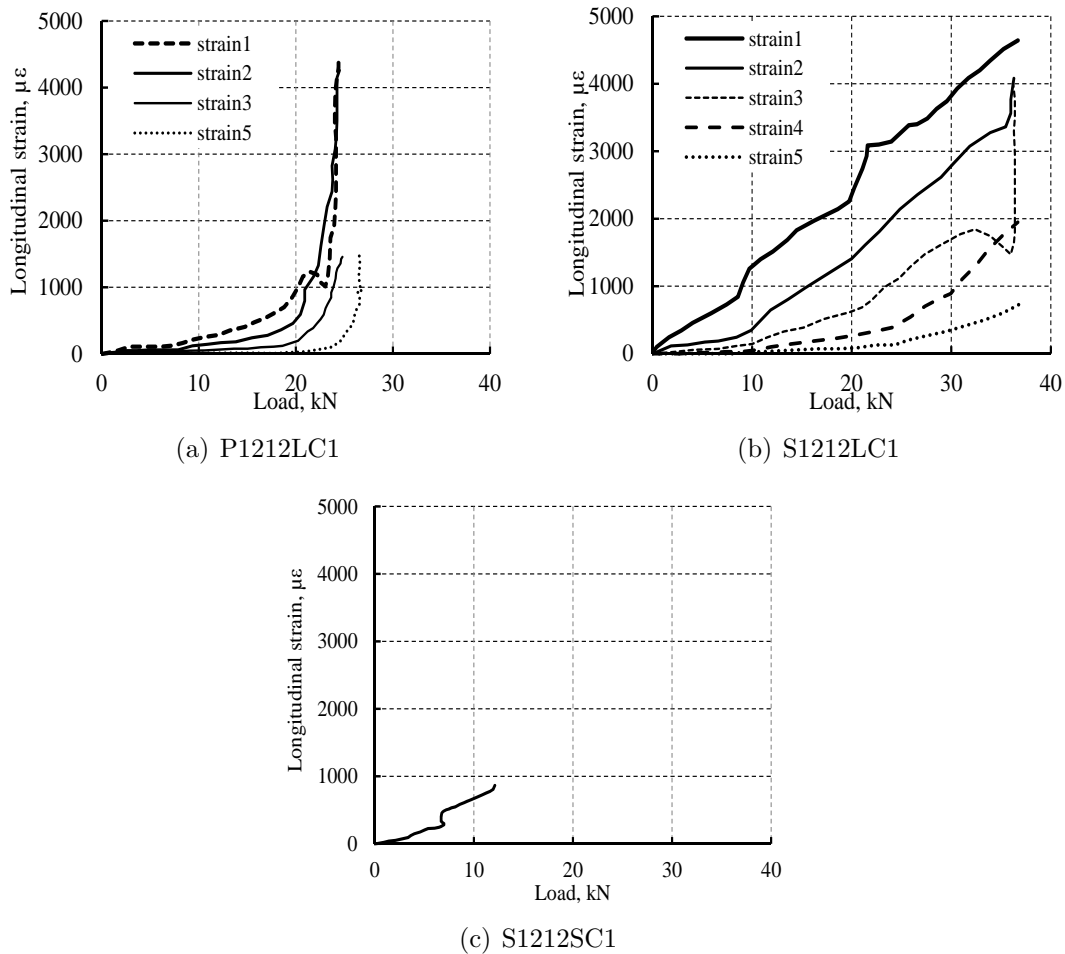


Figure 4.4: Longitudinal strain distributions along the bond length of NSM C1 bars.

end at a load of 49.05 kN. The cracks widened and increased with the applied load increase until failure. A concrete layer was found on the surface of the damaged epoxy paste due to the partial concrete-epoxy interface failure, which happened before the epoxy splitting (Fig. 4.5b).

During the loading of specimen S1830LG2, with a groove width of 30 mm, two very narrow diagonal cracks initially appeared on the top surface of the epoxy paste near the loaded end, followed by additional cracks that appeared with the load increase, which started to propagate towards the free end from a load of 55.91 kN until failure. The specimen failed due to transverse tension, splitting into two equal parts at a load of 59.88 kN. In the case of specimen S1830LG2W, diagonal cracks were visible on the top surface of the epoxy paste.

Table 4.2: Results of the tested GFRP NSM bars (first series).

Specimen ID	P_f (kN)	P_f/P_{max} (%)	τ_{av1} (MPa)	τ_{av2} (MPa)	S_{le} (mm)	S_{fe} (mm)	Failure mode
S1515LG1`	42.51	82.16	7.208	4.78	2.374	0.08136	ES,CS
S2020LG1`	35.00	67.65	5.939	3.04	—	—	ES,CS
S1818LG2	58.68	37.90	8.10	5.55	1.103	0.0996	C-E
S1830LG2	59.88	38.65	8.27	4.72	0.6737	0.0889	CF
S1830LG2W	56.29	36.34	7.78	4.71	0.3389	0.0048	CF
S1818LG2I	61.38	39.63	8.48	5.96	0.5896	0.045	CF
S1818LG2IS	55.69	35.95	7.58	—	0.3915	0.0888	CF
S1818LG2C	63.77	41.16	8.78	—	0.4787	0.0373	CF
S1818LG2*	58.08	37.49	8.25	5.60	1.1590	0.0461	ES
S1830LG2W*	56.90	36.73	7.86	4.76	1.1086	0.1432	ES,C-E
S1818LG2I*	56.90	36.73	7.86	5.49	0.9487	0.1490	ES,C-E
S2218LG2U	52.40	33.82	7.32	5.05	0.9658	0.0493	ES,C-E
S1818SG2	24.23	15.64	13.39	9.35	0.4191	0.2106	ES

C-E = concrete-epoxy interface failure; ES = epoxy splitting; CS = concrete splitting and CF = concrete tensile failure.

The cracks started at the dividing line between the two grooves widths and propagated towards the narrow groove at a load of 49.05 kN. The cracks propagated diagonally until failure. The epoxy paste failed to transfer the tensile stresses along the bond length. A concrete tensile failure occurred at a load of 56.29 kN. Two diagonal cracks formed on the top surface of the concrete surrounding the narrow part, followed by a longitudinal crack (Fig. 4.5c) which finally divided the tested specimen into two parts.

For specimen S1818LG2I, with mechanical interlocking, two narrow diagonal cracks appeared on the top surface of the epoxy paste near the loaded end at a load of 43.16 kN; more cracks appeared as the load increased. The epoxy paste failed to transfer the tensile stresses from the epoxy filled the grooves to that filled the mechanical interlocking. The specimen failed due to transversal tension in the concrete at a load of 61.38 kN, and split into two parts as shown in Fig. 4.5d. The mechanical interlocking enhanced the failure load by approximately 4.6 %. On the other hand, specimen S1818LG2IS (with mechanical interlocking and shear connectors) had no visible cracks either in the epoxy paste or in the concrete surface

until failure. Two deep diagonal cracks were observed on the top surface of the concrete (Fig. 4.5e), but the final failure was due to a longitudinal crack which divided the specimen into two parts. Furthermore, the epoxy paste filling the groove between the steel plates split, but the steel plates supported the epoxy paste well, filling the mechanical interlocking. Specimen S1818LG2C, with a steel cover plate with shear connectors, attained the same mode of failure as the previous specimens (concrete tension failure) at a failure load of 63.47 kN (Fig. 4.5f). Small parts of the grooved surface of the GFRP bar were detached. The covering plate confined the concrete, reduced the transverse strains of the epoxy paste and enhanced the failure load of the specimen by approximately 8.67%.

The results of the previous six specimens, which have type G2 NSM bars, clearly indicated that the use of stepped grooves, mechanical interlocking with and without shear connectors, and covering plate with shear connectors prevented the epoxy-concrete interface slippage and enhanced the load carrying capacity in the case of the MI and the covering plate by small percentages due to concrete tension failure. On the other hand, the epoxy paste failed to transfer the tensile stresses along the bond length in the case of the specimens which had stepped grooves and mechanical interlocking. Moreover, the cohesion bond at the bar-epoxy interface failed at low loads followed by mechanical bond at this interface owing to the grooved surface of the GFRP bars.

The mechanical bond resulted in high tensile stresses on the epoxy paste causing the epoxy cracking. The epoxy paste exerted high compressive stresses on the groove sides confined with the surrounding concrete. The compressive stresses and specimen confinement generated a high elastic energy inside the system causing concrete tension failure. Changing the material properties of the epoxy paste and/or decreasing the confinement of the inside part of the concrete may delay or change the mode of failure. Further the use of stepped grooves, mechanical interlocking with and without shear connectors, and covering plate with shear connectors may be a solution of the epoxy concrete failure in the case of smooth grooved surfaces.

Four specimens (S1818LG2*, S1830LG2*, S830LG2W* and S1818LG2I*) with the introduction of confinement release were tested to study the effect on the concrete surrounding the inside part of the test specimen in the cases of wide grooves, stepped grooves and mechanical interlocking. The results obtained indicated that the tested

specimens had nearly the same failure loads as those of the original tested specimens (confined) but with changes in the mode of failure. The failure mode of specimens S1818LG2* and S1830LG2* was the sudden splitting of the epoxy with detachment of a portion of concrete surrounding the groove. Moreover, specimens S1830LG2W* and S1818LG2I* failed with epoxy spilling along the part of the bond length with 30 mm groove width or at the transverse interlocking, with a portion of concrete surrounding the groove at these locations; and concrete-epoxy interface failure along the rest of the bond length (groove part with 18 mm groove width). This means that the use of stepped grooves and/or transverse interlocking prevents concrete-epoxy interface failure until epoxy splitting. Furthermore, changing the material properties of the epoxy paste may enhance the failure loads of the previous specimens by transferring the stresses along the bond length and at the positions of groove geometry change.

4.2.2.2 Average bond stress slip curves

Effect of groove dimensions and groove shape. Fig. 4.6a illustrates the effect of groove dimensions and groove shapes on the average bond stress slip relations. The results showed a slight increase in the average bond stress, when increasing the groove width for a given depth, due to the tensile failure of the tested specimen with a wide groove. The increase in the groove width or using stepped grooves prevented concrete-epoxy interface failure and decreased the loaded end slip. The effect of a U-shaped groove with the same groove perimeter as the corresponding square groove did not change the behaviour of the joint due to the splitting of epoxy.

Effect of the mechanical interlocking and the covering plate. The use of mechanical interlocking, with or without shear connectors, increased the average bond strength and decreased the slip due to the enhancement of the concrete-epoxy bond and transverse confinement. The average bond strength was also enhanced using covering plates with shear connectors which decreased the stresses on the groove sides and confined transversally the concrete surrounding the groove. The percentage of increase in the average bond stresses of the previous specimens was small due to tensile concrete failure; as shown in Fig. 4.6b.



Figure 4.5: Modes of failure of specimens with GFRP bars.

Effect of the un-confinement of the inside concrete part. Fig. 4.7a illustrates the effect of the un-confinement of the inside concrete part on the behaviour of specimens S1818LG2 and S1818LG2* with narrow groove width. The un-confined specimen, S1818LG2*, experienced a higher slip than specimen S1818LG2 combined with a change in the mode of failure from concrete-epoxy interface failure followed by epoxy splitting to epoxy splitting extended to the concrete surrounding the groove. The change of slip value and mode of failure of these two specimens may be due to the higher deformations which occurred in both the epoxy paste and the concrete surrounding the groove of the unconfined specimen as opposed to the confined one.

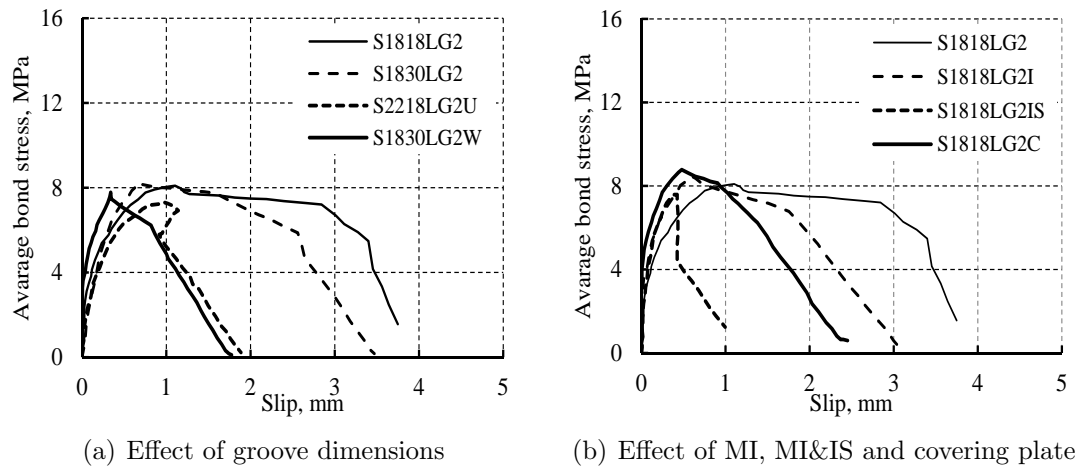
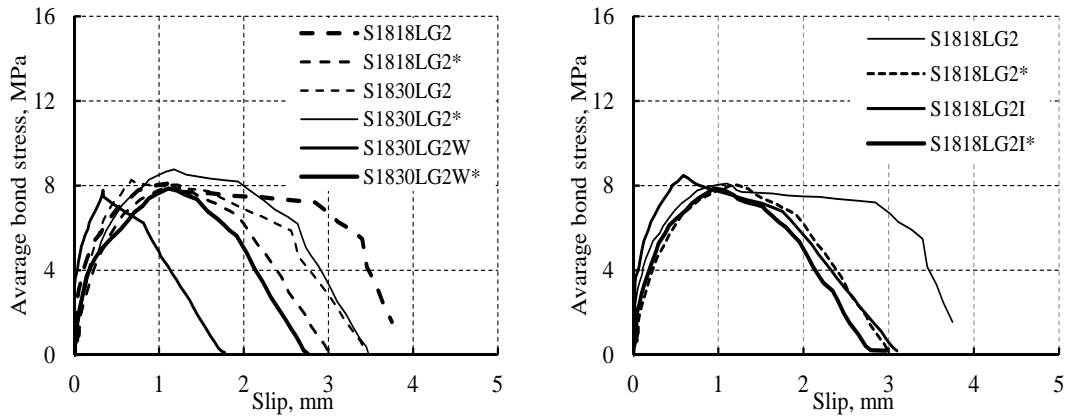


Figure 4.6: Average bond stress slip curves of NSM GFRP bars.

For specimens with a wider groove, the average bond strength of the un-confined specimen increased compared to that of the confined one, with an increase in slip. Furthermore, the mode of failure changed from concrete tensile failure to epoxy failure extended to the concrete surrounding the groove. On the other hand, no change was observed in the average bond strength for the unconfined specimen with stepped groove compared to the confined one, showing an increase in slip for the un-confined specimen.

By contrast, the average bond strength of the un-confined specimen with mechanical interlocking decreased while the slip increased compared to that of the confined one. The mode of failure changed from concrete tensile failure to a combination of epoxy splitting together with a portion of concrete surrounding the groove at the transverse mechanical interlocking positions, with concrete-epoxy interface failure along the bond lengths in between.

This means that the mechanical interlocking prevented the concrete-epoxy interface failure but the epoxy paste could not transfer the stresses from the narrow grooves to the transverse mechanical interlocking. Furthermore, the specimens with mechanical interlocking experienced lower slips than the reference specimens, S1818LG2, in both cases (confined and un-confined) due to the enhancement in the concrete-epoxy bond as shown in Fig. 4.7b.



(a) Specimens with different groove dimensions (b) Effect of confinement on specimens had MI

Figure 4.7: Effect of the inside concrete part confinement on the behaviour of specimens with NSM G2 bars.

Effect of the bond length. The effect of the bond length was studied by comparing the results of specimens S1818SG2 and S1818LG2 with bonded lengths of 48 mm and 192 mm respectively (see Fig. 4.8). The specimen with the short bond length attained higher average bond stress than that of the long bond length due to the non-uniform distribution of bond stress along the bond length, as discussed above. The failure of the specimen with a short bond length was due to epoxy splitting with extension to a portion of concrete surrounding the grooves; causing a sharp descending response in the average bond slip relation. While the specimen with a long bond length failed at the concrete-epoxy interface, thus displaying a similar response to the specimen with the short bond length after failure, as shown in Fig. 4.8

4.2.2.3 Effect of the confinement of the inside concrete part on the transverse strain

The three strain gauges strain 1, strain 2 and strain 3 mounted on the top surface of the epoxy paste (see Fig. 3.6b) recorded negative strains (compressive stresses on epoxy) at the beginning of loading, as shown in Fig. 4.9a. After that, the recorded strains changed to positive strains (tensile stresses on epoxy) at different loads depending on the location of the strain gauges from the loaded end until failure. Similar behaviour was reported in [69].

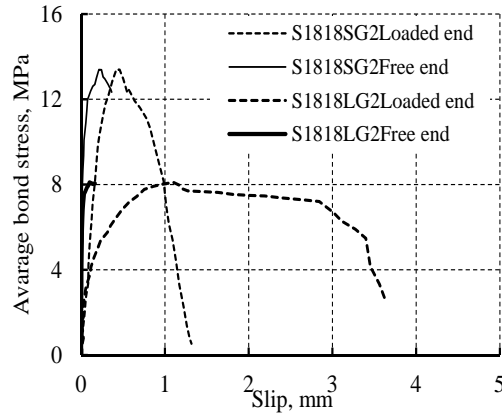


Figure 4.8: Effect of bond length on the behaviour of specimens with NSM G2 bars.

The tensile stresses in the FRP bar produced tensile strains at the bar-epoxy interface due to the contraction of the FRP bar. These tensile stresses also produced compressive strains on the epoxy paste. As the load increased, the bond mechanism changed from interfacial cohesion (up to this point it was very low between the used epoxy and GFRP bars) to a strong mechanical bond between the grooved bar and the epoxy. At this moment, the bar exerting compressive stress on the bar-epoxy interface produced tensile strains on the epoxy paste. The strain gauge closest to the loaded end (strain 1) had the highest values of tensile strains in epoxy for the case of the un-confined specimen, S1818LG2*, at nearly 75 % of its failure load (see Fig. 4.9a).

By contrast, the strain gauges placed on the concrete surface recorded positive strains (tensile strain in concrete) at the beginning of loading. As the applied load increased, the recorded strains changed to negative values (compressive strain in concrete). The introduction of un-confinement removed restrictions and allowed the inside concrete part to have higher strains than those of the confined specimen.

For this reason, the tensile strains were higher on the epoxy paste for the un-confined specimen than those of the confined one. On the other hand, the compressive strains on the concrete surface for the un-confined specimen were lower than those of the confined one due to the dissipation of energy when the free concrete part deformed (Fig. 4.9b). For the two tested specimens, the compressive strains recorded using strain 1c, decreased before failure due to lower stresses transferred through this portion of the bond length near the loaded end with the appearance of

the epoxy cracks. The compressive stresses transferred rapidly to the next portion of the bond length, thus increasing the compressive strains recorded by strain 2c until failure, as shown in Fig. 4.9b.

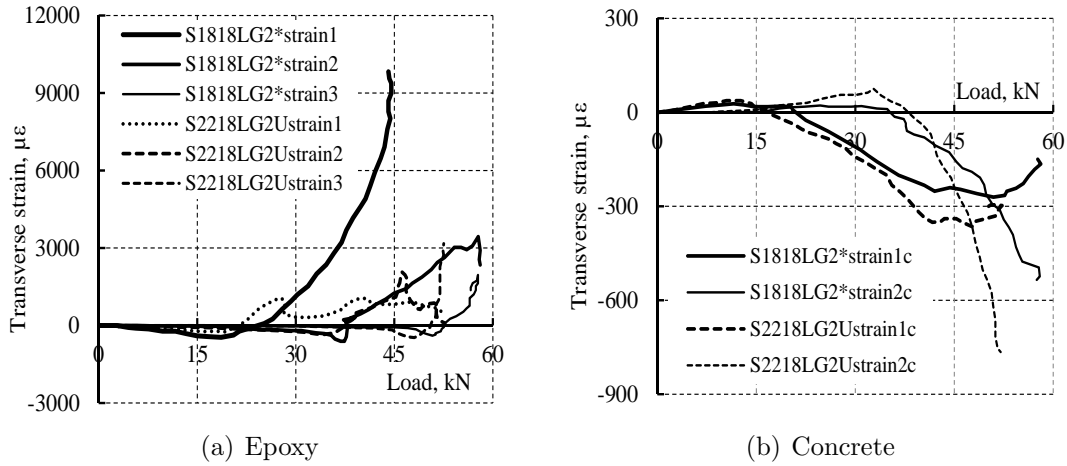


Figure 4.9: Effect of the inside concrete part confinement on the transverse strain.

4.2.3 Effect of FRP properties on the failure load and bond behaviour

Fig. 4.10a shows the relation between the axial stiffness ($E_f A_b$) and failure loads of specimens S1212LC1, S1515LC2, S1515LG1 and S1818LG2 with bars C1, C2, G1, and G2, respectively. The tested specimens attained different failure loads depending on their axial stiffness (see Fig. 4.10a). For specimens with CFRP bars (S1212LC1 and S1515LC2), the failure load decreased as the axial stiffness increased. By contrast, for specimens with GFRP bars (S1515LG1 and S1818LG2), the failure load increased as the axial stiffness increased. Bilotta et al. [71] reported that the failure load increased as the axial stiffness increased until axial stiffness equalled 8000 kN and then no further increase was observed when increasing the axial stiffness. The previous results compared with those reported by Bilotta et al. [71] indicated that the FRP material type, adhesive properties, surface treatment and test conditions changed the effect of the axial stiffness on the failure loads.

Fig. 4.10b shows the average bond slip relations of the four specimens. The specimen with C2 bars attained the highest average bond stress with the lowest

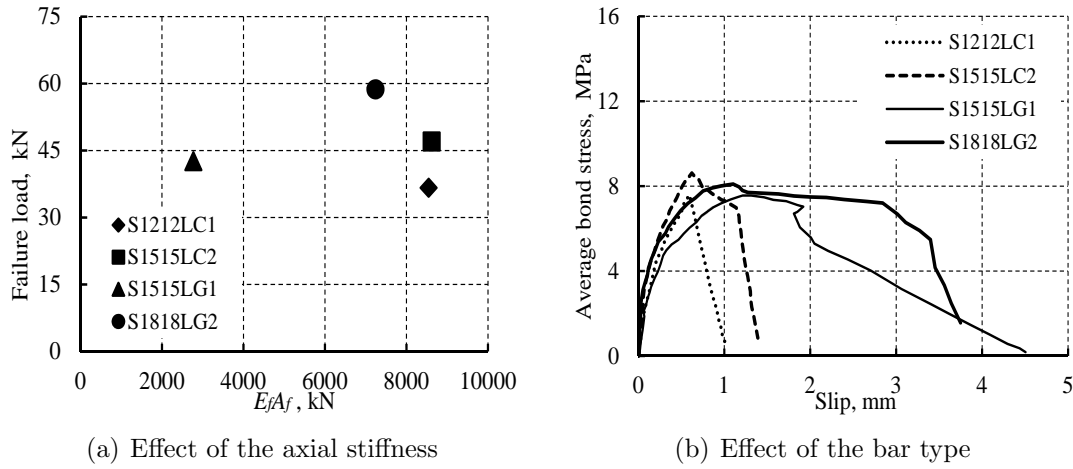


Figure 4.10: Behaviour of specimen with different FRP bars.

slip; this may be due to the cohesion bond between the C2 bars and the epoxy paste with the aid of the friction bond resulting from the surface texture of the bar. By contrast, for the specimen with G1 bars, the cohesion bond failed at low shear stresses and the friction bond resulting from the SC and HW governed the bar-epoxy bond. Due to the lower stiffness of the G1 bars, the elongation of the bar increased causing high tensile strains in the epoxy paste and increasing the slip. For the other two FRP bars, C1 and G2, the bar-epoxy bond was due to cohesion for C1 bars and friction for G2 bars. The specimen with a G2 bar attained higher average bond strength than that of C1 bars. The failure of the two specimens was mainly due to epoxy failure; either by cohesion at the bar-epoxy interface for the specimen with a C1 bar or by epoxy splitting for the specimen with G2 bars.

4.2.4 Conclusions

In this series, 26 specimens were tested to study the effect of groove surface (pre-formed and saw cut), groove geometry (dimensions and shapes), bond length, FRP bar type and of the incorporation of different modifications on the NSM-concrete interaction (transverse interlocking with or without shear connectors, covering plate with shear connectors, and confinement of the surrounding concrete). The material properties of FRP bars and the introduced variables had different effects on the bond behaviour of the tested specimens. The bar-epoxy interaction was a critical

factor affecting the mode of failure for most of the tested specimens. From the test results, the following conclusions were obtained:

- With the test conditions and the materials used, increasing the bond length of NSM bars increases the failure load regardless of the bar type, the groove details, failure mode and bar surface texture. On the other hand, the specimens with medium bond lengths and C1 bars (smooth surface texture) attained the best average bond stress distribution along their bond lengths. For specimens with NSM C1 bars, the bar-epoxy interface failure was the critical failure mechanism due to the bar surface treatment. The cohesion bond between the bar and the epoxy paste was the main factor governing the mode of failure of the tested specimens. For square grooves, increasing the groove size from $1.5d_b$ to $2d_b$ delayed the bar-epoxy interface failure and increased the failure load by 14.8%. On the other hand, using bar type C2 (with textured surface) increased the failure load of the tested specimen by approximately 34% over the corresponding specimen with bar type C1 (smoother surface) due to the effect of the surface treatment and bar size.
- For specimens with NSM G1 bars (with helical wrapping and some sand coating), epoxy splitting, and the splitting of the concrete surrounding the grooves were the modes of failure of the tested specimens, with a failure load efficiency that reached 82.16%. On the other hand, for specimens with a G2 bar (grooved surface), the tested specimens had different modes of failure depending on the tested variables, with a failure load efficiency that reached 41.16 %. The surface wrapping or grooved surface of the GFRP bars prevented pullout of the FRP bars from the epoxy paste.
- The use of mechanical interlocking in the epoxy-concrete interface with or without shear connectors, stepped grooves and covering plate enhanced the concrete-epoxy bond and slightly increased the failure loads by approximately 8.67 % for the case of covering plate (failure was due to either transverse tensile failure of the specimen or epoxy splitting). Changing the epoxy properties may enhance the failure load by enhancing the lateral strains and transferring more stresses to the positions of mechanical interlocking or, if applicable, to the stepped grooves. Further, the use of stepped grooves, mechanical interlocking

with and without shear connectors, and covering plate with shear connectors may be a solution of the epoxy concrete failure in the case of smooth grooved surfaces.

- The un-confinement of the inside part of the tested specimens affected the transverse strains either in the epoxy or in the concrete surrounding the grooves with an insignificant effect on the failure load due to the epoxy splitting failure. The un-confinement of the inside part of the tested specimen increased the lateral tensile strains in the epoxy paste and then increased the recorded slip. On the other hand, specimens with an un-confined inside part had different modes of failure from that of ordinary specimens.

4.3 Results and discussion of the second series

Results for the specimens that were tested in this series are discussed in the following section. The main factors considered are failure load, failure mode, average shear stress at the interfaces (bar-epoxy and epoxy-concrete), and slip recorded at the loaded and free ends of the FRR bar. The results are summarized in Table 4.3 and Table 4.4 for CFRP and GFRP bars respectively. P_f is the maximum load of the NSM joint, P_{fav} is the average maximum load of similar specimens and P_{max} is the ultimate tensile load of the FRP bars. $\eta_{av} = P_{fav}/P_{max}$ is the load efficiency factor and τ_{av1} , τ_{av2} , S_{le} and S_{fe} , are the average bond stress at the bar-epoxy interface, the concrete-epoxy interface, the loaded end slip and the free end at the maximum load of the NSM joint respectively. τ_{av1} and τ_{av2} are calculated by equations (4.3 and 4.4, [68]):

$$\tau_{av1} = \frac{P_{fav}}{\pi d_b L_b} \quad (4.3)$$

$$\tau_{av2} = \frac{P_{fav}}{L_b(b + 2b)} \quad (4.4)$$

4.3.1 Specimens with CFRP bars

4.3.1.1 Failure modes and load slip response

In this section the effect of groove width, groove shape, bar size and type of FRP bar on the bond behaviour of NSM CFRP bars is reported and discussed. Two specimens were tested in order to study the effect of each factor (Table 4.3). As shown in Table 4.3, the failure load and mode of failure for each pair of similar specimens were very similar and show good repeatability. The mode of failure of specimens with NSM C1 bars (those with a smoother surface) that were bonded with epoxy type A was bar-epoxy interface failure. The failure initiated with a longitudinal splitting crack on the surface of the epoxy near the loaded end (see detail in Fig. 4.11a). As the loading increased, the longitudinal crack propagated towards the free end of the bonded bar. On reaching the free end, bar-epoxy interface failure occurred. Furthermore, as the width of the groove increased (with constant depth = d_b) the failure load increased. The failure load of specimens with trapezoidal grooves (L1620AC1T) was very similar to that of specimens with narrow grooves

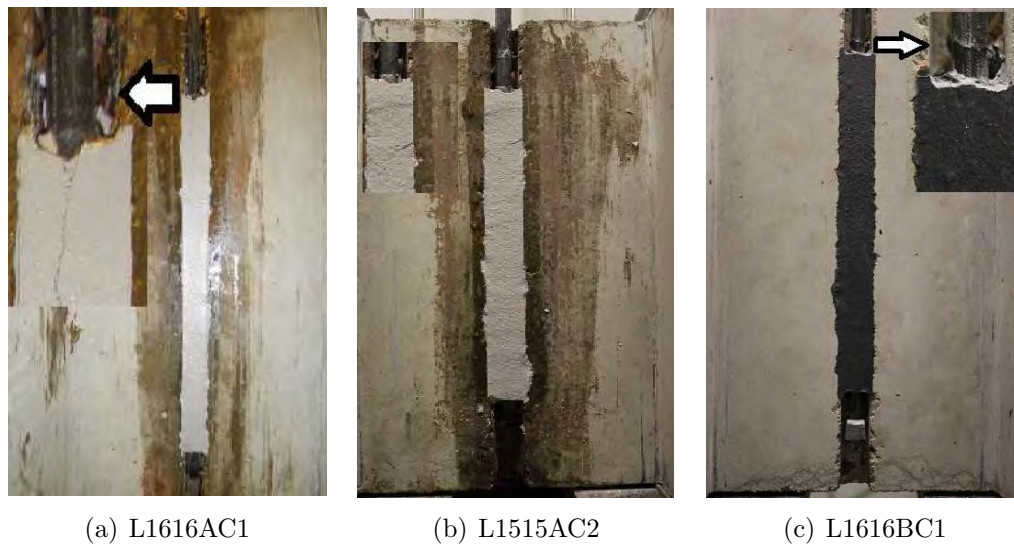
(L1612AC1). Epoxy splitting cracks formed near the loaded end and propagated towards the free end as the load increased. At the failure load, bar-epoxy interface failure occurred.

Table 4.3: Results of the tested CFRP NSM bars (second series).

Specimen ID	P_f (kN)	P_{fav} (kN)	η_{av} (%)	τ_{av1} (MPa)	τ_{av2} (MPa)	S_{le} (mm)	S_{fe} (mm)	Failure mode
L1612AC1-1	36.80					0.828	-	LC, B-E
L1612AC1-2	36.65	36.72	31.1	7.61	4.34	0.62	0.060	LC,B-E
L1616AC1-1	40.12					0.824	-	LC,B-E
L1616AC1-2	39.97	40.00	33.8	8.28	4.33	0.79	0.079	LC,B-E
L1620AC1T-1	36.53					0.63	0.055	LC,B-E
L1620AC1T-2	36.23	36.38	30.8	7.54	3.94	0.80	0.057	LC,B-E
L1515AC2-1	44.91					0.63	0.086	LC,CC
L1515AC2-2	44.65	44.78	35.0	8.20	5.18	0.48	0.076	,B-E
L1616BC1-1	48.99					0.63	0.086	B-E
L1616BC1-2	47.31	48.15	40.8	9.98	5.22	0.94	0.195	B-E
T1616BC1-1	54.79					1.12	0.088	B-E
T1616BC1-2	58.09	56.44	47.8	9.36	4.90	1.28	0.075	B-E

B-E = bar-epoxy interface failure; CC =concrete cracking and LC = epoxy longitudinal cracking.

Specimens with C2 bars (with textured surfaces) presented bar-epoxy interface failure with epoxy cracking extended to cause concrete cracking. The failure initiated with the formation of a longitudinal splitting crack followed by transverse cracking on the top surface of the epoxy paste (see Fig. 4.11b). As the load increased the longitudinal crack propagated towards the free end until a failure load of 44.78 kN was reached. To study the effect of adhesive properties and bond length on NSM bond behaviour, specimens L1616BC1 and T1616BC1 with NSM C1 bars bonded with epoxy type B were tested. The specimens showed bar-epoxy interface failure at loads of 48.15 kN and 56.44 kN respectively. No visible cracks formed in either the concrete or epoxy paste (see Fig. 4.11c). This means that changing the epoxy paste or increasing the bond length enhanced the failure load of the joint by approximately 20.4% (L1616BC1 compared to L1616AC1) and 17.2 % (T1616BC1 compared to L1616BC1) respectively, without forming splitting cracks on either the surface of the epoxy paste or the concrete.



(a) L1616AC1

(b) L1515AC2

(c) L1616BC1

Figure 4.11: Failure modes of specimens with NSM CFRP bars.

As explained previously in this section, the results obtained from specimens tested with NSM CFRP bars indicate that the failure load increased with an increase in the groove width. On the other hand, the trapezoidal grooves had no effect on the failure load due to epoxy splitting followed by bar-epoxy interface failure. Increasing the bar diameter increased the failure load of the joint in NSM C2 bars (L1515AC2) by approximately 21.95% compared to the joint in C1 NSM bars (L1616AC1) with nearly the same axial stiffness ($E_b A_b = 7976:8296$ kN). In contrast, the two NSM bars (C1 and C2) had nearly the same average bond stress. Moreover, as explained above, changing the adhesive properties or increasing the bond length both enhanced the failure load of the joint.

Fig. 4.12 illustrates the load slip behaviour of specimens with NSM CFRP bars and epoxy A. Fig. 4.12a shows the load slip behaviour of specimens with a groove width equal to $1.5d_b$. At the beginning of loading, as the load increases the slip increases linearly until it reaches 41.6 % of the failure load. From there until failure the slip increases at a higher rate than before. After the maximum load a sharp decrease is observed in the load slip relationship. Specimens with wider grooves ($2d_b$) or with a trapezoidal groove shape (Figs. 4.12b and 4.12c) follow load slip behaviour similar to that of specimens with a groove width of ($1.5d_b$), with a slight increase in the failure load of specimens with wider groove width (L1616AC1).

Specimens with C2 NSM bars (Fig. 4.12d) followed the same load slip behaviour as specimens with NSM C1 bars, with a higher failure load and lower slip due to bar size. Fig. 4.13 illustrates the load slip behaviour of specimens with NSM C1 bars bonded using adhesive type B (L1616BC1 and T1616BC1). As the load increases the slip increases until it reaches the failure load. After this point, the load decreases slowly as the bar slip increases until the test is stopped. These results indicate that the use of adhesive type B led to ductile behaviour that was greater after the maximum load than in similar specimens with NSM C1 bars bonded using adhesive type A.

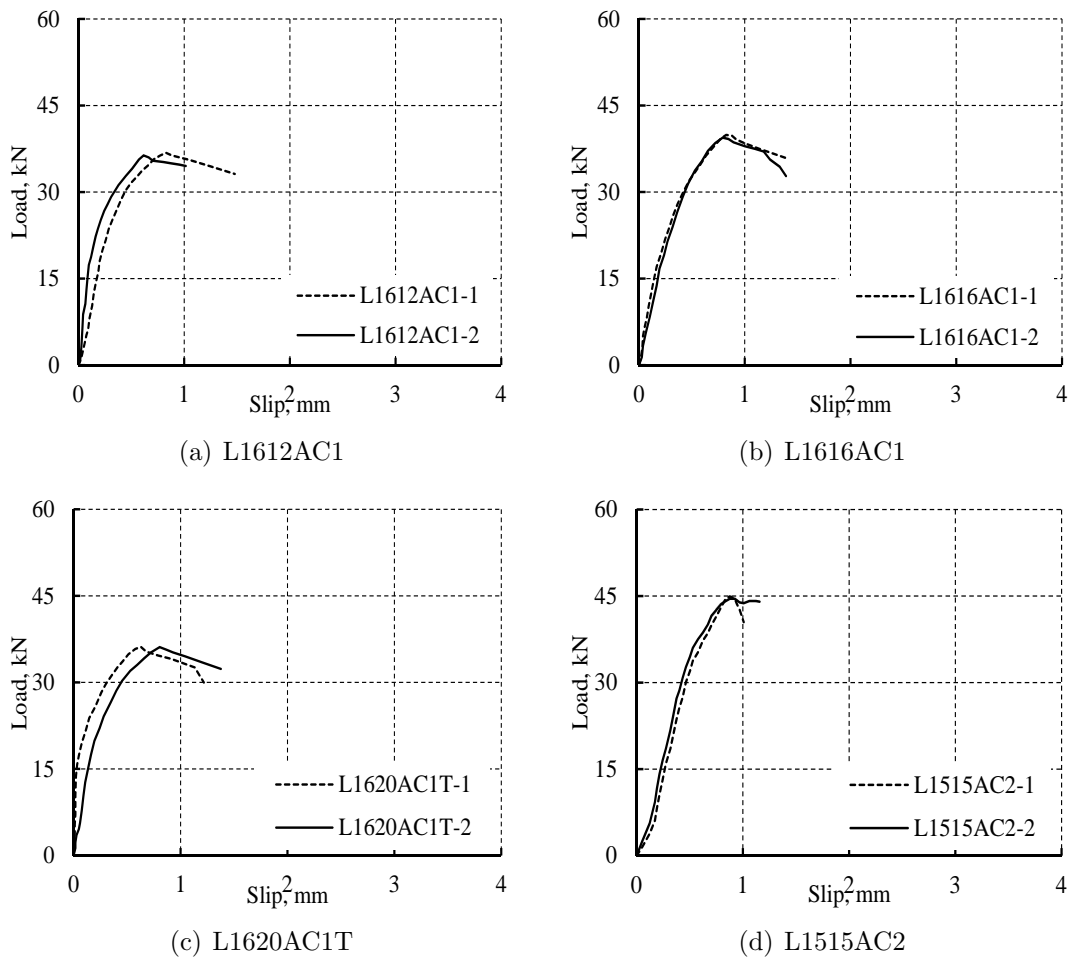


Figure 4.12: Load slip curves of specimens with NSM CFRP bars bonded with epoxy type A.

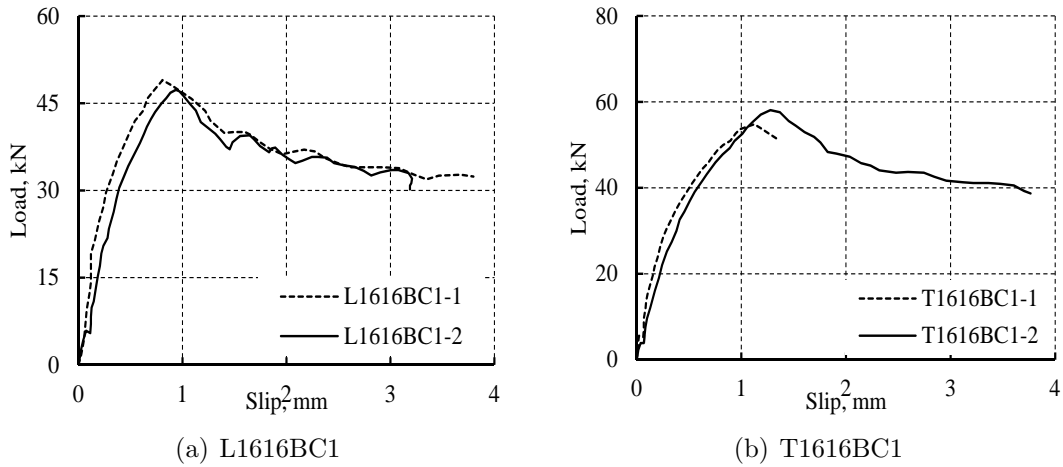


Figure 4.13: Load slip curves of specimens with NSM CFRP bars bonded with epoxy type B.

4.3.1.2 Effect of bar type on transverse strain distribution in epoxy and concrete

Figs. 4.14a and b illustrate the transverse strains in the epoxy paste filling the grooves and the concrete surrounding the groove, respectively, for specimens with NSM C1 bar. All strain gauges instrumented on the epoxy paste recorded negative strains at the beginning of loading, followed by positive strains until failure, with different strain values depending on the strain location.

At the beginning of the loading process the NSM bar exerted tensile stress on the epoxy paste at the bar-epoxy interface due to Poisson's lateral contraction of the FRP bar under tension. This caused transverse compressive stresses on the top surface of the epoxy paste. As the load increased, the tensile stresses converted to compressive stresses due to the friction bond at the bar-epoxy interface, which was very small due to the smooth surface of the bar. These compressive stresses caused transverse tensile stresses on the top surface of the epoxy paste, similar to the observation reported in [69].

In contrast, the transverse strain was tensile (small values) in the concrete surrounding the groove, and then converted to compressive strains until failure. No crack was observed in the concrete due to the transverse strains' small values, and the failure occurred in the bar-epoxy interface.

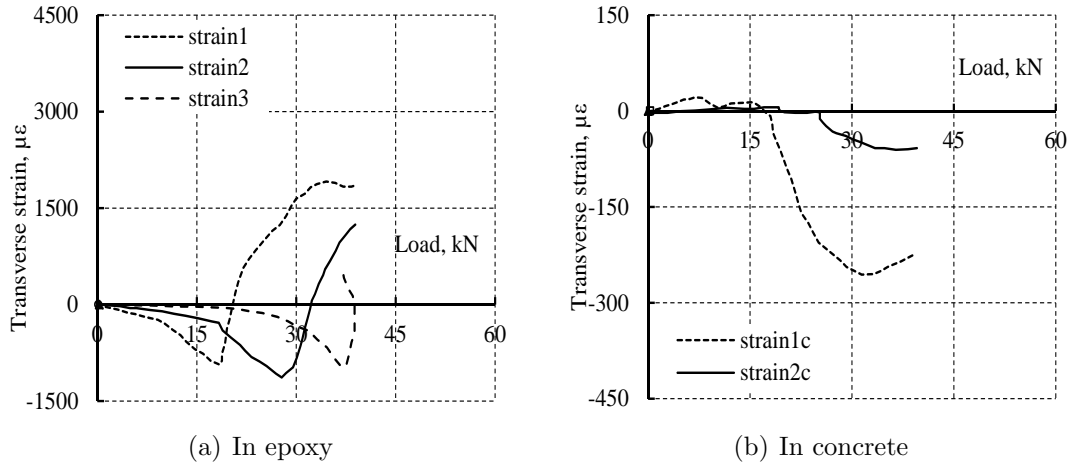


Figure 4.14: Transverse strain distribution for specimen L1616AC1.

The same behaviour was observed in specimens with NSM C2 bars with higher tensile transverse strains due to the surface treatment of the bar (Fig. 4.15a) recorded by strain1 (near the loaded end). The transverse tensile strains in the epoxy paste exerted compressive stresses in the concrete surrounding the grooves, causing transverse compressive strains in the concrete. The resulting compressive and shear stresses in the concrete surrounding the groove formed very narrow tensile cracks on the surface of the concrete. From these results it can be concluded that the bar with surface treatment enhanced the bond between the bar and the epoxy paste, and exerted greater compressive and shear stresses on the concrete surrounding the grooves, causing cracking in the concrete.

4.3.2 Specimens with GFRP bars

4.3.2.1 Failure modes and load slip response

In this section the effect of groove width, groove shape, bar size and adhesive properties on the bond behaviour of NSM GFRP bars is reported and discussed. Two specimens were tested to study the effect of each factor on bond behaviour. In the cases of specimens L1616BG1 and L1616CG1 a third specimen was tested because the difference between the load capacities of the specimens tested first was greater than in the other cases (Table 4.4). The mode of failure of specimens with NSM G1 bars bonded with epoxy type A was epoxy splitting followed by the de-

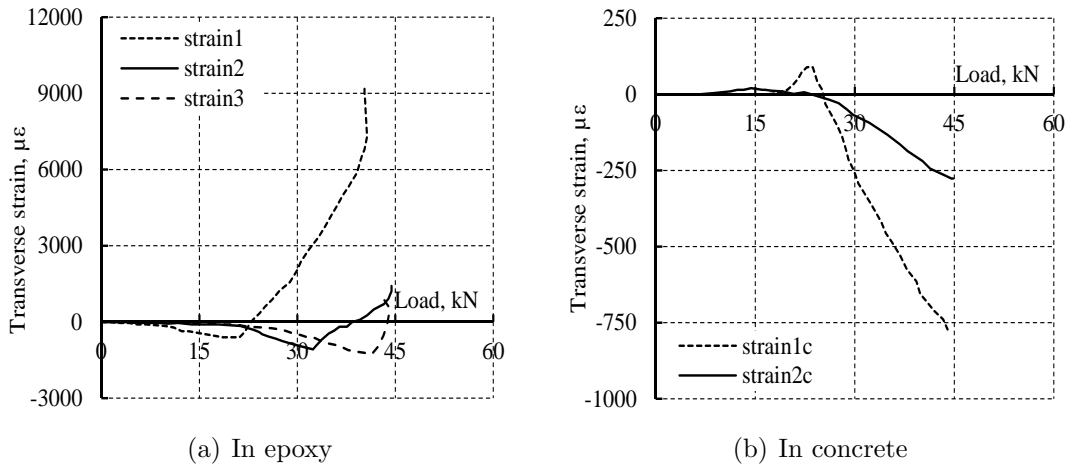


Figure 4.15: Transverse strain distribution for specimen L1515AC2.

tachment of the concrete surrounding the groove. The failure initiated with the formation of a longitudinal splitting crack in the epoxy paste near the loaded end. As the load increased, the longitudinal crack propagated towards the free end of the bonded GFRP bar. At the failure load, epoxy splitting occurred with detachment of the concrete surrounding the grooves (Fig. 4.16a). However, the failure load increased by approximately 12% when the width of the groove increased from $1.5d_b$ (L1612AG1) to $2d_b$ (L1616AG1) with constant depth ($2d_b$), with no change in the mode of failure.

The results for specimens L1612AG1, L1616AG1 and L1620AG1T indicate that the failure load of the first specimen tested was lower for each groove size than that of the second specimen tested with the same groove size by a nearly constant value for the three groove geometry. With the first specimen tested for each groove geometry (L1612AG1-1, L1616AG1-1 and L1620AG1T-1), the NSM GFRP bar was bonded in the center of the groove (the epoxy cover was 2.5 mm over the grooved surface of the bar) while for the second specimen of each groove geometry the NSM bar was bonded in order to allow the epoxy cover to increase to 3 mm with the same groove depth. This increase increased the failure load for the three specimens tested by approximately 10%. Changing the groove shape to a trapezoidal or U groove, or using mechanical interlocking, had no effect on the failure load of the specimens tested since the failure was due to epoxy splitting (see Fig. 4.16b).

Table 4.4: Results of the tested GFRP NSM bars (second series).

Specimen ID	P_f (kN)	P_{fav} (kN)	η_{av} (%)	τ_{av1} (MPa)	τ_{av2} (MPa)	S_{le} (mm)	S_{fe} (mm)	Failure mode
L1612AG1-1	31.43					1.46	0.036	LC,CS
L1612AG1-2	35.63	33.53	49.4	6.95	3.97	1.42	0.047	,ES
L1616AG1-1	36.23					1.60	0.094	LC,CC
L1616AG1-2	38.92	37.57	55.4	7.78	4.07	1.30	-	,ES
L1620AG1T-1	33.22					1.23	0.052	LC,CC
L1620AG1T-2	36.82	35.02	51.6	7.25	3.80	1.45	-	,ES
L1916AG1U-1	35.80					1.41	0.024	LC,CC
L1916AG1U-2	36.33	36.06	53.1	7.47	3.91	1.85	0.036	,ES
L1616AG1I-1	35.28					1.52	0.067	LC,CC
L1616AG1I-2	33.33	34.31	50.6	7.11	3.72	1.46	0.045	,ES
L1818AG2-1	59.97					1.26	0.057	LC,CS ,ES
L1818AG2-2	57.53	58.75	38.5	8.11	5.67	0.99	0.072	LC,CC ,ES
L1616BG1-1	56.67					3.08	0.258	CC, BD
L1616BG1-2	44.56					3.06	0.233	CC, BD
L1616BG1-3	48.06	49.76	73.3	10.49	5.49	2.68	0.371	CC,BD
L1616CG1-1	56.34					2.36	0.363	CC,BD
L1616CG1-2	45.36					2.47	0.213	CC,BD
L1616CG1-3	52.34	51.35	75.7	10.64	5.57	2.86	0.230	CC,BD
L1616DG1-1	52.10					3.59	0.298	CC,BD
L1616DG1-2	57.79	54.95	81.0	11.38	5.96	3.65	0.290	BD

BD = bar surface damage; CC = concrete tension failure; CS = concrete splitting; ES = epoxy splitting; and LC = longitudinal cracking of the epoxy.

These factors may have a great effect on bond behaviour in the case of smooth grooves where the critical mode of failure is concrete-epoxy interface failure. The failure mode of specimens with G2 bars initiated with the formation of a longitudinal splitting crack in the epoxy paste. As the load increased, the longitudinal crack propagated and formed tensile cracks in the concrete surrounding the groove until failure. The mode of failure was epoxy splitting with a concrete splitting crack for the first specimen tested (see Fig. 4.16c), and epoxy splitting with detachment of concrete surrounding the groove for the second.

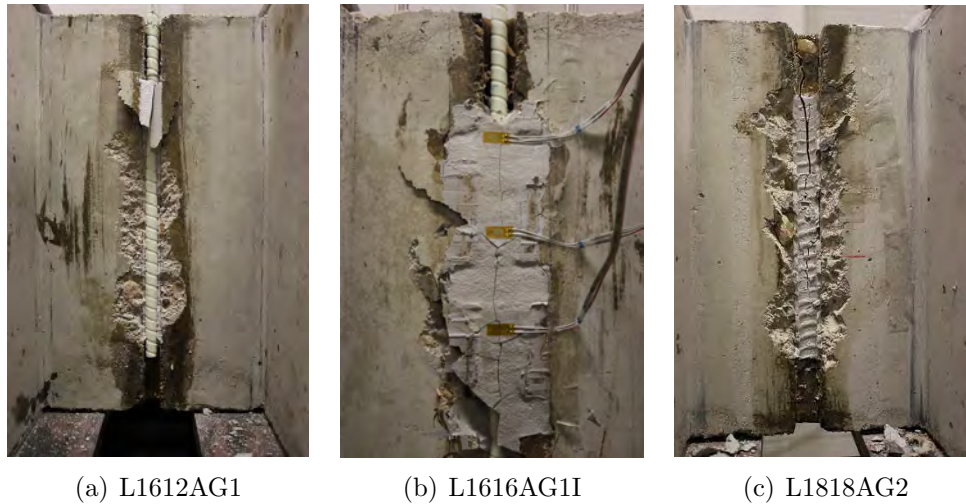


Figure 4.16: Failure mode of specimens with NSM GFRP bars bonded with adhesive type A.

To gauge the effect of the adhesive properties, the G1 bar was bonded to square grooves of $2d_b$ using epoxy types B, C and D. For specimens with epoxy type B, concrete cracks formed near the free end of the bonded bar and the bar slipped slowly until failure. After testing, the epoxy paste was removed and it was observed that the grooved surface of the bar was damaged (see Fig. 4.17a). The same mode of failure was observed for epoxy type C specimens (see Fig. 4.17b). The failure load of epoxy types B and C specimens was mainly influenced by the failure of the grooved surface of the GFRP bar. The failure mode of specimens with G1 bars and bonded using epoxy type D was bar surface damage at a load capacity higher than that in specimens bonded with epoxy types B and C (see Fig. 4.17c).

It has already been noted that for specimens with GFRP bars, increasing the groove width by 33 % increased the load capacity of the joint with NSM G1 bars by approximately 12 %, while increasing the bar diameter of GFRP bars from 8 mm for G1 to 12 mm for G2 (approximately 50 %) increased by approximately 75.2 % the failure load of the specimens with a groove width of $1.5d_b$ (L1612AG1 and L1818AG2). The mode of failure was the same. Furthermore, changing the adhesive type from A to B, C and D for specimens with NSM G1 bars increased the failure load of the joints tested by 32.4 %, 36.7 % and 46.3 % respectively.

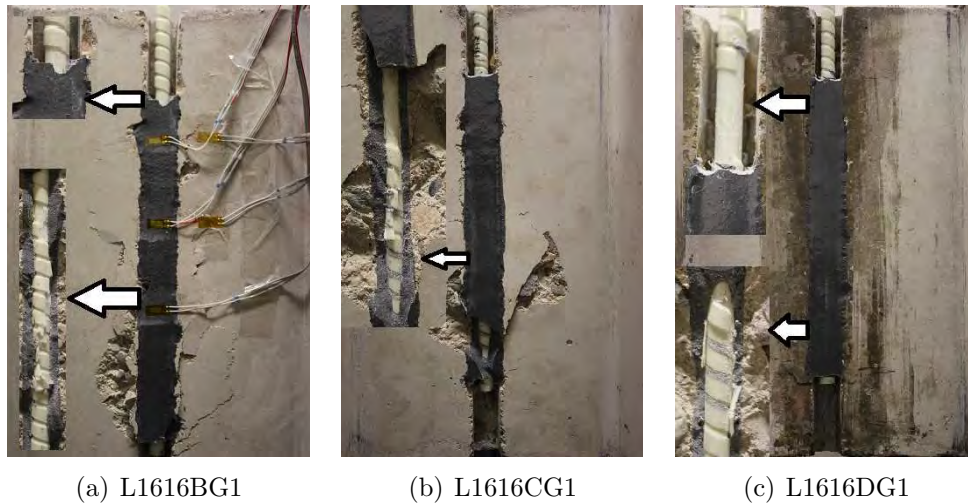


Figure 4.17: Failure mode of specimens with NSM GFRP bars bonded with adhesive types B, C and D.

Fig. 4.18 shows load slip curves of specimens with NSM GFRP bars bonded using epoxy type A. Load slip behaviour was linear up to 10 kN for specimens L1612AG1 and L1616AG1, but the slip increased non-linearly as the load increased until the maximum load, after which a sudden drop occurred (Figs. 4.18a and 4.18b). Specimens with trapezoidal L1620AG1T grooves (Fig. 4.18c) followed the same response as L1612AG1 with lower slip values. An increase in the epoxy cover (L1612AG1-2, L1616AG1-2 and L1620AG1T-2) increased the failure load of the specimens. Figs. 4.18d and e illustrate specimens with a U groove and specimens with mechanical interlocking, whose load slip behaviour follows that of specimens L1616AG1. There is no increase in the failure load due to epoxy cover splitting. On the other hand, for specimens with G2 bars (Fig. 4.18f), which are stiffer than those with G1 bars due to their increased diameter, the average shear stress and slip decreases, thus increasing the load capacity of the joint.

Fig. 4.19 illustrates the load slip behaviour of specimens with NSM G1 bars bonded with epoxy types B, C and D. The bond slip response is linear at the beginning of loading, and as the load increases the slip increases rapidly until failure. The load capacities of these joints are higher than those of similar joints bonded with epoxy type A. Epoxy types B, C and D distribute the bond stresses better along the bond length.

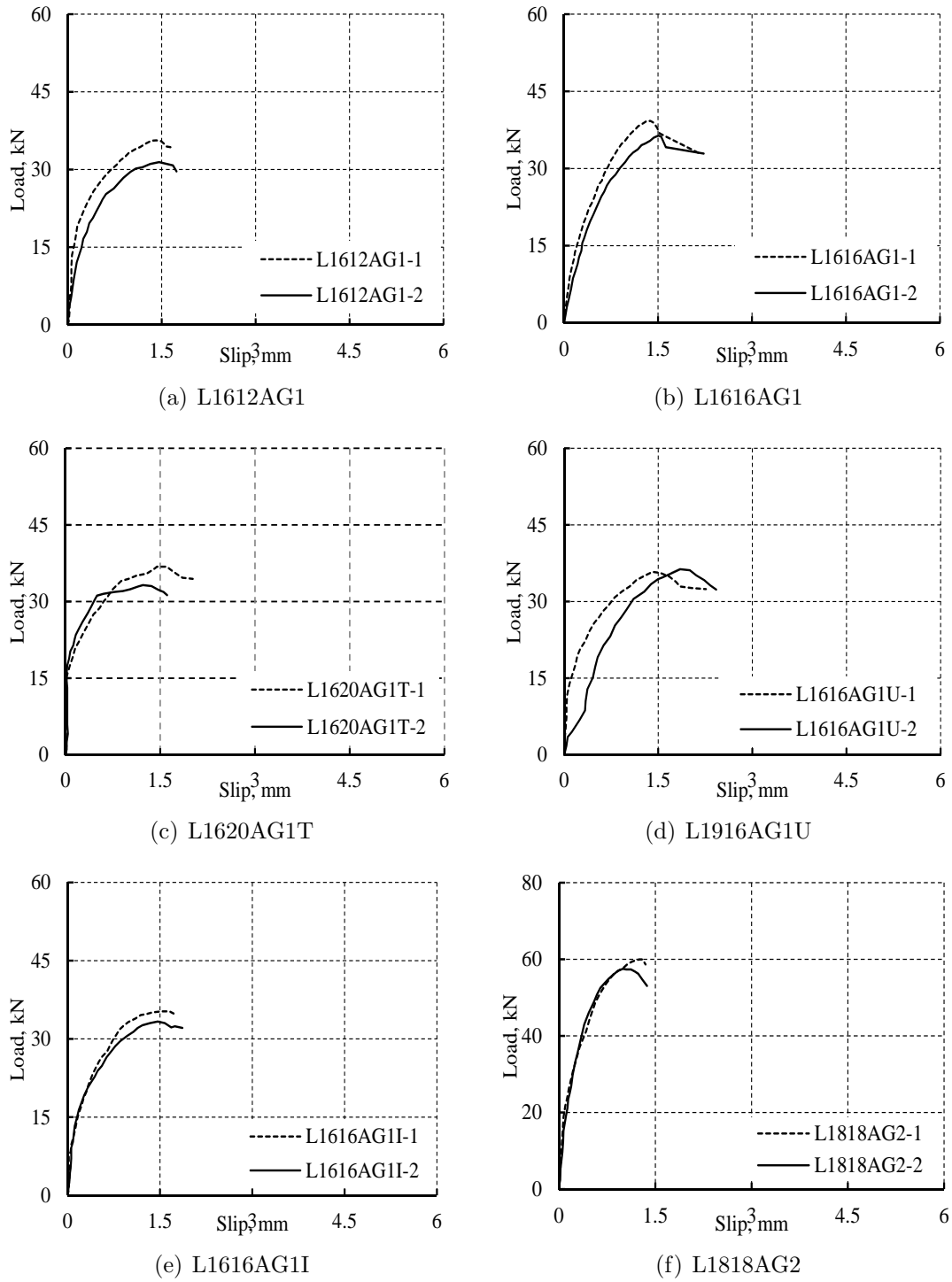


Figure 4.18: Load slip curves of specimens with NSM GFRP bars bonded using epoxy type A.

After the maximum load, the load decreases slowly with increasing slips, unlike specimens bonded with epoxy type A. During the descending loading stage, short cracks in the concrete can be observed, starting at the free end of the bond length.

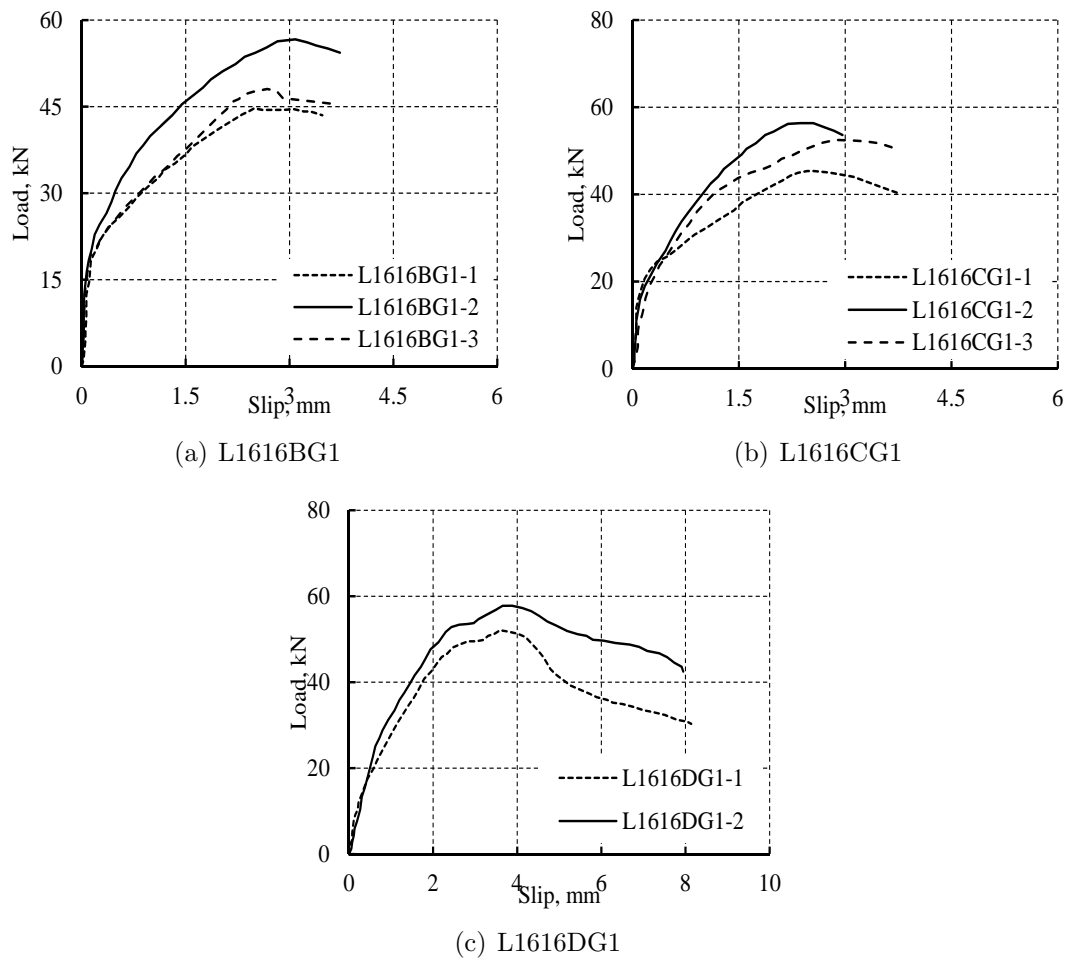


Figure 4.19: Load slip curves of specimens with NSM GFRP bars bonded using epoxy types B,C and D.

4.3.2.2 Transverse strain distribution in epoxy and concrete

Figs. 4.20a and b show that the transverse strain distribution in epoxy paste and concrete respectively was similar to that observed in the specimens with C1 bars. However, the surface treatment of the FRP bars affected greatly the values of transverse strains both in the epoxy paste and the concrete. The GFRP bars with grooved surfaces increased the tensile stresses in epoxy causing extended epoxy

splitting, resulting in concrete cracks. The recorded transverse strains for specimens with trapezoidal grooves (L1620AG1T, Fig. 4.21) followed a similar response to specimens with square grooves (L1616CG1), with lower strain values. The three strain gauges for specimens with trapezoidal grooves recorded nearly equal values. This shows that increasing the groove size toward the free end of the bond length redistributed shear stresses either in the epoxy or at the epoxy-concrete interface, thereby decreasing the transverse strains in the epoxy and concrete.

For specimens with a U groove (Fig. 4.22), the epoxy cover was increased and the resistance of the epoxy cover to splitting increased. The transverse strains recorded by the two gauges (strain 1 and strain 2) had similar maximum values due to the ability of the epoxy cover to transfer the stresses between the strain gauges along the bond length. The recorded strains in concrete (strain 1c and strain 2c) were also similar. However, the use of mechanical interlocking decreased the transverse strains recorded by the three strain gauges in the epoxy recorded by the three strain gauges. This shows that the mechanical interlocking confined the epoxy paste filling the grooves transversally, and permitted the formation of splitting cracks until failure (see Fig. 4.23). At failure the epoxy paste split suddenly.

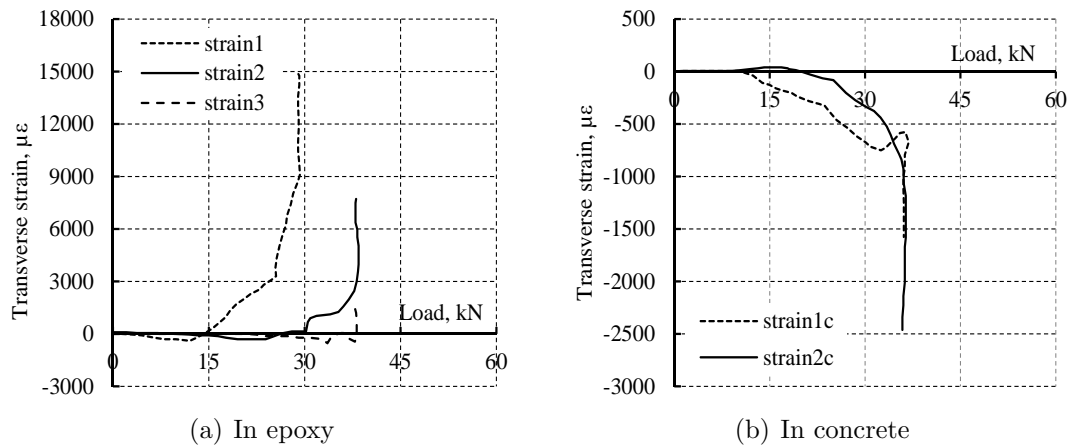


Figure 4.20: Transverse strain distribution for specimen L1616AG1.

The transverse strain distribution in the epoxy paste for specimens with G2 bars (Fig. 4.24a) followed a similar trend to specimens with G1 bars. Due to the larger bar size, the recorded strain values for the former were approximately 50% of those recorded for the latter.

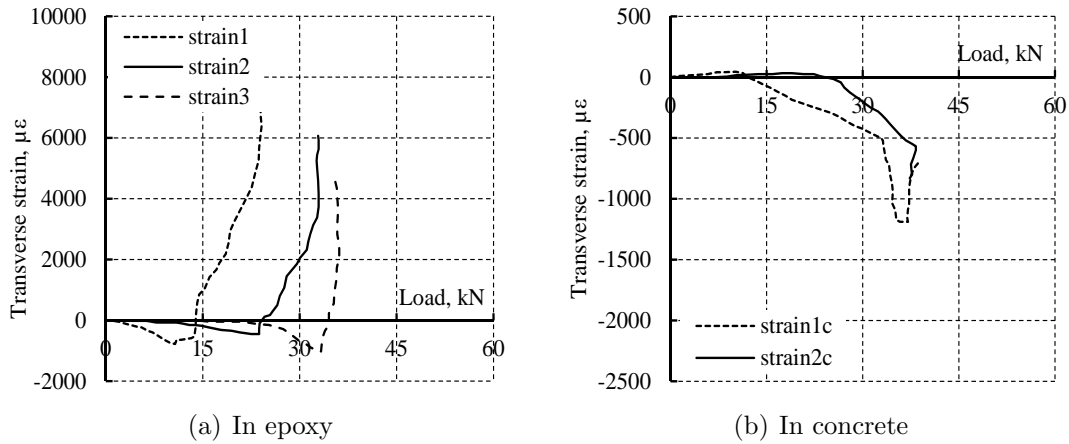


Figure 4.21: Transverse strain distribution for specimen L1620AG1T.

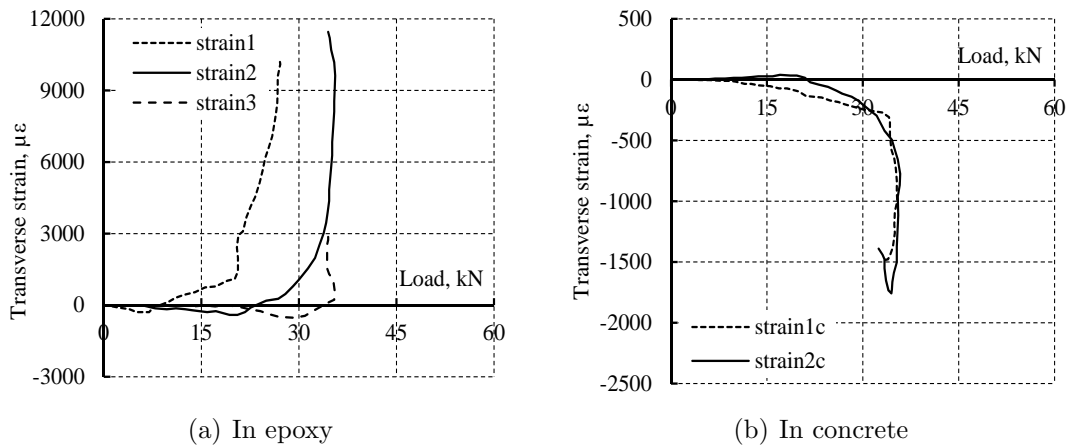


Figure 4.22: Transverse strain distribution for specimen L1916AG1U.

This demonstrates that increasing the bar size decreased the interfacial stresses at the bar-epoxy interface. The transverse strain in the concrete for G2 specimens was higher than that of specimens with G1 bars due to their higher capacity (Fig. 4.24b). For specimens with G2 bars, the transverse strains recorded by the strain 1c and strain 2c gauges increased as the load increased, up to loads of 56 kN and 59 kN respectively. At these loads, concrete tensile cracks formed beneath the strain gauges, and then tensile strains were recorded until failure.

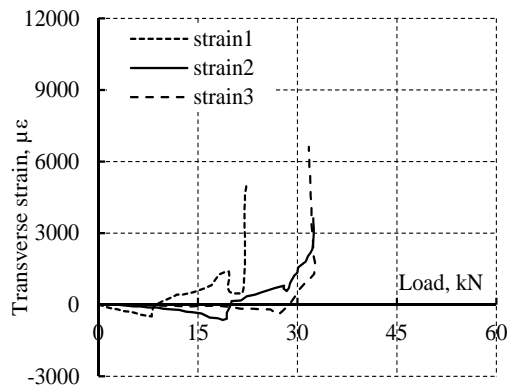


Figure 4.23: Transverse strain distribution for specimen L1616AG1I.

In specimens with NSM G1 bars bonded with epoxy types B and C (Figs. 4.25a and 4.26a), the three strain gauges instrumented to the epoxy paste recorded similar values at different load stages. This shows that the epoxy distributed the bond stresses well along the bond length and reduced transverse strains in the epoxy and concrete (see Figs. 4.25b and 4.26b).

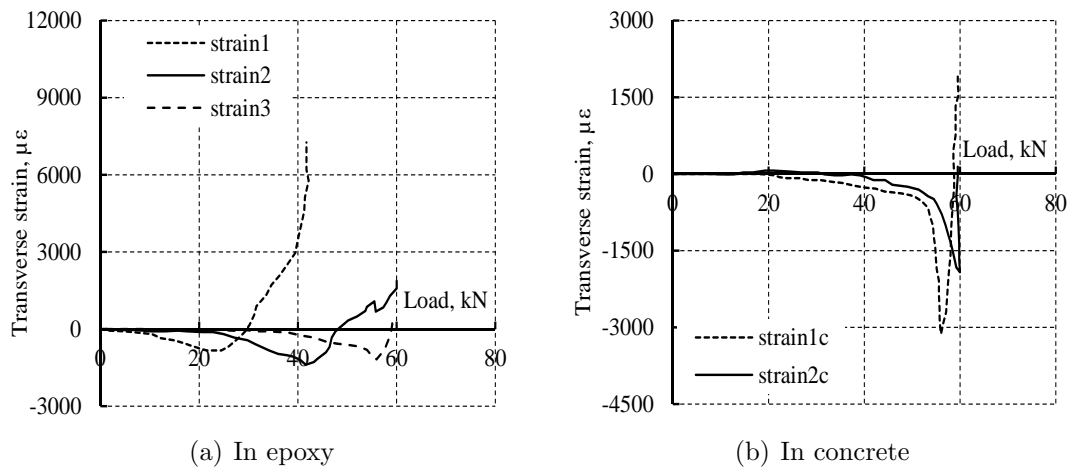


Figure 4.24: Transverse strain distribution for specimen L1818AG2.

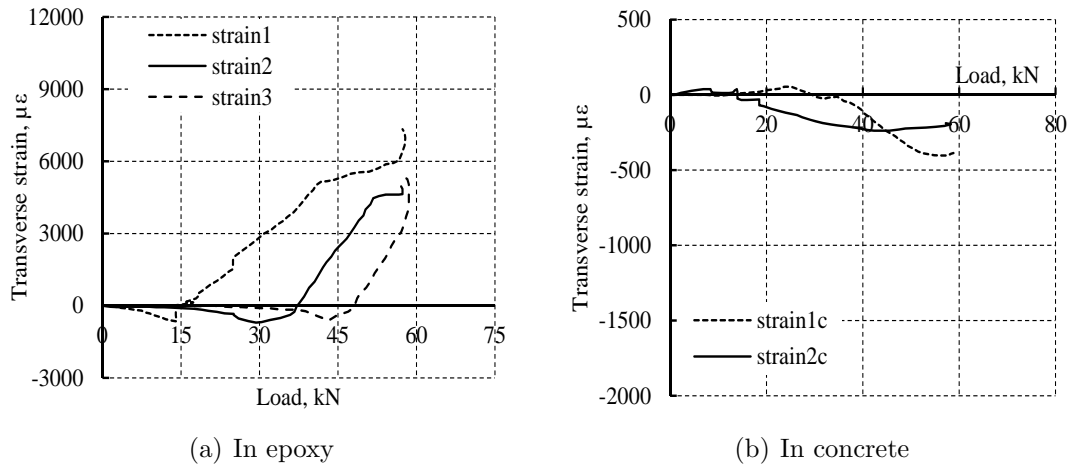


Figure 4.25: Transverse strain distribution for specimen L1616BG1.

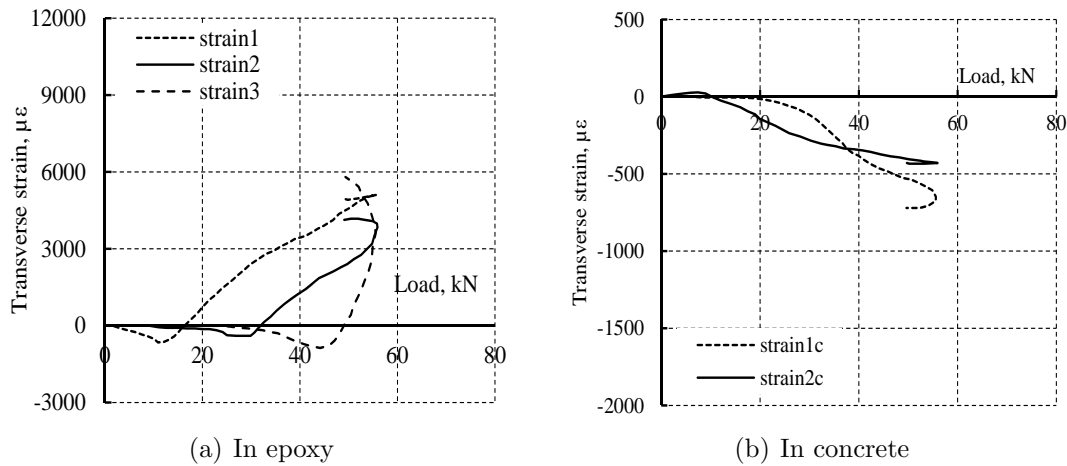


Figure 4.26: Transverse strain distribution for specimen L1616CG1.

4.3.3 Discussion of the effect of different parameters on behaviour and failure load

4.3.3.1 Groove dimensions, groove geometry and bar size

The effect of groove geometry on the specimens tested with NSM CFRP bars is illustrated in Fig. 4.27a. The specimens with a trapezoidal groove that had the same groove perimeter (average width) as those with square grooves showed lower slips until their failure load. For the specimens with square grooves, increasing the groove

width by 33.3 % increased the failure load by 8.85%. Specimens with NSM C2 bars experienced lower slips and higher failure loads than specimens with NSM C1 (see Fig. 4.27b) although they had nearly the same axial stiffness ($E_b A_b = 7976\text{-}8296$ kN). This may have been due to the effect of bar size enhancing the bar-epoxy bond. The results indicate that increasing the bar diameter by 13.12 % increased failure load by 21.95 %, with the same mode of failure at maximum load (i.e. bar-epoxy interface failure). All these results agree with those reported in section 4.2.

Figs. 4.28a and b illustrate the effect of groove geometry (U groove, trapezoidal groove or groove with mechanical interlocking) and bar size on the bond behaviour of specimens with NSM GFRP bars. The groove geometry had no significant effect at the beginning of loading. The slip until failure was higher for specimens with a U groove, trapezoidal grooves and mechanical interlocking compared to specimens with a square groove (L1616A1G1). On the other hand, for specimens with square grooves, increasing the groove width by 33.3 % increased the failure load by 12 %. Increasing the bar size by 50 % (with the same mechanical properties and surface treatment) increased the failure load by approximately 75.2 %.

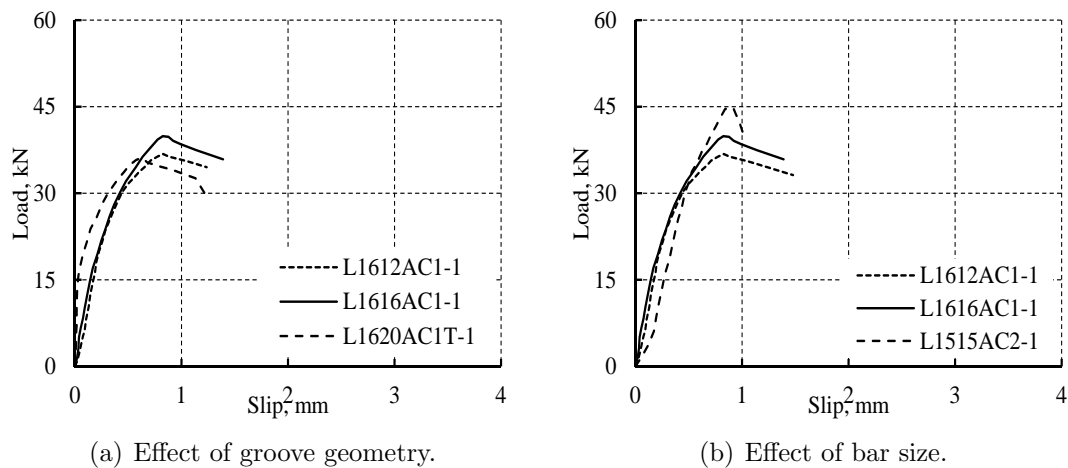


Figure 4.27: Effect of groove dimensions, geometry and bar size on behaviour of specimens with NSM CFRP bars.

The results from previous studies help to emphasize the effect of construction details on bond behaviour. Those reported in [68] indicate that changing the groove size increased the failure load of the NSM FRP bars. Fig. 4.29a shows the results obtained from specimens tested with square grooves in [68] and those with variable

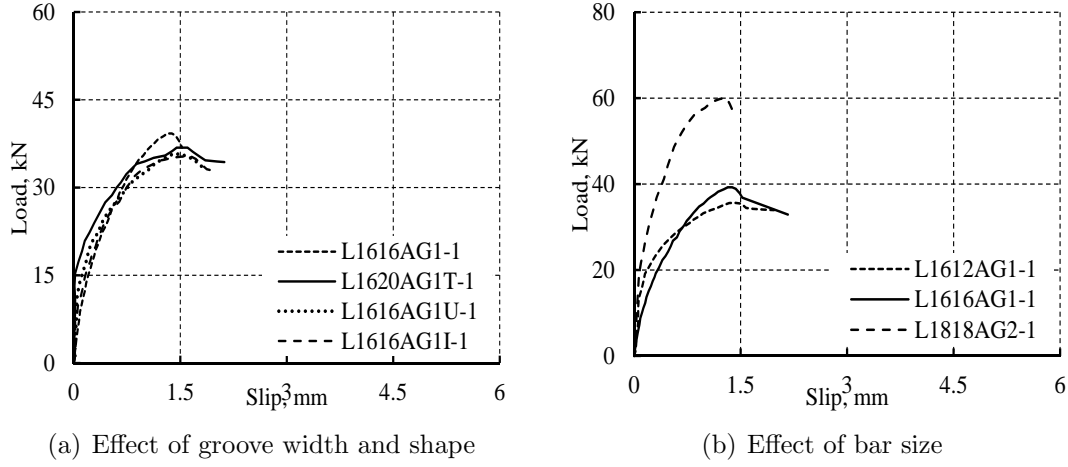


Figure 4.28: Effect of groove width, shape and FRP bar size on behaviour of specimens with NSM GFRP bars.

width-to-depth ratio with constant depth in [69] ($w =$ groove width and $K = d/d_b$). For specimens with square grooves [68], three groove sizes, $1.5d_b$, $2d_b$ and $2.5d_b$ ($d_b = 8$ mm), with bonded lengths of $4d_b$, $12d_b$ and $24d_b$, were tested. The bars were bonded to the grooves using epoxy paste, and the specimens showed epoxy-concrete interface failure.

It can be seen from the results that for specimens with bond lengths $4d_b$, $12d_b$ and $24d_b$, changing the groove width from $1.5d_b$ to $2.5d_b$ increased the failure load by approximately 13.6 %, 22.1 % and 17.9 % respectively, while changing the bond length from $4d_b$ to $24d_b$ increased the failure load by approximately 321.5 % and 337.8 % for specimens of groove sizes $1.5d_b$ and $2.5d_b$ respectively.

For the specimens tested in [69], two bond lengths in which the groove width-to-depth ratio was changed were examined. As shown in Fig. 4.29a, for specimens with a long bond length ($24d_b$), increasing the groove width from $1.5d_b$ to $2d_b$ and from $2d_b$ to $2.5d_b$ ($d_b = 8$ mm) increased the failure load by approximately 39.3 % and 8 % respectively.

In contrast, for specimens with a short bond length the groove width had no appreciable effect on the failure load. For specimens with groove widths $1.5d_b$, $2d_b$ and $2.5d_b$, increasing the bond length from $4d_b$ to $24d_b$ increased the failure load by approximately 158.6 %, 246 % and 292.5 % respectively, with the same mode of failure.

The results reported in [72] (Fig. 4.29b) indicate that the failure loads of NSM CFRP bars increased as groove size and /or bond length increased. For specimens with bonded lengths $3d_b$, $5d_b$ and $10d_b$, changing the groove size from $1.5d_b$ to $2d_b$ ($d_b = 12$ mm) increased the failure load by 11%, 26% and 11.3% respectively, while for specimens with groove sizes $1.5d_b$ and $2d_b$ increasing the bond length from $3d_b$ to $5d_b$ increased the failure load by 68 % and 90.9 % respectively. Increasing the bond length from $3d_b$ to $10d_b$ increased the failure load by 170.6 % and 201.2 % respectively.

The results reported in [70] (Fig. 4.29b) indicate that increasing the bond length for specimens with groove sizes of $1.5d_b$ and $2d_b$ from $6d_b$ to $24d_b$ ($d_b = 9.5$ mm) increased their failure load by 195.6 % and 112.6 % respectively. Increasing the groove size from $1.5d_b$ to $2d_b$ increased the failure load of the joints with bond lengths of $6d_b$ and $24d_b$ by 24% and 13% respectively, and decreased the failure load of the joints with bond lengths of $18d_b$ and $24d_b$.

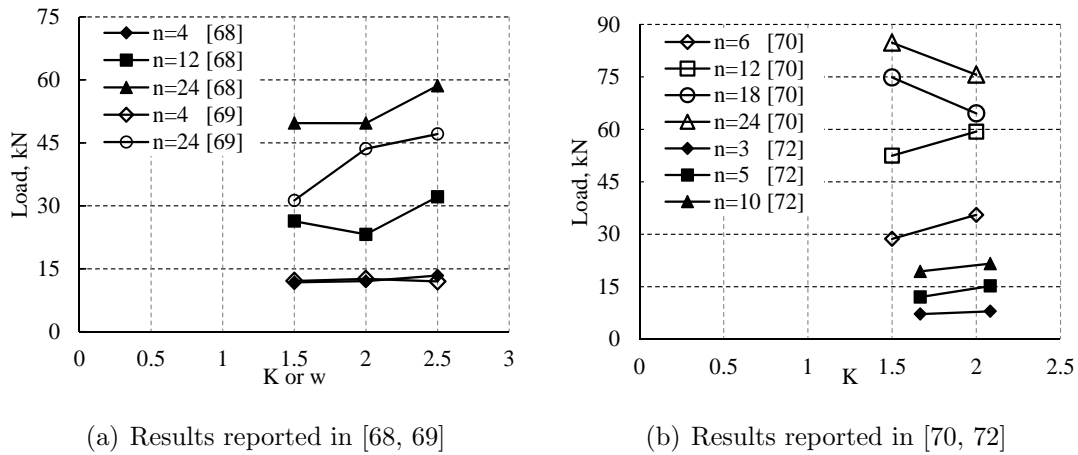


Figure 4.29: Effect of groove dimensions and bond length on the capacity of specimens reported in [68–70, 72], ($K = d/d_b$; $w =$ groove width; $n = L_b/d_b$; $L_b =$ bond length).

The above results point to bond length being one of the main factors affecting the failure load of NSM joints, with an increase in bond length increasing the load regardless of the effect of other factors. When bond length was increased by 66.6 % and 83.3 % the failure load increased by 68 % and 337 % respectively [72, 96]. Groove size and geometry seem to be a secondary factor. An increase in groove size

increased or decreased the failure load depending mainly on adhesive properties. The maximum percentage increase in the failure load was the 39.5 % obtained from the groove size changes (33.3 % to 66.6 %) reported in [69, 70, 72, 96] and the present work.

In this study bar diameter seemed to be another important factor in the increase of the load capacity of NSM joints. Increasing the diameter of CFRP bars by 13.12% increased the failure load of the NSM by 21.95% with the same mode of failure at the maximum load (i.e. bar-epoxy interface failure). And increasing the bar diameter of the NSM GFRP bars by approximately 50% from 8 mm to 12 mm increased the failure load of the specimens with a groove width of $1.5d_b$ by approximately 75.2%, with the same mode of failure.

From all the above results the bond length seemed to be one of the main factors affecting the failure load of the NSM joints. The increase in the bond length increased the failure load of the joints regardless of the effect of the other factors. Increasing the bond length by 66.6 % and 83.3 % increased the failure load of the NSM joints till 68 % and 337 % respectively [72, 96].

The groove size and groove geometry seemed to be one of the secondary factors affecting the failure load of the NSM joints. Increasing groove size increased or decreased the failure load depending mainly on the adhesive properties. The maximum percentage of increase in the failure load was 39.5 % obtained from the groove size changes (33.3 % to 66.6 %) reported in [69, 70, 72, 96] and in the present work.

In the present work the bar diameter seemed also to be one of the main factors increasing the load capacity of the NSM joints. Increasing the diameter of CFRP bars by 13.12% increase the failure load of the NSM by 21.95% with the same mode of failure at the maximum load (i.e. bar-epoxy interface failure). In addition, increasing the bar diameter of the NSM GFRP bars from 8 mm to 12 mm (approximately 50%) increased the failure load of the specimens with groove width $1.5d_b$ by approximately 75.2% with the same mode of failure.

4.3.3.2 Adhesive type and concrete strength

The results of this work are evidence of the influence of adhesive type on the bond behaviour of NSM FRP reinforcement. This influence has also been reported in previous studies [[68–70].

The results indicate that with the same axial stiffness, a change in the epoxy type increased the failure load of NSM FRP bars. For specimens with these bars (see Fig. 4.30a), using epoxy type B instead of epoxy type A increased the failure load by approximately 22.57% and changed the mode of failure from bar-epoxy slip with a sudden drop in load capacity to bar-epoxy slip with ductile failure (a slowly decreasing load with a considerable increase in the slip). Failure load increased for the specimens tested with NSM GFRP bars bonded with epoxy type B, C and D by approximately 32.4%, 36.7% and 46.3% respectively over those bonded with adhesive type A.

Moreover, the failure mode changed from epoxy splitting causing concrete splitting (L1616AG1) to bar surface damage causing concrete cracking (L1616BG1, L1616CG1, L1616DG1) near the free end of the bond length. Fig. 4.30b shows the load slip curves of joints bonded with the four types of adhesive A, B, C and D.

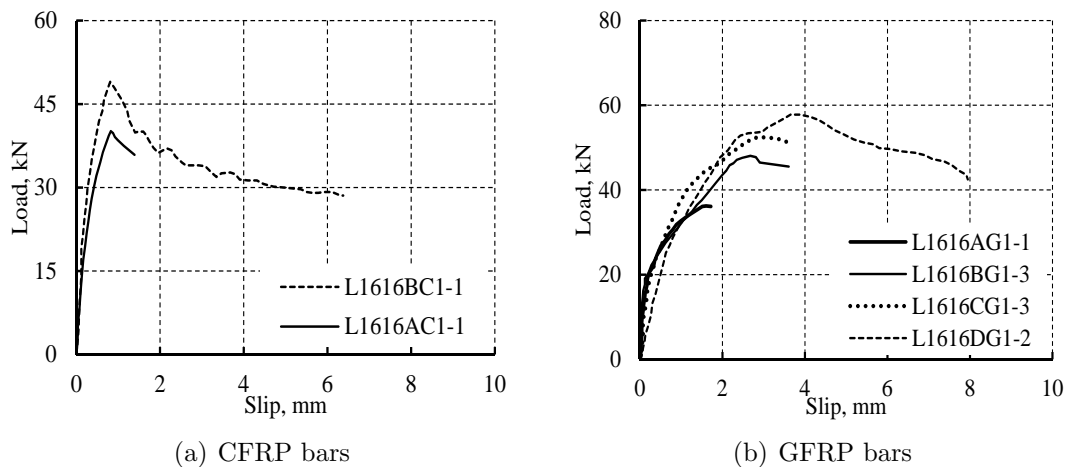


Figure 4.30: Effect of adhesive properties on the behaviour of tested specimens.

The effect of adhesive type (epoxy and cement) reported in [[68–70] is illustrated in Fig. 4.31. This shows the great extent of the effect of the adhesive type on the failure load of NSM FRP joints with different groove dimensions and bond lengths. The failure load increased with an increase in the groove size for specimens with epoxy paste, while it decreased with an increase in the groove size for specimens with cement mortar.

In this study (Figs. 4.32 and 4.33), using adhesive types B and C decreased the transverse strains in both the epoxy and the concrete and prevented epoxy splitting and/or concrete cracking until damaged of the grooved surface of the bar. Finally, the results of the tested specimens L1616AC1, L1515AC2 and L1818AG2 were compared with the results from the corresponding specimens (S1616LC1, S1515LC2 and S1818LG2 reported in section 4.2 to study the effect of concrete strength.

The first three specimens were cast with concrete with an average compressive strength ranging between 22 and 25 MPa, while the second three were cast with concrete with an average compressive strength ranging between 35.2 and 42.2 MPa. All the specimens were bonded using the same resin (epoxy A). The results indicate that concrete strength had no effect on the load capacity of the specimens tested in terms of epoxy splitting or bar-epoxy interface failure.

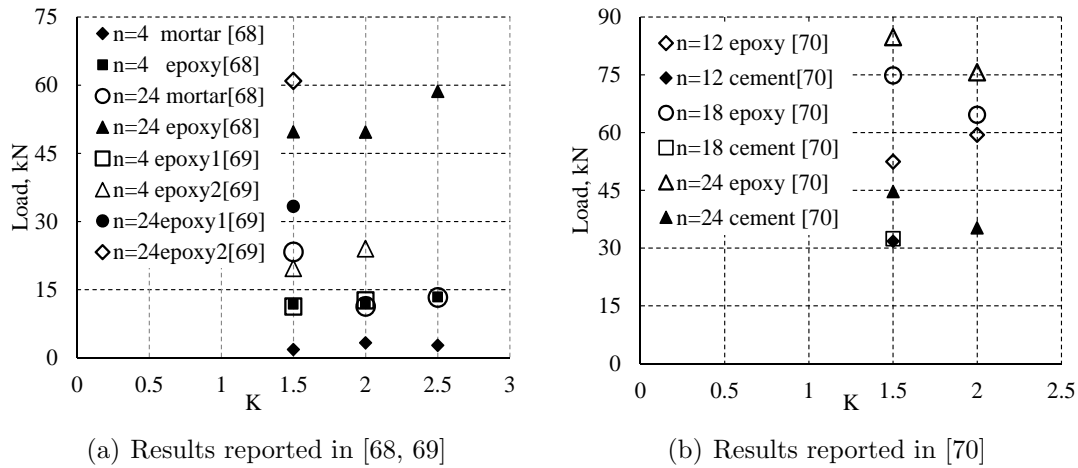


Figure 4.31: Effect of adhesive types on the failure load of tested specimens reported in [[68–70]], ($K = d/d_b$; $n = L_b/d_b$).

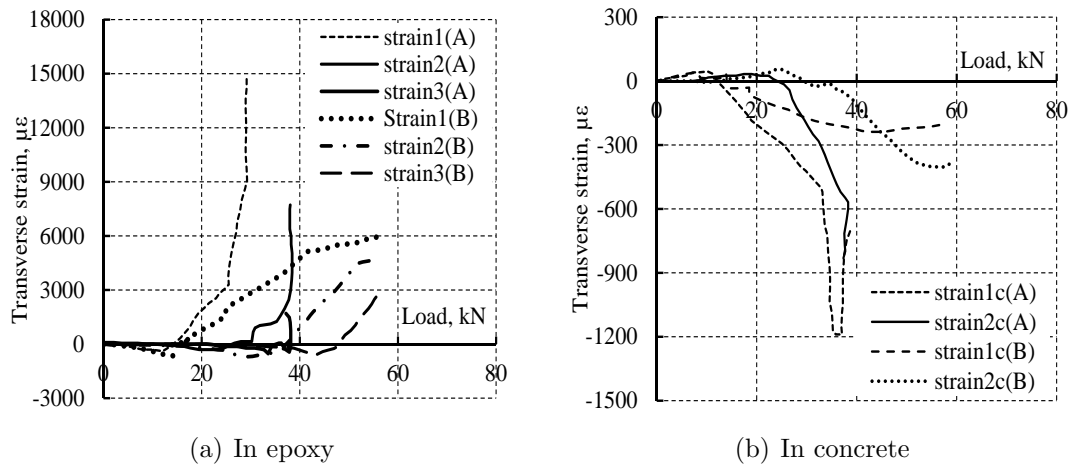


Figure 4.32: Transverse strain distribution for specimens L1616AG1 and L1616BG1.

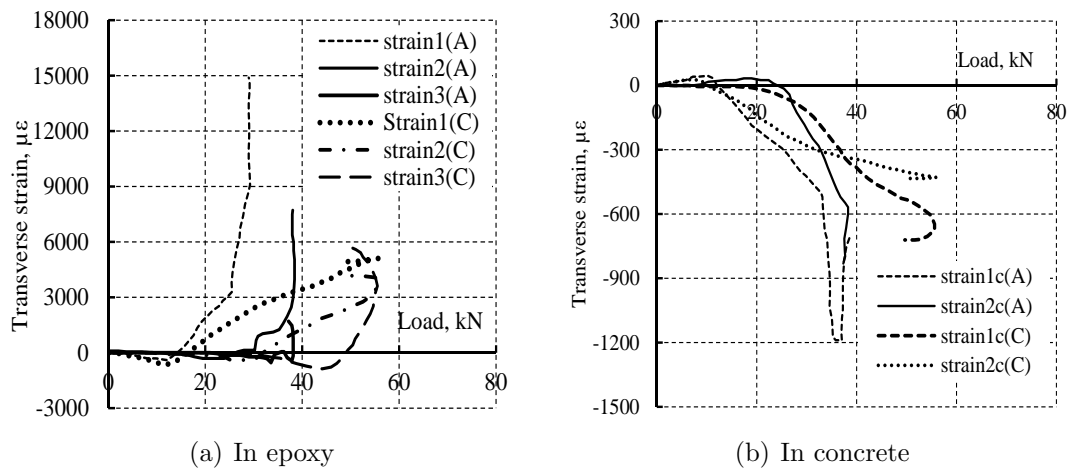


Figure 4.33: Transverse strain distribution for specimens L1616AG1 and L1616CG1.

4.3.4 Conclusions

In this series, the modified pullout test was used to perform a study of the effect of different factors on the bond behaviour of NSM FRP bars in concrete. A group of 32 specimens was tested and the effect of adhesive properties, bar type, bar size, FRP properties, groove geometry, bond length, and the use of mechanical interlocking, were examined. Two epoxy resins from different suppliers were used; the second was modified by adding two different percentages (1.88 %, 3.76 %) of a special additive in order to obtain resins with different properties, so that finally

four types of adhesive were used. The material properties of the FRP bars and the variables introduced had different effects on the bond behaviour of the specimens that were tested. Bar surface treatment, bar size and epoxy properties were the critical factors affecting the mode of failure for most of the specimens. From the test results, the following conclusions were obtained:

- The properties of the adhesive showed a high influence on the bond behaviour. The response of the joint was improved in terms of load capacity and ductility when a more ductile adhesive which allowed a better redistribution of stresses along the bond length was used. This was shown in the load slip responses, as well as in the analysis of the transverse strains.
- For specimens with NSM C1 bars (those with a smoother surface), bar-epoxy interface failure due to bar surface treatment was the critical failure mechanism. For both specimens (L1616BC1 and T1616BC1), increasing the bond length of the NSM CFRP bars by 25% increased the failure load by approximately 17.2%, with only a small difference in average bond stress. This means that the type B epoxy distributed the stresses along the bond length evenly, preventing sudden failures and allowing advantage to be taken of longer bond lengths.
- Increasing groove width increased the failure load of the NSM FRP bars regardless of FRP properties and the surface treatment. The percentage of increase was small (approximately 8.85 %) either due to bar-epoxy interface failure in the case of NSM CFRP bars or epoxy splitting in the case of NSM GFRP bars. For specimens with NSM G1 bars, increasing the epoxy cover from 3.5 mm to 4 mm (0.5 mm) increased the failure load of specimens with square grooves by approximately 10 %. Groove shape and transverse interlocking had no effect on the failure mode and load capacity, which were the result of epoxy splitting.
- Increasing the bar diameter from 8 mm to 9 mm for CFRP bars with nearly the same axial stiffness (C1 and C2) increased the failure load by approximately 21.95 %, while increasing the bar diameter from 8 mm to 12 mm increased the failure load of the NSM GFRP bars by approximately 72 % without changing the mode of failure.

- With the same bond length and groove dimensions, the failure load of specimens with NSM CFRP bars increased by approximately 20.4% when the epoxy type was changed from A to B (bar-epoxy interface failure). The failure load of specimens with NSM GFRP bars bonded with adhesive types B, C and D increased by approximately 32.4 %, 36.7 % and 46.3 % respectively over the specimen bonded with adhesive type A without changing the mode of failure.
- An analysis of these results taken jointly with those reported by other authors [68–70, 72] and in 4.2 indicates that the main factors affecting bond behaviour, failure load and the mode of failure of NSM FRP bars are bond length, bar size and adhesive properties. When epoxy resin is used, the failure load increases as the groove size increases otherwise the failure load decreases when the resin is cement mortar. For this reason the groove size seems to be a secondary factor affecting the failure load, which depends mainly on the adhesive properties.
- Comparing the result obtained from the specimens tested with the corresponding results reported in 4.2 indicates that concrete strength had no effect on the load capacity of the specimens tested, which was determined by epoxy splitting or bar-epoxy interface failure.

4.4 Results and discussion of the third series

Results of tested specimens in the third series are presented and discussed in this section. Table 2 shows the test results for specimens with CFRP bars while Table 3 shows the test results for specimens with GFRP bars. In these tables, the maximum load of the NSM joint (F_{max}), the average value of maximum load for analogous specimens ($F_{max,av}$), the maximum tensile stress in the FRP bar ($f_{f,max} = F_{max,av} / A_f$, A_f is the cross section area of the FRP bar), the efficiency factor ($\eta = f_{f,max} / f_{fu}$), the average value of the maximum bond stress at the bar-epoxy interface ($\tau_{max,av}$ at $F = F_{max}$) and free end slip (S_{fe}) are reported. The average bond stress slip curves for all the tested specimen are also reported and discussed. The average bond stress (τ_{av}) from equation 4.5 while the loaded end slip (S_{le}) is obtained from equations 3.1 and 3.2

$$\tau_{av} = \frac{F}{\pi d_b L_b} \quad (4.5)$$

where τ_{av} is the average bond stress at the bar-epoxy interface, F is the applied force, d_b is the bar diameter, L_b is the bond length. The test results are discussed in detail in the following.

4.4.1 NSM CFRP results

4.4.1.1 Bond behaviour in the longitudinal direction

In this section the load capacity, failure mode and average bond stress of the CFRP bars are discussed. As seen in Table 4.5, the load capacity of the NSM joint increased as the bond length increased whatever the epoxy type. But the load capacity also increased when the epoxy type changed from A to B or from A to D, although at a different percentage. The predominant failure mode of specimens with NSM CFRP bars was bar-epoxy interface failure (Fig. 4.34a), except for the two specimens T16DC-a and T16DC-b that failed due to concrete cracking (Fig. 4.34b). Longitudinal splitting cracks appeared in the epoxy paste in specimens bonded with epoxy A (Fig. 4.34a), while concrete tensile cracks appeared on the concrete's surface in specimens bonded with epoxy D (specimens T16DC-a and T16DC-b, Fig. 4.34b).

Table 4.5: Results of the tested CFRP NSM bars (third series).

Specimen ID	n (L_b/d_b)	F_{max} (kN)	$F_{max,av}$ (kN)	$f_{max,av}$ (MPa)	η (%)	$\tau_{max,av}$ (MPa)	S_{fe} (mm)	Failure mode
M16AC-a	12	26.89					0.097	B-E
M16AC-b	12	27.77	27.33	543.8	23.1	11.32	0.028	B-E
L16AC-a	24	40.12					-	LC,B-E
L16AC-b	24	39.97	40.00	795.9	33.9	8.28	0.076	LC,B-E
T16AC-a	30	48.0					0.044	LC,B-E
T16AC-b	30	48.70	48.35	962.0	41.0	6.41	0.003	LC,B-E
M16BC-a	12	39.32					0.127	B-E
M16BC-b	12	39.54	39.43	784.5	33.4	13.07	0.243	CC,B-E
L16BC-a	24	48.99					0.078	CC,B-E
L16BC-b	24	47.31	48.15	958.0	40.8	9.98	0.195	B-E
T16BC-a	30	54.79					0.088	B-E
T16BC-b	30	58.09	56.44	1123.0	47.8	9.36	0.075	B-E
M16DC-a	12	30.12					0.109	B-E
M16DC-b	12	27.92	29.52	587.4	25.0	12.23	0.035	B-E
L16DC-a	24	49.92					0.003	B-E
L16DC-b	24	44.43					0.118	B-E
L16DC-a	24	44.37	46.24	920.0	39.2	9.58	0.085	CC,B-E
T16DC-a	30	53.77					0.001	CC
T16DC-b	30	61.67	57.52	1144.0	48.7	9.53	0.231	CC

B-E = bar-epoxy interface failure; CC = concrete cracking and LC = epoxy longitudinal cracking.

In specimens with NSM bars bonded with epoxy A, increasing L_b from $12d_b$ to $24d_b$ (2 times) increased $F_{max,av}$ by 46.36%, while increasing L_b from $12d_b$ to $30d_b$ (2.5 times) increased $F_{max,av}$ by 76.91%. In other words, an increase in L_b of 25% (from $24d_b$ to $30d_b$) increased $F_{max,av}$ by 20.88%.

In specimens with NSM bars bonded with epoxy B, increasing L_b from $12d_b$ to $24d_b$ increased $F_{max,av}$ by 22.11%, while an increase from $12d_b$ to $30d_b$ increased $F_{max,av}$ by 43.14%. In other words, increasing L_b by 25% increased the load capacity by 21.03%. Changing the epoxy type from A to B increased $F_{max,av}$ by 43.98%, 20.38% and 16.73% for bond lengths $12d_b$, $24d_b$ and $30d_b$ respectively. To assess the effect of epoxy type on the load capacity, specimens bonded with epoxy D were also tested. Results for these specimens indicated that increasing L_b from $12d_b$ to $24d_b$

increased the $F_{max,av}$ by 56.64%, while increasing L_b from $12d_b$ to $30d_b$ increased $F_{max,av}$ by 94.85%. In contrast, changing the epoxy type from B to D decreased $F_{max,av}$ by 9.91% and 3.97% for the bond lengths $12d_b$ and $24d_b$, while it increased $F_{max,av}$ by 1.91% for specimens with bond length equal $30 d_b$.

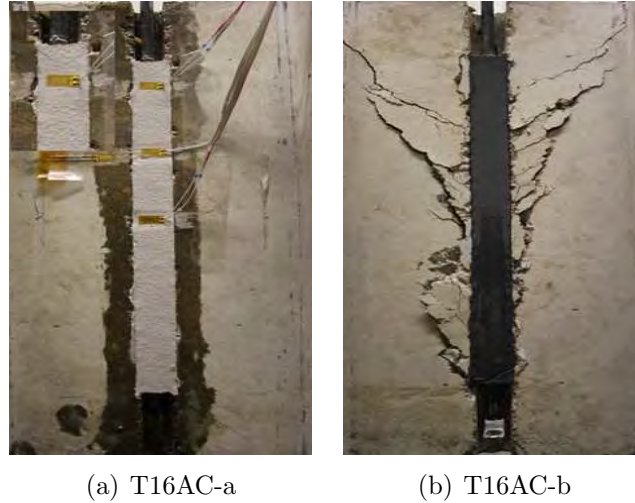


Figure 4.34: Failure mode of specimens with CFRP bars.

From these results it is clear that the effect of epoxy type on load capacity was influenced by the bond length (and vice versa). When the difference in mechanical properties between epoxy D and A was 1193 MPa (+19.8 %), 14.6 MPa (+20.8 %) and 2.1 MPa (+11.1 %) for the modulus of elasticity, compressive strength and tensile strength respectively, specimens bonded with epoxy D had higher load capacities, by approximately 8 %, 15.6 % and 19.97 % for bond lengths $12d_b$, $24d_b$ and $30d_b$ respectively, than those bonded with epoxy A (with the same failure mode). Although the difference in epoxy properties between types B and D was 1100 MPa (+13.8 %), 10.7 MPa (+10.7 %) and 2.0 MPa (+8.7 %) for modulus of elasticity, compressive strength and tensile strength respectively (similar absolute values to those between epoxy D and A), changing the epoxy from B to D caused a slight increase in the load capacities of the NSM bars at bond length ($30d_b$), while at other lengths ($12d_b$ and $24 d_b$) the load experienced a slight reduction. It would seem that the modification in the resin enhanced the bond behaviour with this kind of FRP bar by improving the cohesion and friction between the bar and the epoxy paste, and decreasing the slip for longer bond lengths.

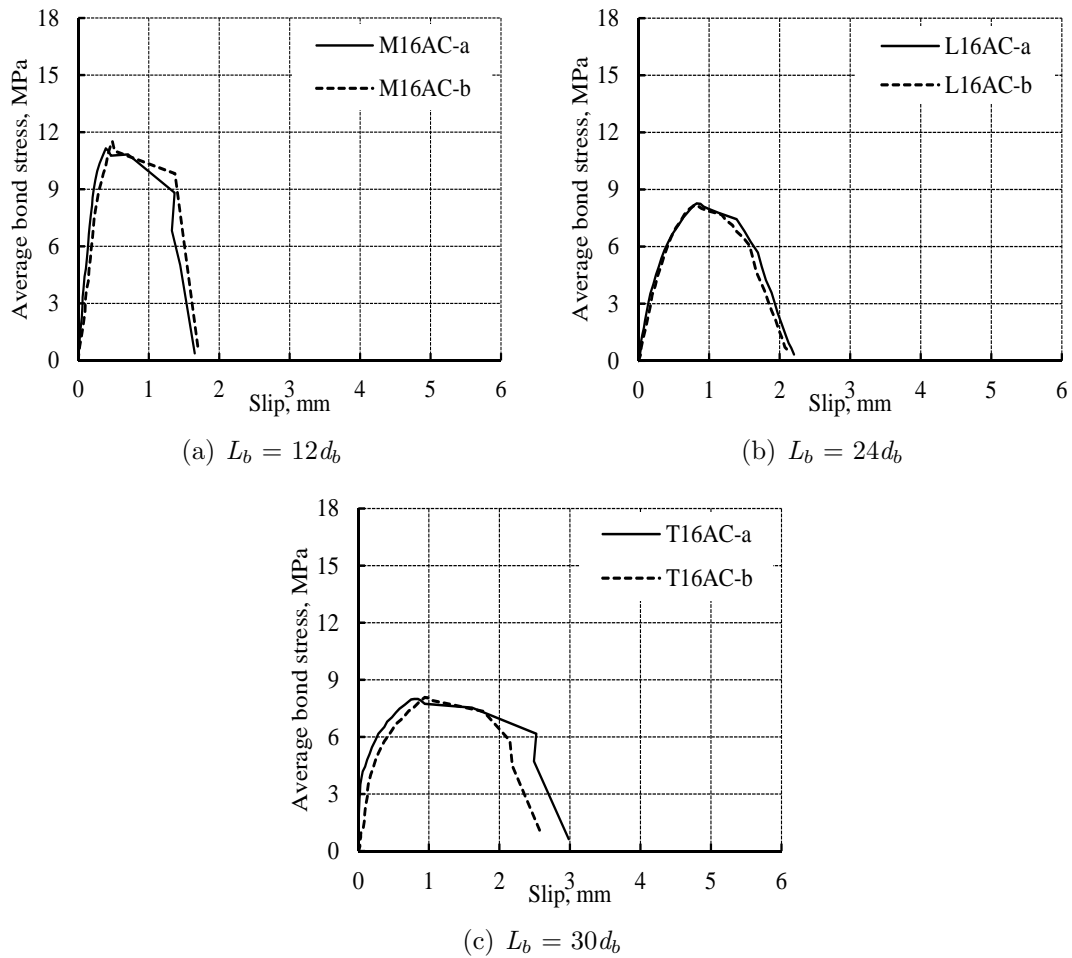


Figure 4.35: Average bond stress slip curves for specimens with CFRP bars bonded with epoxy A.

Figs. 4.35, 4.36 and 4.37 allow the effect of L_b and epoxy type on τ_{av} to be compared. In Fig. 4.35 the average bond stress slip curves for specimens bonded with epoxy A is shown. It can be seen that as L_b increases, the average bond stress decreases due to the non-uniform stress distribution along the bond lengths $12d_b$ and $24d_b$, while there is no effect on the average bond stress when the bond length changes from $24d_b$ to $30d_b$ as the failure converts from a bar-epoxy interface failure to concrete cracking. The same findings were also observed in the case of specimens bonded with epoxy B and D. On the other hand, these specimens experienced higher average bond stress than those bonded with epoxy A for all bond lengths (see Fig. 4.36 and 4.37).

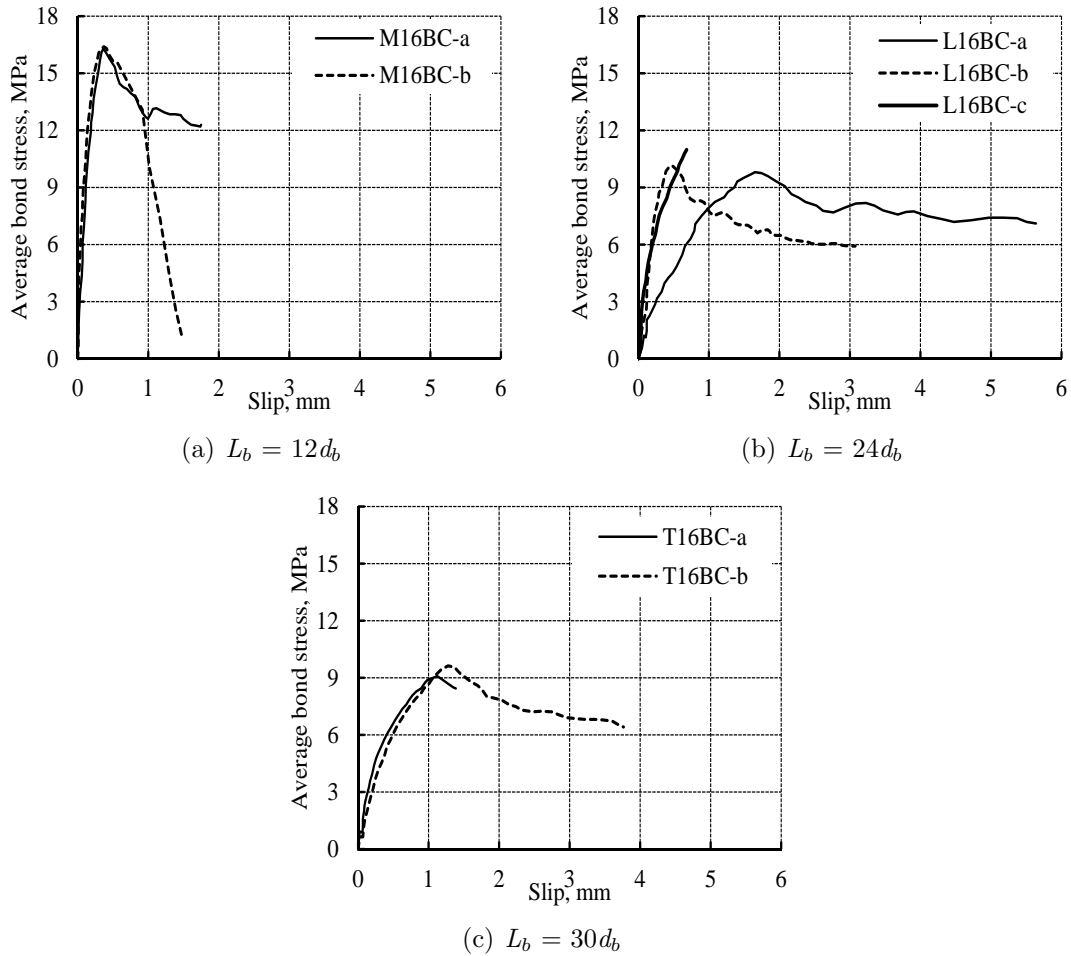


Figure 4.36: Average bond stress slip curves for specimens with CFRP bars bonded with epoxy B.

4.4.1.2 Transverse strain

In this section the effect of epoxy type and bond length on bond behaviour in the transverse direction of specimens with NSM CFRP bars is reported and discussed. As already shown in Fig. 3.6 strain gauges were glued the top surface of epoxy paste and concrete in order to measure the transverse strain. The number of strain gauges varied according to the bond length but the strain gauges were instrumented in the same positions in all specimens, i.e. Strain 1 was set at a distance of 24 mm from the loaded end for all bond lengths and so on. This is shown in Fig. 3.6.

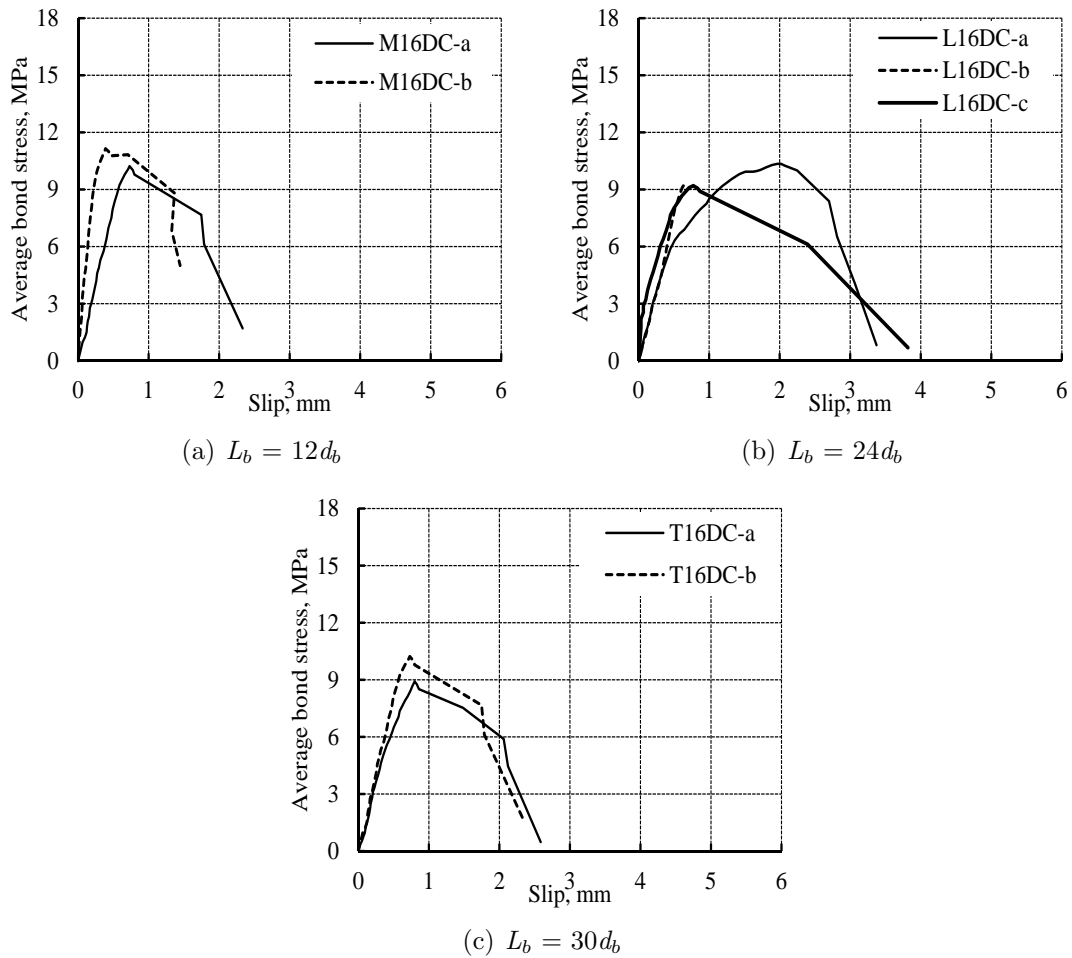


Figure 4.37: Average bond stress slip curves for specimens with CFRP bars bonded with epoxy D.

Figs. 4.38, 4.39, 4.40, 4.41 and 4.42 show the transverse strain distributions in epoxy and concrete for specimens with NSM CFRP bars. At the beginning of loading, the strain gauges recorded negative (compressive) strain in the epoxy paste. With an increase in the load, the strain gauges recorded positive (tensile) strain until failure, as shown in Figs. 4.38, 4.40a and 4.41. By contrast, the recorded strain in concrete was positive at the beginning of loading and became negative as the load increased (Fig. 4.39, 4.40b and 4.42).

For low load values, Poisson's side contraction of the glued bar caused tensile stresses at its interface with the epoxy paste that transformed to compressive stresses on the unrestricted surface of the adhesive. With increasing the load, the friction

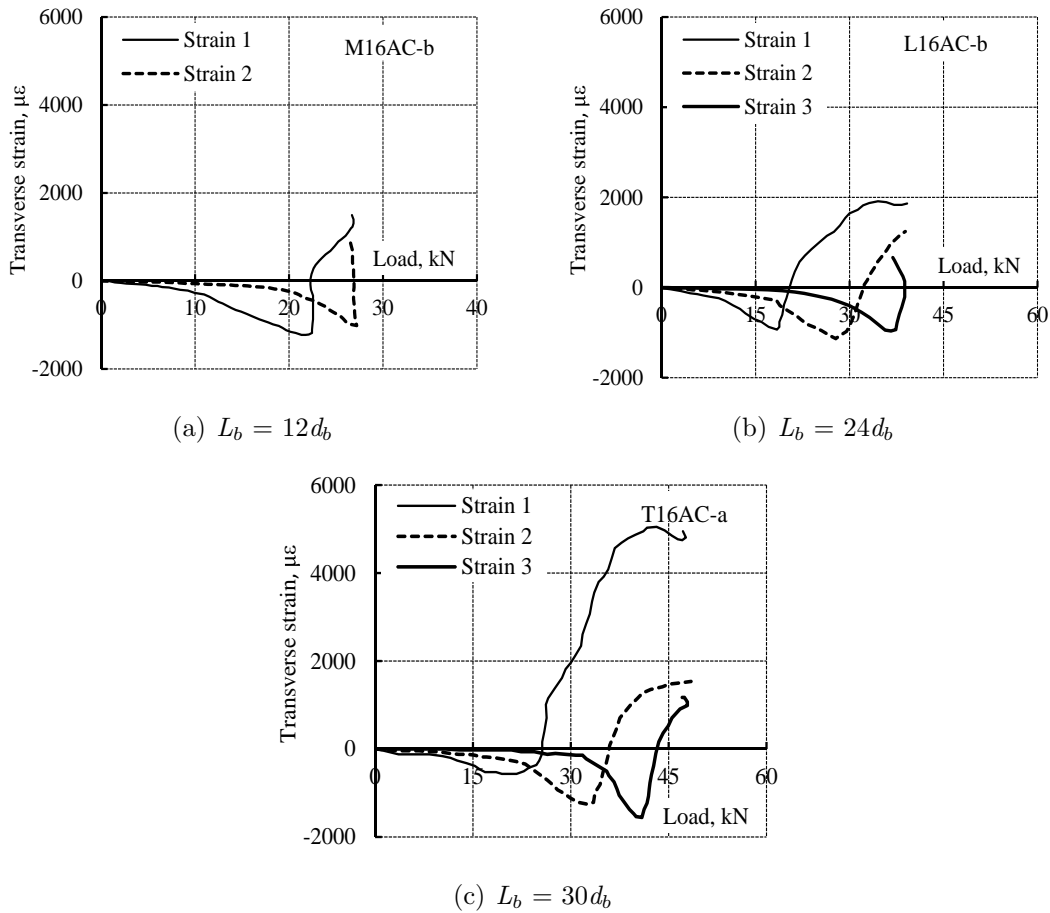


Figure 4.38: Transverse strain distribution on epoxy paste for specimens with CFRP bars bonded with epoxy A.

governed the bond at the interface between the bar and the adjacent epoxy. This friction made the bar to create compressive stresses at its interface with the epoxy paste, and this compression generated tensile stresses at the free surface of this paste as stated before in [69].

The previous stresses exerted by the bar at its interface with the epoxy were transmitted through this paste to the surrounding concrete. The previous stresses utilized by the bar at its interface with the epoxy paste were diffused through this paste to the surrounding concrete see more in [97, 98], where specimens with NSM FRP bars with a bond length of 192 mm were tested. The effect of the strain gauge position, L_b and adhesive type on the recorded values of transverse strains is explained below.

For specimens with epoxy A, the tensile transverse strains at failure recorded by Strain 1, Strain 2 and Strain 3 in specimens with bond lengths $12d_b$, $24d_b$ and $30d_b$ increased as L_b increased, with increasing failure loads and tensile transverse strains in epoxy (Fig. 4.38). This caused, in turn, a general increase in concrete transverse compressive strains (see Fig. 4.39).

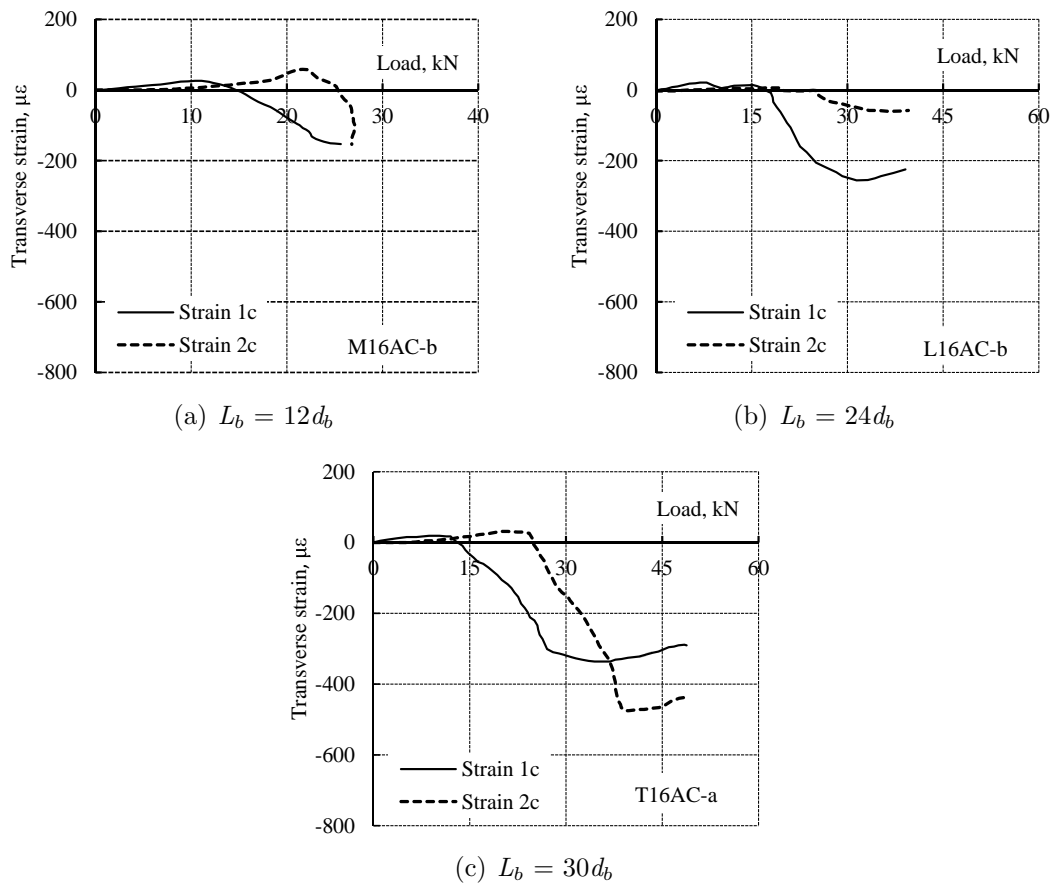


Figure 4.39: Transverse strain distribution on concrete for specimens with CFRP bars bonded with epoxy A.

In specimens with CFRP bars bonded with epoxy B, the strains measured in the epoxy were lower than those recorded for similar specimens bonded with epoxy A (see Fig. 4.39), probably due to the higher strength and modulus of epoxy B.

In specimens with CFRP bars bonded with epoxy D, the compressive transverse strain measured in the epoxy was higher than that recorded for the similar specimens with epoxy B, but the tensile transverse strain was lower, as shown in Fig. 4.39b

and 4.40b. The change from B to D may have enhanced the cohesion at the bar-epoxy interface and increased the compressive strains recorded on the epoxy surface. As the load progressed, the lower modulus of epoxy D allowed a redistribution of the stresses along the bonded length, which reduced the tensile strains recorded in epoxy.

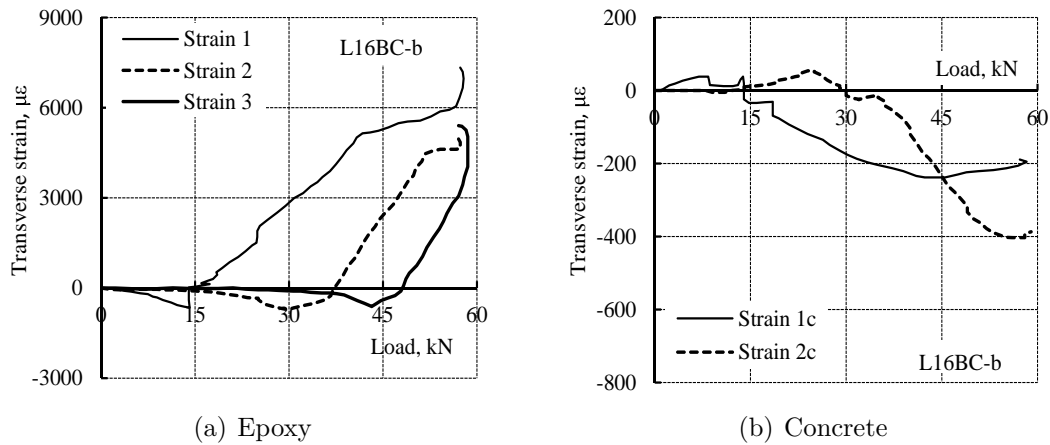


Figure 4.40: Transverse strain distribution for specimens with CFRP bars bonded with epoxy B (L16BC-b).

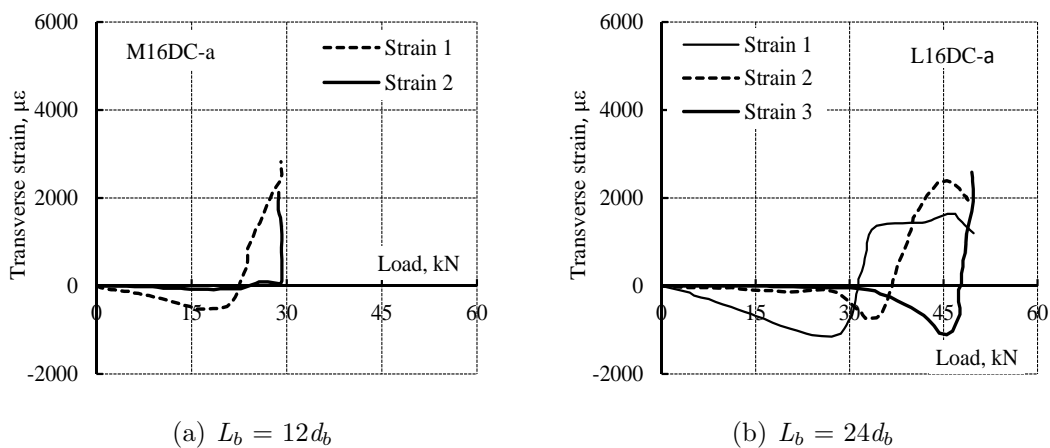


Figure 4.41: Transverse strain distribution on epoxy for specimens with CFRP bars bonded with epoxy D.

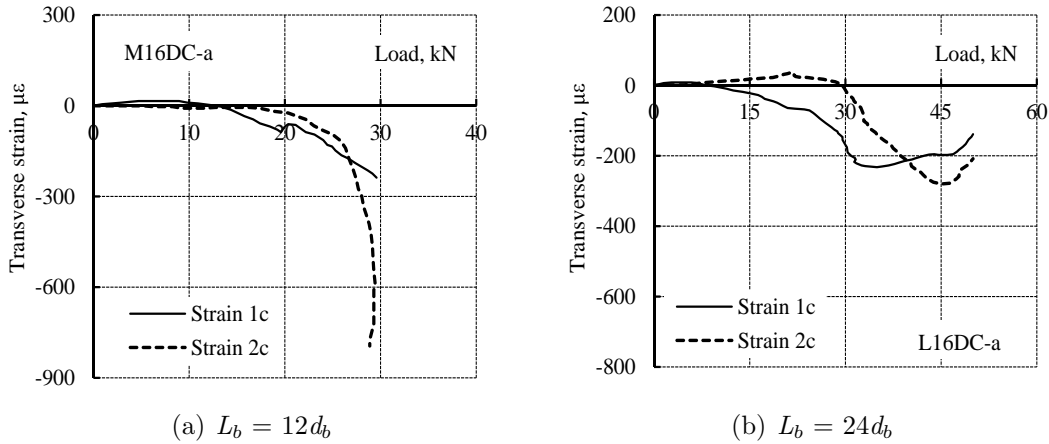


Figure 4.42: Transverse strain distribution on concrete for specimens with CFRP bars bonded with epoxy D.

4.4.2 NSM GFRP results

4.4.2.1 Bond behaviour in the longitudinal direction

The effect of load capacity, failure modes and the average bond stress of specimens with GFRP bars are herein discussed. As seen in Table 4.6, the load capacity of the NSM joint increased as the L_b increased whatever the epoxy type. Moreover, the load also increased as the epoxy type changed from A to B or from A to D. The failure mode of specimens with GFRP bars depended on the epoxy type. In specimens with GFRP bars bonded with epoxy A, at the beginning of loading, longitudinal splitting cracks appeared on the epoxy surface. As the load increased, the longitudinal crack propagated until failure. At failure, epoxy splitting caused either the detachment of the surrounding concrete or concrete cracking depended on the bond length (see Fig.4.43a). For specimens with NSM GFRP bars bonded with epoxy B and D, failures took place with concrete cracking and bar-epoxy interface failure, or bar damage depending mainly on bond length (see Figs. 4.43b and c).

In specimens with GFRP bars bonded using epoxy A, increasing L_b from $12d_b$ to $24d_b$ increased $F_{max,av}$ by 33.75%. Increasing L_b from $6d_b$ to $12d_b$ and from $6d_b$ to $24d_b$ increased $F_{max,av}$ by 77.25% and 158.49% respectively, while increasing it from $12d_b$ to $24d_b$ and from $12d_b$ to $30d_b$ increased the average load by 45.6% and 77.34% respectively. For specimens with NSM bars bonded with epoxy D, increasing

Table 4.6: Results of the tested GFRP NSM bars (third series).

Specimen ID	n (L_b/d_b)	F_{max} (kN)	$F_{max,av}$ (kN)	$f_{max,av}$ (MPa)	η (%)	$\tau_{max,av}$ (MPa)	S_{fe} (mm)	Failure mode
M16AG-a	12	28.32					0.002	LC,CC
M16AG-b	12	27.86	28.09	558.9	41.4	11.64	0.685	LC,CC
L16AG-a	24	36.23					0.0945	LC,CC
L16AG-b	24	38.92	37.57	747.5	55.5	7.78	-	,ES
S16BG-a	6	18.99					0.265	CC,B-E
S16BG-b	6	19.51	19.25	383.0	28.3	15.95	0.751	CC,B-E
M16BG-a	12	35.31					0.327	CC,B-E
M16BG-b	12	32.93	34.12	678.9	50.3	14.14	0.125	CC,CS
L16BG-a	24	56.67					0.258	CC,BD
L16BG-a	24	44.57					0.233	CC,BD
L16BG-b	24	48.06	49.76	990.1	73.3	10.31	0.371	CC,BD
T16BG-a	30	60.87					0.073	CC,CS
T16BG-b	30	60.15	60.51	1203.9		10.03	0.019	CC,CS
S16DG-a	6	19.83					0.815	CC,B-E
S16DG-b	6	22.39	21.11	420.0	31.1	17.50	0.246	CC,B-E
M16DG-a	12	33.60					0.665	CC,CS
M16DG-b	12	33.14	33.37	663.9	49.2	13.83	0.664	CC,B-E
L16BG-a	24	52.10					0.298	CC,BD
L16BG-b	24	57.79	54.95	1093.3	81.0	11.38	0.290	BD

BD= bar surface damage; B-E= bar-epoxy interface failure; CC= concrete tension failure; CS= concrete splitting; ES= epoxy splitting; and LC= longitudinal cracking of the epoxy.

L_b from $6d_b$ to $12d_b$ and from $6d_b$ to $24d_b$ increased $F_{max,av}$ by 58.08% and 160.3% respectively, while increasing it from $12d_b$ to $24d_b$ increased $F_{max,av}$ by 64.67%.

From these results it is clear that as L_b increased the percentage of increase in the load capacity was higher in the case of epoxy B and D than that of epoxy A, and also that the load increased as the bond length increased whatever the epoxy type. Changing the adhesive type from A to B enhanced $F_{max,av}$ of the joint by approximately 21.47% and 32.45% for bond lengths $12d_b$ and $24d_b$ respectively. Likewise, changing the adhesive type from A to D enhanced $F_{max,av}$ of the joint by approximately 18.8% and 46.26% for bond lengths $12d_b$ and $24d_b$ respectively. Using epoxy D enhanced $F_{max,av}$ of the joint by smaller percentages than when epoxy B was used.

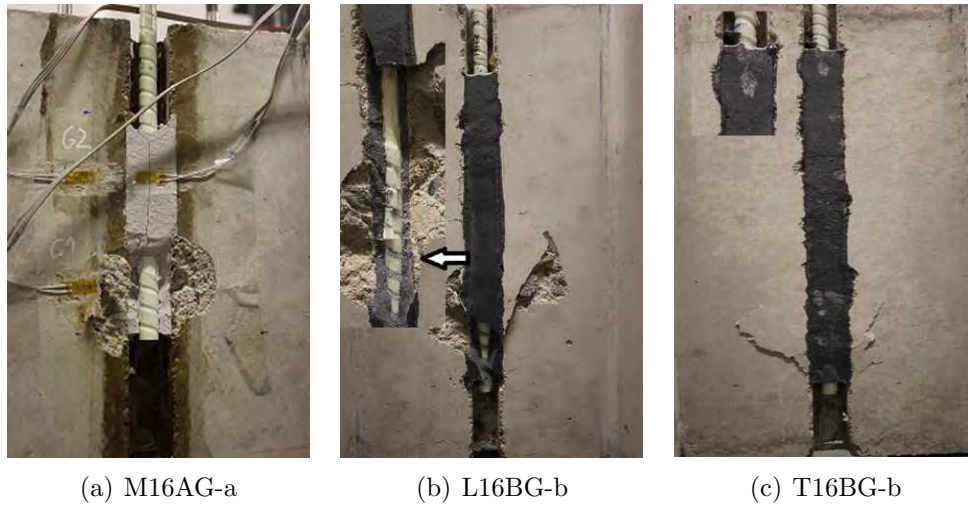


Figure 4.43: Failure mode of specimens with GFRP bars.

Although, as mentioned previously, the difference in epoxy properties between epoxy D and A was nearly equal to that between epoxy B and D, specimens bonded with epoxy D had higher load capacities than those bonded with epoxy A with the dissimilar failure mode. This may have been due to their respective chemical and physical properties, which may have enhanced the cohesion and friction between the bar and the epoxy paste. It seems that in the cases of epoxy B and epoxy D, as the grooved surface of the GFRP bars permitted slips at the bar-epoxy interface, decreasing modules of elasticity of the epoxy paste allowed the bar to deform and then distribute the bond stress evenly along the bonded length of the bar, without any bar damage in the case of epoxy D.

In this section the effect of L_b and epoxy type on τ_{av} is explained. Fig. 4.44 shows the average bond stress slip curves for specimens bonded with epoxy A. It can be seen that increases τ_{av} decreases as a result of the non-uniform stress distribution lengthwise L_b . These results assured those reported in [68, 70, 97, 98]. The specimens with GFRP bars bonded with epoxy B and D experienced higher τ_{av} and higher slip than the corresponding specimens bonded with epoxy A (see Figs. ?? and 4.46). This may have been due to damage to the grooved surface of the bar, which increased bar slip. Specimens with NSM GFRP bars, and lower E_f , experienced higher slips than those with NSM CFRP bars bonded with the same epoxy type.

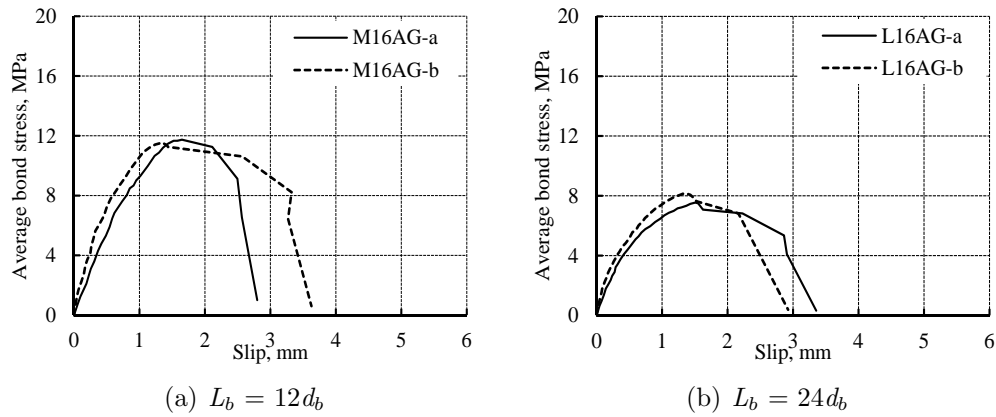


Figure 4.44: Average bond stress slip curves for specimens with GFRP bars bonded with epoxy A.

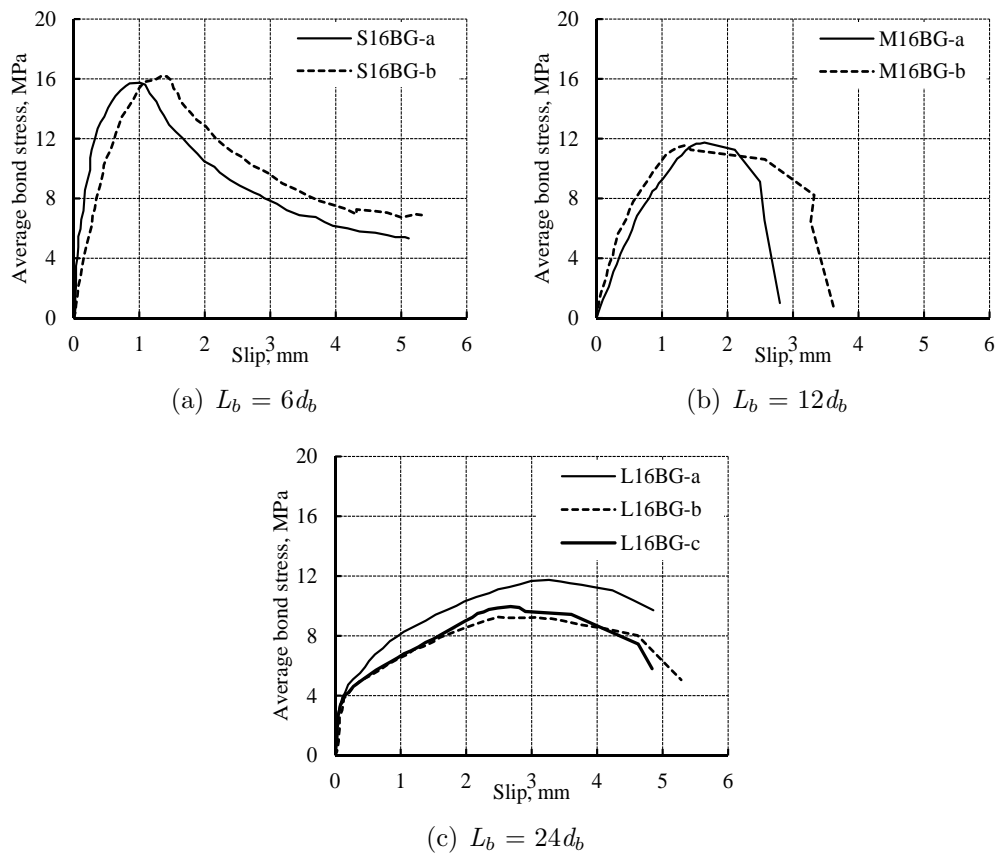


Figure 4.45: Average bond stress slip curves for specimens with GFRP bars bonded with epoxy B.

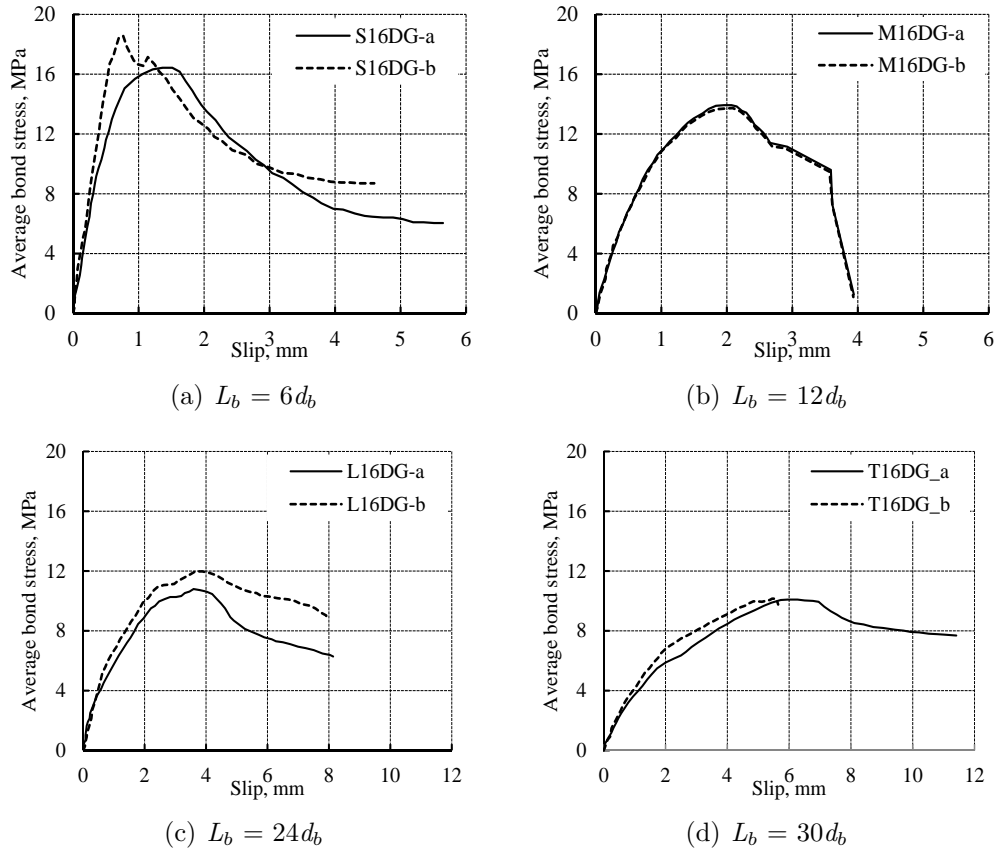


Figure 4.46: Average bond stress slip curves for specimens with GFRP bars bonded with epoxy D.

4.4.2.2 Transverse strain

This section illustrates the effect of epoxy type and L_b on bond behaviour in the transverse direction of specimens with GFRP bars. Fig. 3.6 shows strain gauges, while Figs. 4.47 - 4.51 show the transverse strain distributions in epoxy and concrete. At the loading started, the strain gauges recorded negative (compressive) strain in the epoxy paste. As the load increased, the strain gauges recorded positive (tensile) strain until failure, as shown in Figs. 4.47, 4.49 and 4.51a. By contrast, the recorded strain in concrete was positive at the beginning of loading and became negative as the load increased, as shown in Figs. 4.48 - 4.51b. The decrease in strain values for specimens S16BG-a and S16DG-a in epoxy and concrete as the load decreased, during the descending branch of the bond slip diagram, may have been due slips at the bar-epoxy interface.

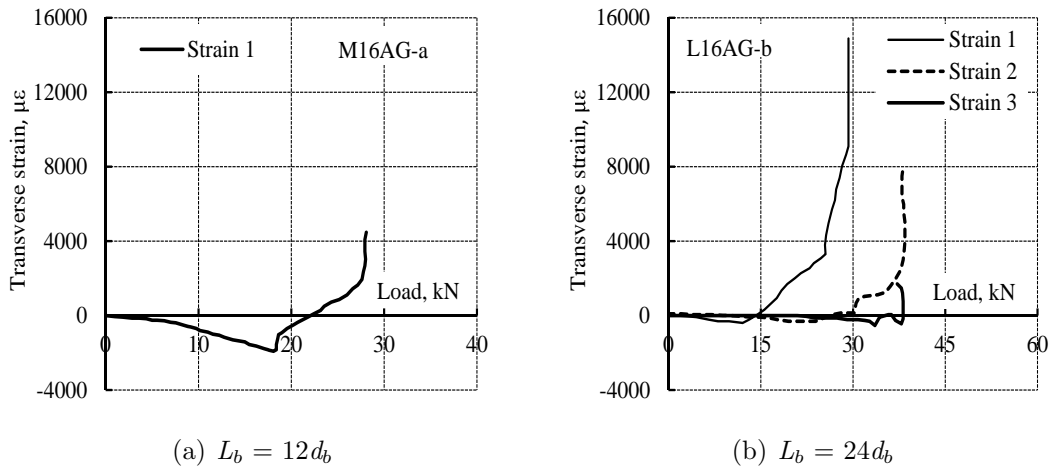


Figure 4.47: Transverse strain distribution on epoxy for specimens with GFRP bars bonded with epoxy A.

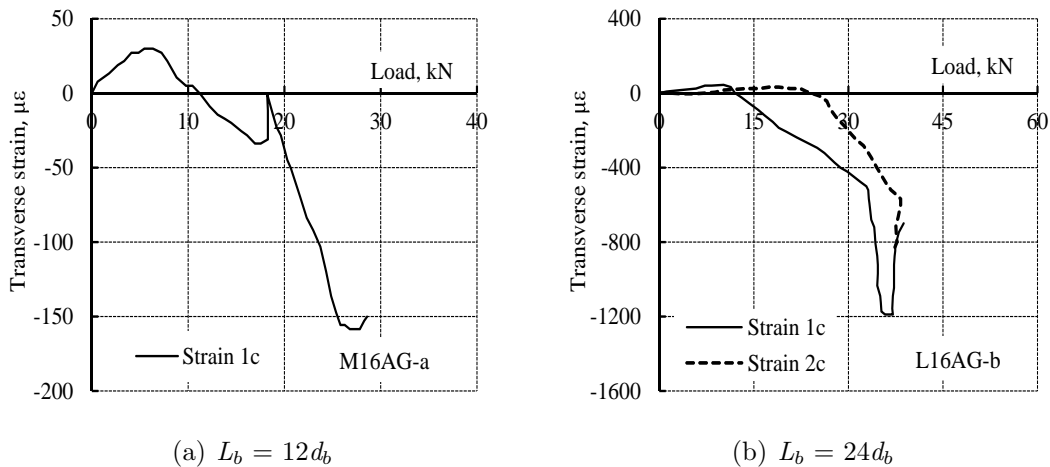


Figure 4.48: Transverse strain distribution on concrete for specimens with GFRP bars bonded with epoxy A.

Initially, for low loads, Poisson's lateral contraction of the bonded bar caused tensile stresses at its interface with the epoxy paste that converted to compressive stresses on the free surface of the adhesive. As the load progressed, the friction governed the bond at the interface between the bar and the surrounding epoxy, which increased as a result of the grooved surface of GFRP bars. This friction made the bar to create compressive stresses at its interface with the epoxy paste, and this compression generated tensile stresses at the free surface of this paste.

The previous stresses exerted by the bar at its interface with the epoxy were transmitted through this paste to the surrounding concrete. Similar observations were stated in [69] for epoxy and in [97, 98] for concrete and epoxy. The values of transverse strain recorded by the strain gauges were dependent on their positions from the loaded end, bond length and adhesive properties as explained in the following section.

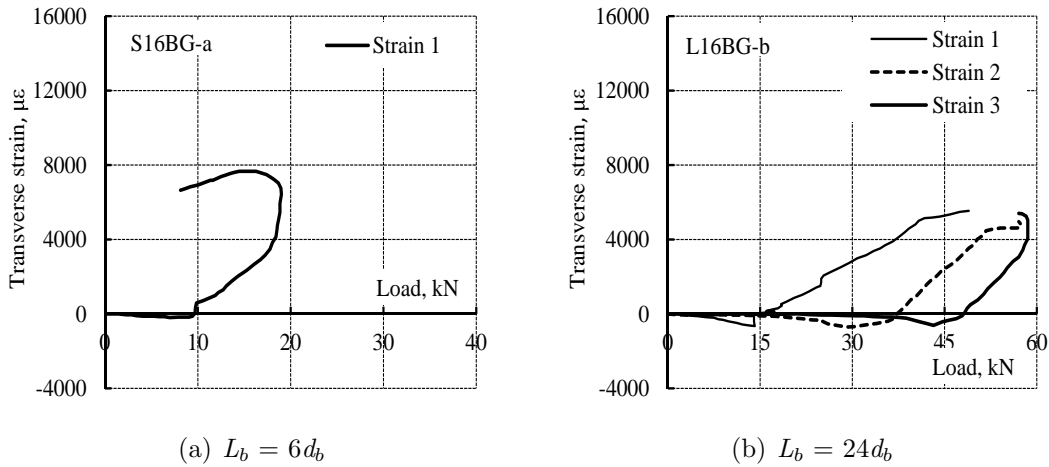


Figure 4.49: Transverse strain distribution on epoxy for specimens with GFRP bars bonded with epoxy B.

For specimens with epoxy A at the same loads, the tensile transverse strains recorded by the strain gauges (Strain 1 and Strain 2) for specimens with bond length $24d_b$ were the highest among all the specimens with GFRP bars (see Figs. 4.47, 4.49 and 4.51a). As the bond length increased, the deformation of the bar near the loaded end increased and, due to bar-epoxy interlocking, the bar generated higher compressive stresses at its interface with the surrounding epoxy, which converted to tensile stresses on the epoxy free surface. The same was noted for compressive strains recorded by Strain 1c and Strain 2c in concrete (see Fig. 4.48, 4.50 and 4.51b).

In specimens with NSM GFRP bars bonded with epoxy B, the shorter the bond length the higher the tensile transverse strain in the epoxy, as shown in Fig. 4.49. After S16BG1 and S16DG1 (specimens with a short bond length bonded with epoxy B and D) reached their maximum load capacity, the transverse strain decreased during the descending stage (Fig. 4.49a and 4.51a).

The load decreased slowly with large bar-epoxy slip values that reduced the friction at the bar-epoxy interface. This was also noted for the transverse compressive strain in concrete (Figs. 4.50a and 4.51b). On the other hand, specimens with bond length $6d_b$ bonded with epoxy D recorded tensile strain lower than that of corresponding specimens bonded with epoxy B. The recorded strain in concrete for specimens with epoxy D was tensile, with the highest values of all the tested specimens (see Fig. 4.51).

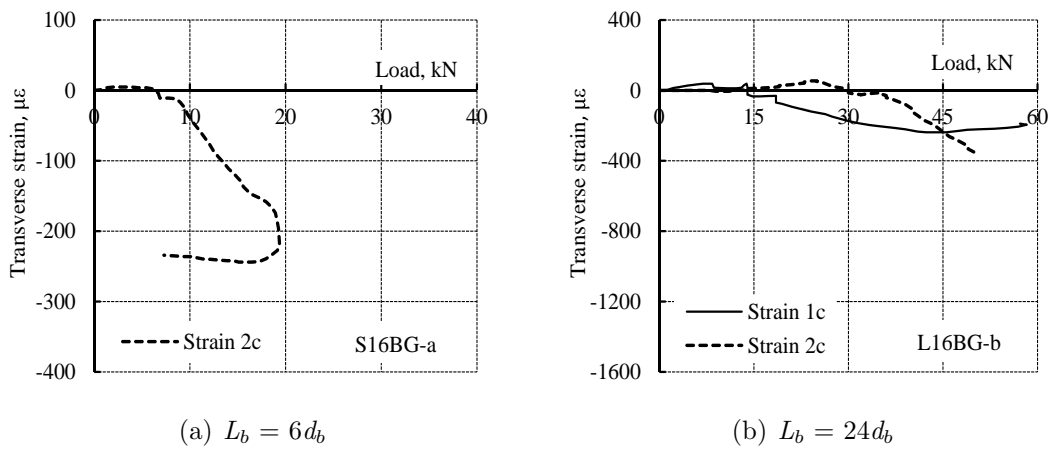


Figure 4.50: Transverse strain distribution on concrete for specimens with GFRP bars bonded with epoxy B.

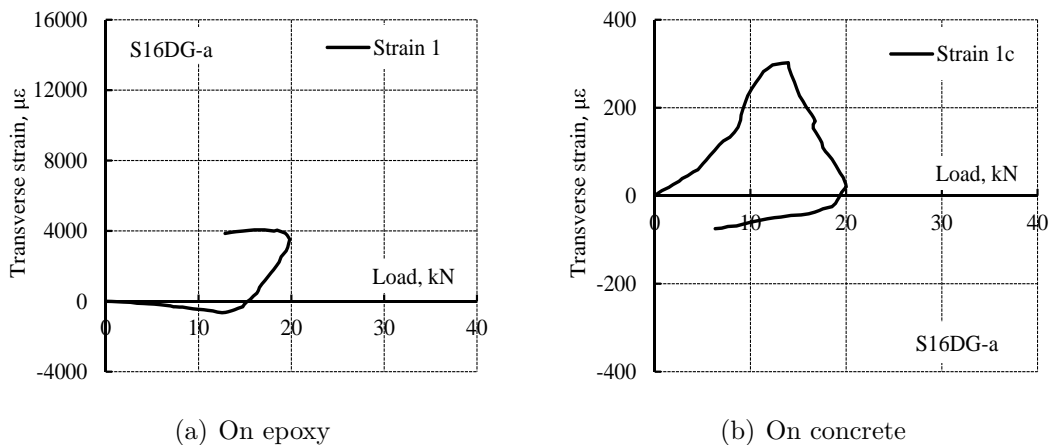


Figure 4.51: Transverse strain distribution for specimens with GFRP bars bonded with epoxy D (S16DG-a).

4.5 Comparison and discussion of results

The results of this study show the influence of adhesive type on the bond behaviour of NSM FRP reinforcement, something that has also been reported in previous studies [14, 19, 71]. The results indicate that with the same axial stiffness, changing the epoxy type increases the failure load of NSM FRP bars. Fig. 4.52 shows the effect of epoxy type on $\tau_{max,av}$ and the load efficiency ($F_{max,av} / F_u$, where F_u is the maximum load for FRP bars) of specimens with CFRP bars for three bond lengths: $12d_b$, $24d_b$ and $30d_b$. Fig. 4.52a shows how $\tau_{max,av}$ increased in line with increases in tensile strength and the modulus of elasticity of the epoxy. By contrast, $\tau_{max,av}$ decreased as the bond length increased, whatever the epoxy type. The percentage decrease in $\tau_{max,av}$ was insignificant as L_b increased from $24d_b$ to $30d_b$.

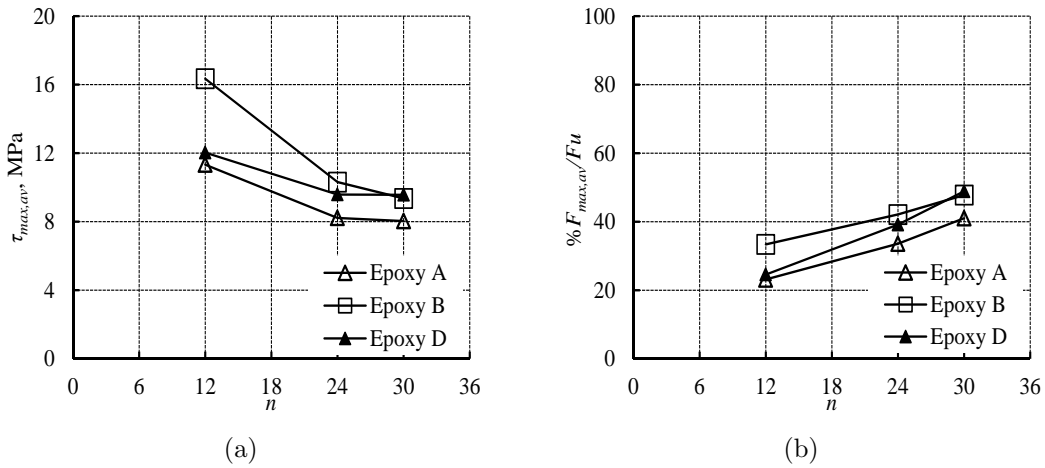


Figure 4.52: Effect of epoxy type and bond length for specimens with CFRP bars on: (a) $\tau_{max,av}$ and (b) $\%F_{max,av} / F_u$; ($n = L_b / d_b$).

On the other hand, the load efficiency of the joint increased as the epoxy properties increased (see Fig. 4.52b). The load efficiency also increased as L_b increased, whatever the type of epoxy. Specimens with GFRP bars bonded with epoxy D (Fig. 4.53) experienced higher bond stress and load efficiency than the corresponding specimens bonded with epoxy A and B. Moreover, the load efficiencies were higher than in the corresponding specimens with CFRP bars, as can be seen by comparing Figs. 4.52b and 4.53b.

The global effect of the adhesive type and bond length at several load capacities are reported to illustrate their effects in the transverse direction. Figs. 4.54a and 4.55a show how the effect of adhesive type on transverse strain changed according to the epoxy type as the load increased for the two FRP materials, carbon and glass. It can also be seen that the tensile strain in epoxy for specimens with GFRP bars was higher than that of specimens with CFRP bars. This may be due to the surface treatment of the GFRP bars increasing the friction at the bar-epoxy interface. On the other hand, the effect on the transverse strain changed in line with the bond length at high loads.

The transverse strain clearly illustrates the effect of bar type and bar surface treatment on the surrounding epoxy and concrete. Moreover, during the test the transverse strain was able to predict crack propagation in the longitudinal direction in the epoxy paste. More experimental and numerical studies are needed to better understand bond behaviour in transverse direction, which may in turn contribute to a better overall understanding of the effect of variables on bond behaviour in NSM systems

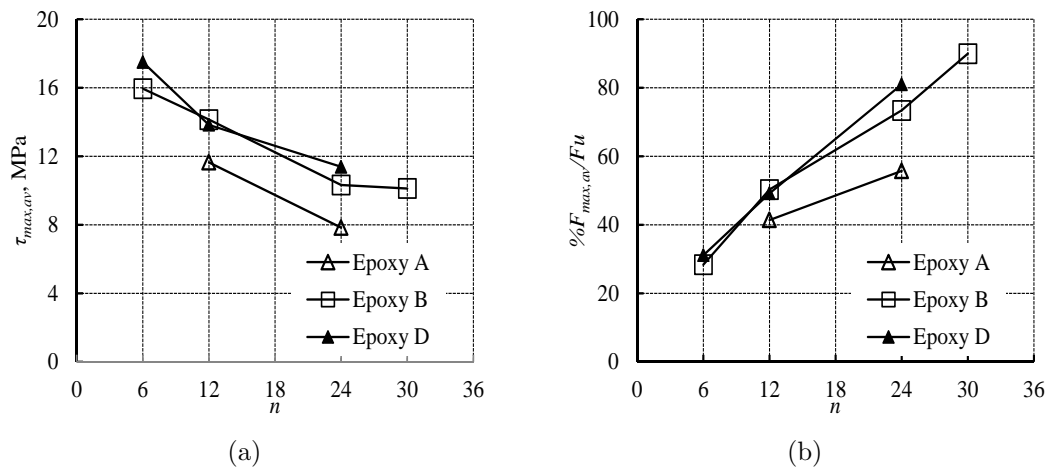


Figure 4.53: Effect of epoxy type and bond length for specimens with GFRP bars on: (a) $\tau_{max,av}$ and (b) $\%F_{max,av}/F_u$; ($n = L_b/d_b$).

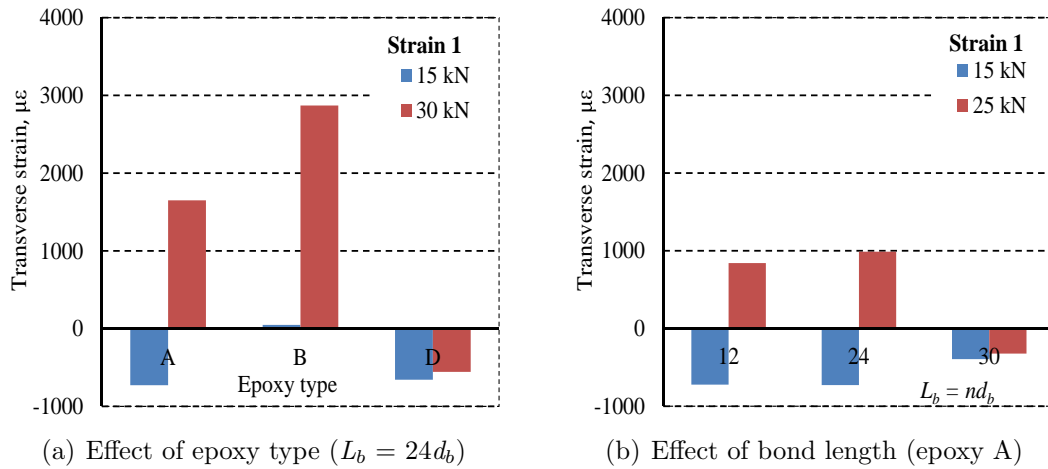


Figure 4.54: Effect of epoxy type and bond length on the transverse strain of NSM CFRP bars.

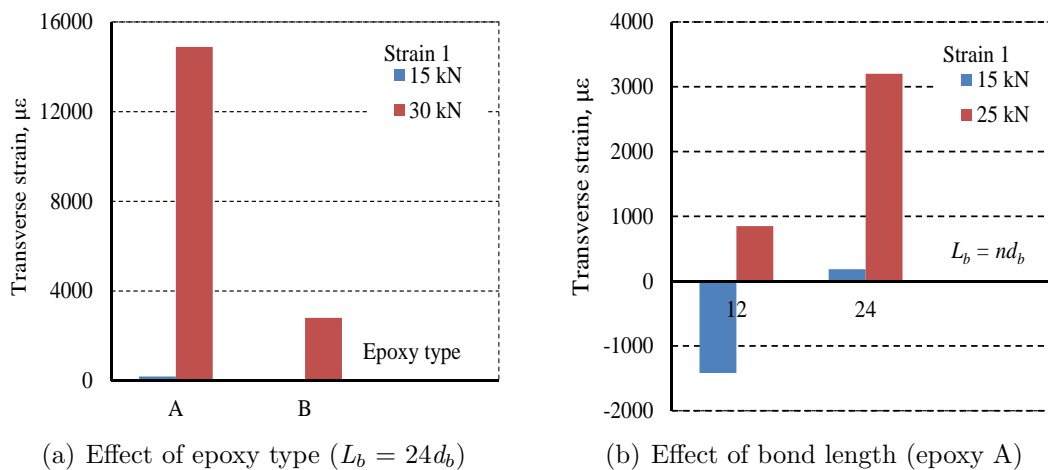


Figure 4.55: Effect of epoxy type and bond length on the transverse strain of NSM GFRP bars.

4.5.1 Conclusions

A modified pullout test was used to investigate the effect of the adhesive properties on the bond performance of NSM FRP bars in concrete. Three types of epoxy adhesive (A, B and D) were used to bond the FRP bars to concrete: type A (MBRACE ADHESIVE HT); type B (POLYFIXER EP); and type D, obtained by modifying type B. Two types of FRP bars, carbon (C) and glass (G), 8 mm in diameter, were used. Three bond lengths ($12d_b$, $24d_b$, $30d_b$) were used

for specimens with CFRP bars while four bond lengths ($6d_b$, $12d_b$, $24d_b$, $30d_b$) were used for specimens with GFRP bars. The load capacity, mode of failure, loaded end slip, and transverse strain in epoxy and concrete were recorded. From the results it was concluded that:

- The adhesive type had a great effect on the bond behaviour of NSM bars in longitudinal and transverse directions. This effect varied according to the bond length and FRP properties.
- The predominant failure mode of specimens with CFRP bars was bar-epoxy interface failure, except in the cases of the two specimens T16DC-a and T16DC-b, which failed by concrete cracking. On the other hand, the predominant failure mode of specimens with GFRP bars depended on the epoxy type. For specimens with GFRP bars bonded with epoxy A, longitudinal splitting cracks looked on the epoxy surface for relatively low loads; these progressed until failure, producing detachment of the surrounding concrete or concrete cracking, depending on the bond length. For specimens with GFRP bars bonded with epoxy B and D, failures took place with concrete cracking, bar-epoxy interface failure, or bar damage, depending mainly on bond length and epoxy type.
- In specimens with CFRP bars, changing the adhesive type from A to B enhanced $F_{max,av}$ of the joint by approximately 44.27 %, 20.38 % and 16.73 % for bond lengths $12d_b$, $24d_b$ and $30d_b$ respectively. Furthermore, changing the adhesive type from A to D enhanced $F_{max,av}$ of the joint by approximately 8 %, 15.6 % and 19.97 % for bond lengths $12d_b$, $24d_b$ and $30d_b$ respectively. Although the differences in properties between epoxy B and D were nearly the same as between epoxy A and D, changing the epoxy from B to D resulted in a slight increase in the load capacities of the NSM bars at bond length $30d_b$, and a decrease at other lengths ($12d_b$ and $24d_b$). It seems that this change in epoxy type alters the bond behaviour with this kind of FRP bar by enhancing the cohesion and friction between the bar and epoxy paste and decreasing the slip at greater bond lengths.
- For specimens with GFRP bars, changing the adhesive type from A to B enhanced $F_{max,av}$ of the joint by approximately 21.47 % and 32.45 % for bond

lengths $12d_b$ and $24d_b$ respectively; changing the adhesive type from A to D enhanced $F_{max,av}$ of the joint by approximately 18.8 % and 46.26 % for bond length $12d_b$ and $24d_b$ respectively. Although the difference in properties between epoxy D and A was nearly the same as between epoxy B and D, specimens bonded with epoxy D had a higher load capacity than those bonded with epoxy A, although with a dissimilar failure mode epoxy D slightly enhanced the load capacity of the joint with respect to specimens bonded with epoxy B. It seems that with this latter kind of epoxy, as the grooved surface of the GFRP bars permitted slips at the bar-epoxy interface, decreasing modules of elasticity (as a result of adding additive to obtain epoxy D) allowed better distribution of the bond stress along the bonded length of the bar, without bar damage in the case of epoxy D.

- Bond length had a great effect on the bond behaviour of NSM joints; increasing it raised the load capacities and lowered the average bond stress of NSM FRP bars whatever the epoxy type. An increase of from $12d_b$ to $30d_b$ for specimens with bars bonded with epoxy A, B and D enhanced $F_{max,av}$ by approximately 76.91 %, 43.14 % and 94.85 % respectively, while an increase from $12d_b$ to $24d_b$ enhanced $F_{max,av}$ by approximately 33.75 %, 45.84% and 64.67 % respectively.
- With the same FRP axial stiffness, the load capacity of NSM FRP bars was dependent on the epoxy type and bond length. This suggests a link between the influence of these two factors, and a need for further experimental and numerical work. Additional experimental and numerical studies are also needed to better understand bond behaviour in a transverse direction, which would contribute to a better understanding of the bond behaviour of the NSM system.

Chapter 5

Pullout test numerical analysis

5.1 Overview

The material and geometric properties of fibre reinforced polymer (FRP) bars or strips, the characteristics of the adhesive and the concrete quality greatly affect the strengthening effectiveness of the near surface mounted (NSM) technique. Constitutive models able to adequately simulate the interface between NSM FRP elements and concrete are decisive for the correct prediction of the load capacity, crack opening and crack spacing of concrete structures strengthened according to this technique. The assessment of the influence of relevant factors that affect the NSM FRP bond behaviour, on the values of the parameters that define these constitutive models is also crucial for reliable numerical simulations of this type of structures by using the finite element method (FEM). Since in the experimental pullout tests used to derive the bond stress slip relationship, cracks have formed in the concrete surrounding the FRP bars, the FEM model to be adopted in this inverse analysis procedure should be capable of simulating the concrete fracture initiation and propagation. In this chapter a FEM-based smeared crack model is used to assess, by inverse analysis, the influence of the following parameters on the bond behaviour of the FRP NSM systems: epoxy properties, bar type, bar diameter, bond length and concrete strength. This assessment is executed by simulating a series of pullout tests in which the effect of different geometric and mechanical properties were investigated experimentally. An experimental-numerical comparison of the load slip response, bond stresses, stress field in the surrounding concrete and the failure modes is performed

to derive relevant information about the influence of the aforementioned parameters on the bond behaviour of the NSM FRP strengthening systems.

5.2 Experimental programme

Some of the experimental pullout test specimens reported in the previous chapters (Chapters 3 and 4) were simulated numerically and their numerical and experimental results were also compared. Type of FRP material (carbon, C, and glass, G), bar diameter (8, 9, 12 mm), modulus of elasticity (64, 134, 170 GPa), type of adhesive (A, B, C, D), concrete strength (1, 2) and bond length ($L = 192$ mm and $T = 240$ mm) were the variables, whose influence on the bond behaviour was investigated. The specimen designation was located in the first column of the Tables 5.1 and 5.2. In addition, the numbers -1, -2 and -3 located at the end of the specimens' designation aim to identify the number of the tested specimen for each series of variables. For instance, L12A2C1-1 represents the first specimen (-1) of concrete type 2 reinforced with carbon fibre type 1 (C1) installed into a groove of size dimension of 12 mm and bonded with adhesive type A along a bond length of 192 mm (L).

Ready mixed concrete was used to cast all the specimens. Concrete properties were obtained from standard cylinder (150×300 mm²) tests. Average concrete compressive strength of 23 and 41 MPa, and average tensile strength of 2.0 and 3.0 MPa, were obtained for the concrete 1 and concrete 2, respectively. The loaded end slip was measured using two displacement transducers (LVDTs), with a measuring length of 50 mm and 0.25 % accuracy, while the free end slip was recorded with another LVDT with a measuring length of 11 mm and accuracy 0.05 %, according to the arrangement shown in Fig. 3.5. Five strain gauges, 32 mm a part, starting at 32 mm from the loaded end, were installed on the surface of the bar of specimen L12A2C1 to measure the tensile strain along the bond length (see section 3.5)

5.3 Experimental results

The experimental results are reported in Tables 5.1 and 5.2 for specimens with CFRP and GFRP bars, respectively. The two tables include for each specimen: the

ultimate tensile strength, f_{fu} , the Young's modulus, E_f , the diameter, d_b , and the axial stiffness, $E_f A_f$, of the bar, maximum pullout force, F_{max} , loaded end slip at F_{max} , d_{max} , and the failure mode. The loaded end slip was obtained by deducing to the average displacement measured by the top LVDTs the axial deformation of the FRP between the loaded end section and the section where the LVDTs are fixed to the FRP bar.

Table 5.1: Main experimental data and results from the pullout test for specimens with CFRP bars.

Specimen designation	d_b (mm)	E_f (GPa)	$E_f A_f$ (kN)	f_{cu} (Mpa)	F_{max} (kN)	d_{max} (mm)	Failure mode
L16A1C1-1	8	2350	170	8544	40.12	0.824	LC,B-E
L16A1C1-2	8	2350	170	8544	39.28	0.792	LC,B-E
L16A2C1-1	8	2350	170	8544	42.02	0.662	B-E
L12A2C1-1	8	2350	170	8544	36.59	0.593	LC,B-E
L15A1C2-1	9	2010	134	8524	44.91	0.627	LC,CC,B-E
L15A1C2-2	9	2010	134	8524	44.65	0.481	LC,B-E
L15A1C2-1	9	2010	134	8524	47.00	0.623	LC,Es
L16B1C1-1	8	2350	170	8544	48.99	0.807	B-E
L16B1C1-2	8	2350	170	8544	47.31	0.936	B-E
T16B1C1-1	8	2350	170	8544	54.79	1.123	B-E
T16B1C1-2	8	2350	170	8544	58.09	1.277	B-E

B-E = bar-epoxy interface failure; CC = concrete cracking; ES = epoxy splitting; and LC= epoxy longitudinal cracking .

Table 5.1 shows that the main mode of failure for specimens with CFRP bars was bar-epoxy interface failure. The mode of failure of specimens with C1 bars (those with a smoother surface) that were bonded with epoxy type A was bar-epoxy interface failure. The failure initiated with a longitudinal splitting crack on the surface of the epoxy near the loaded end (see detail in Fig. 5.1a). By increasing the load, the longitudinal crack propagated towards the free end of the bonded bar. Once the crack reached the free end, bar-epoxy interface failure occurred. On the other hand, the failure of specimen L12A2C1, with small groove size, initiated with the formation of cracks in the epoxy paste at the positions of the strain gauges installed on the top surface of the bonded bars. The epoxy split near the free end, followed by a bar-epoxy interface failure with large slip of the bar. Specimen L16A2C1 failed

Table 5.2: Main experimental data and results from the pullout test for specimens with GFRP bars.

Specimen designation	d_b (<i>mm</i>)	f_{fu} (<i>MPa</i>)	E_f (<i>GPa</i>)	$E_f A_f$ (<i>kN</i>)	F_{max} (<i>kN</i>)	d_{max} (<i>mm</i>)	Failure mode
L16A1G1-1	8	1350	64	3216	36.23	1.604	LC,CC,ES
L16A1G1-2	8	1350	64	3216	38.92	1.300	LC,CC,ES
L16B1G1-1	8	1350	64	3216	56.33	3.082	CC,BF
L16B1G1-2	8	1350	64	3216	44.56	3.061	CC,BF
L16B1G1-3	8	1350	64	3216	48.06	2.678	CC,BF
L16C1G1-1	8	1350	64	3216	56.34	2.364	CC,BF
L16C1G1-2	8	1350	64	3216	45.36	2.466	CC,BF
L16C1G1-3	8	1350	64	3216	52.34	2.863	CC,BF
L16D1G1-1	8	1350	64	3216	52.10	3.593	CC,BF
L16D1G1-2	8	1350	64	3216	57.79	3.650	BF
L18A1G2-1	12	1350	64	7238	59.97	1.256	LC,CS,ES
L18A1G2-2	12	1350	64	7238	57.53	0.994	LC,CS,ES
L18A1G2-2	12	1350	64	7238	58.59	1.1590	LC,ES

B-E = bar-epoxy interface failure; CC = concrete cracking; CS = concrete splitting; ES = epoxy splitting; BF = bar surface damage and LC= epoxy longitudinal cracking.

with no visible cracks either in epoxy or in concrete at a failure load higher than that of specimen L12A2C1.

Specimens with C2 bars (with textured surfaces) presented bar-epoxy interface failure with epoxy cracking extended to cause concrete cracking. The failure initiated with the formation of a longitudinal splitting crack followed by transverse cracking on the top surface of the epoxy paste. By increasing the load, the longitudinal crack propagated towards the free end until a failure load of 44.78 kN. For specimen L15A2C2, cast with concrete 2, the failure was initiated by the splitting of the epoxy cover and extended to cause damage in the surrounding concrete. Since bar-epoxy interface failure occurred in the specimens strengthened with CFRP bars, the concrete strength had slight effect on the load capacity of these specimens. To study the effect of adhesive properties and bond length on NSM bond behaviour, specimens L16BC1 and T16BC1 with C1 bars bonded with epoxy type B were tested. The specimens showed bar-epoxy interface failure at loads of 48.15 kN and 56.44 kN (average values of the two specimens of each series), respectively. No visible cracks

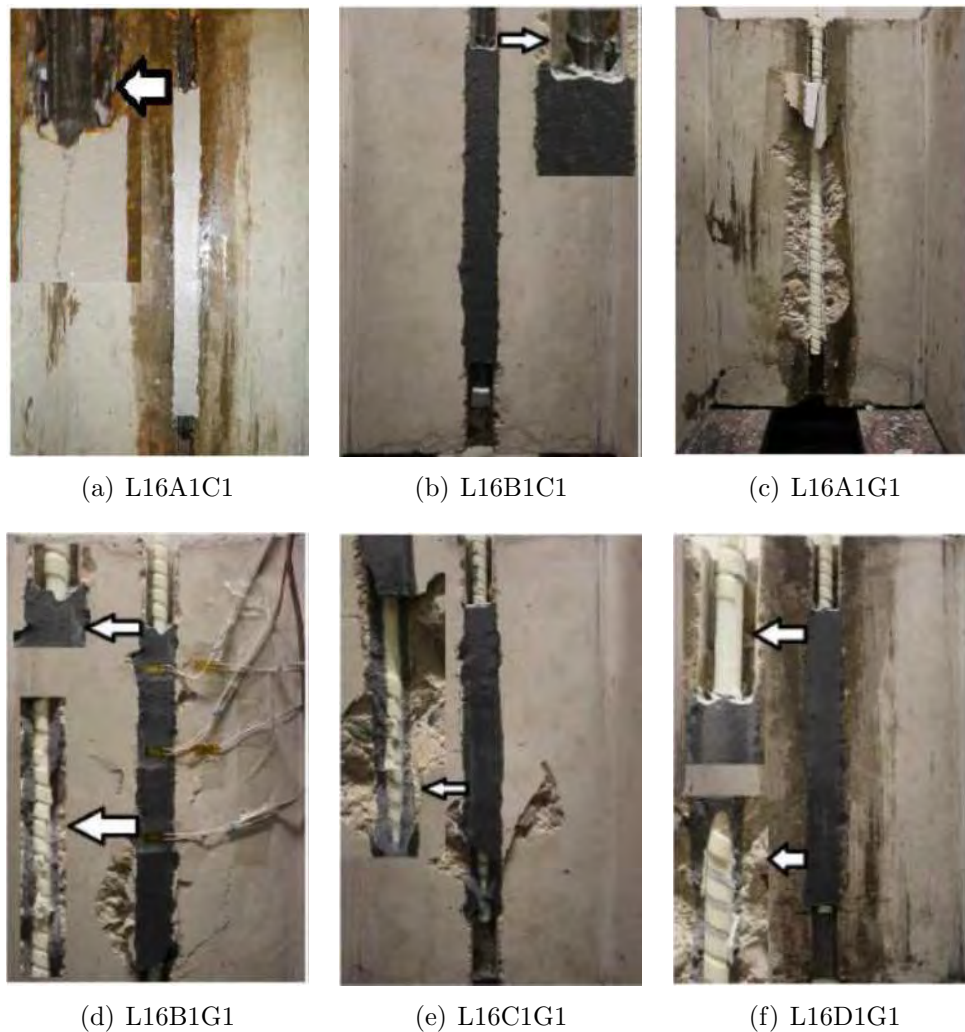


Figure 5.1: Failure mode of the tested specimens.

formed in either the concrete or epoxy paste (see Fig. 5.1b). This means that changing the epoxy paste or increasing the bond length has increased the failure load in 20.4% (L16B1C1 compared to L16A1C1) and in 17.2% (L16C1G1 compared to L16B1C1), respectively.

The main failure modes of specimens with GFRP bars were epoxy splitting and bar surface damage as indicated in Table 5.2. The failure mode of specimens with G1 bars bonded with epoxy type A was epoxy splitting followed by the detachment of the concrete surrounding the groove (see Fig. 5.1c). The failure initiated with the formation of a longitudinal splitting crack in the epoxy paste near the loaded

end. By increasing the load, the longitudinal crack propagated towards the free end of the bonded GFRP bar till the failure load, which was followed by the detachment of the concrete surrounding the groove.

To assess the effect of the adhesive properties, the G1 bar type was bonded using epoxy types B, C and D. For specimens bonded with epoxy type B, concrete cracks formed close to the free end of the bonded bar, and the bar slipped gradually until failure. Some damage was observed in the grooved surface of the bar after removing the epoxy paste once the test was finished (see Fig. 5.1d). The failure mode of specimens with G1 bars and bonded using epoxy types C and D was bar surface damage at a load capacity higher than that of specimens bonded with epoxy types B (see Fig. 5.1e and 5.1f). In addition, changing the adhesive type from A to B, C and D for specimens with G1 bars has increased the maximum load by 32.4%, 36.7% and 46.3 %, respectively. Besides, by increasing the diameter of GFRP bars from 8 mm for G1 to 12 mm for G2 has increased the maximum load in approximately 47%, with the same failure mode. The concrete strength had no effect on the maximum load and mode of failure of specimens with G2 bars (the failure was epoxy splitting).

5.4 Numerical analysis

5.4.1 FEM model

The finite element programme FEMIX V4 is based on the displacement method, being possible to simulate a structure with several types of finite elements and constitutive models for the nonlinear behaviour of concrete, steel and composite materials [99, 100]. In the present work the programme is used to perform an inverse analysis in order to obtain the local bond slip laws for the NSM FRP systems, by approaching as much as possible the relevant results registered experimentally in the tested specimens. The pullout test configuration shown in Fig. 3.5 is modeled as a plane stress problem. Half part of specimen is considered to reduce the computational time taking advantage of the symmetry conditions (see Fig. 5.2).

The displacement in direction 2 is equal to zero for the points located in the symmetry axis, while the displacement in direction 3 of the nodes of the upper concrete surface (90×350 mm) is assumed null to simulate the support conditions

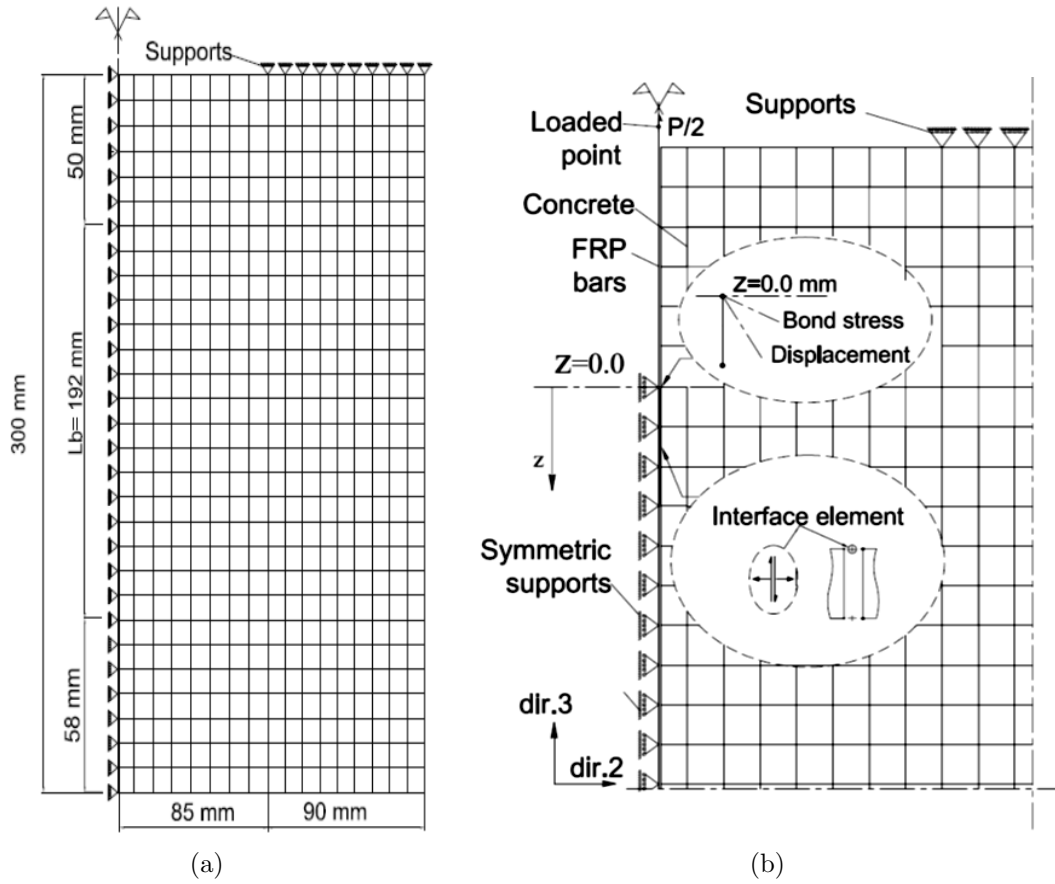


Figure 5.2: Finite element mesh of half of specimen: (a) complete mesh and (b) details of the model.

of the specimen in the experimental test setup (see Figs. 3.5 and 5.2). Four-node Lagrangian plane stress elements with a 2×2 Gauss-Legendre integration scheme are used to simulate the concrete block, while cable 2D linear elements with two integration points are adopted to simulate the FRP bars. The load is applied by imposing a displacement increment of 0.005 mm in the loaded point in direction 3 (Fig. 5.2b), by using the arc-length method [29]. The size of the mesh elements was 8 mm surrounding the bonded length and increases to 12 mm otherwise.

The FRP bars and the external part of concrete specimen (90×350 mm, Fig. 3.5) are modeled as linear elastic materials. The Young's modulus values for FRP bars (64, 134 and 170 GPa) and for concrete (23 and 38 GPa) determined in the experimental tests are used. Poisson ratio values of 0.0 and 0.2 for FRP and concrete, respectively, are also considered. For modelling the crack initiation and propagation

in the concrete surrounding the FRP systems, the material nonlinear behaviour in the central part of the specimen (with a thickness of 180 mm) is simulated with a multidirectional fixed smeared crack model described elsewhere [99]. The values adopted for the parameters of the constitutive model are indicated in Table 5.3. The physical meaning of the parameters defining the post-cracking tensile behaviour of concrete is represented in Fig. 5, while the meaning of the remaining variables of this constitutive model is provided in [99]. Due to the relatively small compressive stresses in the concrete generated in the pullout tests, this model assumes a linear-elastic behaviour of the concrete in compression. The $\tau - s$ bond law described in Eq. 5.1, and represented in Fig. 5.4a, is used to characterize the sliding component of the constitutive law adopted to model the FRP-concrete interface [78], therefore integrating the sliding between FRP-adhesive, adhesive-concrete and the elastic and inelastic deformability of the adhesive. For this purpose, four node line interface finite elements with two-point Lobatto integration rule are used to simulate the bond behaviour between concrete and FRP bar [101]. For the normal stiffness a constant value of $5.0e+05$ N/mm² is assumed.

$$\tau(s) = \begin{cases} m_{in}s, & s_{lin} \leq s \\ \tau_{max}\left(\frac{s}{s_{max}}\right)^\alpha, & s_{lin} < s \leq s_{max} \\ \tau_{max}\left(\frac{s}{s_{max}}\right)^{-\alpha}, & s > s_{max} \end{cases} \quad (5.1)$$

In Eq. 5.1, τ_{max} is the maximum bond shear strength, s_{max} is the corresponding slip, α and $-\alpha$ are parameters defining the shape of the pre and post-peak branches, respectively, and m_{in} represents the initial stiffness of the bond law, assumed to be linear up to a slip of s_{lin} (Fig. 5.4a, [101]). The influence of the different parts of the local bond slip law on the global response of a specimen tested in a bond test is represented in Fig. 5.4b [101]. The effect of the bond parameters is reported and discussed in [101].

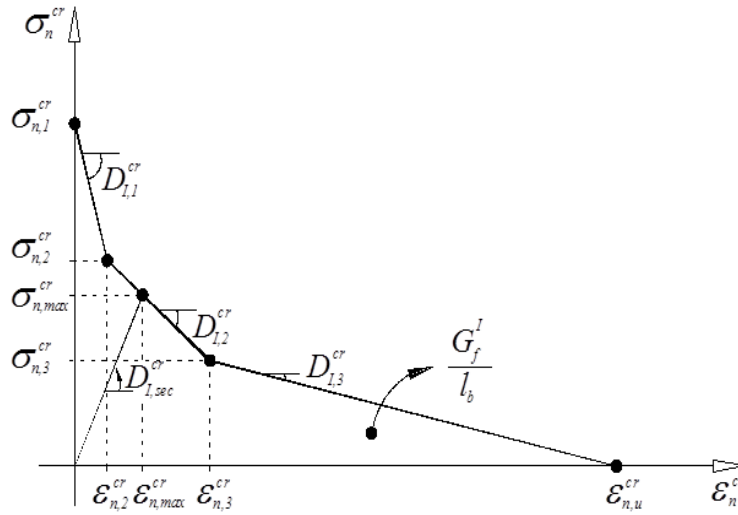


Figure 5.3: Trilinear stress strain diagram to simulate the fracture mode I crack propagation ($\sigma_{n,2}^{cr} = \alpha_1 \sigma_{n,1}^{cr}$, $\sigma_{n,3}^{cr} = \alpha_2 \sigma_{n,1}^{cr}$, $\epsilon_{n,2}^{cr} = \xi_1 \epsilon_{n,u}^{cr}$, $\epsilon_{n,3}^{cr} = \xi_2 \epsilon_{n,u}^{cr}$).

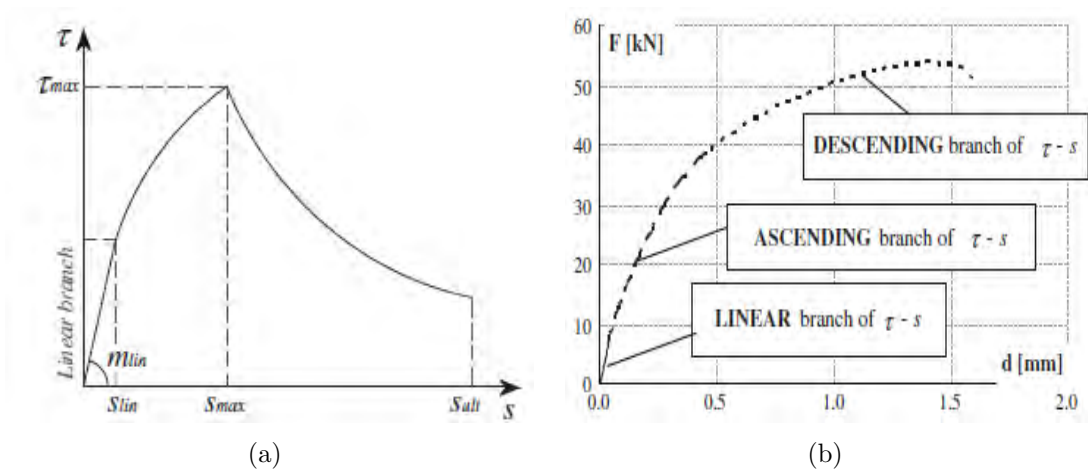


Figure 5.4: (a) local bond stress slip relationship and (b) qualitative correlation between $\tau - s$ and $F - d$ relationships in a bond test [101].

Table 5.3: Values of the parameters of the concrete constitutive model [102].

Parameters	Concrete 1	Concrete 2
Poisson's ratio	$\nu_c = 0.20$	$\nu_c = 0.20$
Initial Young's modulus	$E_c = 23000$ MPa	$E_c = 38000$ MPa
Compressive strength	$f_c = 23$ MPa	$f_c = 41$ MPa
Tri-linear softening diagram parameters	$f_{ct} = 2.0$ MPa; $G_f = 0.113$ N/mm; $\xi_1 = 0.4$; $\alpha_1 = 0.8$; $\xi_2 = 0.6$; $\alpha_2 = 0.2$	$f_{ct} = 3.0$ MPa; $G_f = 0.113$ N/mm; $\xi_1 = 0.4$; $\alpha_1 = 0.8$; $\xi_1 = 0.6$; $\alpha_1 = 0.2$
Parameter defining the mode I fracture energy available to the new crack yield surface	$P_1 = 2$	$P_1 = 2$
Shear retention factor	Exponential ($P_2 = 2$)	Exponential ($P_2 = 2$)
Crack band-width, l_b	Square root of the area of the integration point	Square root of the area of the integration point
Threshold angle	$\alpha_{th} = 30^\circ$	$\alpha_{th} = 30^\circ$

5.5 Numerical results and comparison

5.5.1 Inverse analysis

The strategy of the inverse analysis is to derive the values of the parameters that define the $\tau - s$ bond law that fit with the minimum deviation the pullout force-versus loaded end slip ($F-d$) up to failure registered in the experimental tests. The loaded end slip is obtained at $z = 0.0$ (Fig. 5.2b). Since s_{lin} has relatively little influence on the ($F-d$) response [101], a value of 0.05 mm is assumed in all simulations. To explain and understand the procedure of the inverse analysis adapted herein, the back fitting analysis of the $\tau - s$ law for the specimen L16A1C1-1 is discussed in detail, then the other specimen are also simulated. Based on the experimental $F-d$ relationship of the specimen L16A1C1-1 (d is the loaded end slip) a first empirical calibration (Calibration 1) was performed. This calibration leads to the values indicated in Table 5.4.

Note that the values of the shear stresses are referred to the perimeter of the bar, since the failure has been considered occurring at the bar-epoxy interface. However, applying the bond stress slip relationship of Calibration 1 led to a pullout force-

Table 5.4: Empirical calibrations of the parameters defining the $\tau - s$ relationship (specimen L16AC1-1).

Calibration	s_{lin} (<i>mm</i>)	s_{max} (<i>mm</i>)	τ_{max} (<i>MPa</i>)	α (<i>-</i>)	α' (<i>-</i>)
1	0.05	0.44	8.30	0.50	0.30
2	0.05	0.44	8.80	0.50	0.30

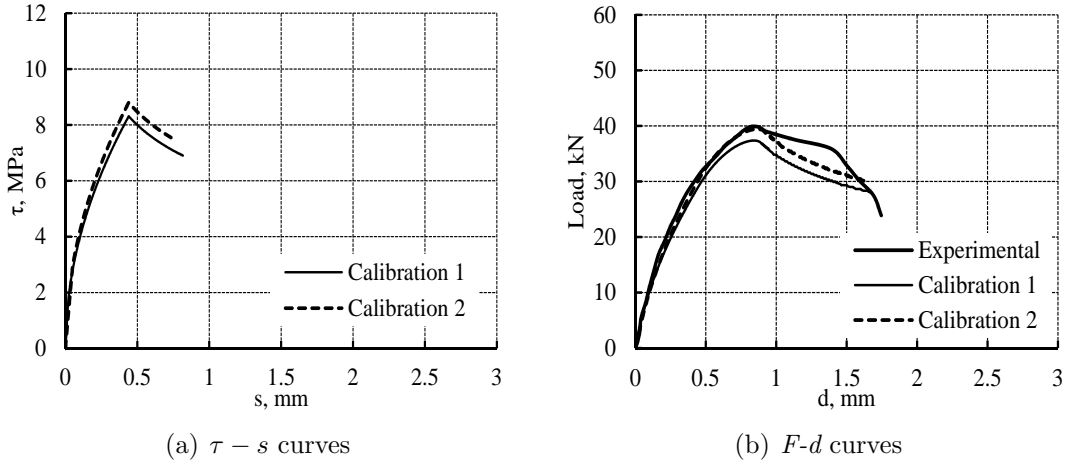


Figure 5.5: Experimental and numerical calibration curves of specimen L16A1C1-1.

displacement curve that is quite lower than the experimental one (see Fig. 5.5b). Then a second calibration (Calibration 2) was performed, in which, bond parameters were determined to fit, as much as possible, the experimental $F-d$ curve up to the peak force. Fig. 5.5a shows that the $\tau - s$ relationship of Calibration 2 allows obtaining a very good fitting with the experimental $F-d$ curve (Fig. 5.5b). Note that the convergence criterion adopted in these simulations was the force norm criterion, having been adopted with a tolerance of 1.0×10^{-3} [101]. It is important to highlight that the numerical $F-d$ curves may stop at certain values of the slip, s_{ult} , because the incremental and iterative method of FEMIX did not converge.

The same approach has been followed to obtain the numerical curves for the other specimens of this series (L16A1C1-2). The empirical calibrations and the comparisons between the experimental and numerical $F-d$ curves for each specimen are included in Appendix A for specimens with NSM CFRP and GFRP bars.

The mean values of the parameters defining the $\tau - s$ law for the two specimens (L16A1C1-1 and L16A1C1-2, see Table 5.5) was used to perform a new simulation. The resulted of the new simulation, $\tau - s$ and $F-d$ curves, (named Average) are obtained.

Table 5.5: Empirical calibrations of parameters define the $\tau - s$ relationship (series L16AC1).

Calibration	s_{lin} (mm)	s_{max} (mm)	τ_{max} (MPa)	α (-)	α' (-)	d_{max} (mm)	F_{max} (MPa)
L16A1C1-1	0.05	0.44	8.80	0.50	0.30	0.86	39.43
L16A1C1-2	0.05	0.44	8.80	0.50	0.30	0.86	39.43
Average	0.05	0.44	8.80	0.50	0.30	0.86	39.43

The values of the parameters of the bond law obtained from inverse analysis for each experimental curve and subsequently averaged for specimen type, as well as the numerical and experimental maximum force ($F_{max,num}$ and $F_{max,exp}$), and the slip at failure, s_{ult} , (when specimen has failed in the experimental tests) are listed in Table 5.6 for specimens with CFRP and GFRP bars.

5.6 Discussion of the numerical results

5.6.1 Specimens with CFRP bars

The $F-d$ curves obtained numerically by inverse analysis are compared to the experimental ones in Figs. 5.6 and 5.7, for the specimens reinforced with CFRP bars. A good agreement between experimental and numerical results in terms of $F-d$ relation and maximum load was obtained. Fig. 5.8 shows the comparisons among the numerical local bond slip, $\tau - s$, curves for specimens with CFRP bars. The two types of CFRP bars, C1 and C2, had the same axial stiffness, developed similar bond law with slight difference in the value of τ_{max} (0.25 MPa, Fig. 5.8a). This difference may be due to the thicker epoxy layer surrounding the C1 bar (diameter of 8 mm and groove dimension of $16 \times 16 \text{ mm}^2$ than that surrounding the C2 bars bar (diameter of 9 mm and groove dimension of $15 \times 15 \text{ mm}^2$. As the failure mode of specimens with CFRP bars was bar-epoxy interface failure, it can be concluded

Table 5.6: Values of the bond law parameters assessed by inverse analysis.

Specimen ID	s_{max} (mm)	τ_{max} (MPa)	α (-)	α' (-)	s_{ult} (mm)	$F_{max,num}$ (kN)	$F_{max,exp}$ (kN)
		Specimens	with	CFRP	bars		
L16A1C1	0.44	8.80	0.50	0.30	1.54	39.43	39.65
L16A2C1	0.40	9.20	0.30	0.20	0.99	41.42	42.02
L12A2C1	0.40	8.70	0.30	0.95	0.80	36.28	36.60
L15A1C2	0.35	8.55	0.55	0.15	1.71	44.61	44.72
L15A2C2	0.43	8.70	0.20	0.35	1.26	45.17	47.00
L16B1C1	0.48	10.35	0.48	0.25	5.69	46.67	48.15
T16B1C1	0.65	9.90	0.50	0.30	5.94	55.22	56.44
		Specimens	with	GFRP	bars		
L16A1G1	0.75	7.90	0.33	0.20	3.03	38.10	37.82
L16B2G1	1.48	10.33	0.27	0.17	4.39	50.80	49.70
L16C2G1	1.35	10.70	0.30	0.23	4.47	51.65	51.40
L16D1G1	1.48	10.33	0.27	0.17	5.82	54.86	54.94
L18A1G2	0.60	8.10	0.20	0.20	1.30	57.83	58.75
L18A2G2	0.50	8.10	0.10	0.10	3.1	559.13	58.59

that the increase of the epoxy layer thickness had a favorable effect in terms of bar confinement. As the epoxy thickness increases, the formation of splitting cracks is delayed [68]. As already demonstrated, during the pullout process micro compressive struts form in the cracked adhesives [78, 100]. The force component of these struts normal to the failure crack at the adhesive-FRP interface increases with the decrease of the adhesive layer thickness, which, according to the Mohr-Coulomb principles, justifies the higher post-peak bond strength of the L15A1C2 specimen. On the other hand, specimens with C1 bars bonded with epoxy B developed bond law with value of τ_{max} higher than those bonded with epoxy A. The aforementioned reasons can also justify this behaviour since the higher the elasticity modulus of the adhesive the higher the axial stiffness of the compressive micro-struts of the adhesive, which leads to a stiffer and stronger bond connexion. There is also a contribution of the higher tensile strength of epoxy B, which in turn delays the damage process derived from the initiation and propagation of cracks in the adhesive.

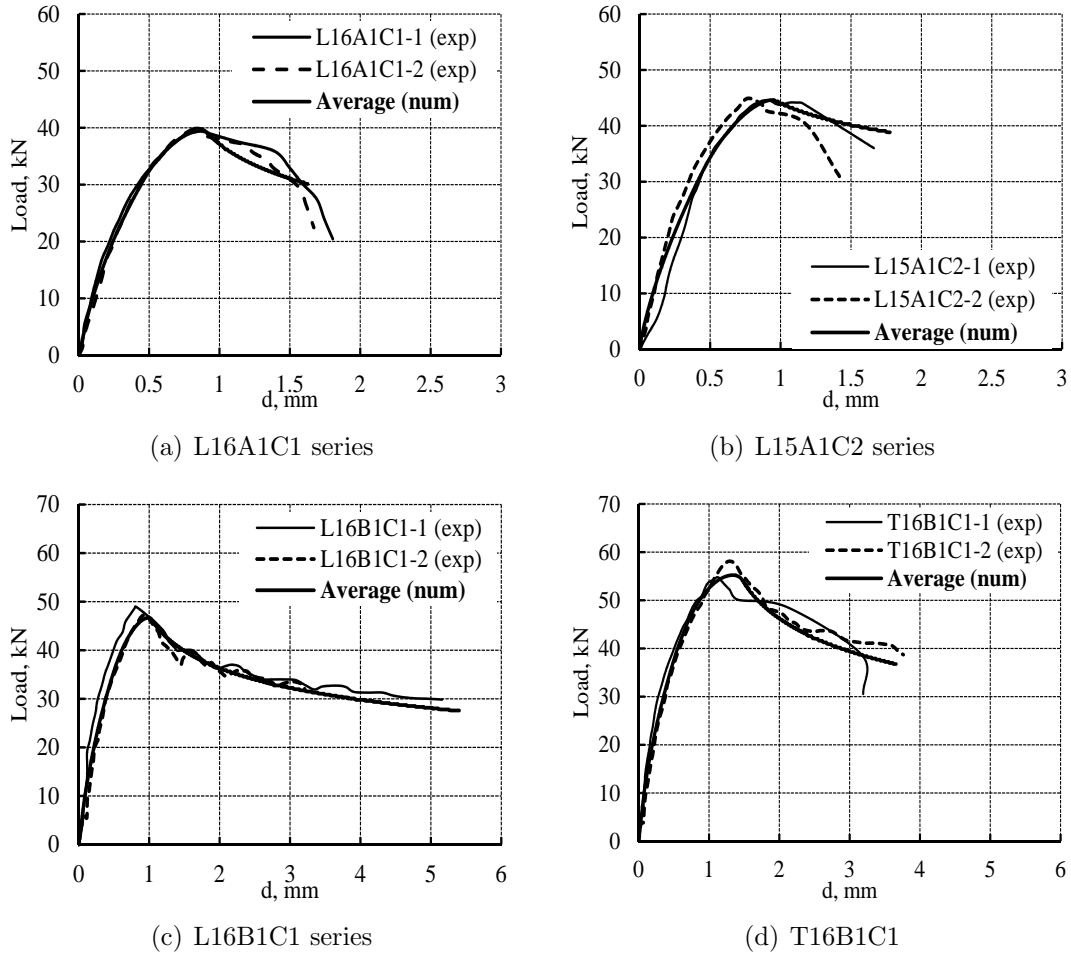


Figure 5.6: Experimental and numerical $F-d$ curves of specimens with CFRP bars (concrete 1).

On the other hand, specimens with C1 bars bonded with epoxy B developed similar bond slip law for the two bond lengths, 192 mm and 240 mm, with slight increase in the value of s_{max} in the specimens with larger bond length (0.175 mm, Fig. 5.8a), which can be justified by the larger volume of the adhesive. This means that the bond law of these specimens is affected only by the value of s_{max} (the failure occurred at bar-epoxy interface). More experimental and numerical analysis is needed to corroborate these observations. Fig. 5.8b shows that, as the concrete strength increases the values of α in Eq. 5.1 decreases, due to the smaller deformability and higher confinement provided by the concrete surrounding the bond zone (i.e, the pre-peak phase of the $\tau - s$ curve is as stiffer as lower is the α value).

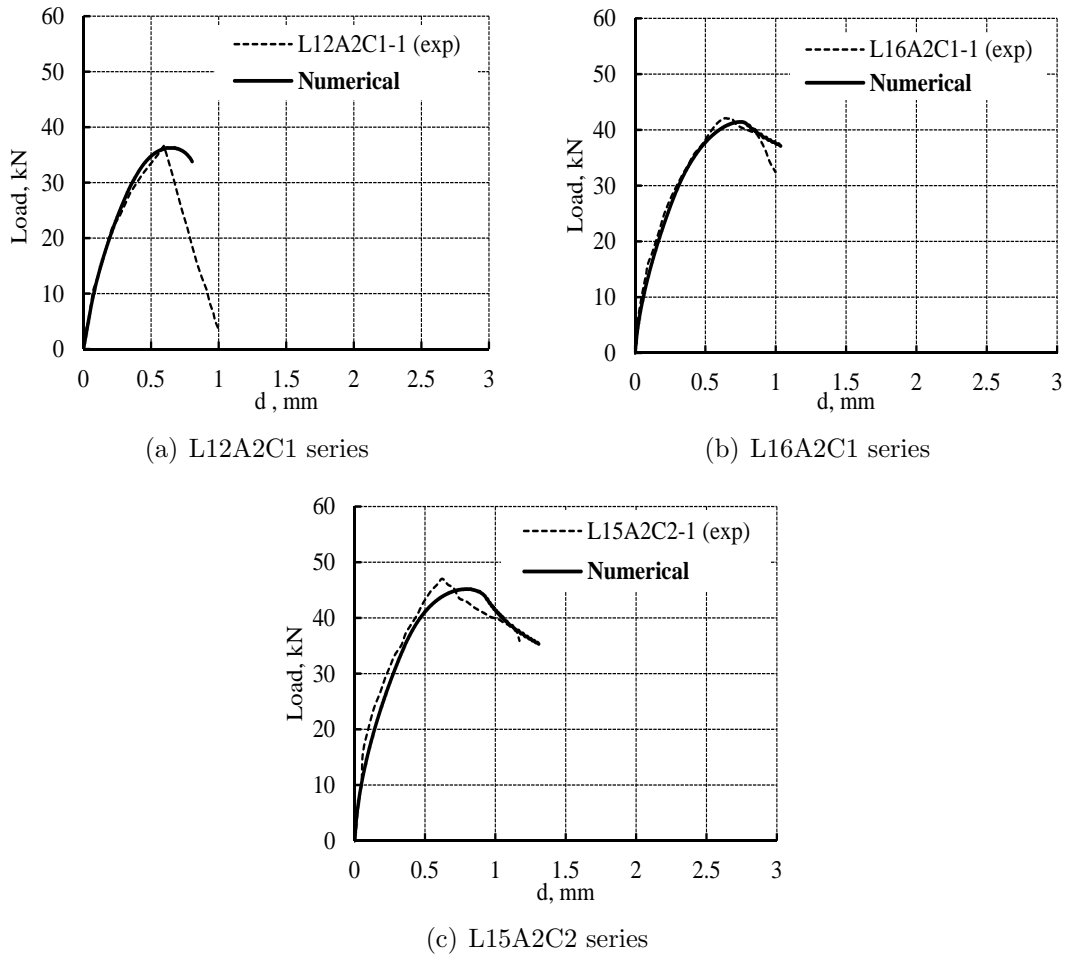


Figure 5.7: Experimental and numerical $F-d$ curves of specimens with CFRP bars (concrete 2).

Due to the same reason, by increasing the concrete strength class the s_{max} has a tendency to slightly decrease, while τ_{max} tends to increase moderately.

5.6.2 Specimens with GFRP bars

Fig. 5.9 shows the experimental and numerical $F-d$ curves for specimens with GFRP bars. Similarly to specimens with CFRP bars, good agreement between the experimental and numerical results in terms of $F-d$ relation and maximum load is obtained. Fig. 5.10 shows a comparison between the numerical local bond slip, $\tau-s$, curves for specimens with GFRP bars. Specimens with GFRP bars developed

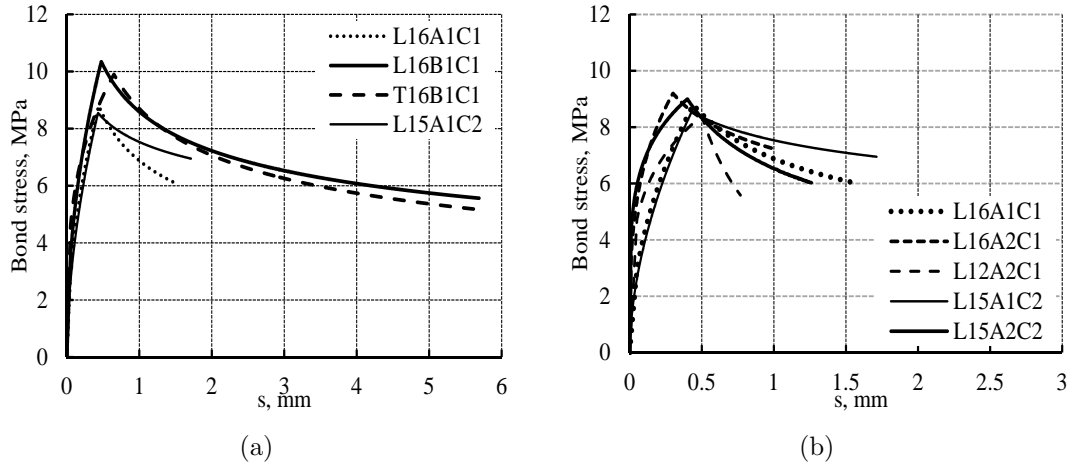
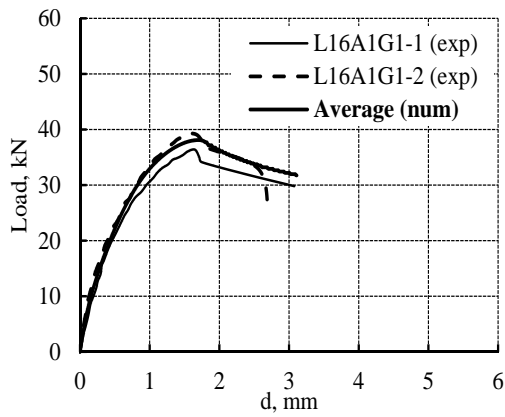


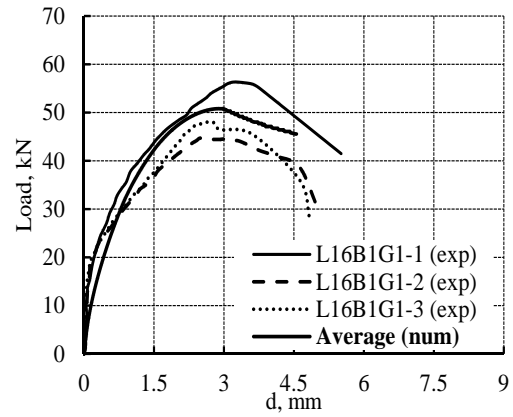
Figure 5.8: Comparisons of the $\tau - s$ curves of specimens with CFRP bars: a) influence of the bar size and adhesive properties; b) influence of the concrete strength and groove size.

bond laws with higher values of v and lower values of τ_{max} , α and α' than those of the corresponding specimens with CFRP bars bonded with epoxy A (Table 5.6). Moreover, for specimens bonded with epoxy B, GFRP bars present also higher values of s_{max} and lower values of α and α' , than those of CFRP bars (Table 5.6), while τ_{max} is similar in both cases. The more ductile response of the specimens reinforced with GFRP bars can be attributable to the smaller axial stiffness (note that the loaded end slip recorded in the LVDTs also includes the deformability of the bars along the bond length). The ribs composing the surface of the GFRP bars might have contributed to the formation of micro-compressive struts in the adhesive, which increased the FRP confinement during the pullout process, resulting a more ductile pullout response for the specimens strengthened with GFRP bars.

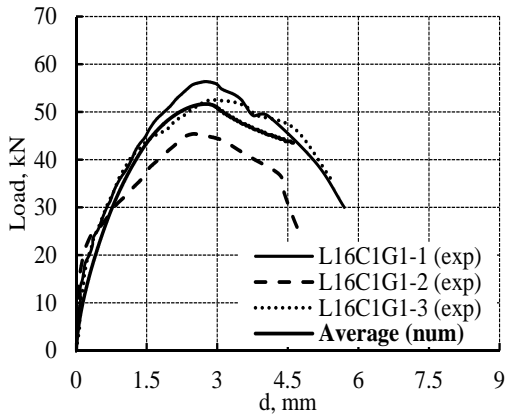
Confirming the conclusions already pointed out for the specimens reinforced with CFRP bars, Fig. 5.10a evidences that the strength and stiffness of the local bond law (given through the values of τ_{max} and s_{max}) increase with the tensile strength and modulus of elasticity of the adhesive, while α and α' are not significantly affected. By comparing L16A1G1 and L18A1G2 it seems that the diameter of the bar has an impact only on the pre-peak phase of the local bond law, by increasing the stiffness of the response with the diameter. Moreover, by increasing the concrete strength the values of the α and α' parameters decrease due to the higher confinement to the



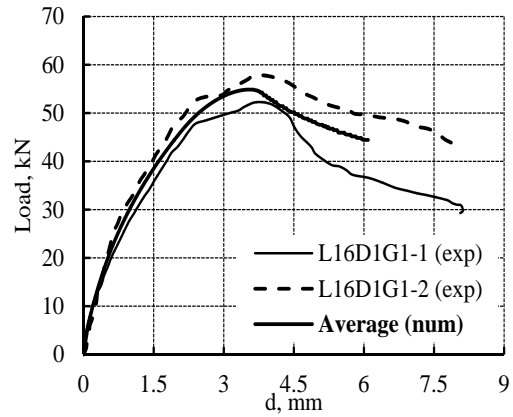
(a) L16A1G1 series



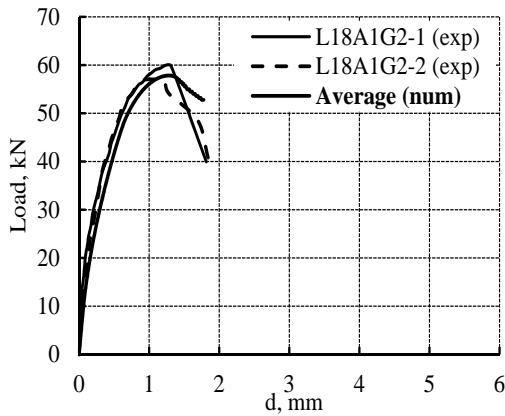
(b) L16B1G1 series



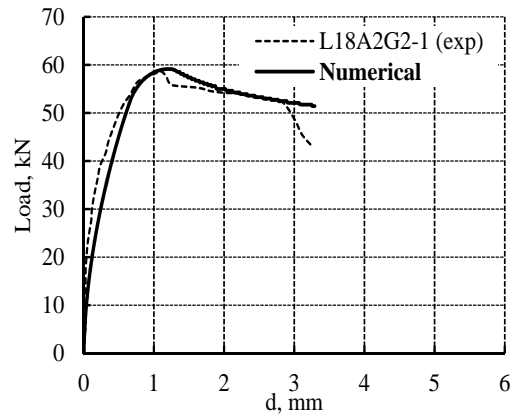
(c) L16C1G1 series



(d) L16D1G1 series



(e) L18A1G2 series



(f) L18A2G2 series

Figure 5.9: Experimental and numerical $F-d$ curves of specimens with GFRP bars.

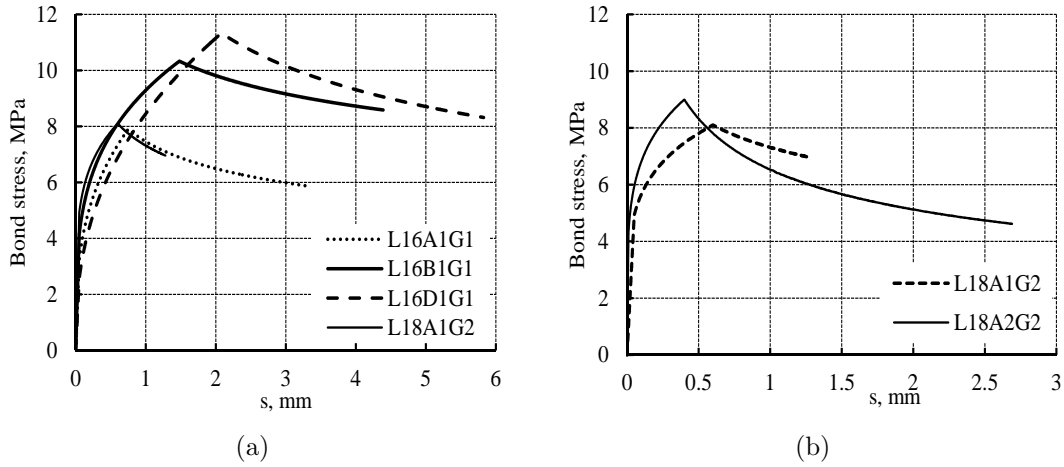


Figure 5.10: Comparisons of the $\tau - s$ curves of specimens with GFRP bars: (a) influence of the bar size and adhesive properties and (b) influence of the concrete strength.

bar provided by the surrounding concrete, resulting a stiffer response up to bond strength and a more ductile post-peak phase (see Fig. 5.10b).

In general, the analysis of the bond behaviour of the tested specimens shows that the increase of the Young's modulus of the bar E_f has a tendency to decrease the s_{max} and α parameters. On the other hand by increasing the Young's modulus of the epoxy has a tendency to increase the values of τ_{max} , s_{max} and s_{ult} . According to the overall behaviour of the tested NSM bars, the ultimate displacement (d_{max}) decreases by increasing E_f . Moreover, by increasing the axial stiffness of the FRP bar ($E_f A_f$), the value of s_{max} tends to decrease, while the tendency of the maximum pullout force (F_{max}) depends mainly on the type of epoxy. Finally, the maximum bond stress, τ_{max} appeared to be the main parameter affecting the maximum pullout force (F_{max}) for the tested specimens. This observation agrees with that reported in [101].

5.6.3 Strain distribution

In this section the strain distribution along the bond length of the NSM FRP bars is obtained from the numerical analysis at various load levels. Fig. 5.11 shows the comparisons between the experimental and numerical strain and bond stress

distribution along the bond length of specimen L12A2C1. The experimental shear stresses are calculated from the experimental readings from two consecutive strain gauges (32 mm apart). Considering the simplified approach adopted in the determination of the bond stress from the strains registered experimentally, it can be concluded that a good agreement between the experimental and numerical results is achieved. The difference in strain values (more evident near the loaded end) is attributed to the splitting of epoxy paste covering the strain gauges. Since the L12A2C1 was the unique specimen instrumented along the bond length, the analysis of the influence of the investigated parameters on the bond behaviour will be herein executed taking the results obtained from the numerical simulations.

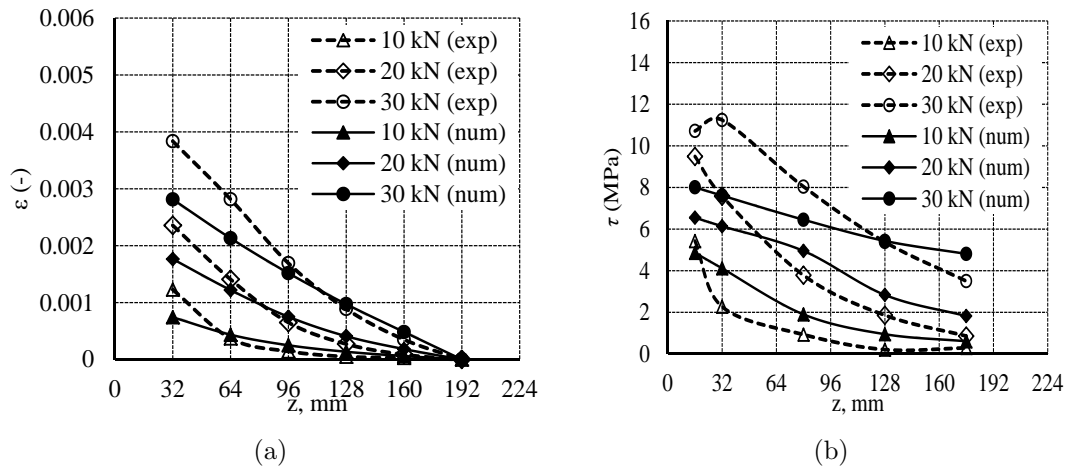


Figure 5.11: Numerical and experimental comparisons: (a) tensile strain and (b) bond shear stress distribution for specimen L12A2C1.

Fig. 5.12a shows the tensile strain distribution in the bond length of the C1 and G1 bars bonded with epoxy A at load levels of 10, 25 and 35 kN. Due to the lower E_f of GFRP bar, the strain values and strain variation was more pronounced in this type of specimens, regardless the level of applied pullout force. However, due to the same reason, the bond stress level and bond stress variation is not so different for the specimens where the unique difference is the type of FRP bar (Fig. 5.12b). Nonetheless, some specific differences can be pointed out.

The value of bond stress for specimens with G1 bars near the loaded end is higher than that of specimens with C1 bars at load level of 10 kN until z equal to 70 mm. By contrast, the bond stress for specimens with G1 bars is lower than in specimens

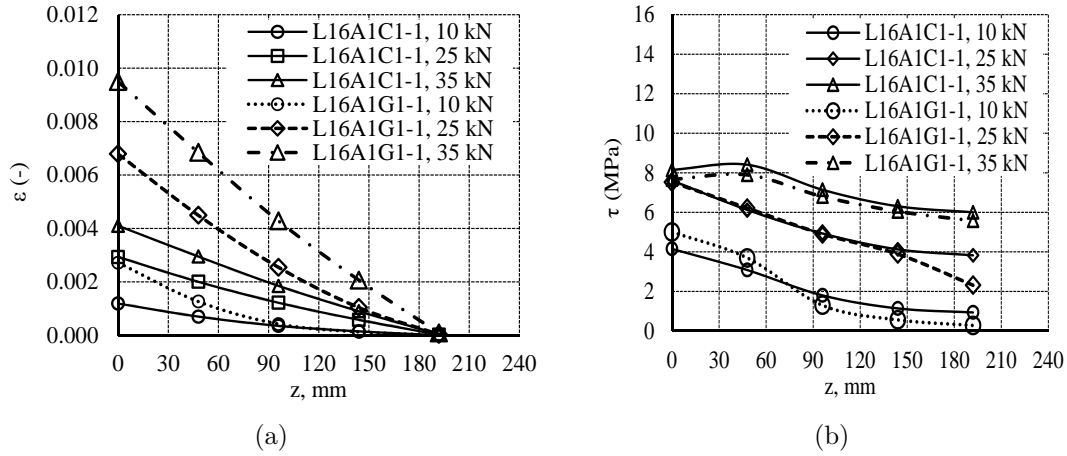


Figure 5.12: Effect of FRP type on the: (a) strain distribution and (b) bond stress distribution.

with C1 bars near the free end at load levels of 10 and 25 kN, and along the whole bond length when the load is 35 kN (Fig. 5.12b). This may be due to the formation of splitting cracks in the epoxy paste of specimens with G1 bars that starts near the loaded end and propagates towards the free end. The longitudinal splitting cracks for specimens with G1 bars were more detectable and wider than those formed in specimens with C1 bars (see Fig. 5.1). The plateau near the loaded end when the load is 35 kN indicates that the local bond stress attained its maximum value, and bond starts to degrade.

The effect of bar size on the strain distribution and bond stress for specimens with GFRP bars is also studied. Fig. 5.13a shows the tensile strain distribution along G1 and G2 bars bonded with epoxy A at the load levels of 10, 25 and 35 kN. The value of tensile strain of the specimens with G1 bar is higher than that of specimens with G2 bar. As expected, as the axial stiffness of the FRP reinforcement, $E_f A_f$, decreases the value of the tensile strain increases. On the other hand, Fig. 5.13b shows the bond stress distribution of G1 and G2 bars at the bar-epoxy interface for the indicated load levels. The value of bond stress for specimens with G1 bars is lower than that of specimens with G2 bars at load level of 10 kN near the loaded end until z equal to 18 mm. By contrast, the bond stress for specimens with G1 bar is higher than that of specimen with G2 bar near the free end started from z equal to 18 and 55 mm at load levels 10 and 25 kN, respectively, and along the whole bond

length at a load of 35 kN. The bond shear stress is concentrated near the loaded end for specimens with G2 bars. It is also seen that when load increase the local bond stresses attain the maximum value and bond starts to degrade for specimens with G1 bars (maximum load = 38.1 kN).

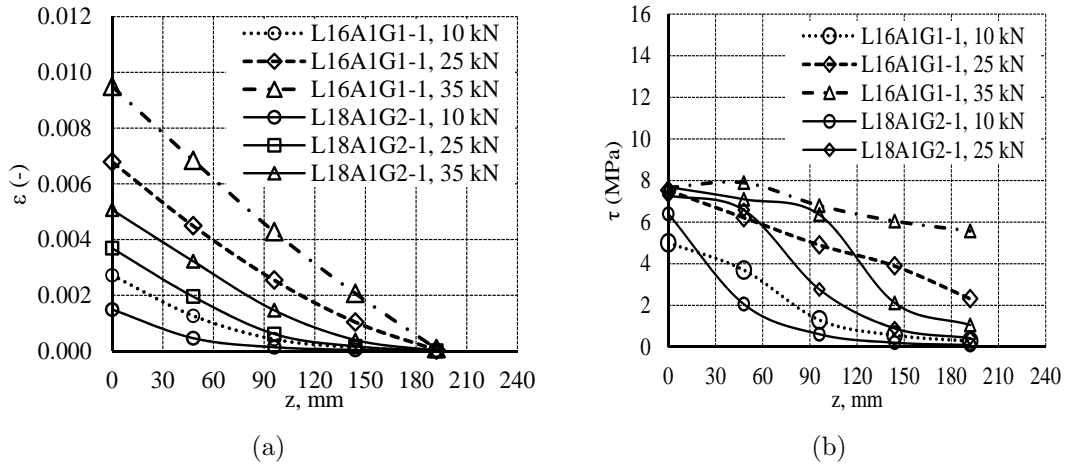


Figure 5.13: Effect of bar size on the: (a) strain distribution and (b) bond stress distribution.

Figs. 5.14a and b show the curves of strain distribution and bond stress distribution, respectively, for specimens L16AG1-1 and L16BG1-1. The strain values obtained from specimens bonded with epoxy A is slightly higher than that obtained from specimens bonded with epoxy B. This may be due to the smaller elasticity modulus and tensile strength of the epoxy A, more prone to the occurrence of splitting cracks, (see Fig. 5.1), with a higher transference of strains to the G1 bar. Near the loaded end, in a distance that increases with the pullout force, the bond stress in specimens bonded with epoxy A is lower than that in specimens bonded with epoxy B. The opposite occurs in the remaining part of the bond length, which indicates that the higher damage occurred in the epoxy A, in consequence of the splitting cracks formed near the loaded end, has a higher stress transfer effect to the zones of smaller damage (near the free end) than the case observed in the specimens with epoxy B.

The effect of the bond length on the strain and bond stress distribution is analyzed by comparing the results obtained in the L16B1C1-1 and T16B1C1-1 specimens that have a bond length of 192 and 240 mm, respectively (for comparison

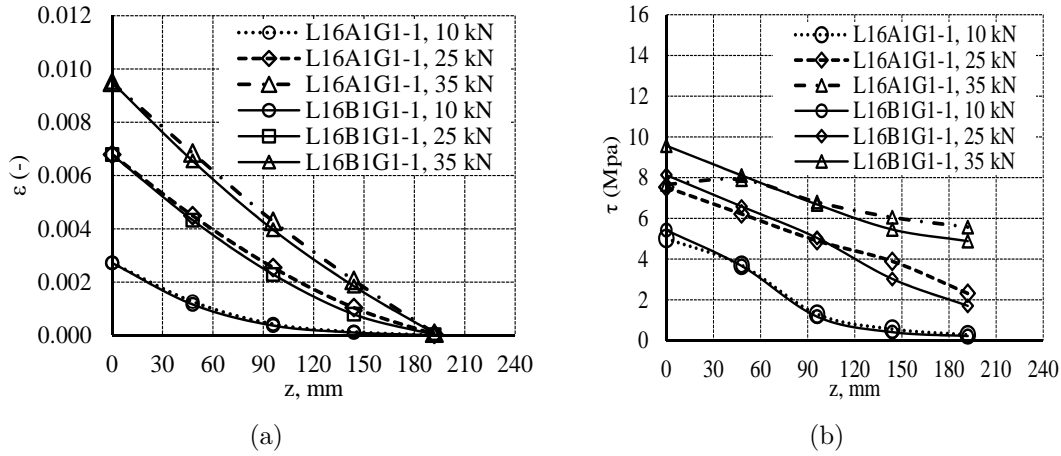


Figure 5.14: Effect of adhesive type on the: (a) strain distribution and (b) bond stress distribution.

purposes only a length of 192 mm starting from the loaded end is represented for both specimens). The bond length has marginal effect on the strain distribution of specimens with C1 bars bonded with epoxy B due to bar-epoxy interface failure (see Fig. 5.15a). However, the bond shear stress obtained in specimen with bond length of 192 mm is slightly higher than that recorded in specimen with bond length of 240 mm, and this tendency increases with the pullout load (see Fig. 5.15b). Fig. 5.8a shows that the local bond stress law of L16B1C1 is a little bit stiffer than the one of T16B1C1. This aspect together the fact that a larger bond length favor the occurrence of larger slip for a certain load level, justify the higher bond stress determined in the former specimen.

5.6.4 Detailed comparisons of the numerical results for specimens with CFRP and GFRP bars

Using the FE model, the tangential component of bond shear strength, τ , and the radial component of tensile stress in concrete, σ_{ct} , are obtained along the bond length and in the first elements (interface and concrete elements) located at the loaded end. Fig. 5.16a and b show the evolution of the relationship τ/τ_{max} (τ_{max} is the maximum bond shear strength) along the bond length at several load levels for specimens L16A1C1-1 and L16A1G1-1, respectively. The figure shows that the

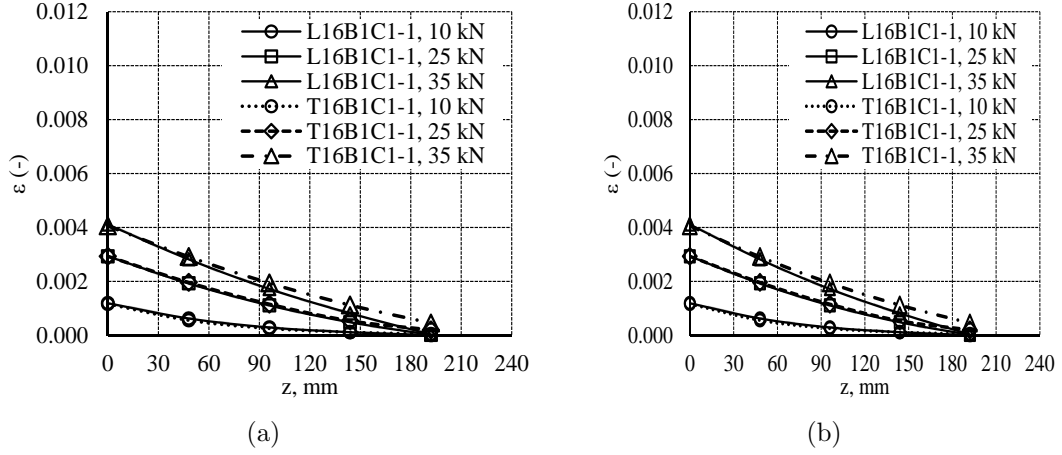


Figure 5.15: Effect of bond length on the: (a) strain distribution and (b) bond stress distribution.

bond stress near the loaded end reached its maximum value, τ_{max} , at 75% of the maximum load of each specimen, when the slip at the loaded end reached s_{max} (Fig. 5.4a). By increasing the loaded end slip during the pullout test simulation, the bond stress, τ , at the loaded end decreases because the local stresses in that part of the reinforcement are in the descending branch of the $\tau - s$ law, while the bond stress increases near the free end until the maximum load of the joint is attained ($F/F_{max} = 1.0$). When maximum load is attained, the slip at the loaded end of the $\tau - s$ law reaches its ultimate value, s_{ult} (Fig. 5.4b).

From the numerical simulations, the stress component in the surrounding concrete, orthogonal to the FRP alignment, σ_{ct} , is obtained in the first bonded finite element closest to the reinforcement at the loaded end (Fig. 5.17). σ_{ct} is calculated by averaging the stress components in the x direction (i.e. dir.2, Fig. 5.2) of the four integration points of this element. The variation of this stress component aims to reproduce the radial stress field in the loaded zone. Figs. 5.18a and b show the distribution of tangential stress, τ , and radial stress, σ_{ct} , in concrete versus the loaded end slip, s , for the specimens L16A1C1-1 and L16A1G1-1, respectively. σ_{ct} has the same trend of τ because the bond behaviour is fully described by the interface finite element (defined by Eq. 5.1), and reaches its maximum values at slip of 0.75 and 1.5 mm for the two specimens L16A1C1-1 and L16A1G1-1, respectively. On the other hand, Figs. 5.19a and b illustrate the $\sigma_{ct}/f_{ctm} - F/F_{max}$ relationship reported for the

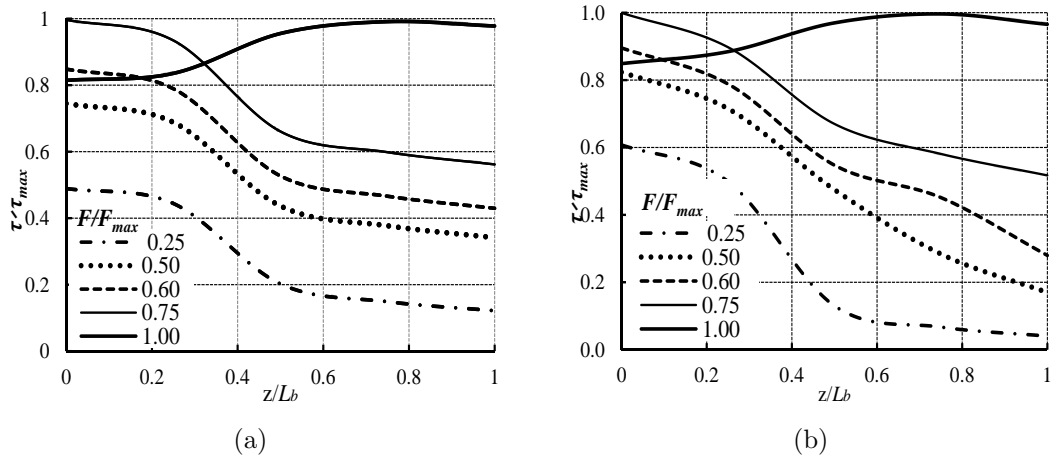


Figure 5.16: Longitudinal bond stress distributions along the bond length for specimens of NSM FRP bars: (a) L16A1C1-1 and (b) L16A1G1-1.

same finite element (Fig. 5.17) for the two specimens L16A1C1-1 and L16A1G1-1, respectively. It is seen that the tensile concrete stress does not reach the tensile concrete strength ($f_{ctm} = 2.0$ MPa).

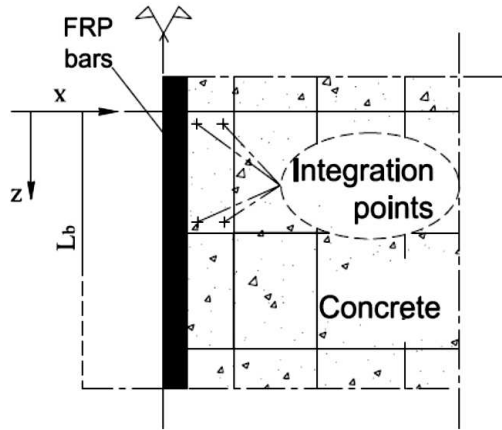


Figure 5.17: Scheme for the calculation of tensile stress in the concrete in the transverse plane.

Fig. 5.20a and b show the distribution of the radial stress in the concrete, σ_{ct} , along the whole bonded length (Fig. 5.17) at a load equal to $0.75 F_{max}$ (τ reached τ_{max} at the loaded end, Fig. 5.16) for specimens L16A1C1-1 and L16A1G1-1. The radial tensile stress in the concrete is positive (i.e. tensile stress) near the loaded end.

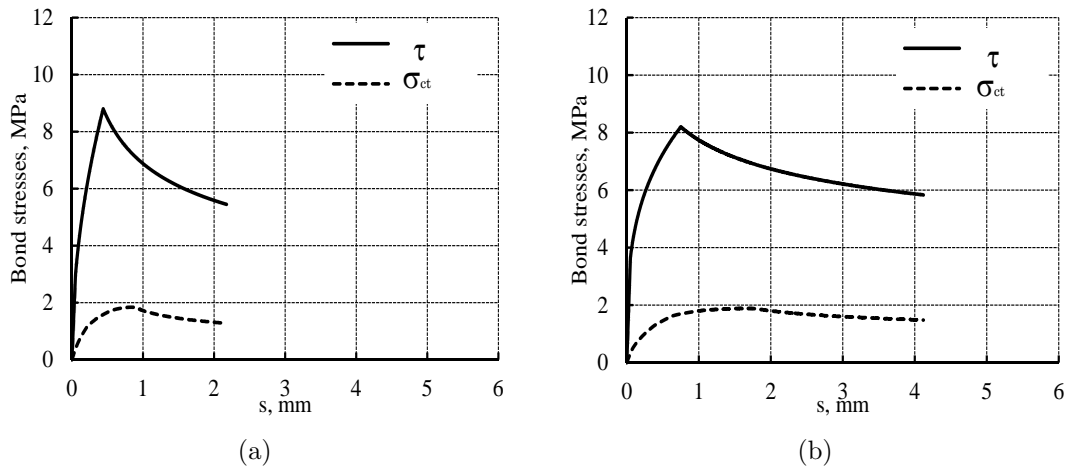


Figure 5.18: Distribution of bond shear stress in the first interface element and tensile stress in the first concrete element at the loaded end: (a) L16A1C1-1 and (b) L16A1G1-1.

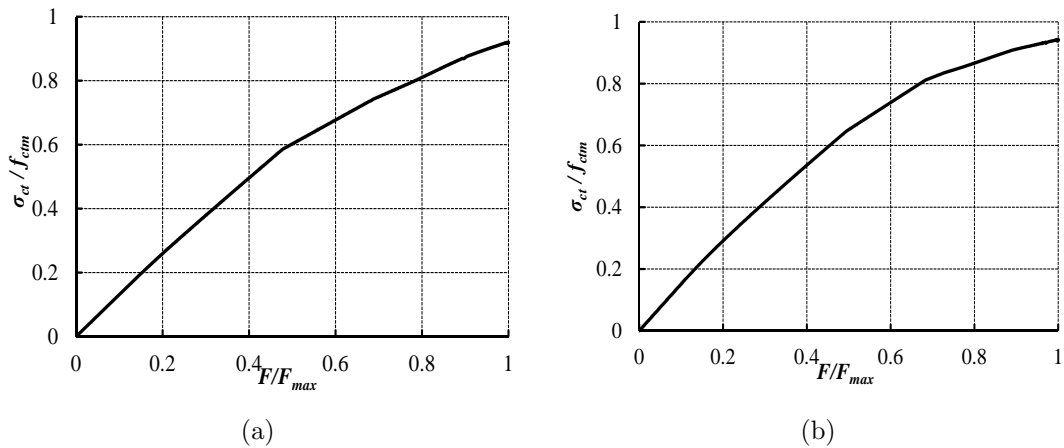


Figure 5.19: Theoretical distribution of normalized tensile stresses in the concrete: (a) L16A1C1-1 and (b) L16A1G1-1.

At a distance of approximately 102 mm σ_{ct} became negative (i.e. compressive stress), with a stress gradient in the free end zone similar to the one registered in the loaded end zone. In Figs. 5.21a and b, the same stress distribution is plotted along the bond length for the entire thickness of the concrete block with a color contour map for the two specimens L16A1C1-1 and L16A1G1-1, respectively. This compressive stress field in the concrete surrounding the FRP bar causes a confinement effect

on the FRP bar that contributes for the better bond performance of NSM systems when compared to the EBR ones. The obtained results indicate that no concrete cracking occurs in the investigated types of NSM bars, which is in agreement with the type of failure modes observed: bar-epoxy interface; epoxy splitting.

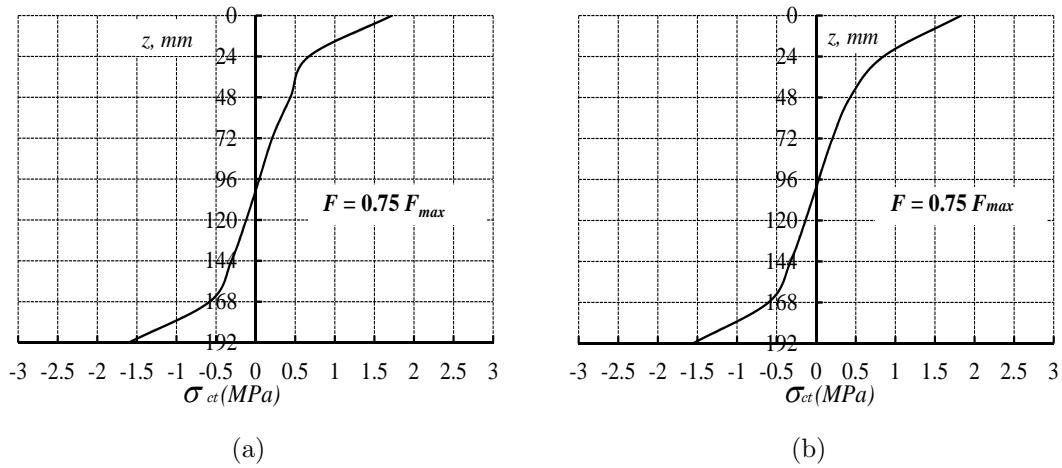


Figure 5.20: Distribution of σ_{ct} along the bonded length ($F = 0.75F_{max}$ at 1st interface element): (a) L16A1C1-1 and (b) L16A1G1-1.

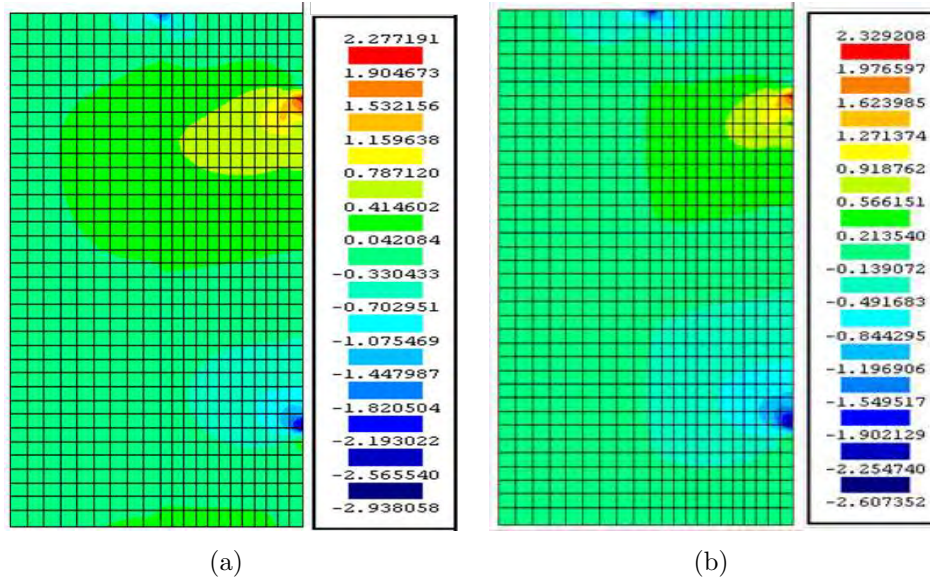


Figure 5.21: FEMIX output (drawmesh) of σ_{ct} along the bonded length ($F = 0.75F_{max}$ at 1st interface element): (a) L16A1C1-1 and (b) L16A1G1-1.

5.7 Conclusions

FEM-based modelling of NSM FRP bond behaviour was used to perform an inverse analysis to derive the local bond stress slip law from experimental results obtained in direct pullout tests. The methodology was found to be suitable to analyze and compare the bond behaviour of various types of NSM FRP bars, as well as to assess the influence of relevant parameters. From the analysis performed in this study, the following conclusions can be drawn:

- The obtained local bond slip, $\tau - s$, equations were found to be capable of simulating the global behaviour of all the tested specimens with various types of NSM bars, epoxy properties, concrete strengths and bond lengths.
- The larger the elasticity modulus of the adhesive, the higher the axial stiffness of the compressive micro-struts formed into the adhesive, which leads to a stiffer and strong bond connexion.
- The strength and stiffness of the local bond law (given through the values of τ_{max} and s_{max}) increase with the tensile strength and modulus of elasticity of the adhesive, while parameters α and α' defining the shape of the pre and post-peak branches are not significantly affected.
- The two types of CFRP bars, C1 and C2, that have the same axial stiffness, developed similar bond law with slight difference in the maximum bond stress value, τ_{max} , and in the post-peak bond stress decay. This difference may be attributed to the thicker epoxy layer surrounding the bar for the case of NSM C1 than that surrounding the NSM C2 bars.
- Specimens reinforced with C1 bars bonded with epoxy B developed similar bond law for the two bond lengths, 192 and 240 mm. The main difference is attributed to the slight increase in the value of the slip at maximum stress, s_{max} , (0.175 mm) in the specimen with larger bond length.
- As the concrete strength increases, the values of the parameters, α and α' , decrease, due to the smaller deformability and higher confinement provided by the concrete surrounding the bond zone. Due to the same reason, by

increasing the concrete strength s_{max} has tendency to slightly decrease, while in the CFRP specimens the τ_{max} tends to increase moderately.

- The local bond stress slip law of NSM GFRP bars is characterized by higher values of s_{max} and lower values of α and α' , than those of NSM CFRP bars, while τ_{max} is similar. The more ductile response of the specimens reinforced with GFRP bars can be attributable to the smaller axial stiffness. The ribs composing the surface of the GFRP bars might have contributed to the formation of micro-compressive struts in the adhesive, which increased the FRP confinement during the pullout process, resulting a more ductile pullout response for the specimens strengthened with GFRP bars.
- Taking the strain results obtained in the unique instrumented specimen (L12A2C1) it was observed that the model was capable of simulating with good accuracy the strain variation along the bond length.
- The radial stress in concrete, σ_{ct} , was tensile near the loaded end, and compressive near the free end zone. The σ_{ct} did not exceed the maximum tensile strength of ($f_{ctm} = 2.0$ and 3.0 MPa for concrete 1 and concrete 2 respectively). The compressive stress field in the concrete provides certain confinement to the FRP bar, which contributes for the better bond performance of the NSM systems in comparison to the EB ones.

Part II

Study of the flexural behaviour of RC beams strengthened using NSM FRP bars/strips

Chapter 6

Flexural test experimental programme

6.1 Introduction

An experimental programme was developed to study the flexural behaviour of reinforced concrete (RC) beams strengthened with near surface mounted (NSM) fibre reinforced polymer (FRP) reinforcement. In the following section (section 6.2) the details of the test matrix of the experimental programme and specimen's preparation are explained. In section 6.3 the flexural test setup is illustrated. The full details of the test instrumentation are reported in section 6.4. In section 6.5, strengthening with the NSM carbon fibre reinforced polymer (CFRP) reinforcement (bars and strips) and glass fibre reinforced polymer (GFRP) bars is described. Finally the material properties used in the experiments are reported and discussed in section 6.6.

6.2 Test specimens preparation

A total of twenty four RC beams with rectangular cross section were constructed and tested, being one of them a control beam without strengthening and the others having different strengthening systems. The tests were prepared and tested in three series. The first series consists of a control beam and seven beams strengthened with NSM GFRP and CFRP bars with limited bond length of 2000 mm. The second series

consists of eight beams strengthened with NSM FRP reinforcements (i.e. CFRP bars /strips and GFRP bars) having a limited bond lengths. In the third series, the RC beams are strengthened with partially bonded NSM FRP reinforcements.

6.2.1 RC beams and internal reinforcement

All the beams have rectangular cross sections of 160 mm wide and 280 mm height. The total length of the beam is 2600 mm. The basic shape and dimensions of the RC beam are shown in 6.1. The bottom tension reinforcement consisted of two 12 mm in diameter deformed steel bars. The ratio of bottom tensile reinforcement ($\rho = A_s / b_w \times d_s$) was 0.005. The tension reinforcement ratio is selected to be similar to that in the field of construction ($\rho_{min} = 0.00362$, $\rho_{max} = 0.0788$). The tensile reinforcement ratio is selected to be in the range of values used in practice. The beams were reinforced in compression with two 8 mm in diameter deformed steel bars. The shear reinforcement consisted of steel stirrups of $130 \times 220 \text{ mm}^2$, 8 mm 8 mm in diameter, spaced at 100 mm except at the middle of the beam as shown in Fig. 6.1.

6.2.2 Specimen casting and curing

Steel moulds were used for casting the RC beams. For each beam series, the moulds were prepared to accommodate the reinforcement cages. The reinforcement cages were carefully placed inside the moulds. Plastic spacers were used to allocate the reinforcement cage at the correct bottom and side distance from the moulds. Fig. 6.2 shows the appearance of the mould, cage and mould with the reinforcement cage inside ready for casting. The eight beams of each series were cast in the same batch together with several cylinders to determine the concrete mechanical properties. During the casting, the concrete was vibrated using a mechanical vibrator.

Just after casting, the top concrete surface was leveled. Figs. 6.3a to c show the procedure of casting for beams and cylinders. All elements (beams and cylinders) were covered with plastic sheets (Fig. 6.3d). Beams and cylinders were demoulded two days after casting and covered with wet cotton and plastic sheets until the age of seven days. At 33-36 days since casting the grooves were cut and the beams and cylinders were kept in the same environmental conditions until testing.

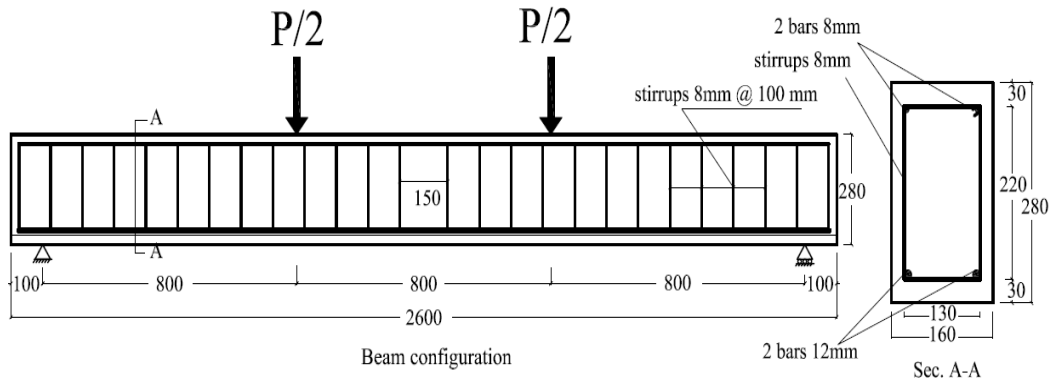


Figure 6.1: Dimensions and reinforcement details of the RC beam.



(a) Mould and reinforcement cage

(b) Cage inside the moulds

Figure 6.2: Appearance of the mould and reinforcement.



(a) Casting



(b) Leveling



(c) Cylinders



(d) Curing

Figure 6.3: Procedure of casting and curing for beams and cylinders.



Figure 6.4: Formation of the grooves in the tension side of beams.

6.2.3 Groove preparation and bonding of the NSM reinforcement

The grooves were formed by making two saw cuts and using a manual hammer to complete the groove formation (Fig. 6.4). Four sizes of grooves were performed depending on the size of the NSM reinforcement. Grooves with sizes $16 \times 16 \text{ mm}^2$ and $24 \times 24 \text{ mm}^2$ were cut for the FRP bars of diameter 8 and 12 mm respectively. On the other hand, grooves with sizes $9 \times 16 \text{ mm}^2$ and $5 \times 25 \text{ mm}^2$ were cut for the FRP strips $2.8 \times 10 \text{ mm}^2$ (i.e. two strips of size $1.4 \times 10 \text{ mm}^2$ were bonded together to form one strip of size 2.8×10^2) and $1.4 \times 20 \text{ mm}^2$ respectively. Fig. 6.5 shows the full details and locations of the grooves for the strengthened beams. The bonding of FRP bars was discussed in detail in section 3.3.3 for pullout specimens while the bonding of strips followed the procedure discussed in section 2.4. The bonding procedure of NSM reinforcement in this study is illustrated in Fig. 6.6.

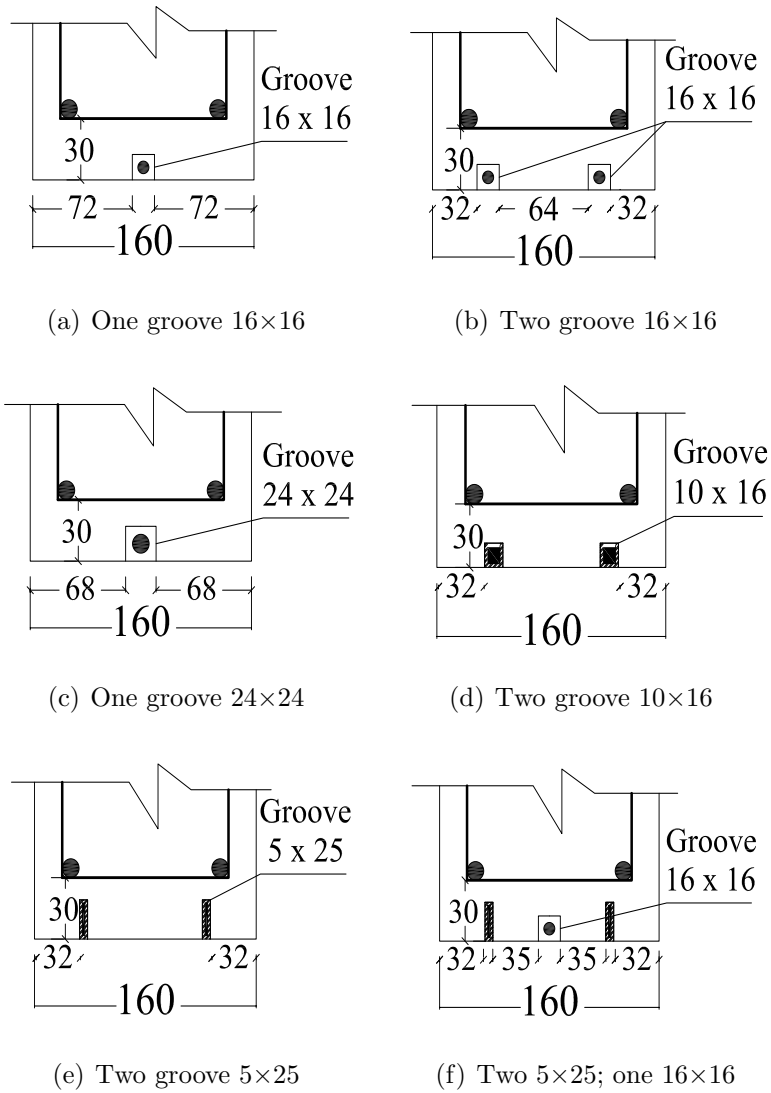


Figure 6.5: Full details and locations of the grooves for the strengthened beams.

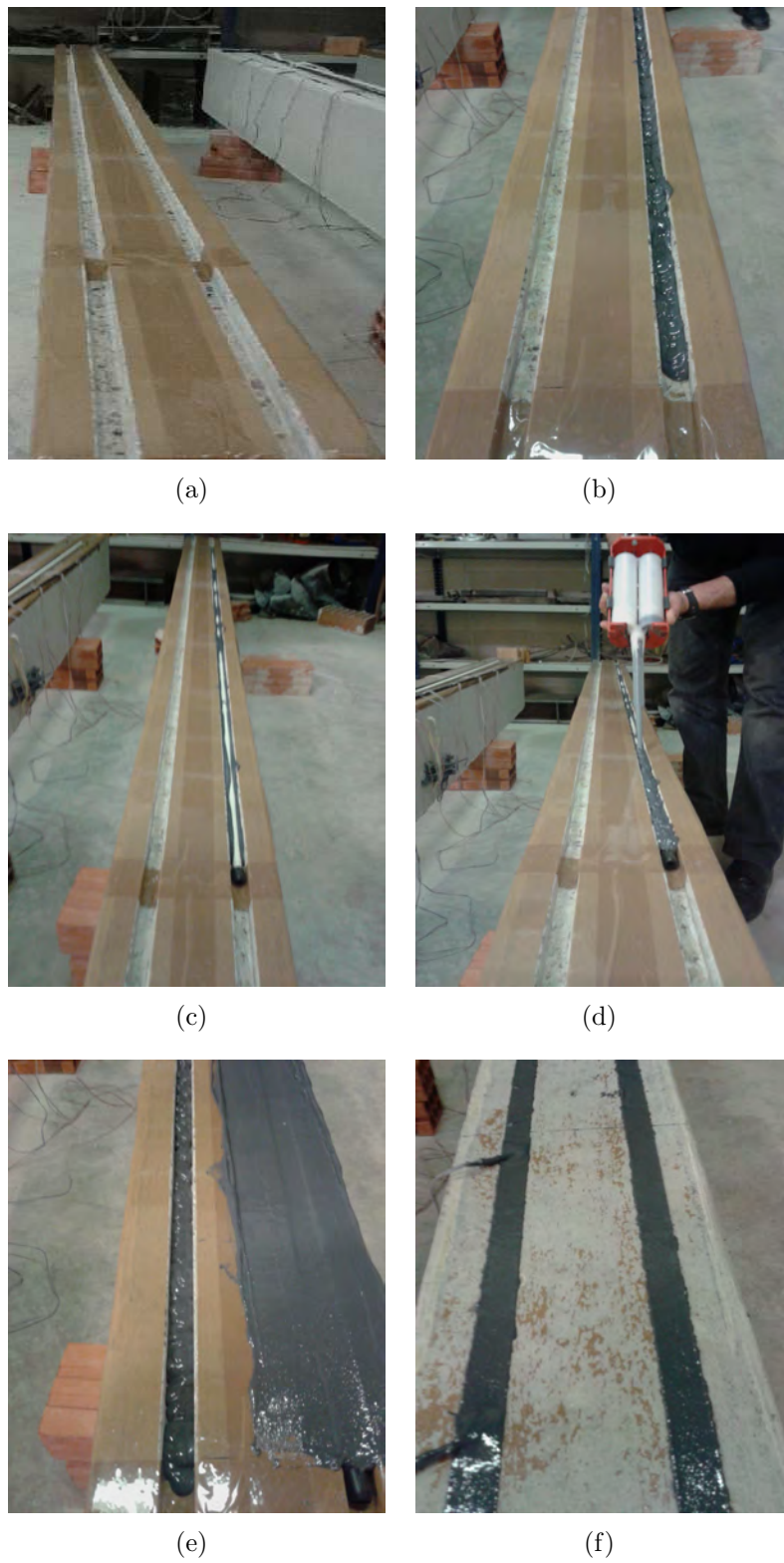


Figure 6.6: Steps of NSM installation in the grooves of the RC beams.

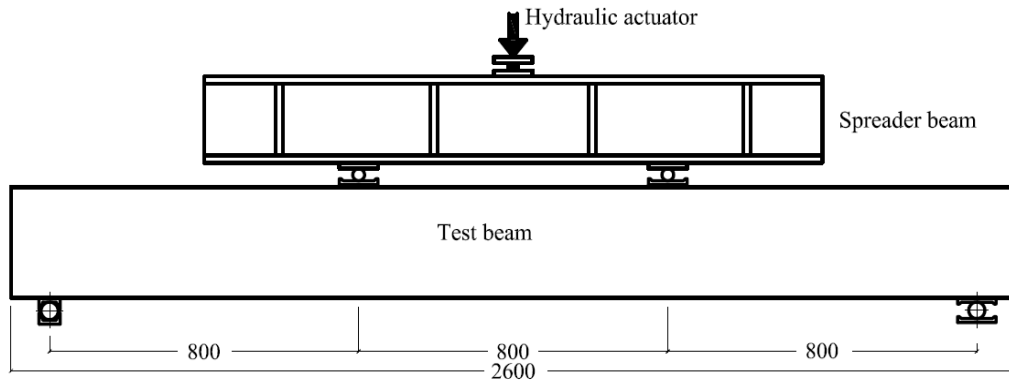


Figure 6.7: Flexural test setup.

6.3 Test setup

All the tested beams were tested under a static four-point load test to study their flexural behaviour and ultimate load capacity. A servo controlled hydraulic jack with a capacity of 300 kN was used to apply the load to the beam through a spreader steel beam (HEB-160). The load was applied in displacement control mode at a rate of 0.6 mm/min, and all data were collected by a data acquisition system. The test setup is shown in Fig. 6.7. The beam was carefully placed over the supports and all the instrumentation was positioned and connected to the data acquisition system. The data were monitored in real time and were downloaded digitally to a PC. Every second, a minimum of two data were recorded.

6.4 Instrumentation

Fig. 6.8 shows a detailed drawing of the beam instrumentation. Seven vertical transducers were used to measure the deflection of the beam. Two additional horizontal transducers were used to measure the free end slips of the NSM reinforcement. Strain gauges were also used to measure strains in NSM FRP reinforcement, internal steel reinforcement, concrete and epoxy. The instrumentation details are described in the following.

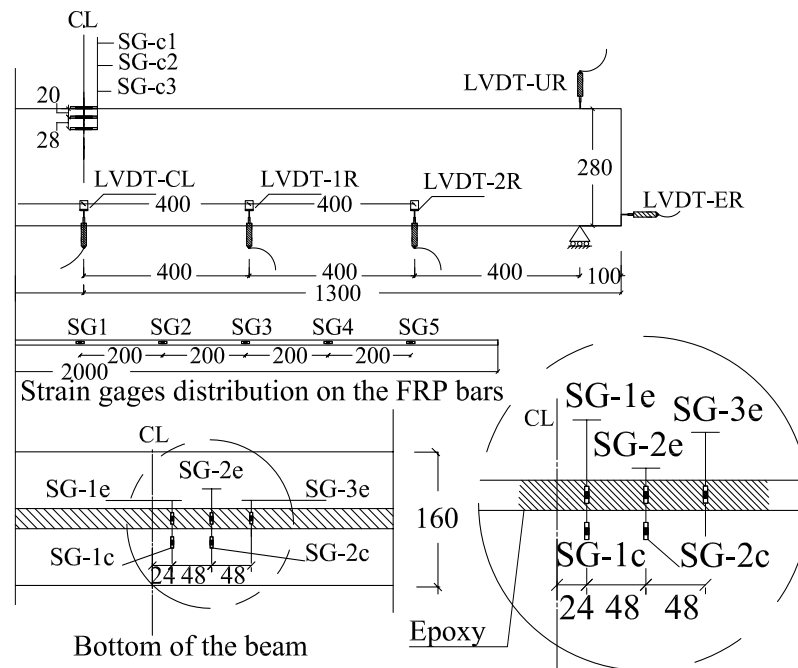


Figure 6.8: Sketch of the tested beams instrumentation.

6.4.1 Deflections at different locations of the beam

In order to measure the deflection of the tested beams, seven vertical transducers (linear variable differential transformers LVDTs and strain gauge based transducers) were used (see Figs. 6.8 and 6.9). The transducers on the supports were Vishay HLS10B type, with a displacement range of 11.2 mm. The transducer at mid-span was a Vishay HS100B type, with a displacement range of 102 mm. All transducers were attached to vertical metallic elements and fixed in vertical position during the test. In all beam series, the needles of the transducers measuring the deflection were positioned on aluminium angles glued to the side of the tested beam Fig. 6.9).

6.4.2 Rotations and mean curvatures in the central zone

Two inclinometers were placed on both sides of the pure bending zone, each one located at 400 mm from the midspan section, and at a height of 50 mm from the top surface of the beam specimen.



Figure 6.9: Arrangement of the vertical transducers and inclinometers.

This configuration allowed sectional rotations to be measured and the average curvature of the pure bending zone to be calculated. The inclinometers used had a measurement range of $\pm 10^\circ$, a sensitivity of 9.6 mV/degree. Both inclinometers were glued to steel sheets that were carefully placed on the correct position of the beam (Fig. 6.9).

6.4.3 Concrete strains on the mid-span section surface

All the tested specimens were instrumented with three concrete strain gauges bonded on the surface of the mid-span section (Fig. 6.8). These strain gauges were evenly distributed along the height of the theoretical concrete compressive block (one on the top surface, one 20 mm from the top and one 48 mm from the top) to quantify the evolution of the concrete strain with load.

The concrete strain gauges used in the experimental programme were type PL-60-11 from TML, with the following characteristics: wire-type, three-wired, with a



Figure 6.10: Arrangement of the concrete strain gauges in the mid-span top section.

resistance of 120Ω , a gauge factor of $2.12 \pm 1\%$, a gauge length of 60 mm and a gauge width of 1 mm with a maximum strain of 2%. The strain gauges were bonded to the previously treated surface of the beam with HBM X-60 two components adhesive.

6.4.4 Concrete and epoxy strains on the bottom of the beam

Some of the tested specimens were instrumented with three strain gauges bonded on the surface of the epoxy paste while another two strain gauges were glued on the concrete surface near the grooves. The strain gauges were used to record the transverse strains both in epoxy paste and in concrete. The arrangement of those strain gauges is shown in Fig. 6.8.

6.4.5 Strains along the NSM FRP reinforcement

In each beam one on the bars used as NSM FRP reinforcement was instrumented with strain gauges bonded on its surface. The arrangement of the strain gauges is shown in Fig. 6.8. The main aim of this instrumentation was to register the NSM FRP strains at different locations, in order to study the influence of cracks on the NSM FRP strain and to obtain bond profiles. Five of the gauges were evenly distributed over the bond length as shown in Fig. 6.11. The FRP strain gauges used in the experimental programme were type 6/350LY41 from HBM, with the following characteristics: wire-type, three-wired, with a resistance of $350 \pm 0.3 \Omega$, a gauge factor of $2.04 \pm 1\%$, a gauge length of 6 mm and a gauge width of 2.7 mm with a



Figure 6.11: Strain gauges on the NSM bars.

maximum strain of 5%. The strain gauges were bonded to the FRP surface with HBM Z70 single component adhesive made of cyanocrylate. Prior to bonding the strain gauge, the surface of the bar was treated and the minimum height of rib was mechanized at each location (Fig. 6.11). A HBM SG250 transparent silicon rubber was applied as a protective coating to isolate the gauges from humidity and alkaline environment of concrete.

6.5 Strengthening of RC beams

6.5.1 Overview

The test programme was planned to test the three series at the same age. Two types of FRP materials (carbon and glass) were used in all groups. In the first series seven beams were strengthened with NSM FRP bars. In this series, one size of CFRP bars (8 mm in diameter) and two sizes of GFRP bars (8 and 12 mm in diameter) were used. In the second series, eight beams were strengthened with FRP bars and strips. The strengthening elements consisted of one size of CFRP bars (8 mm in diameter), two sizes of GFRP bars (8 and 12 mm in diameter), two sizes of CFRP strips ($1.4 \times 10 \text{ mm}^2$ and $1.4 \times 20 \text{ mm}^2$) and high strength and high modulus unidirectional CFRP sheets (thickness = 0.117 mm). In the third series, eight beams were strengthened with partially bonded FRP bars and strips. The

CFRP bars used in the experimental programme were selected to have similar axial stiffness ($E_f A_f$) to the CFRP strips for comparison purposes. Material properties of the CFRP strips and bars obtained from characterization tests and those provided by manufacturers are summarized in Table 6.1 while their surface treatment are shown in Fig. 6.12.

Two types of epoxy adhesive (BASF and ROBERLO) were used for bonding the FRP reinforcements to the concrete. The identification of the tested specimens is as follows: the first letter indicates the beam state (S = partially bonded length of 384 mm, M = partially bonded length of 480 mm and L = limited bond length of 2000 mm); the following letter indicates the type of epoxy (A = BASF and B = ROBERLO), the following digit indicates the number of NSM FRP reinforcement, the following two characters indicate the type of bar (C = carbon bar, G = glass bar, S = carbon strip, 1 = type 1, 2 = type 2). Finally, the last characters (when applicable) indicate the applied modification of the NSM-concrete interaction introduced (+C1, +G1 = one addition NSM bar was added, T = transverse sheets, IS = mechanical interlocking with shear connectors and ES = end supporting steel tubes.

Table 6.1: FRP properties.

FRP ID	FRP type	d_b (mm)	$w \times h$ (mm ²)	$f_{fu}^{(f)}$ (MPa)	f_{fu} (MPa)	$E_f^{(f)}$ (GPa)	E_f (GPa)	Surface treatment
C1	CFRP	8	-	2200- 2500	3350	158- 165	170	SST
S1	CFRP	-	1.4×10	2500	-	165	-	SS
S2	CFRP	-	1.4×20	2500	-	165	-	SS
G1,G2	GFRP	8,12	-	1000	1350	60	64	GR

SST = smooth surface texture, SS = smooth surface, GR=grooves, (f) = from manufacturer.

6.5.2 The first series

Fig. 6.13 shows the strengthening scheme of the beams of this series. Two beams (LB1C1 and LB1G1) were strengthened with one NSM C1 and G1 bar respectively to study the effect of the type of NSM bars. Two beams (LB2C1 and LB2G1)

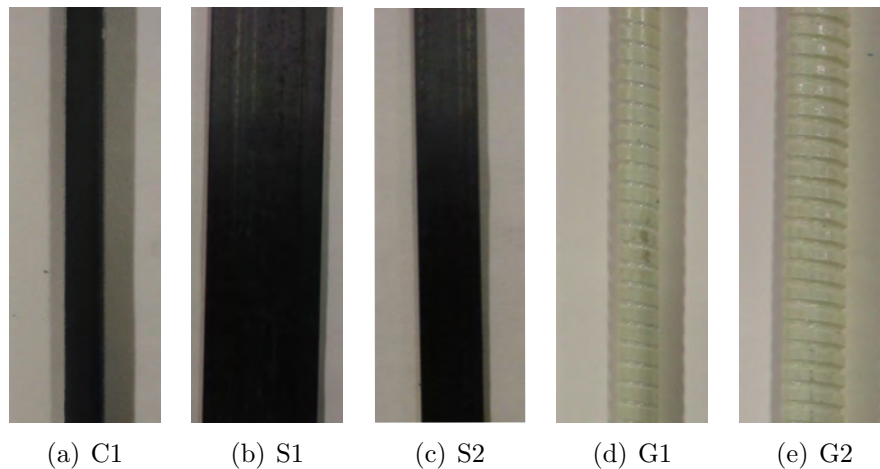


Figure 6.12: Surface treatment of the FRP reinforcement used in the flexural test.

strengthened using two NSM C1 and G1 bars respectively were tested to study the effect of number and type of NSM bars on the flexural behaviour. On the other hand, to study the effect of epoxy type on the maximum capacity and behaviour of the beams, two more beams (LA2C1 and LA2G1) strengthened with two NSM C1 and G1 bars respectively, bonded with epoxy A were tested. To study the effect of NSM strengthening arrangement, one beam (LB1G2) strengthened with one NSM G2 bar bonded with epoxy B was tested. Finally, one beam without strengthening was tested as control beam (CB). The test specimens' configuration of the eight tested beams included in this series is indicated in Table 6.2.

6.5.3 The second series

Fig. 6.14 shows the strengthening scheme of the beams of this series. Eight RC beams were prepared and strengthened with limited bond length of NSM FRP reinforcement (bars /strips, $L_b = 2000$ mm). The beams configurations' are shown in Table 6.3. The beam LB2S1 was strengthened with two strips S1 while beam LB2S2 was strengthened with four strips S2 used in pairs bonded together to study the effect of NSM dimensions compared to that of the beam L1BC1. To study the effect of the area of the NSM reinforcements and cut off effect, the two beams LB2C1IS and LB2C1T were studied and compared with beam LB2C1. The three beams (LB2C1, LB2C1IS and LB2C1T) were strengthened with two NSM C1 bars.

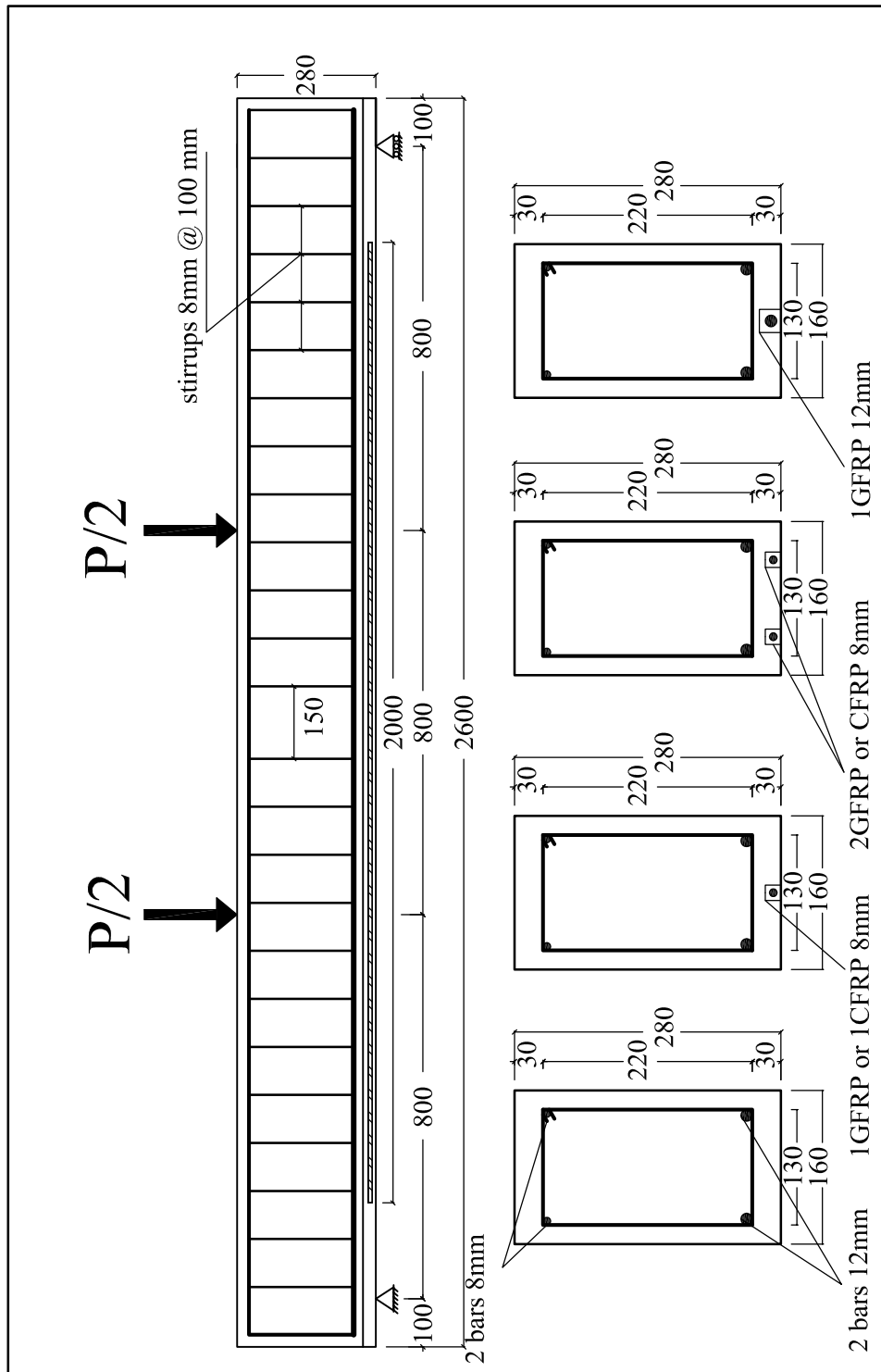


Figure 6.13: Strengthening scheme of the beams in the first series.

Table 6.2: Test specimens' configuration of the first series.

Beam ID	d_b (mm)	N_b (-)	FRP type	Epoxy type	Test variable
CB	-	-	-	-	CB
LB1C1	8	1	CFRP	B	Strengthening
LB1G1	8	1	GFRP	B	FRP type
LB2C1	8	2	CFRP	B	NSM area
LB2G1	8	2	GFRP	B	NSM area
LB2C1	8	2	CFRP	A	Epoxy type
LB2G1	8	2	GFRP	A	Epoxy type
LB1G2	12	1	GFRP	B	NSM arrangement

d_b = Diameter of the NSM bar, N_b = Number of NSM FRP bars.

For beam LB2C1IS (Fig. 6.15), transverse interlocking $16 \times 16 \text{ mm}^2$ were cut to introduce transverse interlocking, as well as confinement through vertical drilled holes of 10 mm in diameter and 200 mm in depth in which steel bars were installed using epoxy paste. For beam LB2C1T transverse wrapping was used (see Figs. 6.15 and 6.16) to confine the cut off zone. To apply the transverse wrapping to the strengthened beams, the surface of concrete was cleaned and roughened and then the CFRP sheets were bonded as shown in see Fig. 6.18.

To study the combined effect of different NSM FRP reinforcement having similar and dissimilar materials and shapes, the beams LB2S1+C1 and LB2S1+G1 were tested. Moreover, to study the effect of FRP material, mechanical interlocking and transverse wrapping on the bond behaviour, load capacity and the mode of failure of the strengthened RC beams the two the beams LB1G2IS and LB1G2T were tested and compared with beam LB1G2 (all these beams had one NSM G2 bar).

For the beam LB1G2IS, grooves of $16 \times 24 \text{ mm}^2$ were cut to introduce transverse interlocking, as well as confinement through vertical drilled holes of 10 mm in diameter and 200 mm in depth in which steel bars were installed using epoxy paste. For the beam LB1G2T transverse wrapping was used as shown in see Figs. 6.15 and 6.16. All the results of the previous beams were also compared with those of the CB tested in the first series.

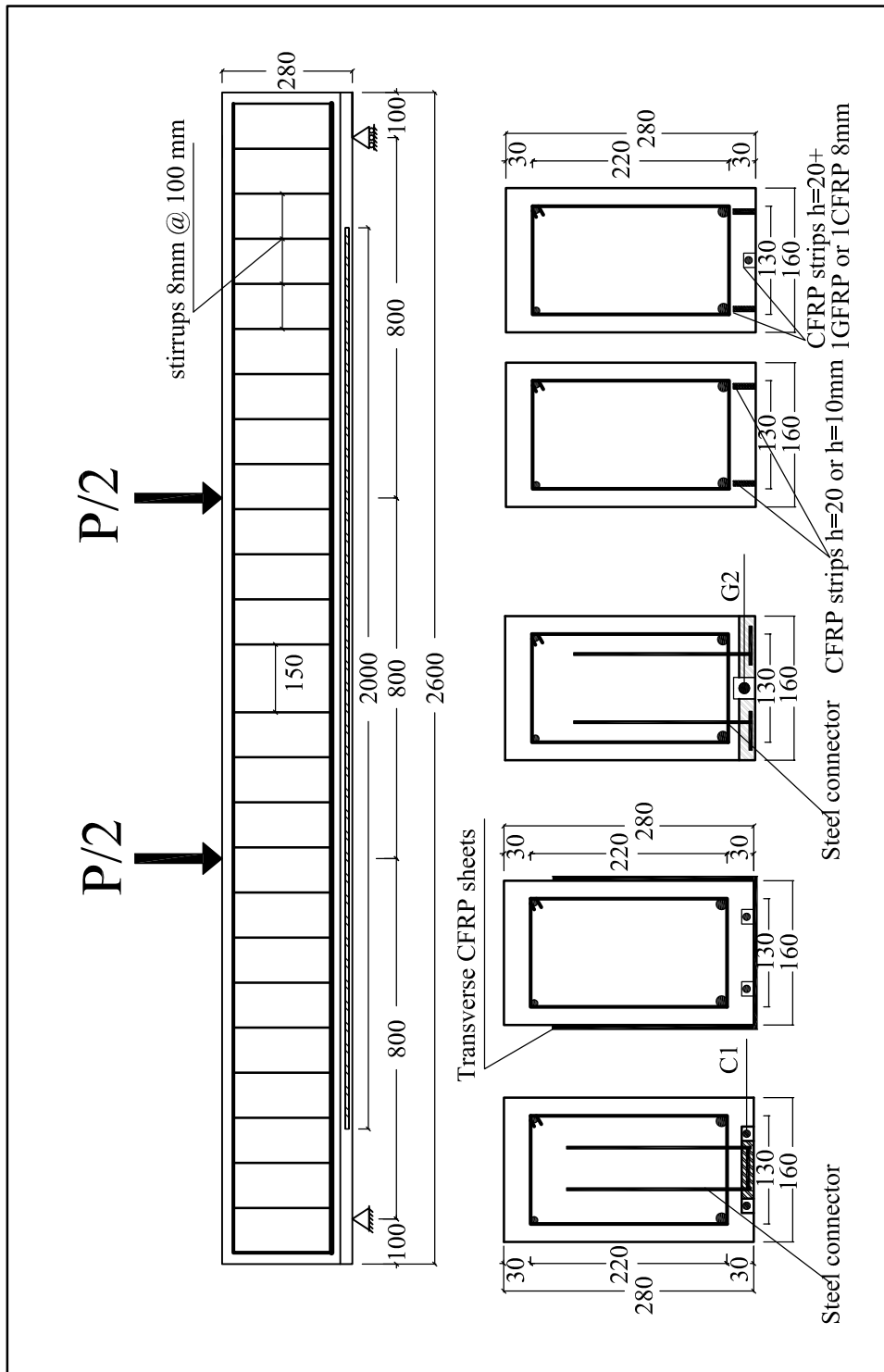


Figure 6.14: Strengthening scheme of the beams in the second series.

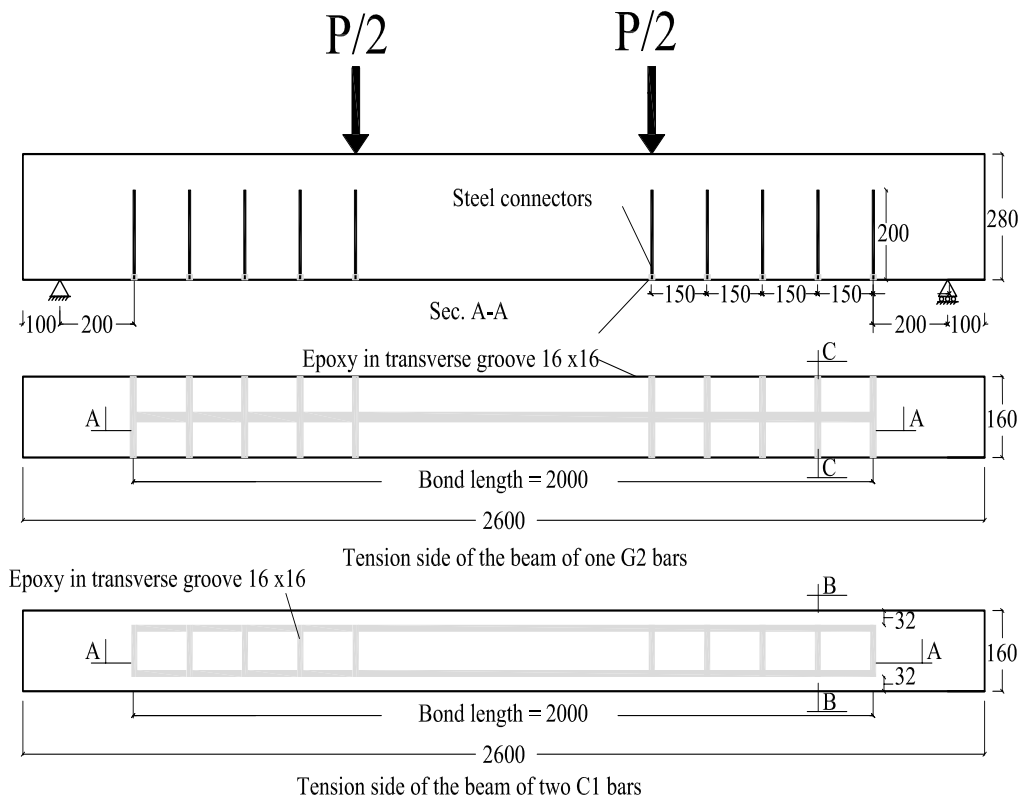
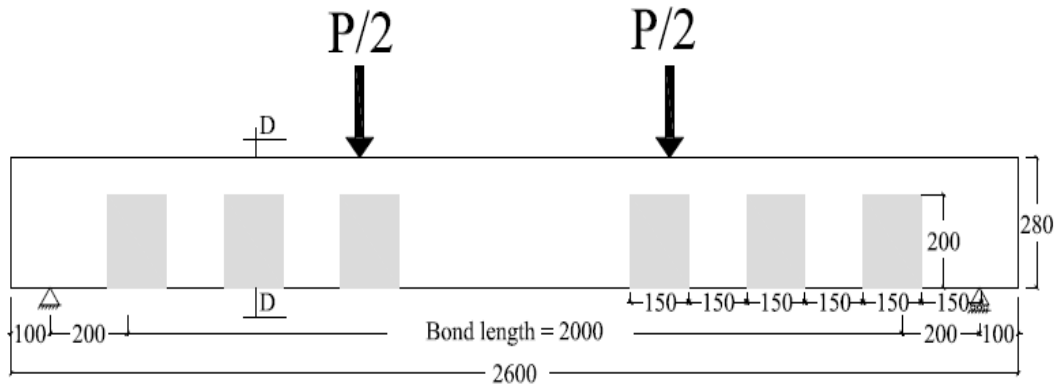


Figure 6.15: Strengthening scheme of the beams with T and IS.

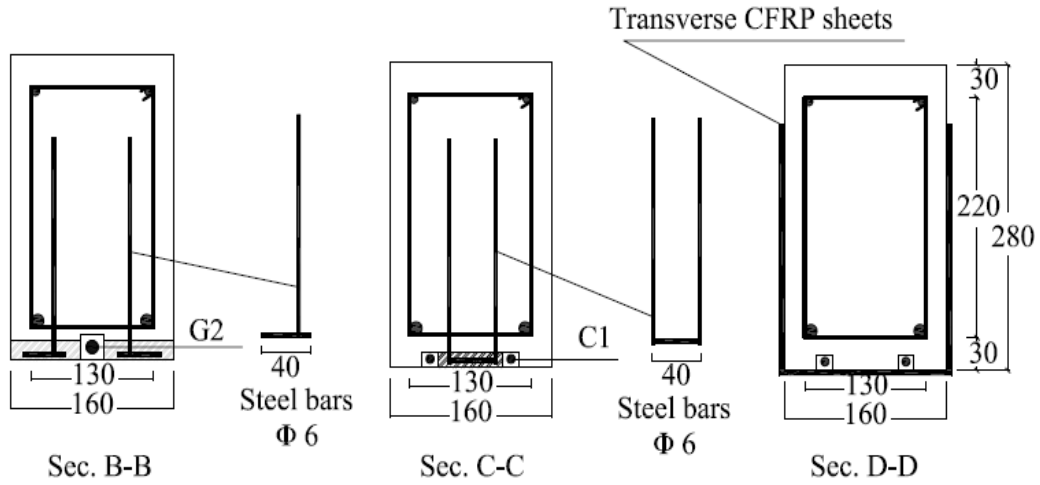


Figure 6.16: Details of the sections of the beams with T and IS.

Table 6.3: Test specimens' configuration of the second series.

Beam ID	d_b (mm)	$w \times h$ (mm ²)	N_b (-)	N_s (-)	FRP type	Test variable
LB2S1	-	2.8×10	-	2	CFRP	FRP shape
LB2S2	-	1.4×20	-	2	CFRP	FRP dimensions
LB2C2IS	8	-	2	-	CFRP	IS
LB2C1T	8	-	2	-	CFRP	T
LB2S2+C1	8	1.4×20	1	2	CFRP	NSM- arrangement
LB2S2+G1	8	1.4×20	1	2	CFRP+GFRP	
LB1G2IS	12	-	1	-	GFRP	IS
LB1G2T	12	-	1	-	GFRP	T

T = Transverse wrapping, N_s = Number of NSM FRP strips, N_b = Number of NSM FRP bars and IS = Mechanical interlocking with shear connectors.

6.5.4 The third series

Fig. 6.17 shows the strengthening scheme of the beams of this series and the detailed configuration of the strengthened section. Two beams, SB2C1 and SB2G1, were strengthened with two NSM C1 and G1 bars respectively with partially bonded length of 384 mm ($48d_b$). Two beams, MB2C1 and MB2G1, were strengthened with two NSM C1 and G1 bars respectively with partially bonded length of 480

mm ($60d_b$). The effect of NSM reinforcement shape on the flexural capacity of the strengthened RC beams with partially bonded length were introduced by testing the beam MB2S1. Moreover the beam MB1G2 was strengthened with one NSM G2 with partially bond length of 480 mm ($40d_b$) was also tested to study the effect of size and materials of the FRP bars. Another beam MB1G2T strengthened with one NSM G2 with partially bond length of 480 mm, $40d_b$, and transversely strengthened using CFRP sheets was tested to study the effect of the transverse confinement.

To study the effect of end supporting of the partially bond length on the behaviour of the strengthened RC beams, the beam MB2C1ES ($L_b = 60d_b$) was prepared and tested. In this beam (Fig. 6.18) steel tubes were bonded to the end of the NSM bars. The steel tubes were supported to steel plates using steel screws. The steel plates were connected to the concrete beam through steel connectors bonded in drilled holes as shown in Fig. 6.18. The detailed information of the eight tested beams included in this series is reported in Table 6.4.

Table 6.4: Test specimens' configuration of the third series.

Beam ID	d_b (mm)	$w \times h$ (mm ²)	N_b (-)	N_s (-)	FRP type	$L_b(nd_b)$ (mm)(-)	Test variable
SB2C1	8	-	2	-	CFRP	384($48d_b$)	Bond length
SB2G1	8	-	2	-	GFRP	384($48d_b$)	L_b + FRP type
MB2C1	8	-	2	-	CFRP	480($60d_b$)	Bond length
MB2G1	8	-	2	-	GFRP	480($60d_b$)	L_b + FRP type
MB2S2	-	1.4×20	-	2	CFRP	480(-)	L_b + NSM shape
MB1G2	12	-	1	-	GFRP	480($40d_b$)	Bond length
MB1G2T	12	-	1	-	GFRP	480($40d_b$)	T
MB2C1ES	8	-	2	-	CFRP	480($60d_b$)	ES

T = Transverse confinement and ES = End anchorage.

6.6 Material Properties

The materials used in the experiments were concrete, steel reinforcement, CFRP strips, sheets and bars and GFRP bars. In this section, their mechanical properties are reported.

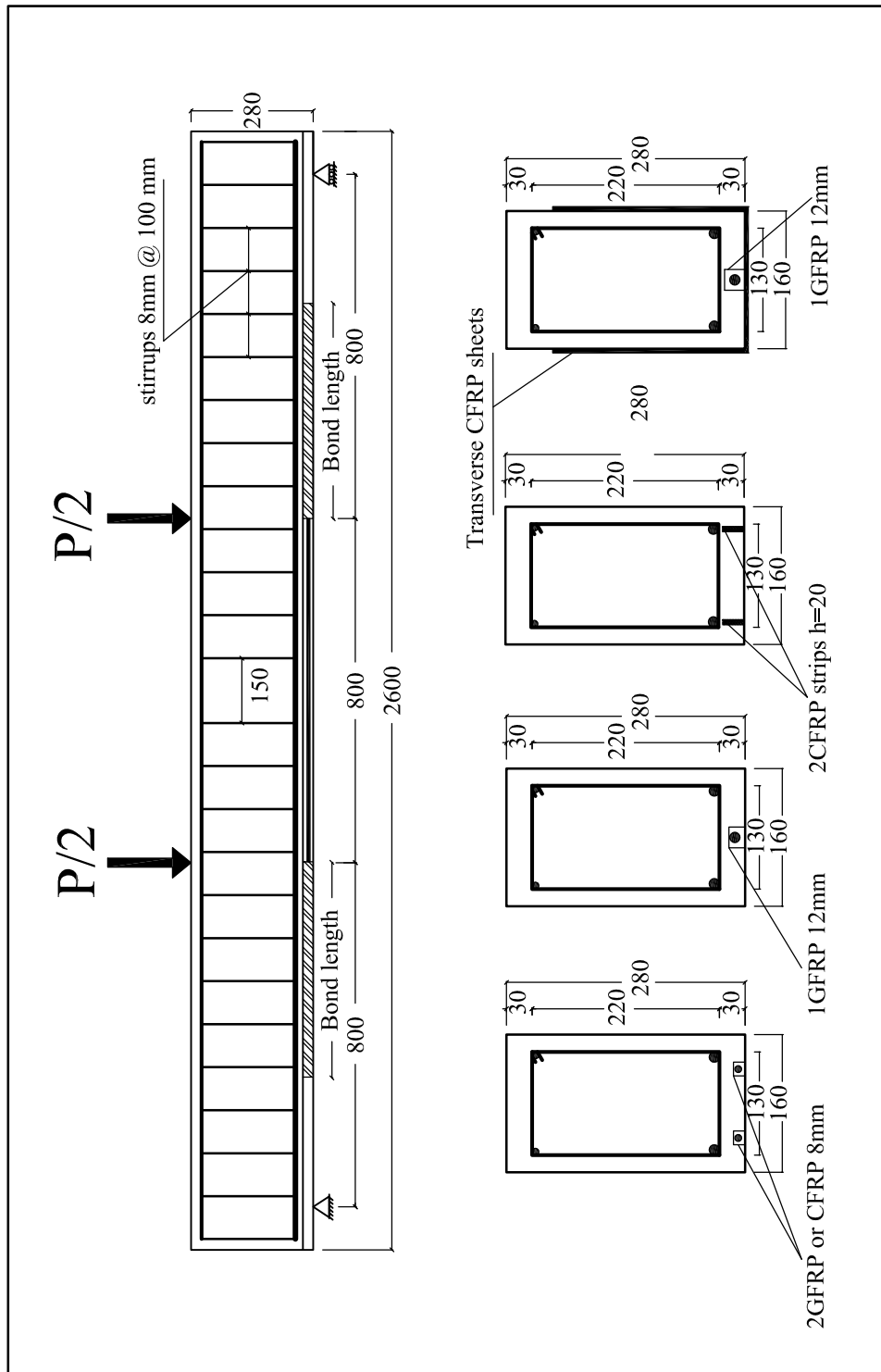


Figure 6.17: Strengthening scheme of the beams in the third series.



(a) End supporting mechanism for specimen MB2C1ES



(b) Transverse wrapping for specimen LB1G1T

Figure 6.18: Preparation of specimens with ES and T.

6.6.1 Concrete

One type of concrete was used to cast all the tested beams. The composition of delivered concrete is given in Table 6.5. In all series, the cylindrical specimens ($150 \times 300 \text{ mm}^2$) and beams were kept in the same exposure conditions of temperature and humidity until testing. Three standard specimens were tested in direct compression to determine the concrete strength in compression. Two standard specimens were tested under splitting test to determine the tensile strength and another three specimens were tested to determine the modulus of elasticity. From these cylinders, the compressive strength f_{cu} , compressive modulus of elasticity E_c and tensile strength f_{ct} were determined. All tests on concrete were carried out at the age of 33 to 36 days. The equipment used to perform these tests was a universal SERVOSIS MUE-60 model with a capacity of 600 kN and a SERVOSIS MES-250 model with a capacity of 2500 kN, respectively.

6.6.1.1 Compressive strength

The compressive strength, f_{cu} , was determined according to UNE 83.304/84 Standard, testing the specimens at the same temperature and humidity conditions than the beam specimens. Three standard cylinders $150 \times 300 \text{ mm}^2$ were tested each

Table 6.5: Concrete composition for the tested beams in kg.

Component	Quantity
Water	175
CIMENT I42,5 R	310
Sand 0/5	698
Sand 0/2	206
Gravel 5/15	1004
Gravel 15/25	0
SIKAMENT 175	5.53

time and the average strength was calculated. The average compressive strength ranged between 30.5 and 32.4 MPa while tensile strength ranged between 2.75 and 2.8 MPa at the time of testing. Table 6.6 shows the properties of concrete for each series.

Table 6.6: Properties of concrete for each series.

series ID	f_{cu} (MPa)	f_{ct} (MPa)	E_c (GPa)
First series	32.4	2.8	31.7
Second series	31.9	2.75	31.4
Third series	30.5	2.8	30.0

6.6.1.2 Modulus of elasticity

The modulus of elasticity of concrete (E_c) was tested using a SERVOSIS (MUE-60) universal testing machine with a capacity of 600 kN. Each of the tested specimens was instrumented with three strain gauges located at 120°. The tests were carried out following ASTM C 469/87 Standard. The procedure consisted of performing three cycles of compressive loading up to a value of 40% of the compressive strength. The modulus of elasticity is evaluated as the mean value of the last two cycles of loading, using the following expression:

$$E_c = \frac{\sigma_2 - \sigma_1}{\varepsilon_2 - \varepsilon_1} \quad (6.1)$$

where ε_1 has a value of 50×10^{-6} , ε_2 is the corresponding strain to 40% of the concrete strength, and σ_1 and σ_2 are the corresponding stresses to the previous strains.

6.6.1.3 Tensile strength

The tensile strength, f_{ct} , is the concrete mechanical property that presents the largest scatter of values. It is influenced by the superficial shape and structure of aggregates and can be substantially reduced by environmental effects [103, 104]. Different definitions for the tensile strength can be distinguished: the axial tensile strength (the tensile strength of a specimen subjected to an axial stress), the flexural tensile strength (that of a specimen subjected to a flexural stress) or the splitting tensile strength (derived from the well-known Brazilian test). In this work, the concrete tensile strength was determined by splitting tensile tests on cylindrical specimens. The tests were carried out using a SERVOSIS MES-250 machine with a capacity of 2500 kN. The splitting tensile strength ($f_{ct,sp}$) was tested according to UNE 83306/85 standard at the same temperature and humidity conditions than the beam specimens were tested.

6.6.2 Steel reinforcement

Four 12 mm deformed steel bars were tested based on UNE-EN ISO 15630-1:2011. An extensometer with 50 mm gauge length was installed to measure the strains. The extensometer was removed before failure to prevent possible damage from the sudden rupture. The ultimate strain at rupture was calculated by measuring the final elongation between two points marked on the bar. The average yield strength and ultimate strength was 540 MPa and 630 MPa, respectively.

6.6.3 FRP bars, strips and sheets

The mechanical properties of the bars were tested following ACI 440.3R-04 [1]. Five specimens were tested for each diameter. The results are shown in Table 3.4 while the surface treatment of the bars are shown in Fig. 3.2. The properties of the CFRP strips as reported by the manufacturer are also shown in Table 6.1. The high strength and high modulus unidirectional CFRP sheets (thickness = 0.117 mm) was

used as transverse wrapping. The properties of these sheets are 240 GPa and 4900 MPa for the modulus of elasticity and tensile strength respectively.

6.6.4 Epoxy

Two types of epoxy resins (A and B) were used for the embedment of the NSM bars. The first type (A), MBRACE ADHESIVE HT (BASF), consisted of primer and epoxy paste. The second type of resin was POLYFIXER EP (ROBERLO). The properties of the epoxy paste are reported before in Table 3.3.

Chapter 7

Flexural test experimental results

7.1 Introduction

The experimental results obtained from the flexural tests described in Chapter 6 are presented in this chapter. From the experimental data, load capacity, fibre reinforced polymer (FRP) and concrete strains and model of failure of the reinforced concrete (RC) beams strengthened of various near surface mounted (NSM) FRP reinforcement have been obtained and subsequently discussed. The effect of construction details, bond length, epoxy type and some applied modification on the load capacity of the tested RC beams are studied. In this study, three series of strengthened RC beams were tested. The tested parameters and the full details of each series were described in Chapter 6. The results of each series are presented and discussed in the following.

7.2 Results and discussion of the first series

In the first series eight beams were prepared and tested under four point bending. The effects of material type (carbon and glass), epoxy properties, bar size and the number of NSM bars were studied. The tested beams were strengthened with a limited bond length in order to imitate as much as possible work-place conditions, as the grooves could only be cut up to the faces of the supporting columns with difficulty. The load capacity, deflection, mode of failure, FRP strain, concrete strain, free end slip and the transverse strain in epoxy and concrete of the tested beams

were all analyzed. The results of the tested beams are given in Table 7.1. In this table, P_{cr} is the cracking load, P_y is yield load, $\eta_y\% = \frac{P_{y, str} - P_{y, CB}}{P_{y, CB}} \times 100$ is the load efficiency at P_y , P_u is maximum load capacity, $\eta_u\% = \frac{P_{u, str} - P_{u, CB}}{P_{u, CB}} \times 100$ is the load efficiency at P_u , δ_u is the maximum deflection and ε_f is the maximum strain obtained in the NSM bars (CB and str referred to the control beam and the strengthened beams respectively). The failure modes of the tested beams are indicated in the last column of the table. The effect of the test variables on the flexural behaviour of the tested beams are discussed below:

Table 7.1: Results of the tested RC beams (first series).

Beam ID	P_{cr} (kN)	P_y (kN)	η_y (%)	P_u (kN)	η_u (%)	δ_u (mm)	$\frac{\varepsilon_f}{\varepsilon_{fu}}$ (%)	Failure mode
CB	14.7	64.5	—	70.4	—	50.8	—	Yielding
LB1C1	18.5	80.1	24.1	109.1	55.3	31.7	66.0	C-E
LB2C1	20.1	100.5	55.8	117.2	66.3	20.3	39.6	CCs
LA2C1	17.5	94.8	47.0	114.5	62.6	22.0	41.6	CCs
LB1G1	16.7	73.7	14.2	99.2	41.2	59.7	97.5	BR,Cs,Es
LB2G1	17.0	82.3	27.6	112.2	59.4	42.4	97.8 ^a	Cs
LA2G1	16.8	81.7	26.7	110.6	56.3	42.3	97.8 ^b	Es,Cs
LB1G2	16.2	83.7	29.8	105.8	50.3	35.3	71.1	C-E

BR = bar rupture; CCs = concrete cover separation; Cs = concrete splitting; C-E = concrete-epoxy interface failure; Es = epoxy splitting; a , b = strain gauge failure at 107 and 102 kN respectively.

7.2.1 Beams strengthened with NSM CFRP bars

7.2.1.1 Load deflection curves and mode of failure

Fig. 7.1 shows the load deflection ($P - \delta$) curves for beams strengthened with carbon fibre reinforced polymer (CFRP) bars. In general the curves present an approximate tri-linear response defined by concrete cracking, steel yielding and post-yielding stages. In the first stage, before cracking, the strengthened beams followed a linear elastic behaviour pattern, like the control one. The NSM bars had an insignificant effect on the stiffness of the load deflection curves with only a slight effect on the cracking loads (see Fig. 7.1 and Table 7.1). In the second stage, from

cracking to steel yielding, the NSM increased the stiffness of the specimen and also the yielding load in relation to the control beam. The load increased by 24.1 % and 55.8 % over the control beam for those specimens strengthened with one and two C1 bars bonded with epoxy B respectively, while for the beam strengthened with two C1 bars bonded with epoxy A the increase was 47 % .

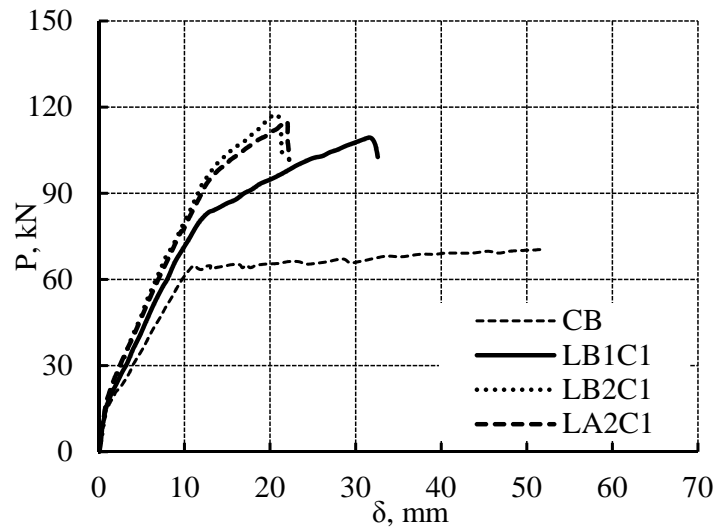


Figure 7.1: Load deflection curve of beams strengthened with NSM CFRP bars.

The last stage comprised the time between the steel yielding and the failure of the beam. In this stage, as the load increased the deflection increased at a higher rate than in the previous stage. At ultimate load, the control beam failed due to yielding of the tension steel reinforcement followed by concrete crushing. The LB1C1 beam, strengthened with one NSM C1 bar, failed due to concrete-epoxy interface failure (Fig. 7.2a) at a load of 109.1 kN.

Specimens LB2C1 and LA2C1, strengthened with two NSM C1 bars, failed due to concrete cover separation starting at the cut off of the NSM bars (Figs. 7.2b and c), with 66.3 % and 62.6 % of increase over the control beam respectively. Increasing the number of NSM C1 bars from one to two increased the yielding and maximum loads of beams LB2C1 by 25.6 % and 7.5 % over LB1C1, respectively. On the other hand, the epoxy type had only a slight effect on the yielding and ultimate loads of the strengthened beam (LA2C1) compared to LB2C1 as the failure was governed by the concrete cover separation.

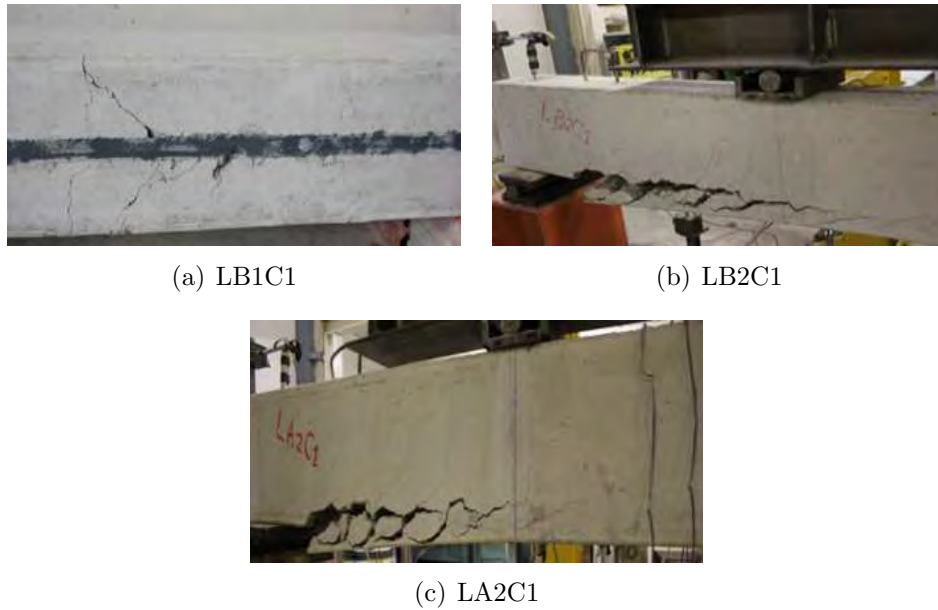


Figure 7.2: Failure modes of beams strengthened with NSM CFRP bars.

7.2.1.2 Load end slip curves

In this section the load end slip curves of the free end of NSM FRP bars, for beams strengthened with C1 bars, are discussed. As shown in Fig. 7.3, the end slip of NSM bars increased as the load increased. In one NSM bar, the cracks formed and propagated in the pure bending moment region, and very narrow cracks appeared at the cut off of the bonded bars just before failure. The cracks in the shear span decreased the effectiveness of the bond length, causing an increase in slip of the NSM bars. The slip recorded by the LVDTs increased as the number and width of the cracks increased. The higher slip values recorded for specimens with two C1 bars compared to those with one bar was due to the decrease in the confinement of concrete with the number of bars and also the width of the cracks formed at the cut just before failure. The load end slip relation may be useful for assessing bond slip laws used to simulate the flexural behaviour of beams strengthened with NSM bars, and formulating equations governing the effect of the NSM technique.

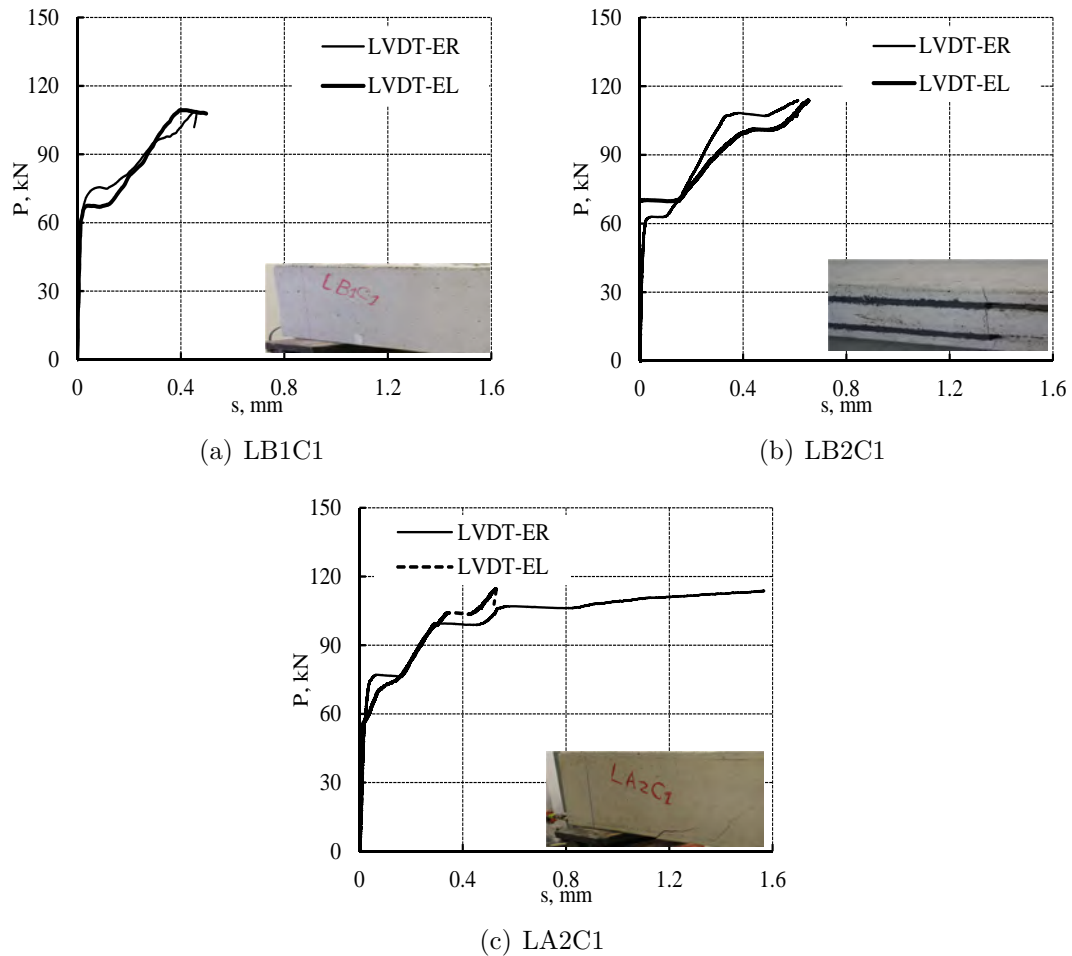


Figure 7.3: Free end slip curves of beams strengthened with CFRP bars.

7.2.1.3 Strain distribution along the CFRP bars

Shown in Fig. 7.4 are the strain distributions along half of the bond length of the CFRP bar at several different loads, recorded using five strain gauges (see Fig. 6.8, x starting at the FRP cut off, $L_1 = L/2 = 1.2$ m). The crack patterns of the half of the pure moment region at a load of 80 kN are also included in Fig. 7.4. Strains for gauge SG2 in beam LB1C1 and gauge SG5 in beam LB2C1 were not recorded due to damage caused during the test. The strain values recorded by all the strain gauges increased with load. The maximum strains registered in the CFRP bars ranged between 39.6 % and 66 % of their ultimate strain, as shown in Table 7.1. At the same loads, the cracks formed in the beams strengthened with one bar

were wider and deeper than those in the beams strengthened with two. The values of strain recorded by SG1 and SG3 for beam LB1C1 were similar, especially at loads of 60 and 80 kN, as the cracks in the pure moment region become wider and deeper than when loads are lower. This means that the bar at the pure moment region acts as a tie supported by the rest of the bond length located in the shear span. The strain in the FRP bars for specimen LA2C1 recorded by SG1 was higher than that recorded for specimen LB2C1, which may have been due to the properties of the epoxy paste, as epoxy type A has a lower modulus of elasticity and tensile strength than epoxy B.

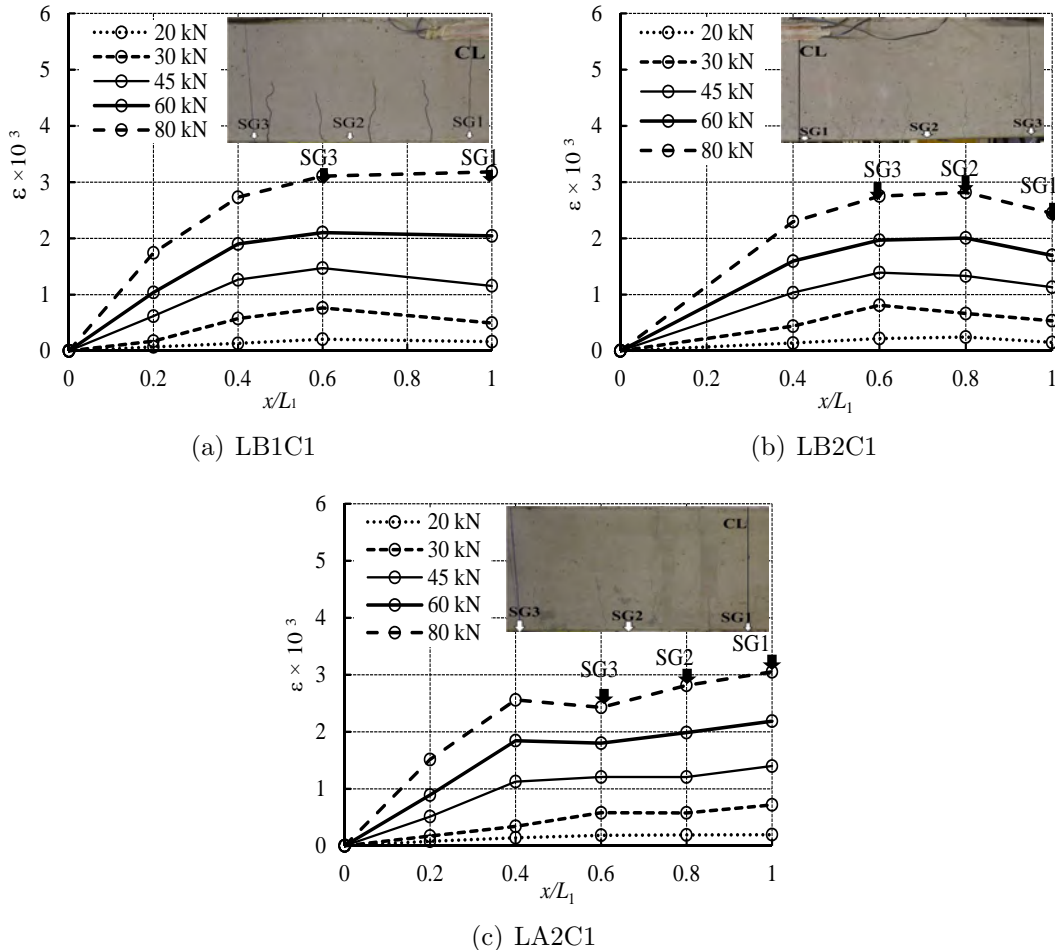


Figure 7.4: Strain distribution along half of the NSM CFRP bars.

7.2.1.4 Sectional strain profile

Strain profiles versus beam depth (z) using strain readings at the central section of the beam for concrete, steel, and CFRP bars are shown in Fig. 7.5. These profiles are drawn at load levels less than the beams' yielding loads. The results are for the three strain gauges located in the concrete at different depths: $Z = 0, 20,$ and 48 mm from the top of the beam, and for the SG1 gauge on the FRP bar (Fig. 6.8). The strain for the steel reinforced part of the section was considered linear so the three gauges SG-c1, SG-c2 and SG-c3 were used to predict the strain in the steel bars. The strain profiles of the strengthened beams were linear at low load levels. As the load increased, the composite action (bond) at mid-span changed as a result of the concrete cracking, resulting in higher strain in the FRP bars (Fig. 7.5a).

The strain in the FRP bars for the LB2C1 beam (Fig. 7.5b) was lower than for LB1C1 due to the higher NSM FRP area. Beam LA2C1, bonded with epoxy A (Fig. 7.5c) presented higher strains for the NSM FRP bars, which may have been due to the effect of the lower modulus of elasticity and tensile strength of epoxy A. This kind of strain profile was also reported in [105, 106] for steel and steel concrete composite beams strengthened with externally bonded CFRP strips and in [25] for concrete beams strengthened with NSM bars.

7.2.1.5 Transverse strain

To test further the bond behaviour of NSM bars under flexural load, the transverse strain in epoxy and concrete was recorded. Fig. 7.6 shows the transverse strain in epoxy paste recorded by three gauges located at different positions from the center line of the strengthened beams (Fig. 6.8). The three strain gauges for beam LB1C1 recorded negative transverse strain that increased until certain loads, depending on the position, were located. When the load increased, the strain decreased until failure due to concrete cracking.

At the beginning of loading, tensile stresses were exerted along the beam in a longitudinal direction, and these exerted compressive stresses in a transverse direction either in the concrete or the epoxy. As the load progressed, the concrete cracked and the bar transferred the stresses through the cracked region, at which point the transverse strains that were recorded decreased.

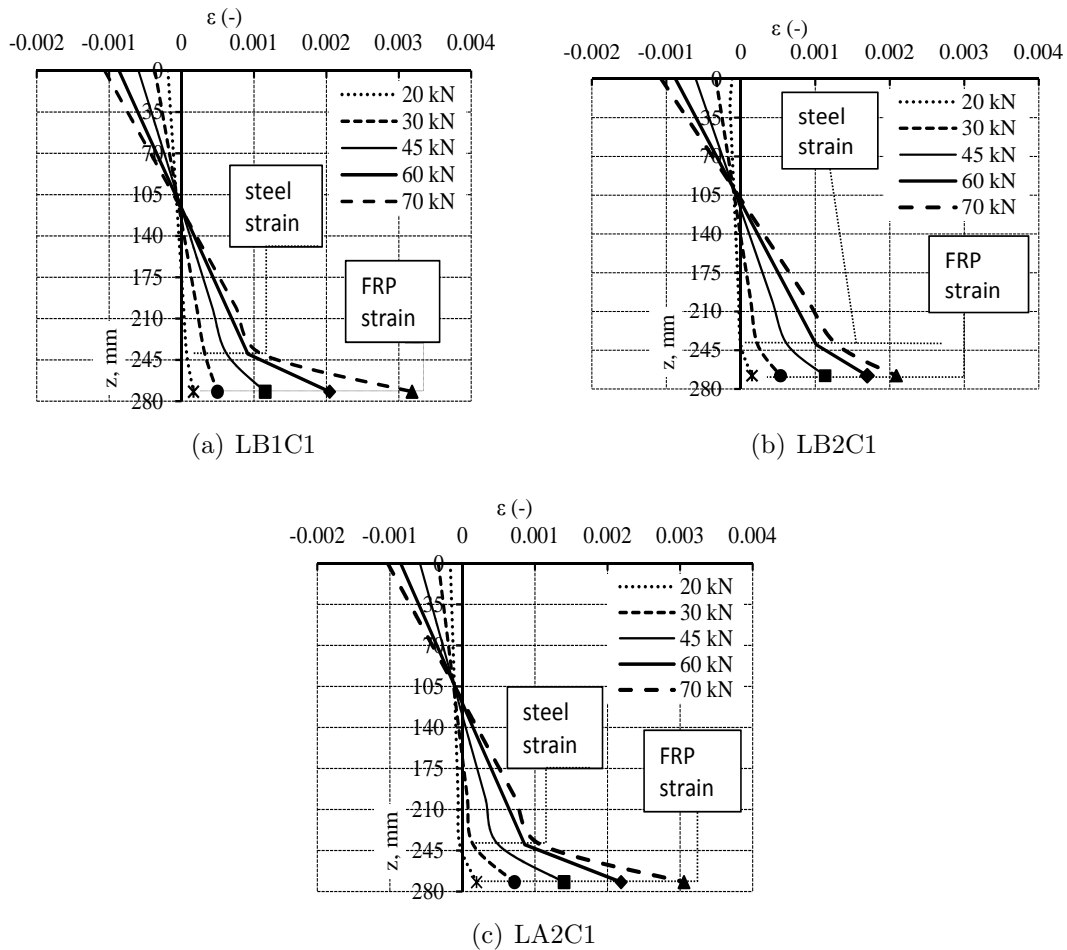


Figure 7.5: Strain profile of beams strengthened with NSM CFRP bars.

The strains recorded confirmed that the behaviour of the NSM bars in bending was dissimilar to that under direct pullout. In direct pullout tests, in contrast to bending tests, the tensile stresses were transferred from the NSM bars to the surrounding concrete through the epoxy paste [98].

For beam LB2C1, the area of NSM bars and epoxy was higher and the value of transverse strain was lower than that recorded for specimen LB1C1. Due to the higher stiffness and tensile strength of epoxy B, the recorded transverse strains for beam LB2C1 were lower than those for beam LA2C1 bonded with epoxy A. On the other hand the recorded strains in concrete for beam LB1C1 were higher than those for beams LB2C1 and LA2C1 (see Fig. 7.6c).

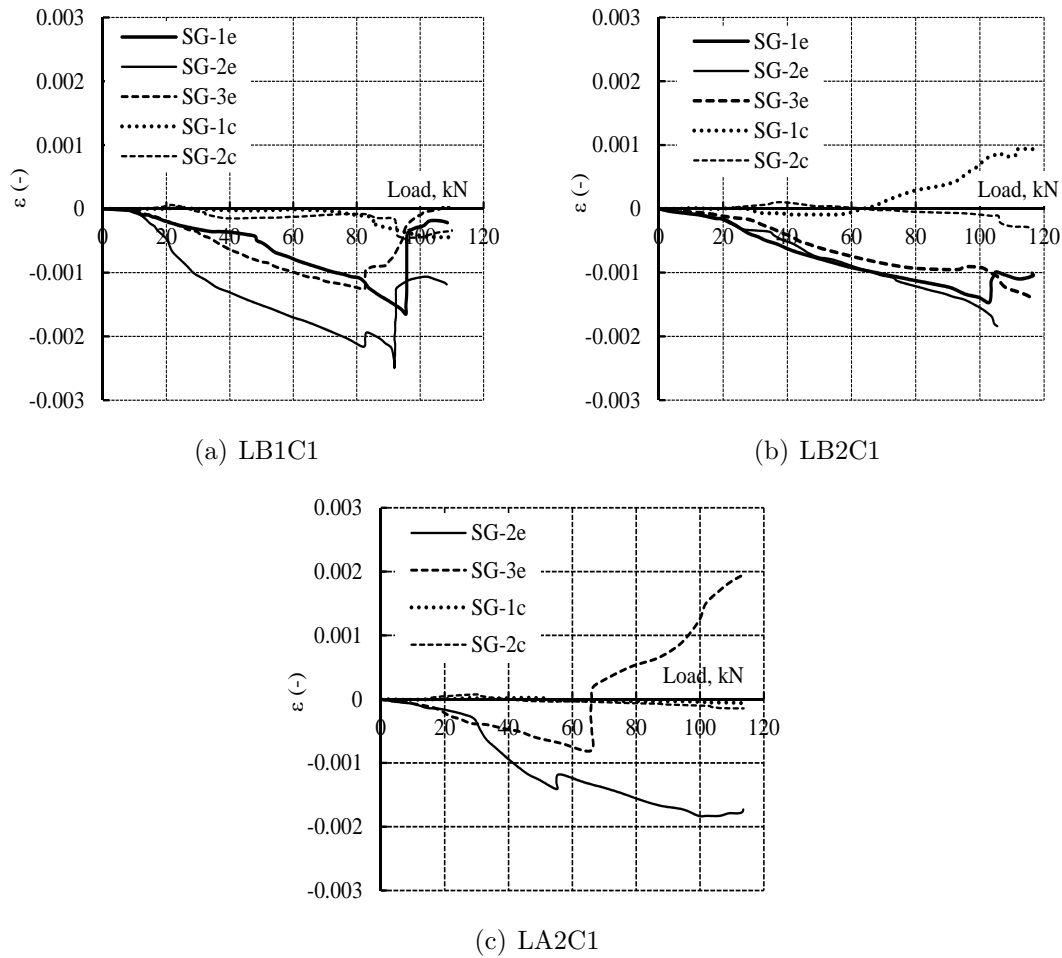


Figure 7.6: Transverse strain distribution on epoxy for beams strengthened with NSM CFRP bars.

7.2.1.6 Deflection and stiffness

To estimate the increase in beam stiffness provided by the proposed strengthening technique, the deflection of the strengthened beams compared to that of the control beam was plotted at several load levels. Fig. 7.7a shows that the deflection of LB1C1 was significantly lower than the deflection registered in the control beam (-17.3 % at $P = 60$ kN). Moreover, the deflection of the strengthened beams decreased as the area of NSM bars increased (-35.2 % at $P = 60$ kN, Figs. 7.7a and b) revealing the influence of the strengthening technique on beam stiffness. In contrast, the epoxy type had no appreciable effect on the strengthened beams' stiffness (Figs. 7.7b and c).

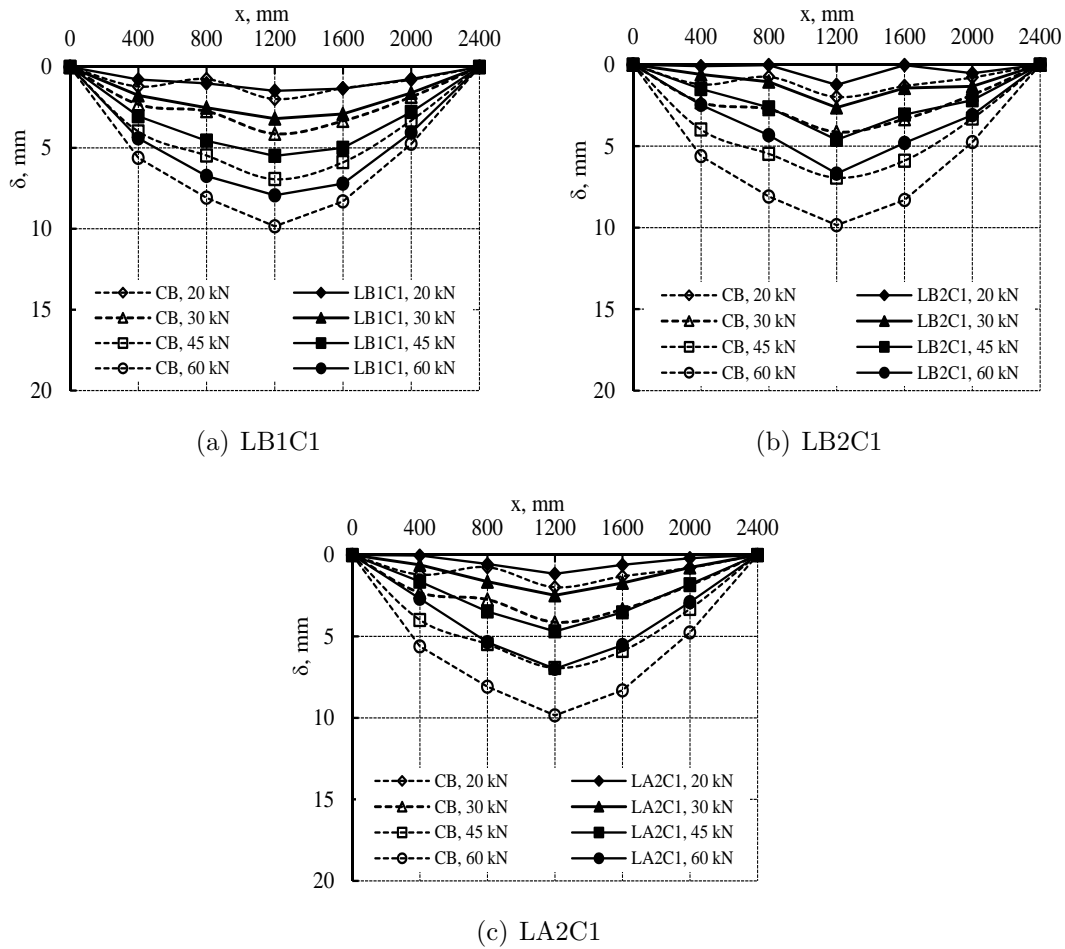


Figure 7.7: Deflection of beams strengthened with NSM CFRP bars.

7.2.2 Beams strengthened with NSM GFRP bars

7.2.2.1 Load deflection curves and mode of failure

Fig. 7.8 shows the load deflection curves for beams strengthened with fibre reinforced polymer (GFRP) bars. The curves generally showed a tri-linear response as noted in section 7.2.1.1. The NSM bars had little effect on the stiffness of the curves until yielding loads were reached (see Fig. 7.8). By contrast, the yielding loads of the beams strengthened with one G1, two G1 and one G2 bars bonded with epoxy B increased by 14.2 %, 27.6 % and 29.8 % over the control beam respectively, and by 26.7 % over the beam strengthened with two G1 bars bonded with epoxy A. These results show that as the area of the NSM bars doubled, the increment of

increase in the yield loads for the strengthened beams also nearly doubled. In the last stage, a greater increase than in the one previous in the stiffness and load of the strengthened beams in relation to the control beam was observed. The LB1G1 beam strengthened with one NSM G1 bar failed due to bar rupture extending to cause epoxy splitting and concrete cover detachment (Fig. 7.9a) at a load of 99.1 kN, which represents an increase of 41.2 % over the control beam.

On the other hand, beams LB2G1 and LA2G1 strengthened with two NSM G1 bars failed due to bar pullout in the form of concrete cover separation (Figs. 7.9b and c), with increases of 59.4 % and 56.3 % respectively. Beam LB1G2 strengthened with one NSM G2 bar failed due to concrete-epoxy interface failure (bar pullout, Fig. 7.9d), with 50.3 % increase over the control beam. The failure of this beam was initiated by a flexural crack starting beneath the location of the point load. As the load progressed, the crack propagated until the NSM bars. The NSM bar and the epoxy paste prevented this crack from growing transversally through the epoxy paste. Finally the crack propagated longitudinally, causing concrete-epoxy interface failure (see Fig. 7.9d).

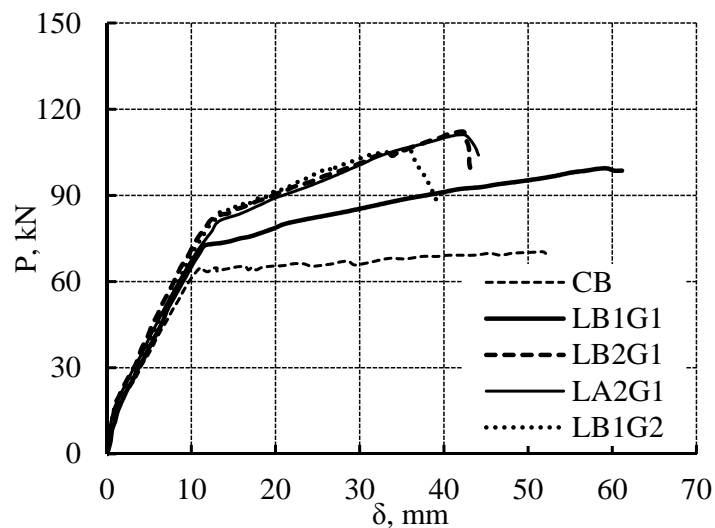


Figure 7.8: Load deflection curve of beams strengthened with NSM GFRP bars.

As observed in relation to the beams strengthened with CFRP bars, increasing the number of NSM G1 bars increased the yielding and maximum loads of specimen LB2G1 compared to LB1G1 by 11.7 % and 13.0 % respectively. The epoxy type,

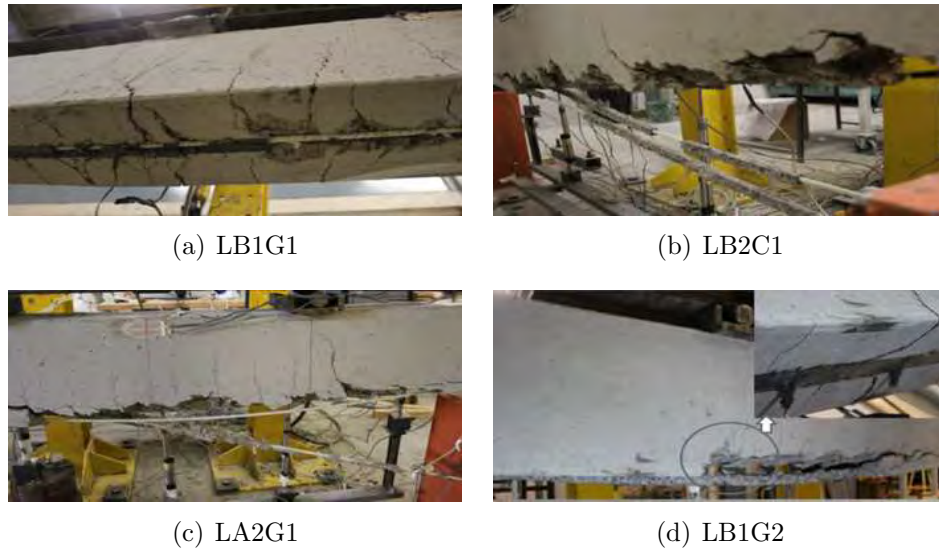


Figure 7.9: Failure modes of beams strengthened with NSM GFRP bars.

meanwhile, had little effect on the yielding and ultimate loads of the strengthened beams as the failure was concrete cover separation. Beam LB1G2 ($A_f = 113 \text{ mm}^2$) failed at a lower load than did LB2G1 ($A_f = 100.5 \text{ mm}^2$), which may have been due to its lower concrete-epoxy interface area compared to beam LB2G1.

7.2.2.2 Load end slip curves

In this section the load end slip curves of the NSM FRP bars of the beams strengthened with G1 and G2 bars are discussed. As shown in Fig. 7.10, these curves are similar to those of specimens strengthened with CFRP bars. Due to the bar surface treatment, the recorded end slips for specimens with G1 bars were lower than for the corresponding beams with CFRP bars.

The recorded end slips for the two beams with two NSM G1 bars were slightly higher than for the beam with one NSM bar, which may have been due to a lower confinement (edge effect) in the case of two NSM bars. On the other hand, the end slips recorded for the beam with G2 bars were also higher than those for the beam with one G1 bar, which may have been due to lower concrete confinement, and the concrete-epoxy interface failure occurring in the specimen with G2 bars. Finally the slip recorded by the LVDTs was affected by the number of the cracks formed in the shear span, which increased the slip of the NSM bars.

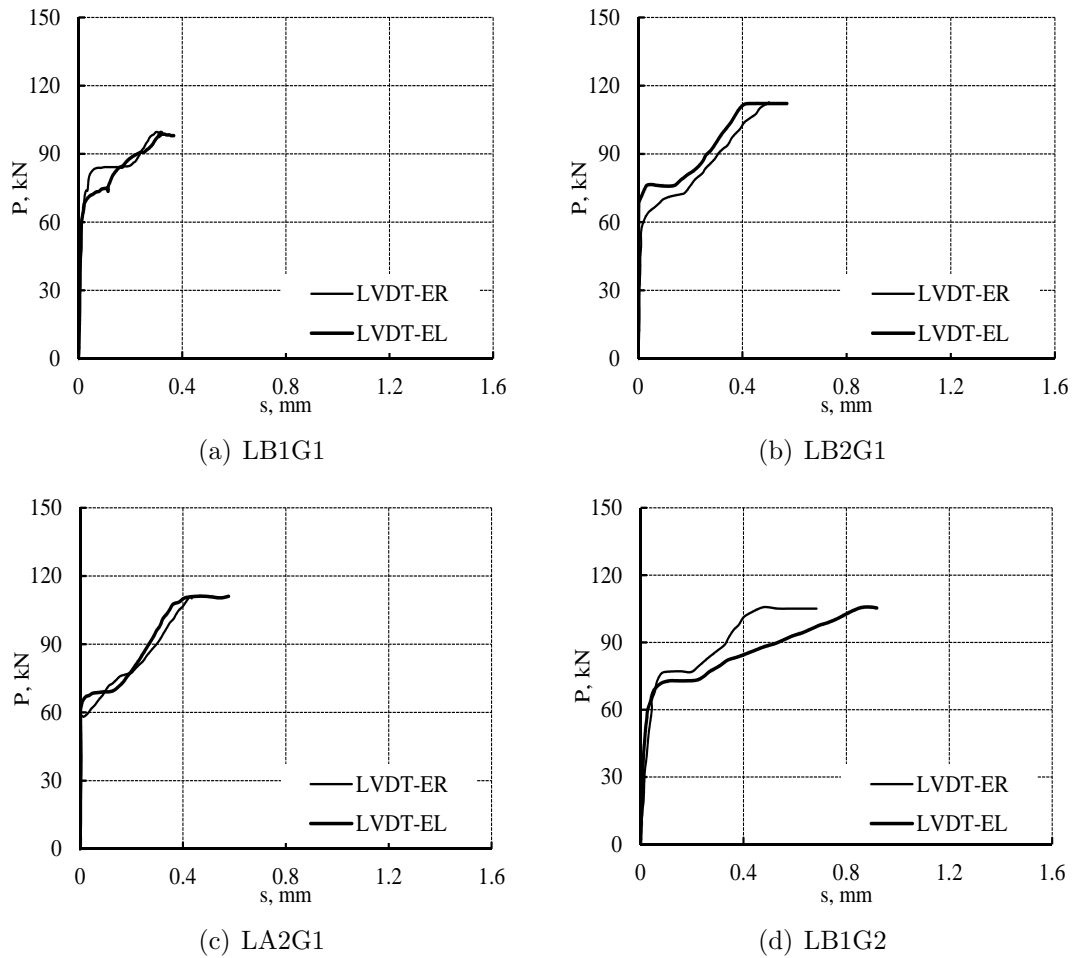


Figure 7.10: Free end slip curves of beams strengthened with GFRP bars.

7.2.2.3 Strain distribution along the GFRP bars

Fig. 7.11 shows the strain distribution at several loads along half of the bond length of the GFRP bar; recorded using five strain gauges (see Fig. 6.8) together with the crack patterns of half of the pure moment region at a load of 80 kN. The strain values recorded by all the strain gauges increased as the load increased and the recorded strain in the FRP bars for beams with NSM GFRP bars was higher than that recorded in the corresponding specimen with CFRP bars due to the low modulus of elasticity of the GFRP bars. The maximum strains registered in the GFRP bars ranged between 71.1 % and 97.8 % of their ultimate strain, as shown in Table 7.1.

The high strain values recorded at failure may have been due to the bar surface damage observed after failure. Due to the lower area, the strain at the same loads in FRP for beams strengthened with one G1 bar (LB1G1) was higher than that for beams with two bars (LB2G1). The values of strain recorded by SG1, SG2 and SG3 for beam LB2G1 were nearly the same, with no cracks forming near the gauges. On average, the strains followed a profile similar to that of the flexural moment, affected locally by the appearance of cracks (Figs. 7.11a and d). Finally, for all beams with GFRP bars, the strain gauges stopped recording at a strain value equal to 0.0163, which may have been due to bar surface damage.

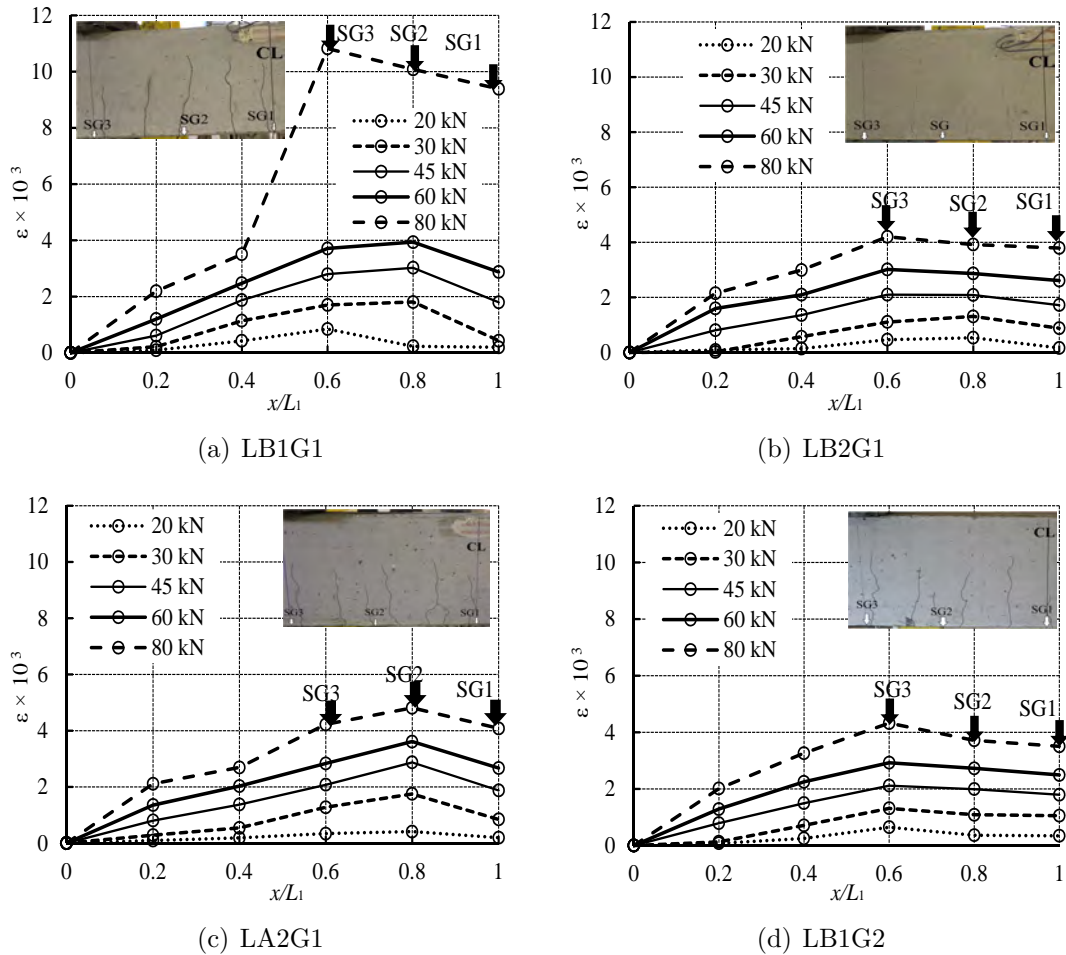


Figure 7.11: Strain distribution along half of the NSM GFRP bars.

7.2.2.4 Sectional strain profile

Fig. 7.12 shows strain profile versus beam depth (z) using strain readings for the concrete, steel, and GFRP bars. The profiles are drawn at load levels lower than the yielding loads of the strengthened beams. It can be seen they are linear at the beginning of loading, and that as the load increases, so does the strain in the FRP bars. For all the beams, the strain recorded in the GFRP bars was higher than in the corresponding specimens with CFRP bars. This was due to the lower modulus of elasticity of GFRP bars and the composite action (bond) at mid-span changing as a result of the concrete cracking (Fig. 7.12). This difference in strain between the FRP bars and the surrounding concrete developed shear stresses in the concrete cover, causing concrete cover separation at the level of internal steel reinforcement in the cases of beams LB1G1, LB2G1 and LA2G1 and concrete-epoxy interface failure in the case of beam LB1G2.

7.2.2.5 Transverse strain

Fig. 7.13 shows the transverse strain in epoxy paste recorded by three gauges located at different positions from the center line of the beams strengthened with GFRP bars (Fig. 6.8). The three gauges for beam LB1G1 recorded negative transverse strain that increased until certain loads, depending on the strain position. With an increase in the load the strain decreased until failure. At the beginning of loading, tensile stresses were exerted along the beam in a longitudinal direction, and these exerted compressive stresses in a transverse direction in either concrete or epoxy. As the load progressed, the concrete cracked and then the bar transferred the stresses through the cracked region. At this point the recorded transverse strains decreased, as noted previously (see section 7.2.1.5).

As the concrete confinement decreased, transverse strain in the epoxy increased. In contrast, the recorded strains in concrete for all the beams were small or negligible, except in the case of specimen LB2G1, which was due to crack formation at this location (see Fig. 7.13).

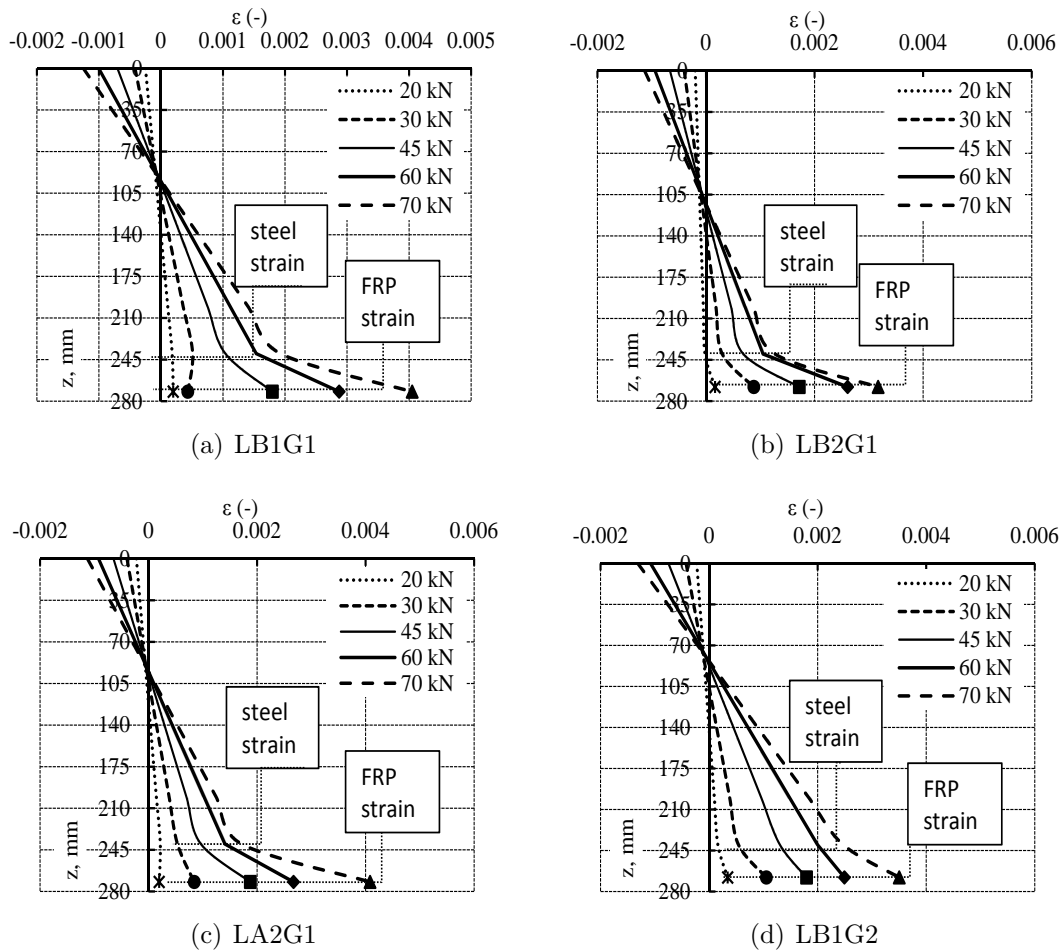


Figure 7.12: Strain profile of beams strengthened with NSM GFRP bars.

7.2.2.6 Deflection and stiffness

The deflection of beams strengthened with GFRP bars compared to that of the control beam was plotted at several load levels to estimate the increase in beam stiffness provided by the strengthening. Fig. 7.14a shows that the deflection of the strengthened beam LB1G1 was similar to that registered in the control beam. Moreover, the strengthened beams' deflection lessened as the area of NSM bars doubled (-14.8 % at $P = 60$ kN) (Figs. 7.14a and b)), revealing the influence of the strengthening technique on the stiffness. In contrast, as the modulus of elasticity and tensile strength of the epoxy paste increased, so did the stiffness of the strengthened beam (Figs. 7.14b and c).

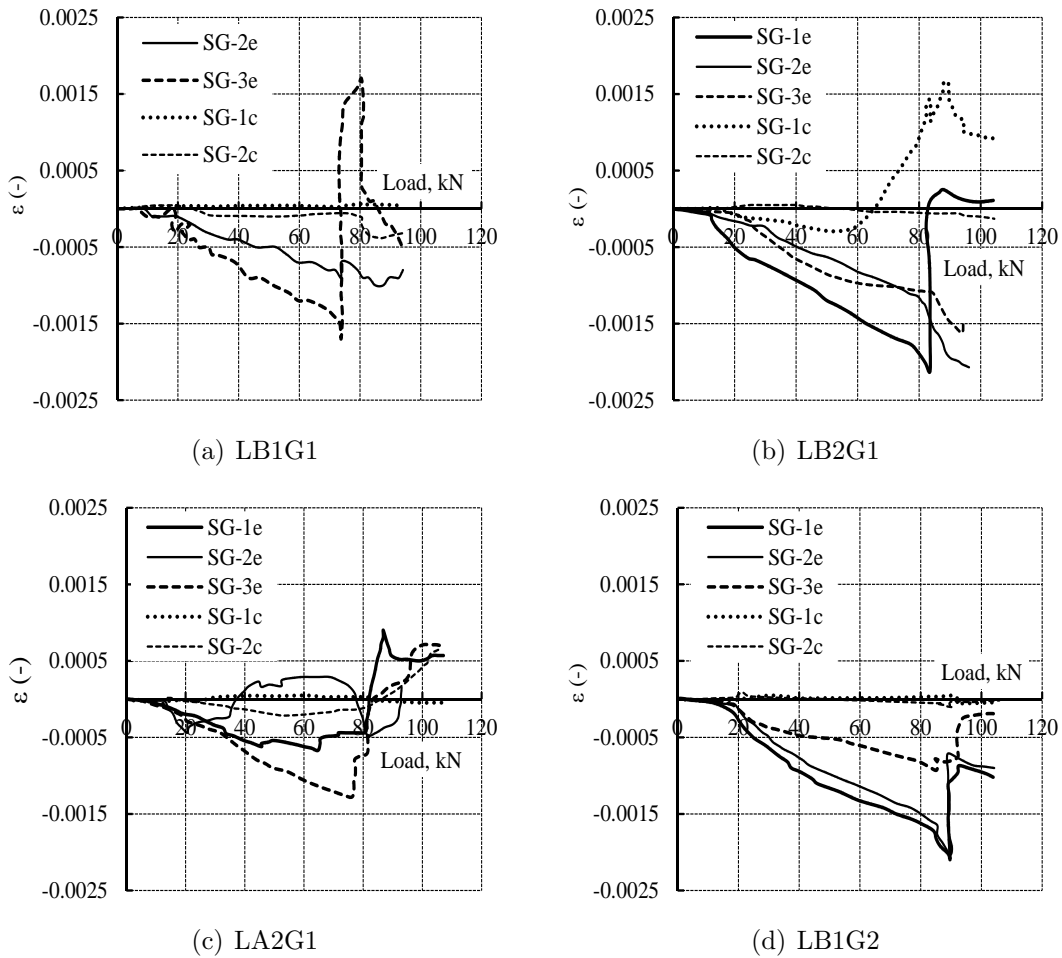


Figure 7.13: Transverse strain distribution on epoxy for beams strengthened with NSM GFRP bars.

7.2.3 Comparison and discussion of results

Fig. 7.15 compares the maximum load (P_u) and the corresponding deflection of the strengthened beams. Those beams strengthened with CFRP bars experienced slightly higher loads than the specimens strengthened with GFRP bars, while the deflections were smaller. On the other hand, epoxy type had little effect either on the load capacity or on the deflection of the beams (see beams with two bars, LB2C1, LA2C1, LB2G1 and LA2G1), as their failure was due to concrete cover separation or concrete splitting. Fig. 7.16 shows the relative stiffness of strengthened beams compared to that of the control beam (CB) at the service load ($\delta = L/400$) and at the yielding load, using Eq. 7.1

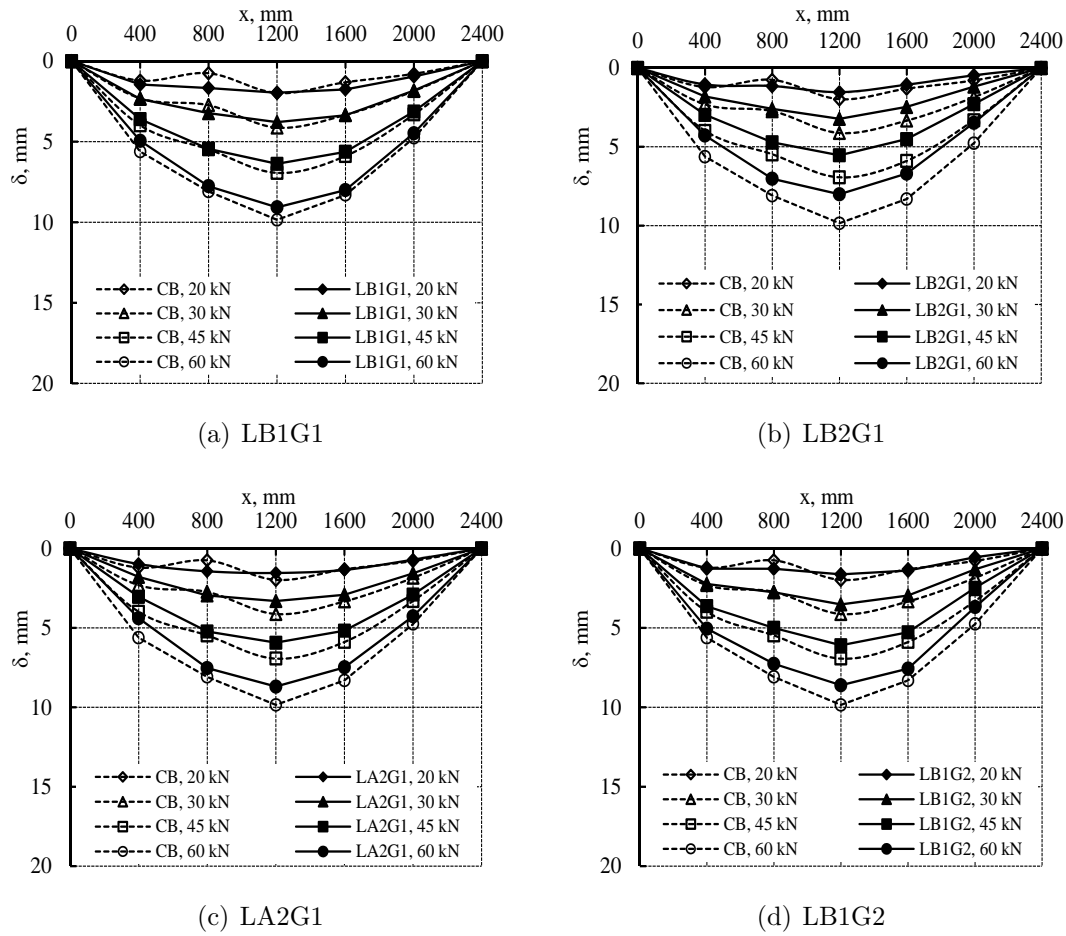


Figure 7.14: Deflection of beams strengthened with NSM GFRP bars.

$$Stiffness\% = \frac{\delta_{CB} - \delta_{str.}}{\delta_{CB}} \times 100 \quad (7.1)$$

where δ_{CB} and $\delta_{str.}$ are the deflections of the control and the strengthened beams respectively. The stiffness of the strengthened beams increased by an amount that mainly depended on the type of FRP material and the area of reinforcement. The beams strengthened with CFRP bars experienced higher stiffness than those of specimens strengthened with GFRP bars, and those bonded with epoxy B (LB2C1 and LB2G1) experienced higher stiffness than the beams bonded with epoxy A (LA2C1 and LA2G1). This seems to show that as the tensile strength and modulus of epoxy increased, so did the stiffness of the strengthened beams.

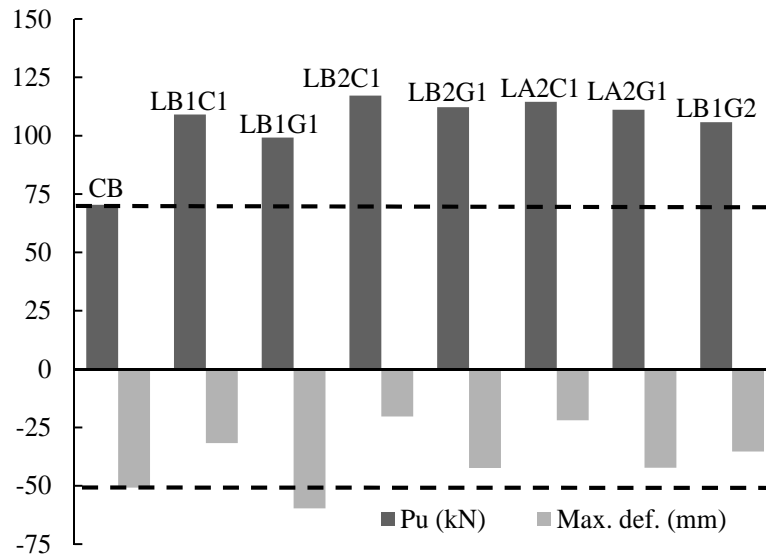


Figure 7.15: Comparison of the load capacity and the corresponding deflection of strengthened beams.

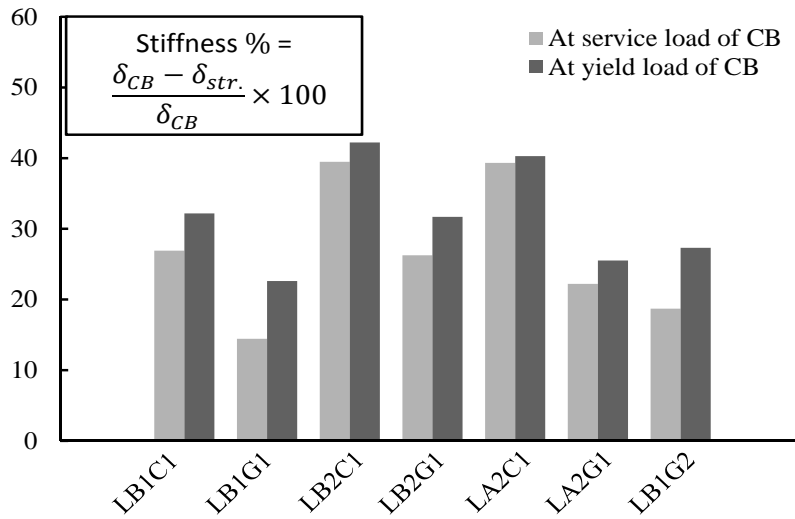


Figure 7.16: Comparison of stiffness of strengthened beams at service load and at yielding load of the CB.

7.2.4 Conclusions

An experimental programme was carried out to study the effect of various different variables on the flexural response of RC beams strengthened by NSM FRP reinforcement of a limited bond length. These variables consisted of the FRP material (carbon or glass), the number of NSM bars and their area, epoxy properties, and the strengthening arrangement. Load capacity, deflection, mode of failure, FRP strain, concrete strain, free end slip and transverse strain in epoxy and concrete of the tested beams were all analyzed. From the test results the following conclusions can be drawn:

- For beams strengthened with CFRP bars, the yielding loads ranged between 124.1 % and 155.8 % of the yielding load of the control beam, depending mainly on the area of the FRP bars and the epoxy properties. As far as maximum loads were concerned, these ranged between 155.3 % and 166.3 % compared to that of the control beam, depending mainly on the area of FRP bars and the failure mode of the beams.
- Increasing the number of NSM C1 bars from one (LB2C1) to two (LB1C1) increased the yielding and the maximum loads by 25.6 % and 7.5 % respectively. The small percentage increment in the maximum load was mainly due to the concrete cover separation mode of failure. The deflection of the strengthened beams decreased as the area of the C1 NSM bars increased. In contrast, the epoxy type had no effect on the strengthened beams' stiffness. The maximum strains registered in the CFRP bars ranged between 39.6 % and 66 % of their ultimate strain, and the cracks formed in beams strengthened with one bar were wider and longer than those of beams strengthened with two bars.
- For beams strengthened with GFRP bars, comparison with the control beam shows an increase in the yielding load ranging between 114.2 % and 129.8 %, while the increment in the maximum load is between 141.2 % and 159.4 %. These values can be mainly attributed to the area of the FRP bars, their arrangement and epoxy properties.
- Increasing the number of NSM G1 bars increased the yielding and maximum loads of the LB2C1 beams by 11.7 % and 13 % respectively, compared to

LB1G1. Increasing the area of the GFRP bars was more effective regarding the increment in maximum load than it was for the CFRP bars, due to the concrete cover mode of failure occurring in that case. The maximum strains registered in the GFRP bars ranged between 71.1 % and 97.8 % of their ultimate strain.

- The recorded end slips for the two beams each with two NSM bars were slightly higher than those of the beam with one NSM bar, due to a lower confinement (edge effect) in the case of two NSM bars, while the type of FRP bars had little effect on the end slip. End slips recorded for beams with one G2 bar were also higher than those for beams with one G1 bar; this may have been due to the effect of concrete confinement and the concrete-epoxy slip of the G2 bar.
- The transverse strains recorded confirmed that the behaviour of NSM FRP bars under direct pullout is dissimilar to the behaviour in bending. In contrast to pullout at the beginning of loading, tensile stresses exerted along the longitudinal direction of the beam caused compressive stresses in the transverse direction in both concrete and epoxy. As the load progressed, the concrete cracked and the bar transferred the stresses through the cracked region, when the recorded transverse strains decreased.
- These results show that the NSM FRP technique is effective for increasing the load capacity and stiffness of RC beams. The technique's load efficiency depends mainly on the area of the FRP bars and their mode of failure, while stiffness enhancement is mainly influenced by the bars' modulus of elasticity.

7.3 Results and discussion of the second series

In this series eight RC beams were prepared and strengthened to study the effect of construction details and FRP characteristics on the flexural performance of RC beams strengthened with NSM reinforcement (bars /strips). The results of the RC beams tested in this series were compared to some of the beams tested in the first series. The results are reported in Table 7.2 and discussed in the following sections.

Table 7.2: Results of the tested RC beams (second series).

Beam ID	P_y (kN)	η_y (%)	P_u (kN)	η_u (%)	δ_u (mm)	$\frac{\epsilon_f}{\epsilon_{fu}}$ (%)	Failure mode
CB	64.5	—	70.4	—	50.8	—	Y
LB1C1	80.1	24.2	109.1	55.0	31.7	66.0	C-E
LB2S1	87.4	35.5	111.7	58.7	24.7	51.4 ^a	S-E
LB2S2	87.3	35.3	118.5	68.3	30.6	60.3 ^a	S-E
LB2C1	100.5	55.8	117.2	66.6	20.3	39.6	CC _s
LB2C1IS	106.5	65.1	137.9	95.9	25.7	52.4	CC _s
LB2C1T	99.6	54.4	156.0	121.6	36.2	71.7	CC _s ,T
LB2S1+C1	103.2	60.0	119.7	70.0	20.4	37.3 ^a , 33.5	CC _s
LB2S1+G1	102.4	58.8	120.7	71.4	21.8	45.1 ^a , 55.1	CC _s
LB1G2	83.7	29.8	105.8	50.3	35.3	71.1	C-E
LB1G2IS	85.1	31.9	130.4	85.2	52.8	97.8	CC
LB1G2T	86.4	34.0	135.0	91.8	55.5	97.8	CC

CC_s= concrete cover separation, C_s = concrete splitting, C-E = concrete-epoxy interface failure, S-E = strip -epoxy interface failure, T= transverse sheet debonding or rupture, Y= yielding and a = strain in FRP strips respectively.

7.3.1 Mode of failure and load deflection curves

7.3.1.1 Effect of NSM shape, dimensions and area

The tested beams experienced dissimilar modes of failure according to the type and dimensions of FRP reinforcement and the applied modification (see Fig. 7.17). Although the three beams LB1C1, LB2S1 and LB2S2 have nearly the same area and properties, the mode of failure of beam LB1C1 was epoxy concrete interface failure (Fig. 7.2a) while for the two beams LB2S1 and LB2S2 were strip-epoxy

interface failure (Fig. 7.17a). The beam LB2C1 having twice the NSM area of the beam LB1C1 failed by concrete cover separation (Fig. 7.2b). The shape of the NSM reinforcement affected the mode of failure and failure load with insignificant effect on the deflection (see Table 7.2). For beams strengthened with CFRP strips, as the depth of the groove decreased the maximum load increased.

The maximum load capacity of the two beams LB2S2 and LB2S1 increased by 68.3 % and 58.7 % over the CB respectively. Moreover, although the two beams L2S2 and LB1C1 had the same groove depth, the percentage of increase of 24.2 % and 35.3 % in the yield load and 68.3 % and 55 % in the maximum load over the CB respectively.

On the other hand, doubling the area of NSM bars increased the yield load of the beam LB2C1 by 16.8 % and 20.4 % with respect to the CB over that achieved by the two beams LB2S2 and LB1C1 respectively while the maximum load of two beams LB2S2 and LB2C1 was nearly the same. From the above it was observed that the NSM strips were more efficient than the NSM bars in terms of load capacity and stiffness.

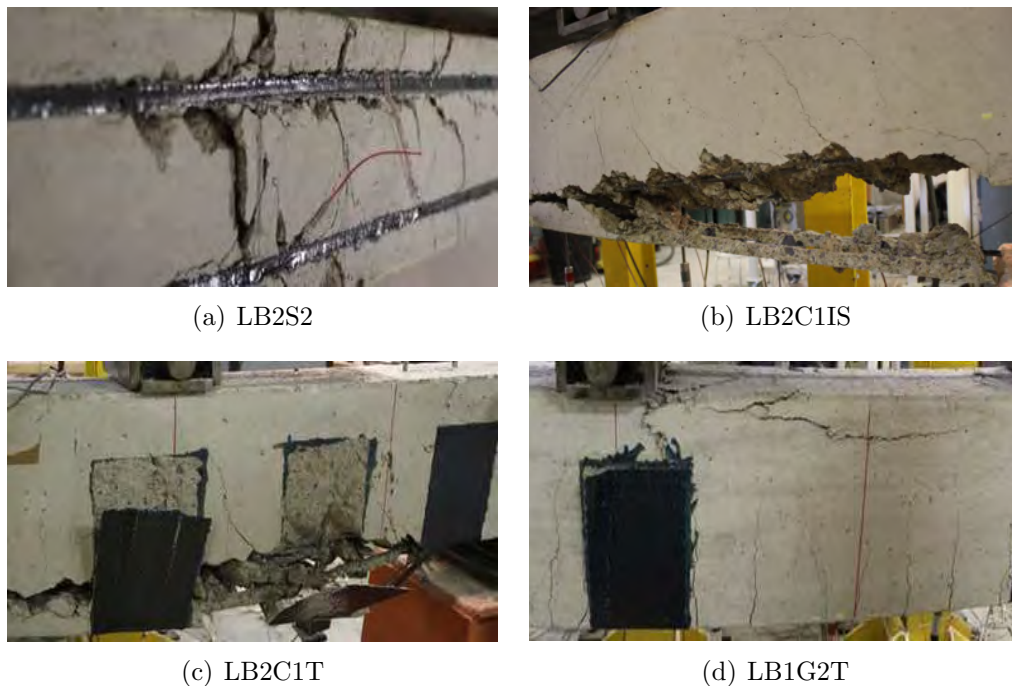


Figure 7.17: Modes failure of the tested RC beams.

Fig. 7.18 shows the load deflection curves of the beams strengthened with NSM CFRP reinforcement. The curves are described by concrete cracking, yield of internal steel and post-yielding stages (i.e. approximately tri-linear response).

The effect of NSM area, shape and dimension on the three stages of the load deflection curves is clearly shown in Fig. 7.18. The stiffness of beams strengthened with NSM strips was higher than that of beams with C1 bars having the same area, while the effect of NSM area on the beam stiffness was observed especially through the post-yielding stage for beam LB2C1.

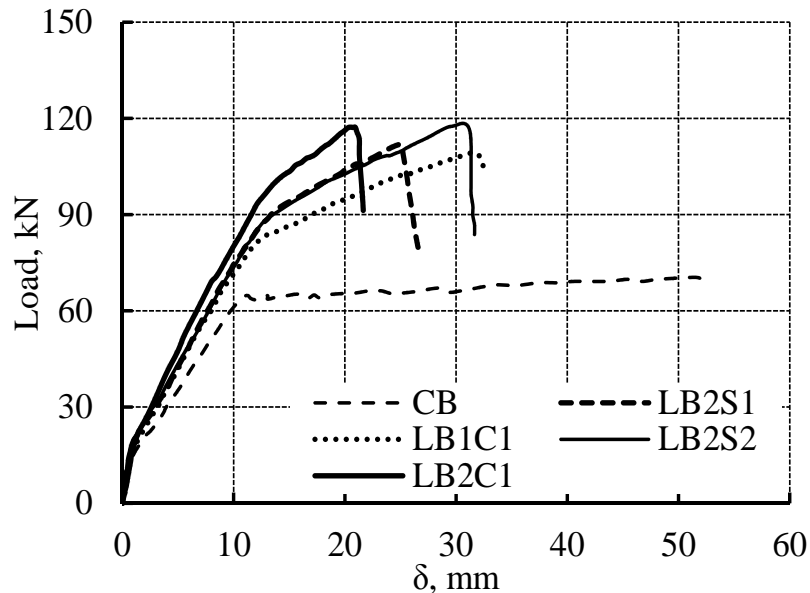


Figure 7.18: Effect of NSM shape, dimensions and area on the load deflection curve of the strengthened beams.

7.3.1.2 Effect of NSM material and arrangement

Fig. 7.19 shows the effect of NSM arrangement on the load deflection curve of the tested RC beams. The three beams LB2C1, LB2S1+C1 and LB2S1+G1 follow nearly the same load deflection response although they have different NSM reinforcement as the failure was concrete cover separation at cut off of the NSM reinforcement (Fig. 7.17b). The effect of G1 bar in specimen L2S1+G1 was obvious at failure as the deflection increased with constant load.

On the other hand, the effect of the modulus of elasticity is also shown in Fig. 7.19, although the area of NSM reinforcement of beam LB1G2 is equal to that of the previous three beams LB2C1, LB2S1+C1 and LB2S1+G1, it had lower yield and failure loads and stiffness

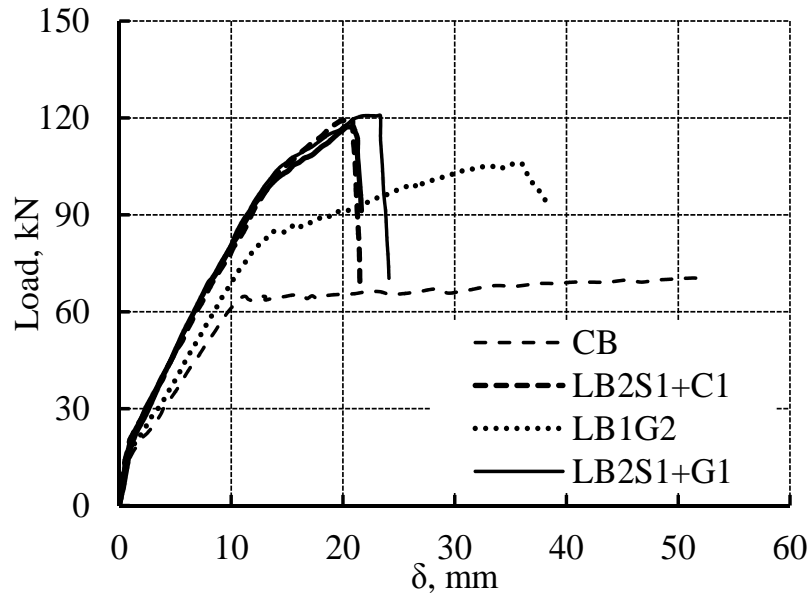


Figure 7.19: Effect of NSM material and arrangement on the load deflection curve of the strengthened beams.

7.3.1.3 Effect of mechanical interlocking with shear connectors and transverse wrapping

Beam strengthened with CFRP bars. This section deals with the effects of mechanical interlocking with shear connectors and transverse wrapping on the failure load, mode of failure and load deflection response of beams with C1 bars. The mode of failure of the three beams LB2C1, LB2C1T and LB2C1IS was concrete cover separation after the transverse sheet debonding or failure of the epoxy filling the grooves for mechanical interlocking (Figs. 7.17b and d).

The beam LB2C1T experienced higher load capacity than the two beam LB2C1IS and LB2C1 as the transverse wrapping confined the beam and delayed the concrete cover separation. The mechanical interlocking with shear connectors increased the

stiffness and yield load of the beam with two C1 bars (see Fig. 7.20) as the effect of connectors decreased deflection and delayed the concrete cover separation.

The maximum load capacity of three beams LB2C1, LB2C1IS and LB2C1T increased by 66.6 %, 95.9 % and 121.6 % over the CB respectively although they had the same yield load.

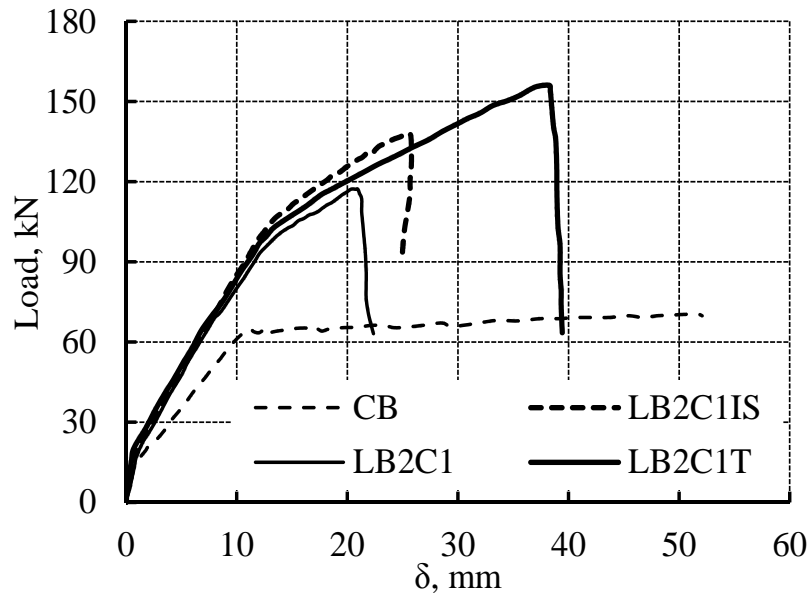


Figure 7.20: Effect of mechanical interlocking with shear connectors and transverse wrapping on the load deflection curve of the strengthened beams with CFRP bars.

Beam strengthened with GFRP bars. In this section the effects of mechanical interlocking with shear connectors and transverse wrapping on the failure load, mode of failure and load deflection response of beams with G2 bars is discussed. The mode of failure of the beam LB1G2 was concrete-epoxy interface failure while for beams LB1G2IS LB1G2T (Figs. 7.9d and 7.17d) was concrete crushing. The beam Lb1G2T and Lb1G2IS experienced higher load capacity than the beam LB1G2. The increase in the failure load was 50.3 %, 85.2 % and 91.8 % for the three beams LB1G2, LB1G2IS and LB1G2T over the control beam respectively with a slight increase in the yield load. The confinement introduced by transverse wrapping and mechanical interlocking prevented the cracks to propagate longitudinally at the concrete-epoxy interface.

In contrast, the specimen with C1 bars and IS (LB2C1IS) had high effect on the stiffness and yield load compared to that achieved by the beam with one G2 bar (LB1G2IS) when compared with the same beams with transverse wrapping LB2C1T and LB1G2T respectively (see Fig. 7.21). This means that the deformation of epoxy filled the transverse interlocking of specimen with G2 bar increased the slip at the concrete-epoxy interface. Also the two beams LB1G2IS and LB1G2T showed that 2000 mm was the bonded length at which nearly the two beams achieved their maximum capacity ($\eta_\varepsilon = 97.8\%$ when the concrete crashed).

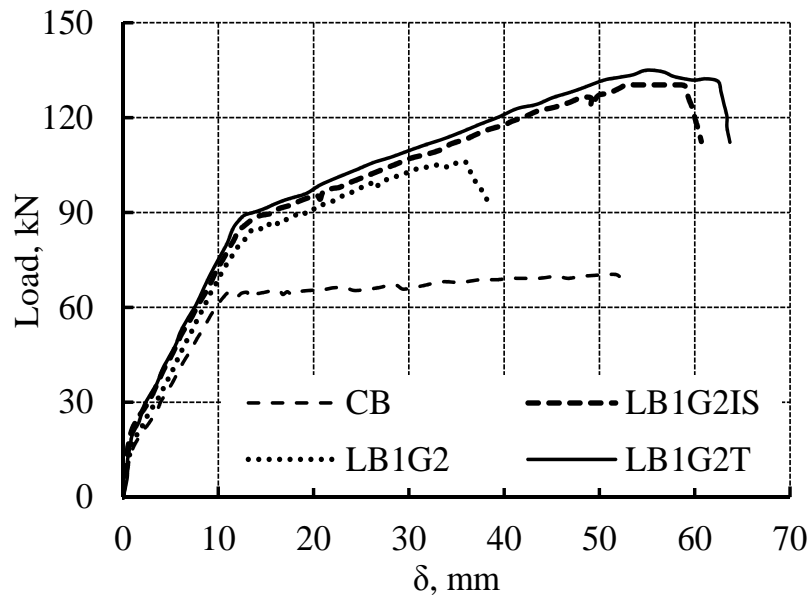


Figure 7.21: Effect of mechanical interlocking with shear connectors and transverse wrapping on the load deflection curve of the strengthened beams with GFRP bars.

7.3.2 Effect of NSM FRP reinforcement (FRPR) on the stiffness of the beams

Fig. 7.22 shows a comparison of the relative stiffness of the beams strengthened with various NSM reinforcements and the effect of construction details at two different load levels. The stiffness of the beams increased as the area and modulus of elasticity of the NSM FRP bars increased. Moreover the use of transverse wrapping and mechanical interlocking increased also the stiffness of the beams.

The transverse confinement (IS or T) prevented the NSM slip and delayed the concrete cover separation thus decreasing the deflection of the beams.

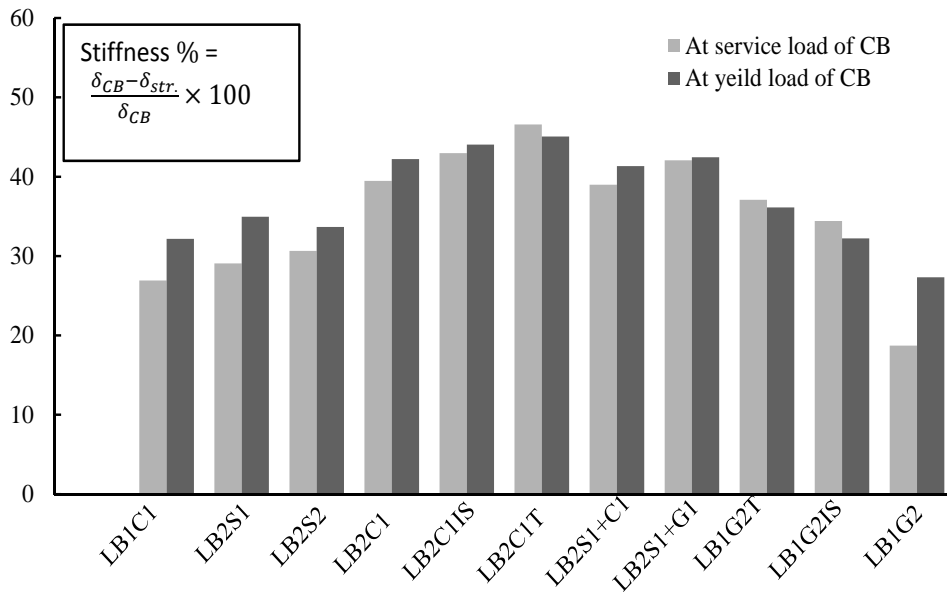


Figure 7.22: Comparison of stiffness of strengthened beams at service load and at yielding load of the CB.

7.3.3 Strain distribution along the FRP reinforcement

For more details about the bond behaviour and response of the RC beams strengthened with NSM reinforcement, the strain distribution along half of embedded length of NSM FRP reinforcement (see Fig. 6.8, x is starting at the free end of NSM reinforcement, $L_1 = L/2$) were recorded and the results are shown in Fig. 7.23. The recorded strain for all the beams presented a relevant increment of increase once the yield load is attained. After yielding the modulus of the steel bars present a drastic reduction while that of the FRP reinforcement E_f remains constant, so the tensile forces in the FRP reinforcement increase. On the other hand, the confinement of the tested beams using IS or T reduced the strain in the NSM CFRP bars.

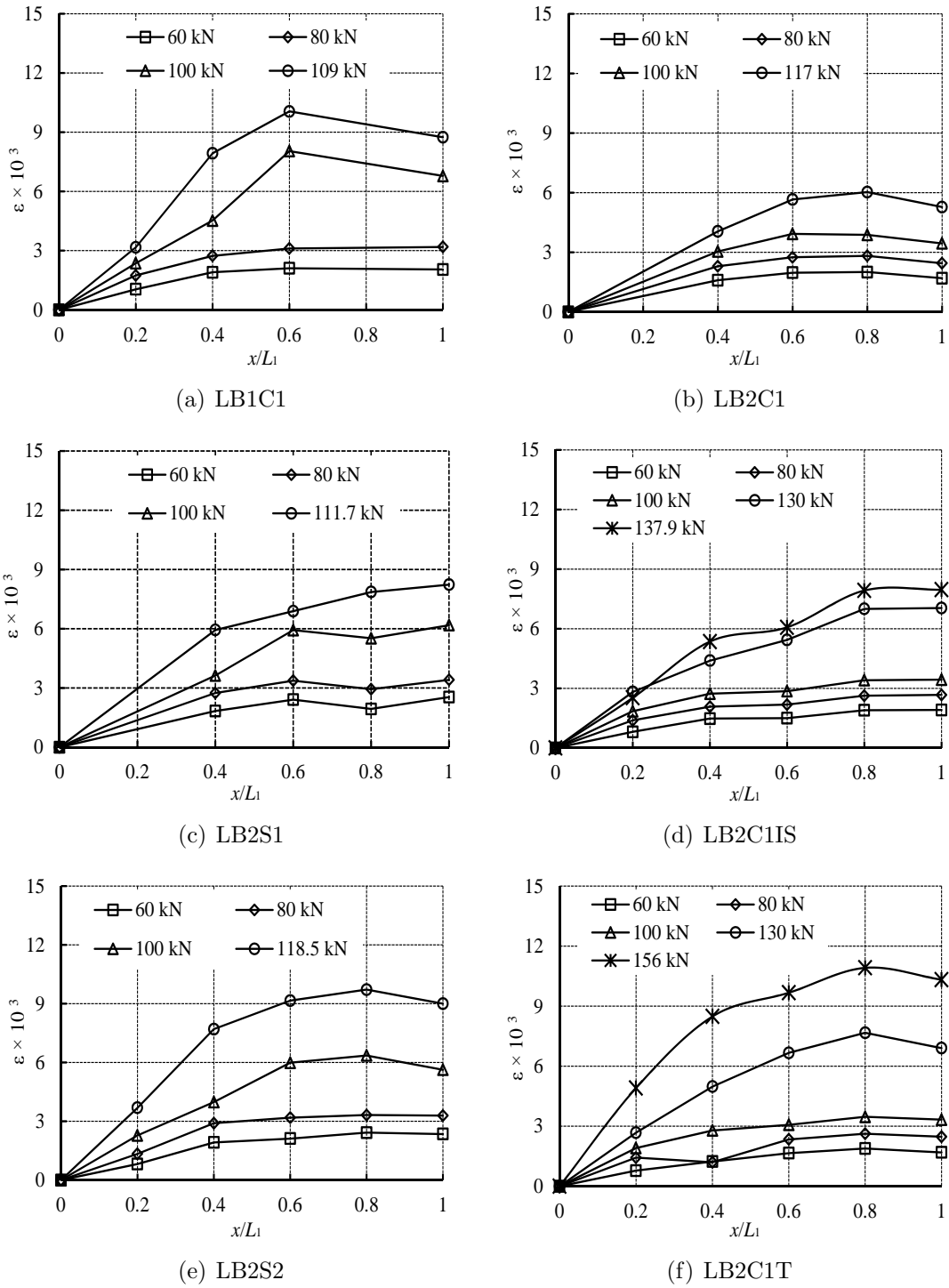


Figure 7.23: Strain distribution along half of the CFRP reinforcement.

Fig. 7.24 shows the effect of NSM combination (i.e. bars and strips) on the recorded strain in the FRP reinforcement. The strain recorded for beam LB2S1+C1 was lower than that recorded for beam LB2S1+G1 as the G1 bar had lower E_f than the C1 bars. For beam LB2S1+G1 the recorded strain in the G1 bar was equal or higher than that in S1 strips in contrast for beam LB2S1+C1, this may have been due to the relative slip between the strips and the bars.

Fig. 7.25 shows the strain recorded for the beams strengthened with G2 bars. The recorded strain in the G2 bars for the three beams was nearly equal before the yielding of steel bars. After yielding, the recorded strain for the beams with IS and T (LB1G2IS and LB1G2T) was lower than that for beam LB1G2 as the confinement delayed the concrete cracking that decreasing the forces transferred to the NSM bars.

The black markers showed the load and position at which the strain gauges recorded a strain value equals to 0.0163(97.8 % of the maximum strain of the GFRP bars) and this strain value the strain gauge stopped recording. This may be due to the failure of the grooved surface of the G2 bars

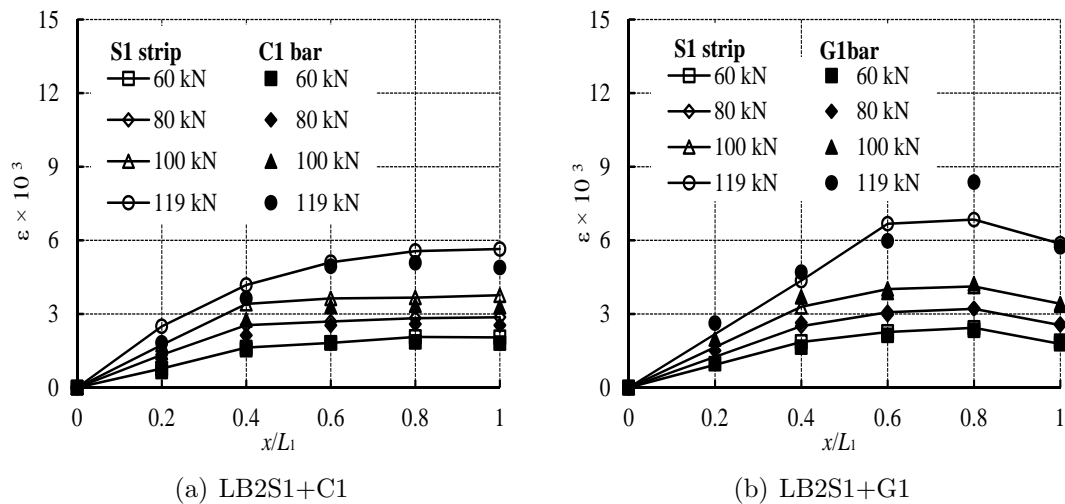


Figure 7.24: Strain distribution along half of the FRP reinforcement.

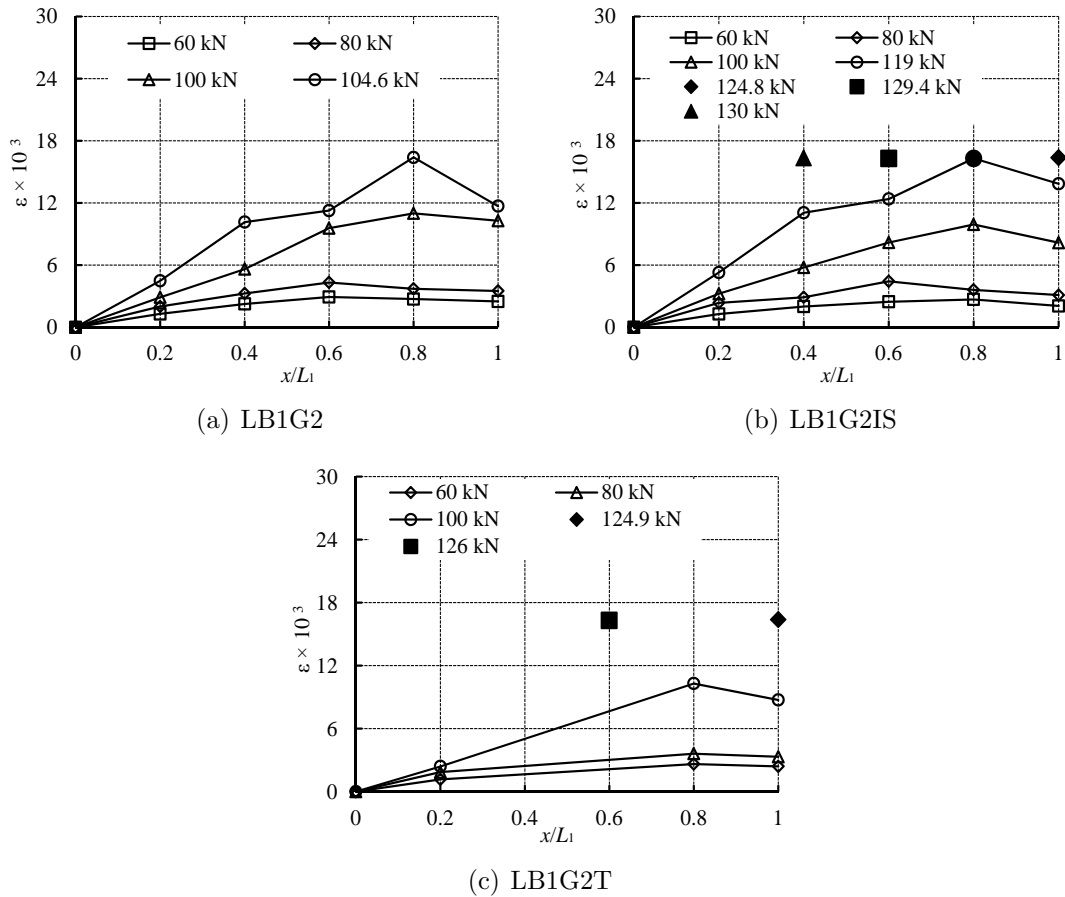


Figure 7.25: Strain distribution along half of the GFRP bars.

7.3.4 Compressive strain in concrete

Figs. 7.26 - 7.28 show the compressive strain in concrete recorded by the three strain gauges SG-c1, SG-c2, and SG-c3. The load strain curves followed the same response as the load deflection curves of the beams. The highest compressive strain was recorded by the strain gauge SG-c1 located at the extreme fibre of the beams. On the other hand, as the area of C1 bars increased the compressive stress in concrete decreased especially after yielding (Figs. 7.26a, b, d and f). The compressive strains also decreased when using CFRP strips (LB2S1 and LB2S2, Figs. 7.26c and e) instead of C1 bars (LB1C1). The effect of combined NSM FRP reinforcement (FRPR) on the compressive stresses in concrete is shown in Fig. 7.27. The effect of E_f of the C1 bar decreased the compressive strain obviously after the yielding of

the beams. On the other hand, a slight effect of the IS and T on the compressive strain is observed (Fig. 7.28).

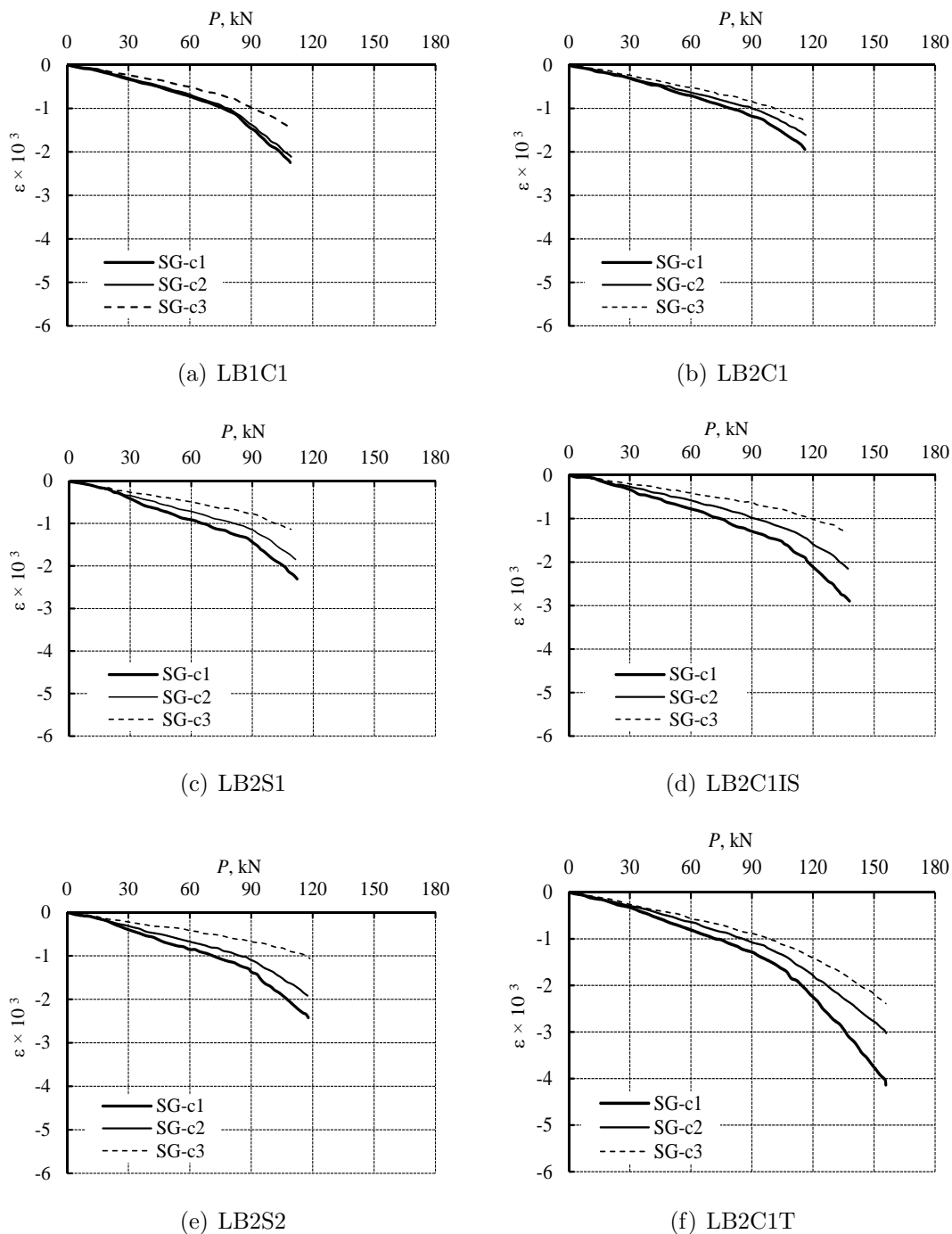


Figure 7.26: Compressive strain in concrete for beams with CFRP reinforcement.

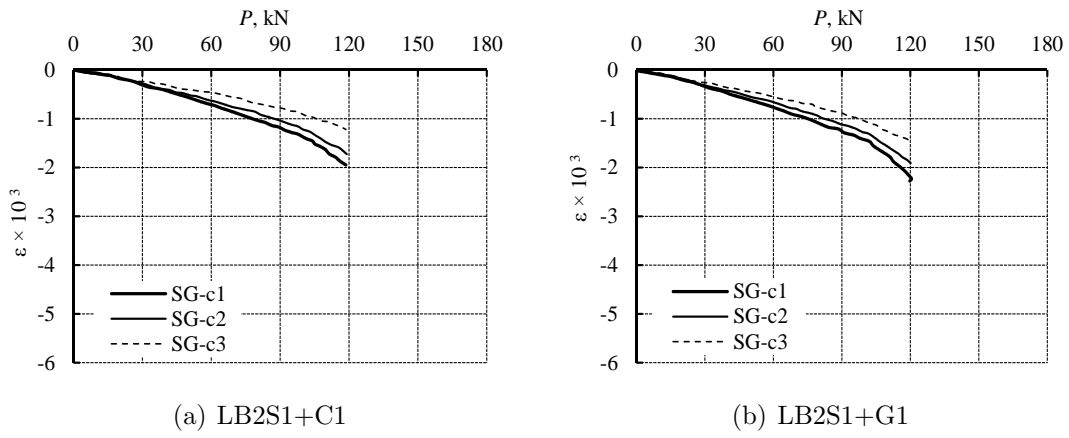


Figure 7.27: Compressive strain in concrete for beams with combined FRPR.

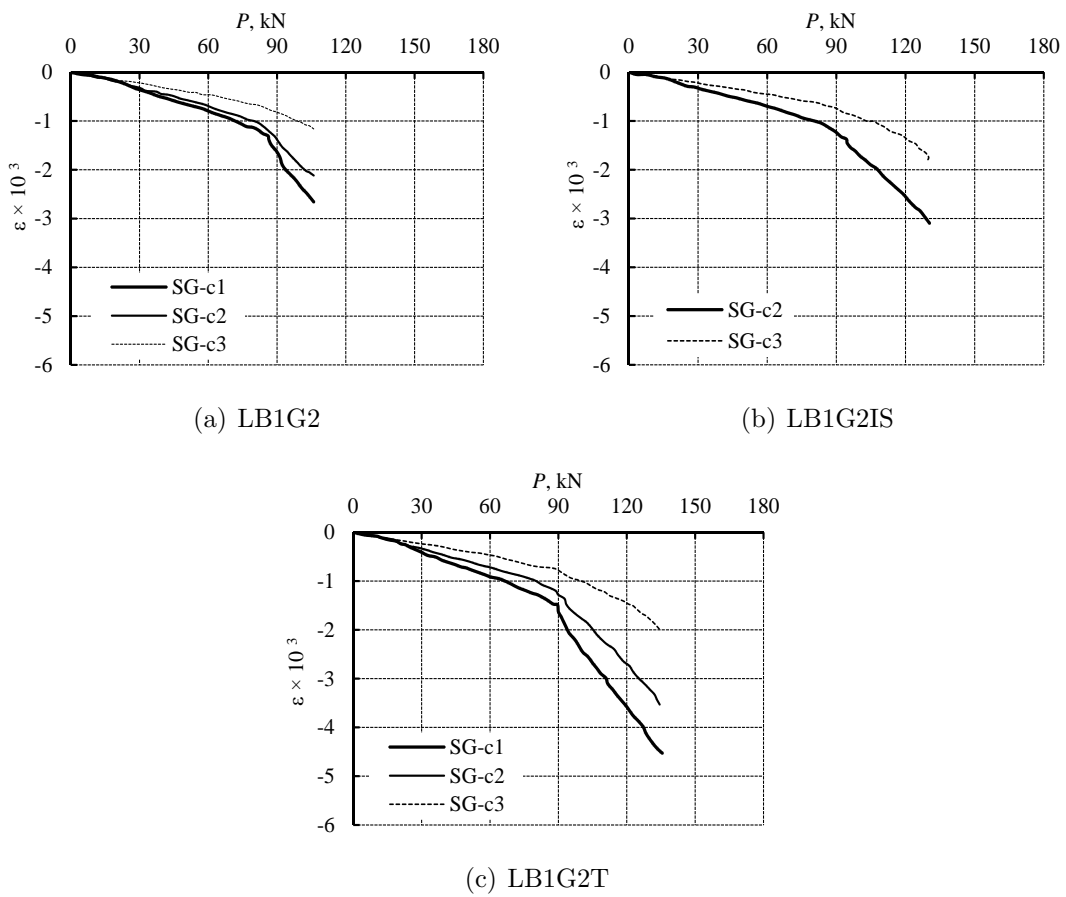


Figure 7.28: Compressive strain in concrete for beams with GFRP bars.

7.3.5 Deflection distribution and stiffness

The deflection distribution along the span of the beams recorded using five LVDTs 400 mm apart as described before in Fig. 6.8. At the same load level, the estimated stiffness of the beams can be compared through the values of deflections. The rate of increment in the deflection increased after the yield load of the beams was reached. The effect of E_f of the G1 on the deflection of the beam LB2S1+G1 compared to LB2S1+C1 was obvious just before failure (Fig. 7.29). On the other hand, Fig. 7.30 shows the effect of shape, area, mechanical interlocking and transverse wrapping on the stiffness of the strengthened beams with CFRP reinforcement.

The beams with NSM strips achieved lower deflection than that of NSM bars having nearly the same E_f (see Fig. 7.30). Moreover as A_f or E_f increased the stiffness of the beams increased and thus the deflection decreased (Figs. 7.30 and 7.31). Finally the use of IS or T decreased the deflection of the beams by increasing the confinement of concrete and composite action of the beams and decreasing the NSM slip (Figs. 7.30 d, f, 7.31b and c).

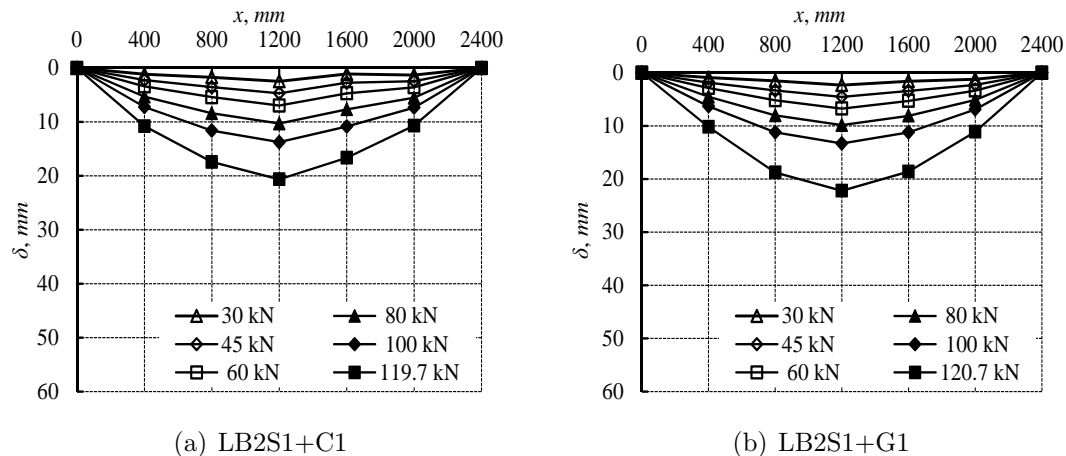
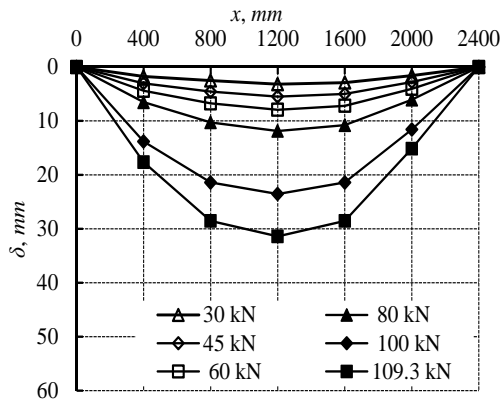
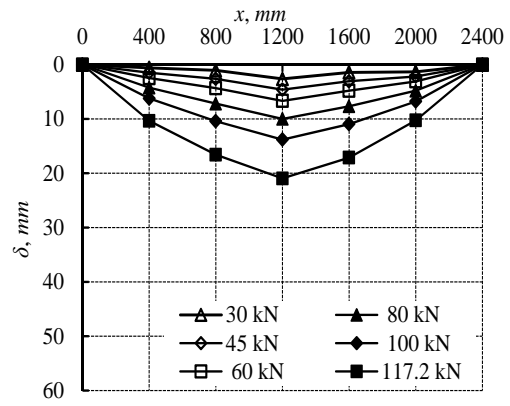


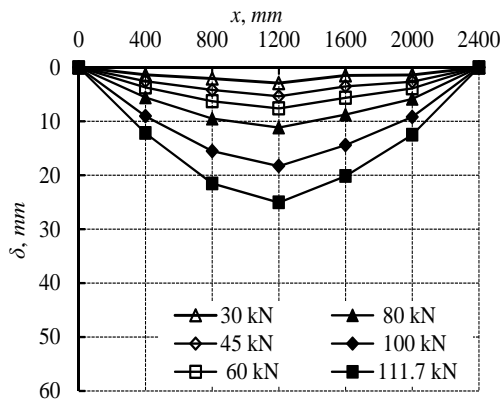
Figure 7.29: Deflection of beams strengthened with combined NSM FRP reinforcement.



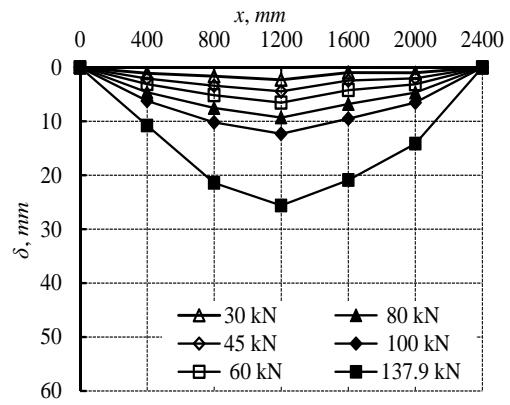
(a) LB1C1



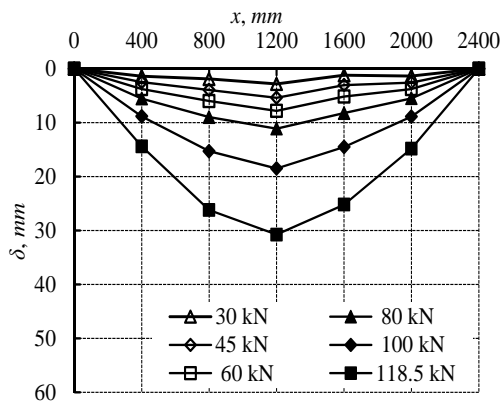
(b) LB2C1



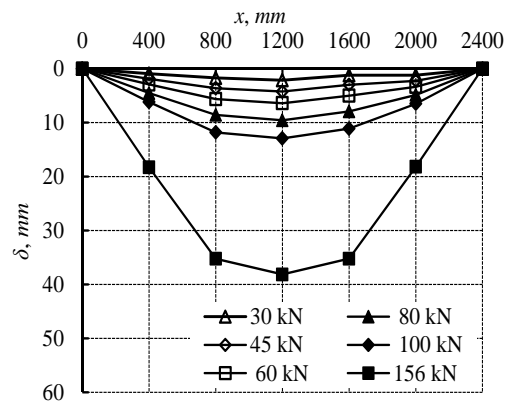
(c) LB2S1



(d) LB2C1IS



(e) LB2S2



(f) LB2C1T

Figure 7.30: Deflection of beams strengthened with NSM CFRP reinforcement.

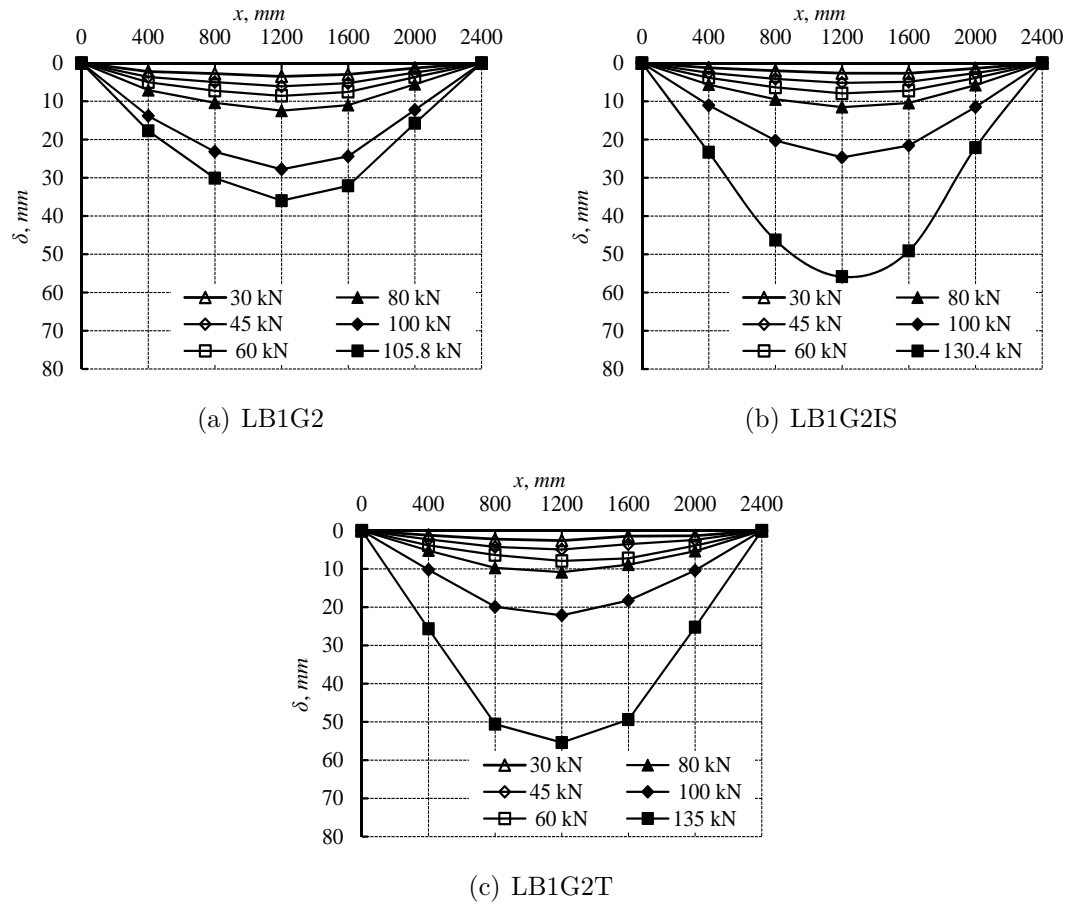


Figure 7.31: Deflection of beams strengthened with NSM GFRP bars.

7.3.6 Conclusions

An experimental programme of flexural tests on eleven RC strengthened beams and one additional un-strengthened control beam was performed to study the effect of construction details and FRP characteristics on the flexural performance of RC beams strengthened with NSM reinforcement (bars /strips). From the results the following conclusions can be drawn:

- For beams strengthened with CFRP strips, as the depth of the groove decreased from 25 to 16 mm for the two beams LB2S2 and LB2S1 respectively, the maximum load increased as the concrete thickness between the NSM strips and the internal steel increased. The maximum load capacity of the two beams LB2S2 and LB2S1 increased by 68.3 % and 58.7 % over the CB respectively.

Moreover, although the two beams LB2S2 and LB1C1 had the same groove depth, the percentage of increase of 24.2 % and 35.3 % in the yield load and 68.3 % and 55 % in the maximum load over the CB respectively.

- Doubling the area of NSM bars increased the yield load of the beam L2C1 by 16.8 % and 20.4 % with respect to the CB over that achieved by the two beams LB2S2 and LB1C1 respectively while the maximum load of two beams LB2S2 and LB2C1 was nearly the same. The three beams LB2C1, LB2S1+C1 and LB2S1+G1 followed nearly the same load deflection response although they had different NSM FRP reinforcement as the failure was concrete cover separation at cut off of the NSM reinforcement.
- The beam LB2C1T experienced higher load capacity than the two beam LB2C1IS and LB2C1 as the transverse wrapping confined the beam and delayed the concrete cover separation. The mechanical interlocking with shear connectors increased the stiffness and yield load of the beam with two C1 bars as the effect of connectors decreased deflection and delayed the concrete cover separation. The maximum load capacity of three beams LB2C1, LB2C1IS and LB2C1T increased by 66.6 %, 95.9 % and 121.6% over the CB respectively although they had the same yield load.
- The beam LB1G2T and LB1G2IS experienced higher load capacity than the beam LB1G2. The increase in the failure load was 50.3 %, 85.2 % and 91.8 % for the three beams LB1G2, LB1G2IS and LB1G2T over the control beam respectively, with a slight increase in the yield load. The confinement introduced by transverse wrapping and mechanical interlocking prevented the cracks to propagate longitudinally at the concrete-epoxy interface.
- The specimen with C1 bars and IS (LB2C1IS) had high effect on the stiffness and yield load compared to that achieved by the beam with one G2 bar (LB1G2IS) when compared with the same beams with transverse wrapping LB2C1T and LB1G2T respectively. The stiffness of the beams increased as the area and modulus of elasticity of the NSM FRP bars increased. Moreover the use of transverse wrapping and mechanical interlocking increased also the stiffness of the beams.

7.4 Results and discussion of the third series

In this series eight strengthened RC beams were prepared and tested in addition to un-strengthened beam (CB). The beams were strengthened with partially bonded NSM reinforcement to study the effect of construction details and FRP characteristics on the flexural performance. The result of the tested beams in this series have been compared to the result of the beams tested in the first and the second series. All the result are reported in Table 7.3.

Table 7.3: Results of the tested RC beams (third series).

Beam ID	P_y (kN)	η_y (%)	P_u (kN)	η_u (%)	δ_u (mm)	Failure mode
CB	64.5	—	70.4	—	50.8	Y
SB2C1	85.5	32.6	85.5	21.4	12.7	CCs
MB2C1	85.3	32.2	97.6	38.6	16.1	CCs
MB2C1ES	93.6	45.1	121.8	73.1	23.3	CCs
LB1C1	100.5	55.8	117.2	66.5	20.3	CCs
MB2S1	83.4	29.3	94.3	34.0	18.0	S-E
LB2S1	87.4	35.5	111.7	58.7	24.7	S-E
SB2G1	74.3	15.2	84.5	20.0	20.3	CCs
MB2G1	73.5	14.0	100.0	42.0	33.2	CCs
LB2G1	82.3	27.6	112.2	59.4	42.4	CCs
MB1G2	76.3	18.3	98.4	39.8	28.0	CCs
MB1G2T	77.2	19.7	117.3	66.6	47.0	T
LB1G2	83.7	29.8	105.8	50.3	35.3	E-C
LB1G2T	86.4	34.0	135.0	91.8	55.5	CC

CC = concrete crushing, CCs = concrete cover separation, Cs = concrete splitting, C-E = concrete-epoxy interface, T = transverse sheet debonding or rupture and Y = yielding.

7.4.1 Load deflection curves and mode of failure

7.4.1.1 Effect of bond length

In this section the effect of bond length on the yielding load, maximum load and mode of failure of the RC beams strengthened with NSM reinforcement is discussed. Four types of NSM FRP reinforcement (C1, S1, G1 and G2) were used with a limited

length of 2000 mm for all beams. Some of the beams were strengthened with partially bonded length ($M = 480$ mm and $S = 384$ mm) and others were strengthened with the total length 2000 mm. Fig. 7.32 shows the load deflection curves of the tested RC beams. It is seen that as the bond length decreased the stiffness and the load capacity of the beams decreased while the deflection increased. The beam SB2C1 failed at its yielding load. The failure of the beams strengthened with NSM C1 bars was concrete cover separation starting at the cutoff of the bars (Fig. 7.33a) although the position of the cut off was changed. The beams strengthened with S1 strips failed at the strip epoxy interface. On the other hand, the failure of the beams strengthened with G1 and G2 bars was concrete cover separation except for beam LB1G2 that failed by concrete-epoxy interface failure (Fig. 7.33b) .

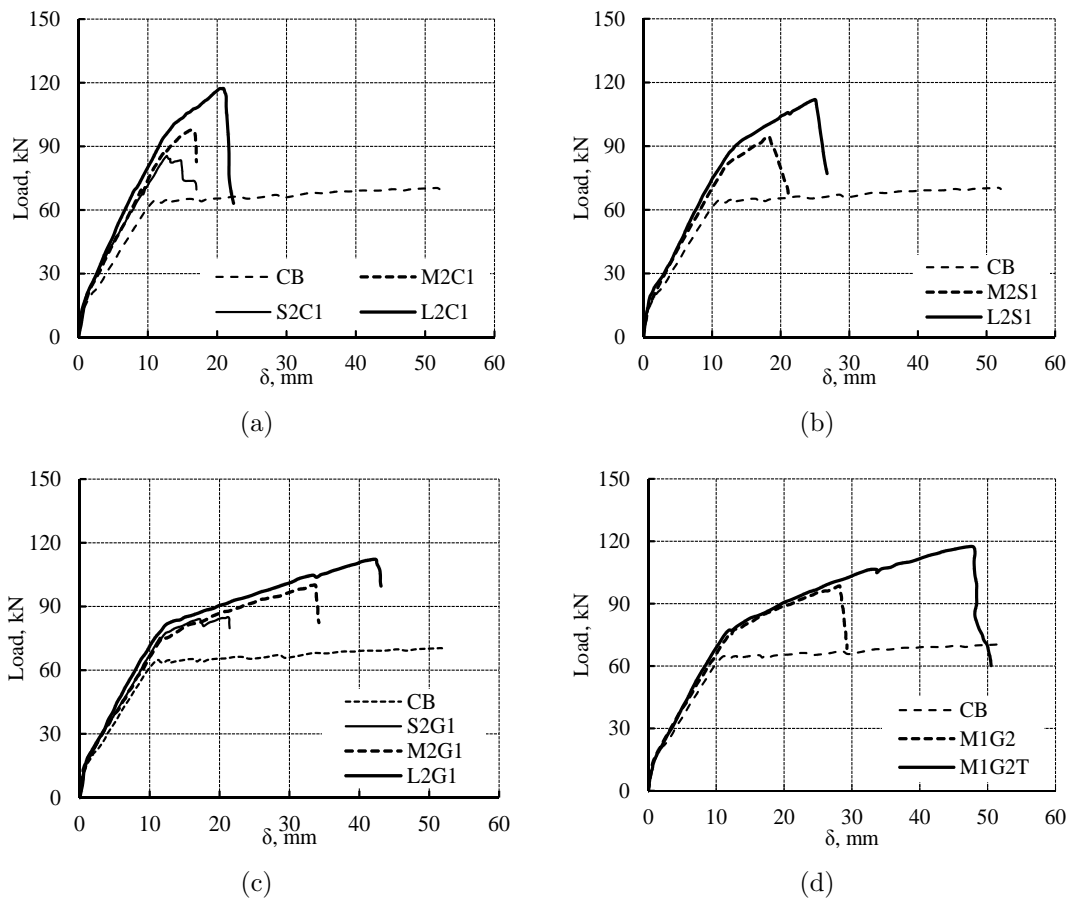


Figure 7.32: Effect of bond length on the load deflection curve of the strengthened beams: (a) C1 bars, (b) S1 strips, (c) G1 bars and (d) G2 bars.

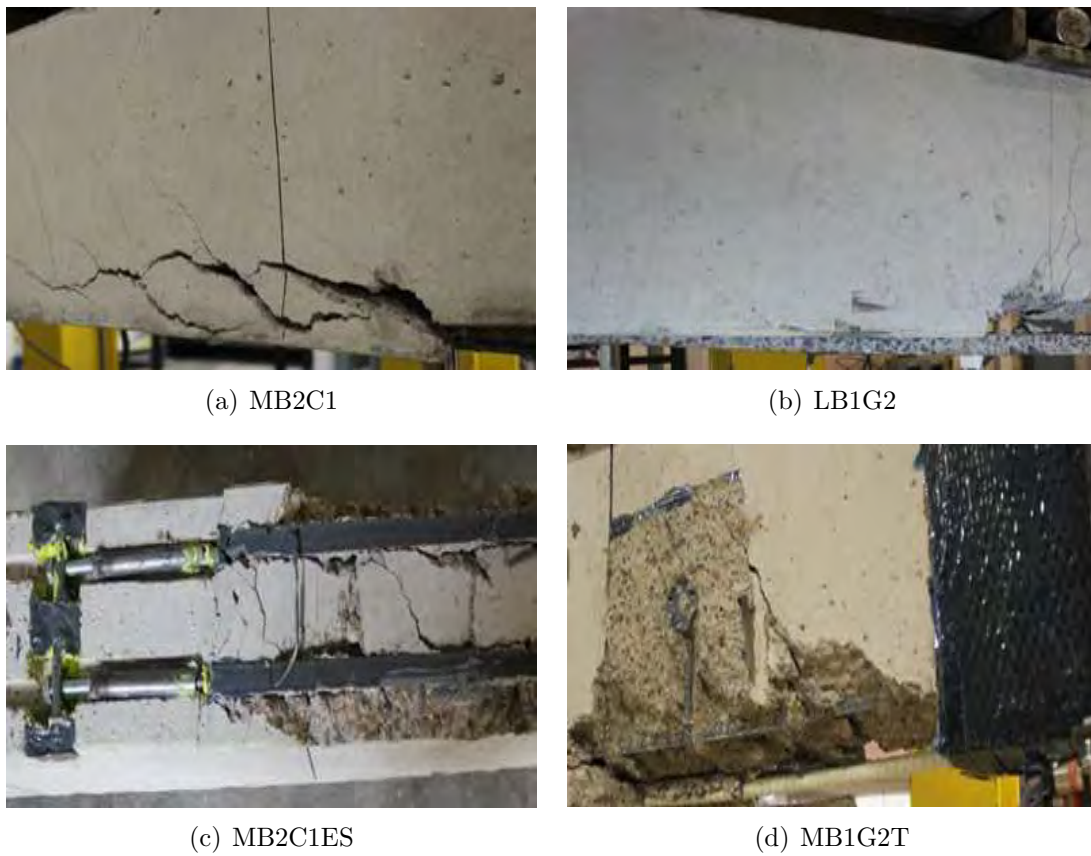


Figure 7.33: Modes of failure of the tested RC beams.

7.4.1.2 Effect of end anchorage and transverse wrapping

As was explained in the previous sections, the critical failure mode of the strengthened beams with partially bonded NSM reinforcement was concrete cover separation. To enhance the load capacity of those beams, two different methods were used to delay or prevent this kind of failure: end supporting of the NSM bars for beams with C1 bars (beam LB2C1ES) and transverse wrapping for beams strengthened with G2 bars (beams MB1G2T and LB1G2T) as shown in Fig. 6.18.

Fig. 7.34 shows the effect of end anchorage and transverse wrapping on the load deflection of the beams. It is seen that the load capacity of the beams MB2C1 and MB2C1ES increased by 38.6 % and 73.1 % over the CB respectively. The beam MB2C1ES failed by concrete cover separation after the FRP bars pulled out from the steel tubes as shown in Fig. 7.33c.

On the other hand the load capacities of the two beams MB1G2T and LB1G2T increased by 66.6 % and 91.8 % while the load capacity of two beams MB1G2 and LB1G2 increased by 39.8 % and 50.3 % over the CB respectively which demonstrated the effect of transverse wrapping.

The mode of failure of beams MB1G2T and LB1G2T was transverse wrapping debonding followed by concrete cover separation (see Fig. 7.33d). Moreover, the stiffness of the beams with end anchorage and transverse wrapping was also increased (see Fig. 7.34).

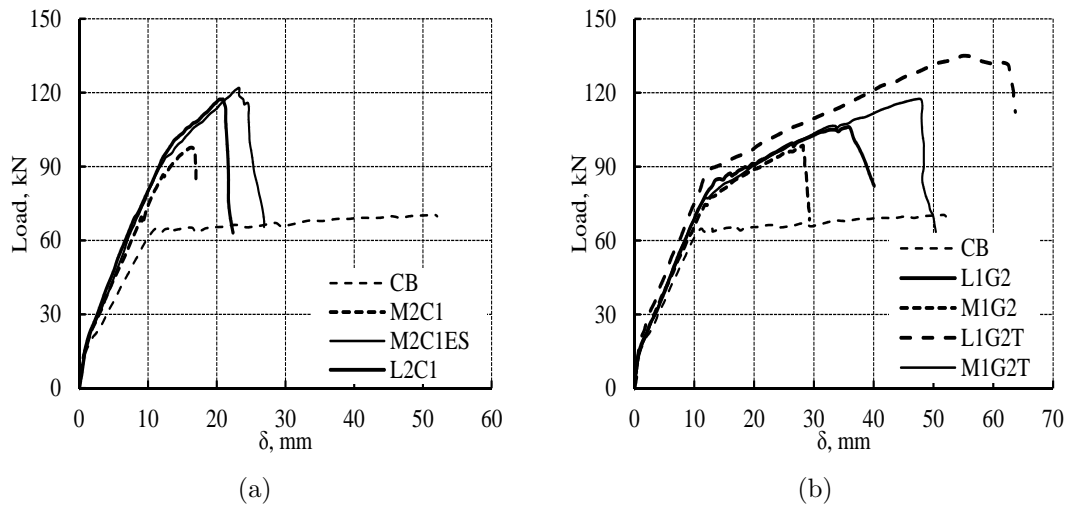


Figure 7.34: Effect of end anchorage of the NSM bars and transverse wrapping on the load deflection curve of the strengthened beams: (a) C1 bars and (b) G2 bars.

7.4.2 Strains in the NSM FRP reinforcement

The NSM FRP reinforcement was instrumented with number of strain gauges, the first strain gauge was glued at the center of the beam and the rest of the strain gauges were arranged as shown in Fig. 6.8. Some of strain gauges were located in the bonded part and others located in the unbonded part depending on the bond length that started from the loaded points and extended towards the support. The load strain curves followed a similar response to the load deflection curves especially for the strain gauges located in the pure bending moment region (see Figs. 7.35 - 7.38).

The recorded strains increased as the area, and modulus of elasticity of the NSM reinforcement decreased. Beyond the yielding load, the slope of load strain curves of the beams with GFRP bars was higher than that of the beams with GFRP bars. The strain in the beam MB2C1ES with NSM bars supported at its ends was also higher than that of the beam MB2C1, but in contrast there was no effect of the transverse wrapping on the strain values of beams with G2 bars. These recorded strains may be helpful to produce the local bond stress along the bond lengths of the RC beams as in pullout tested.

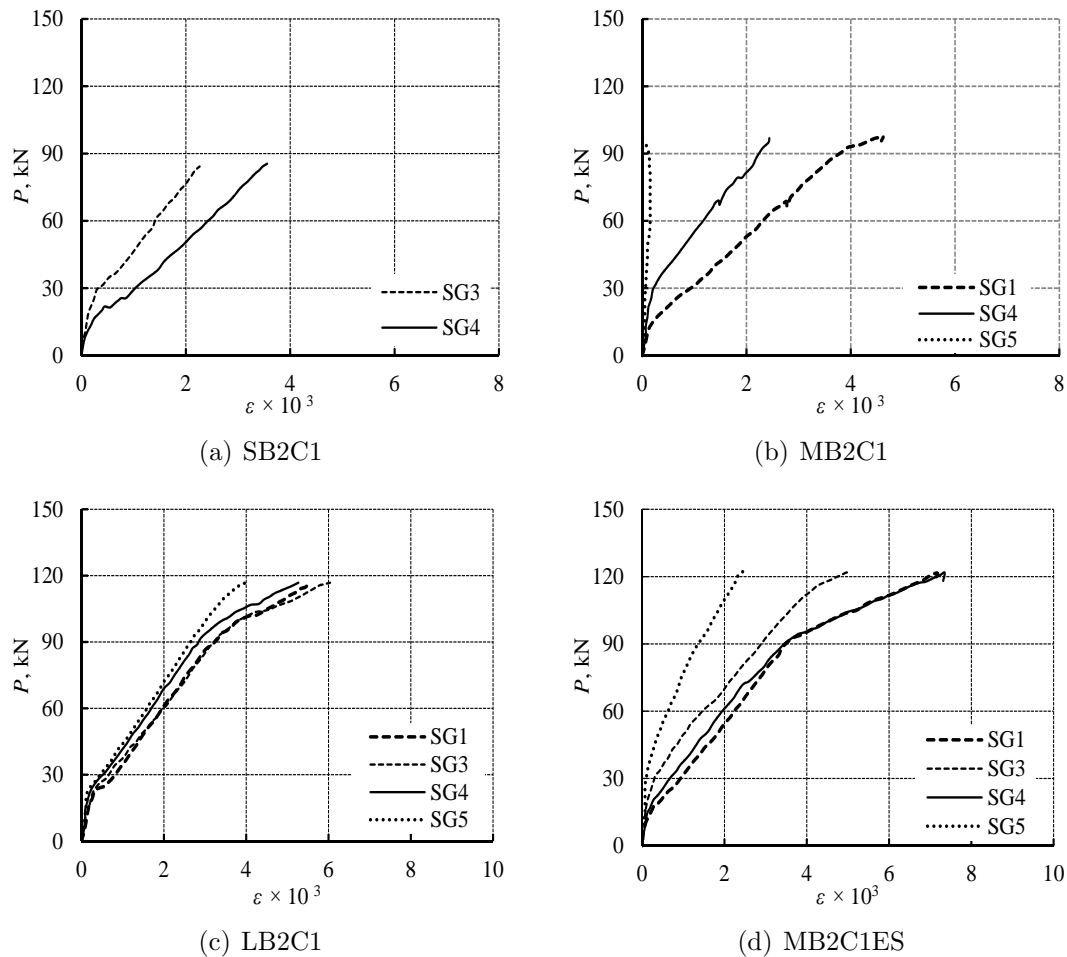


Figure 7.35: Strain in the NSM CFRP bars.

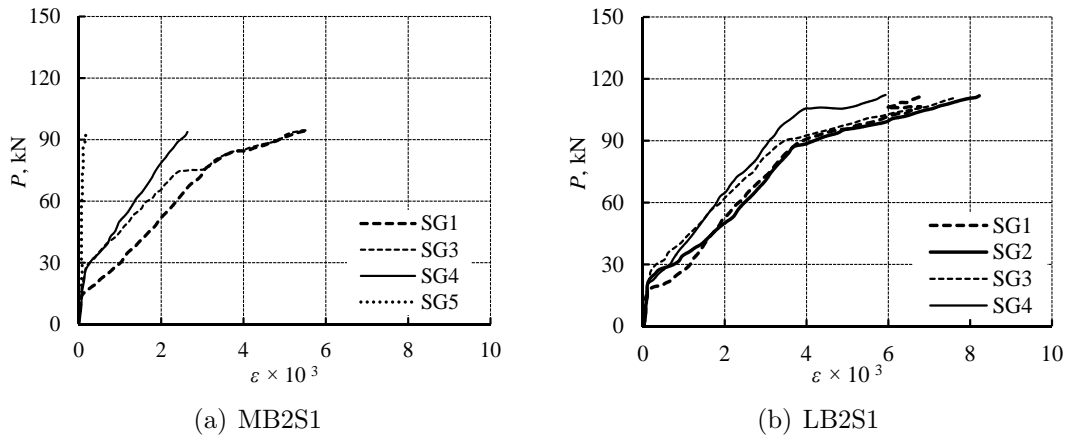


Figure 7.36: Strain in the NSM CFRP strips.

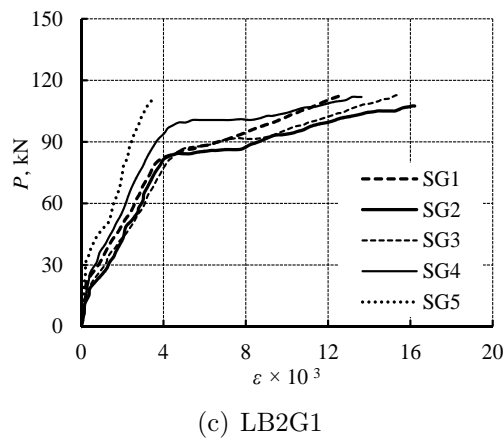
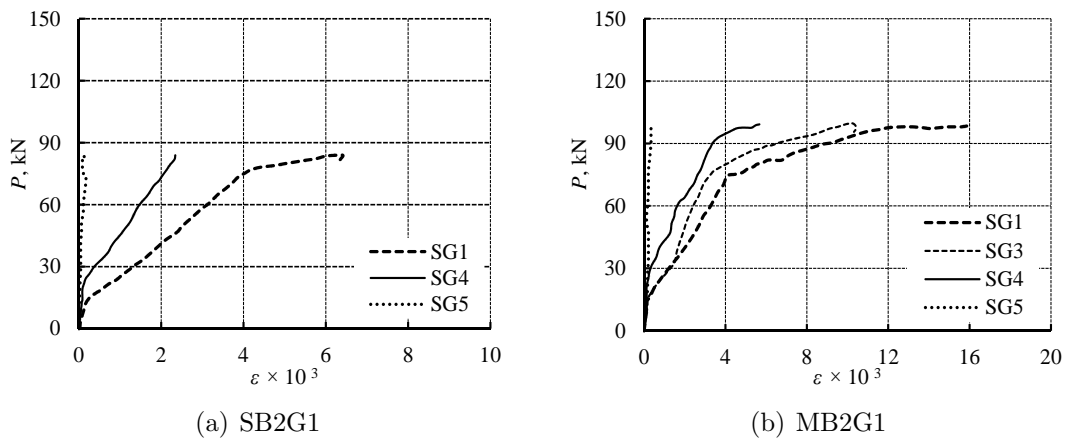


Figure 7.37: Strain in the NSM G1 bars.

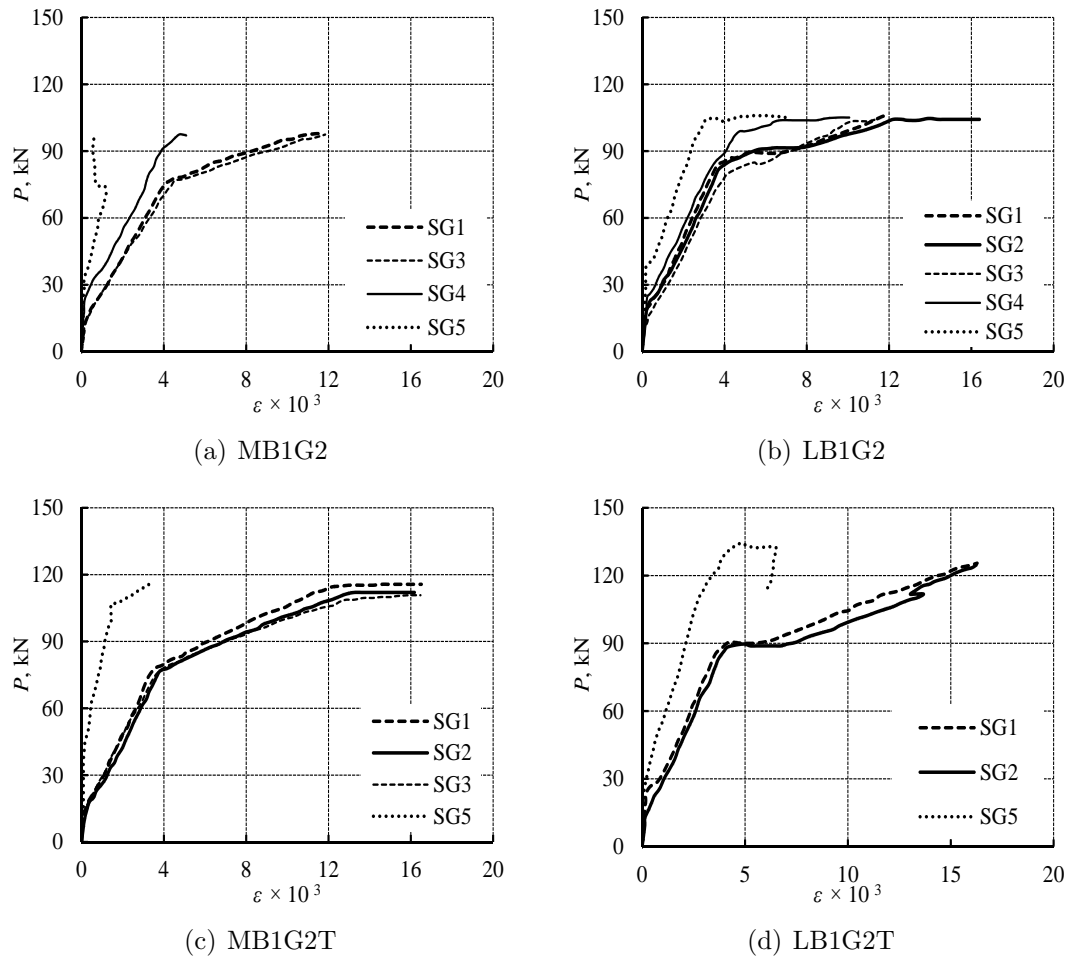


Figure 7.38: Strain in the NSM G2 bars.

7.4.3 Compressive strain in concrete

Figs. 7.39 - 7.42, show the evolution of concrete compressive strain with load of the tested beams. The strains measured by the three strain gauges (SG-c1, SG-c2 and SG-c3) increased as the load increased following a response similar to that of the load deflection curves. The compressive strain decreased as the bond length increased especially after steel yielding. For specimens with CFRP reinforcement the NSM area and shape had slight effects on the compressive strain recorded before the internal steel yielded (Figs.7.39 and 7.40).

After steel yielding, the values of strain for beams strengthened with GFRP bars increased with higher rate than that of the beams strengthened with CFRP

bars due to their lower E_f (Figs.7.39 and 7.41). Finally specimens with G2 bars experienced lower compressive strains than specimens with G1 bars as G2 bars had slightly higher area than G1 bars (Figs.7.41 and 7.42).

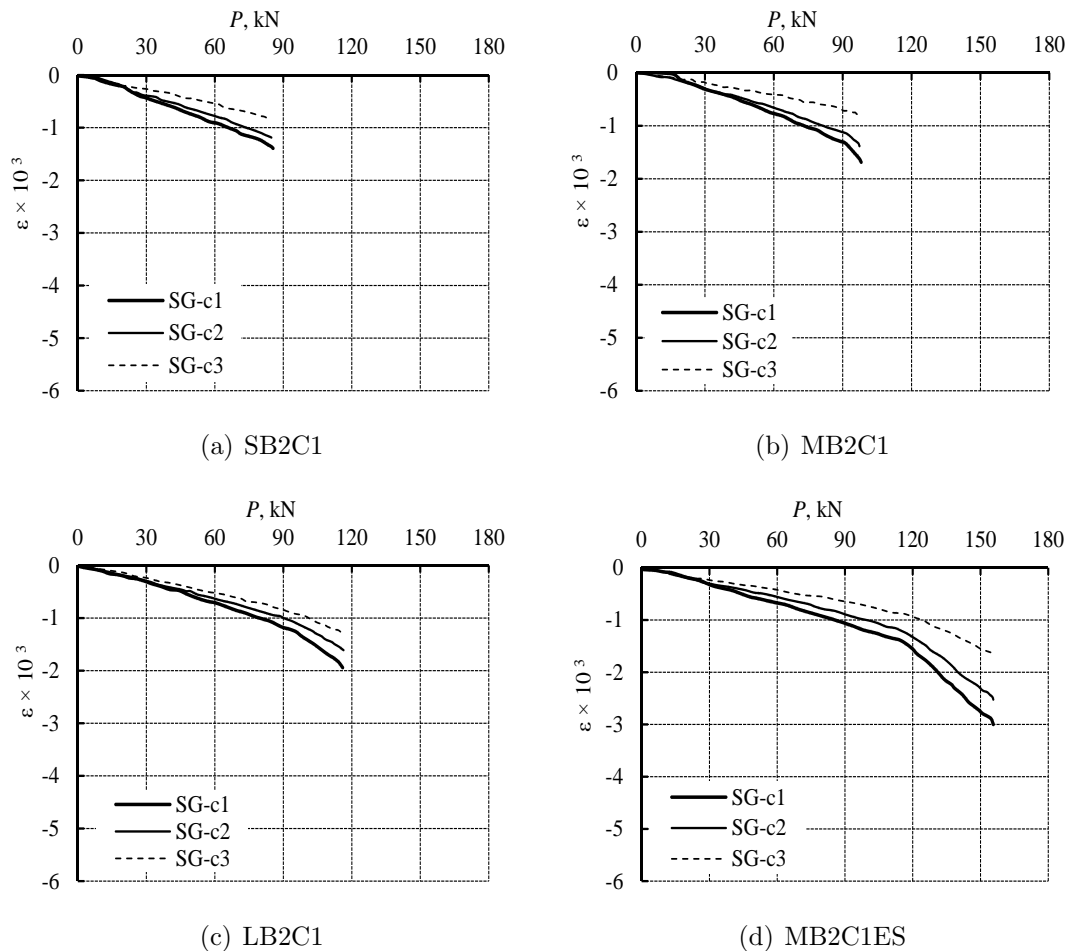


Figure 7.39: Compressive strain in concrete for beams with NSM CFRP bars.

7.4.4 Deflection and stiffness

Fig. 7.43 shows the effect of bond length and ES on the stiffness of beams strengthened with CFRP bars. The deflection distribution along the strengthened beams is compared for several load levels. The deflection of the strengthened beams decreased as the bond length increased or using ES, this reveals that as the bond length increased or using ES the composite action increased.

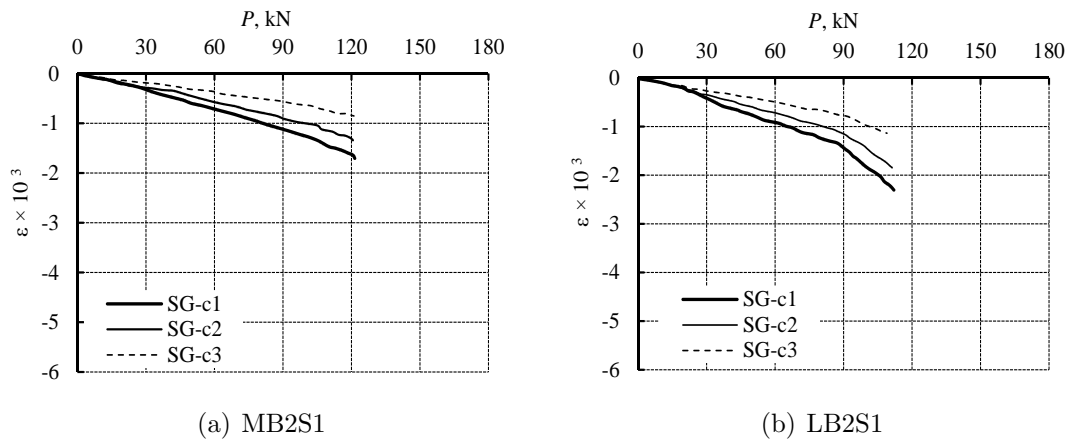


Figure 7.40: Compressive strain in concrete for beams with NSM CFRP strips.

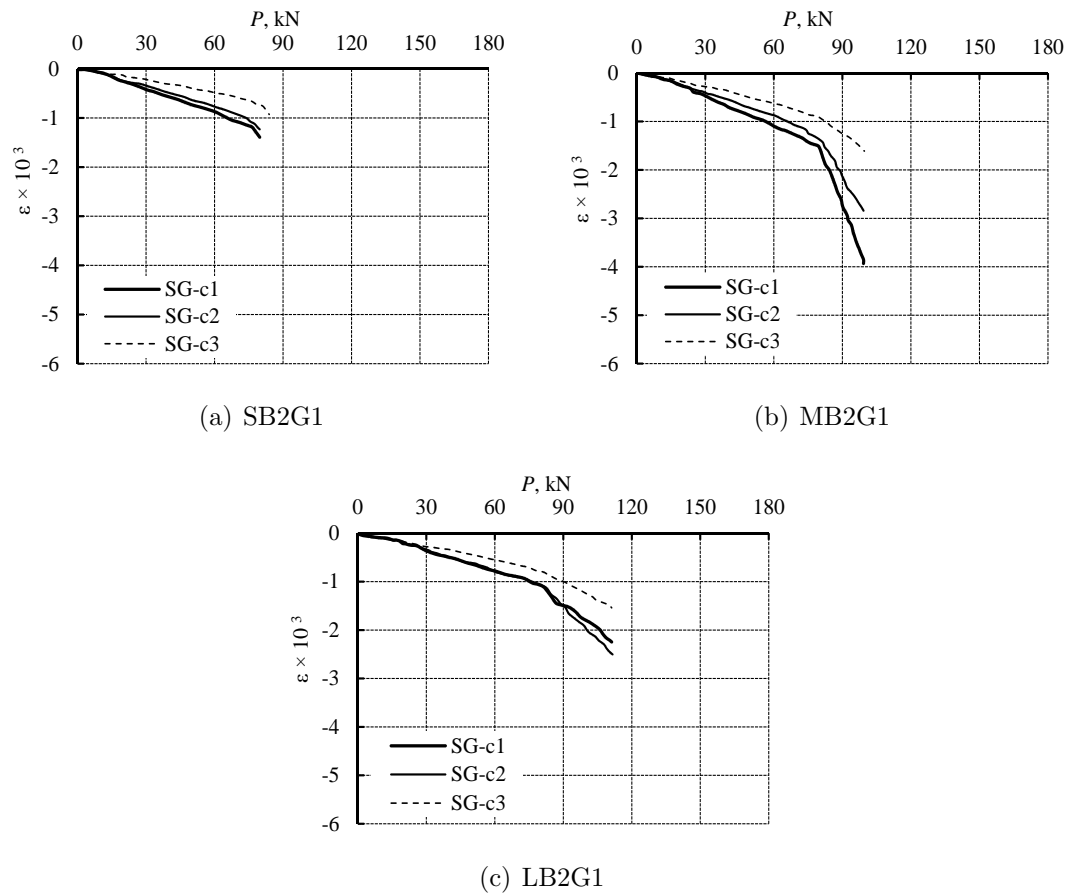


Figure 7.41: Compressive strain in concrete for beams with NSM GFRP G1 bars.

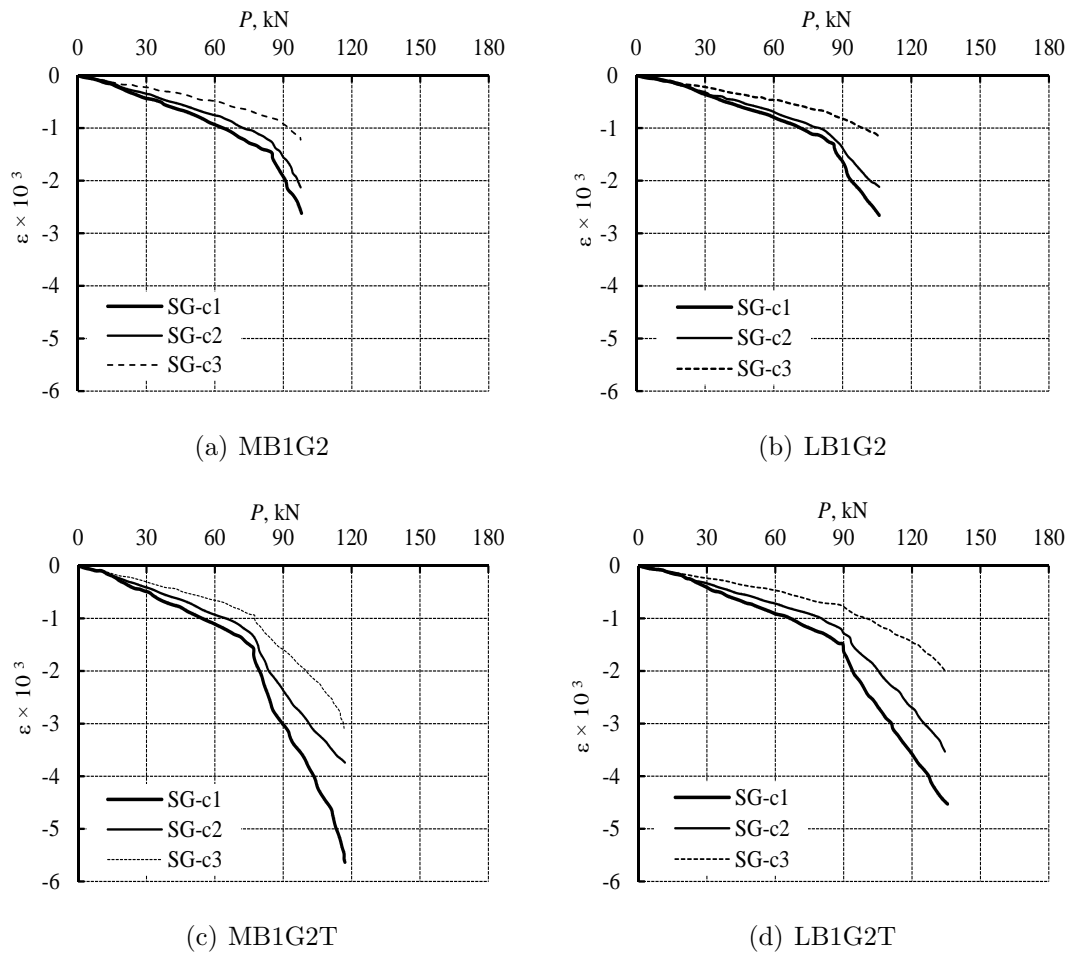


Figure 7.42: Compressive strain in concrete for beams with NSM GFRP G2 bars.

For the beams strengthened with NSM strips, deflection decreased as the bond length increased (Fig. 7.44). Figs. 7.45 and 7.46 show the effect of bond length on the deflection of the beams strengthened with GFRP bars. The deflection of the beams decreased as the bond length increased. On the other hand, a slight deflection increase was experienced by the beams strengthened with one G2 bars compared to that of beams with two G1 bars; this may be due to the effect of its low concrete-epoxy interface area. Moreover, the deflection of the beams strengthened with G2 bars decreased when the transverse wrapping was applied to the beams, which confined the NSM system (bar and epoxy), as shown in Fig. 7.46. On the other hand, as the modulus of elasticity of the NSM bars increased, the deflection of the strengthened beam decreased (Figs. 7.43 and 7.45).

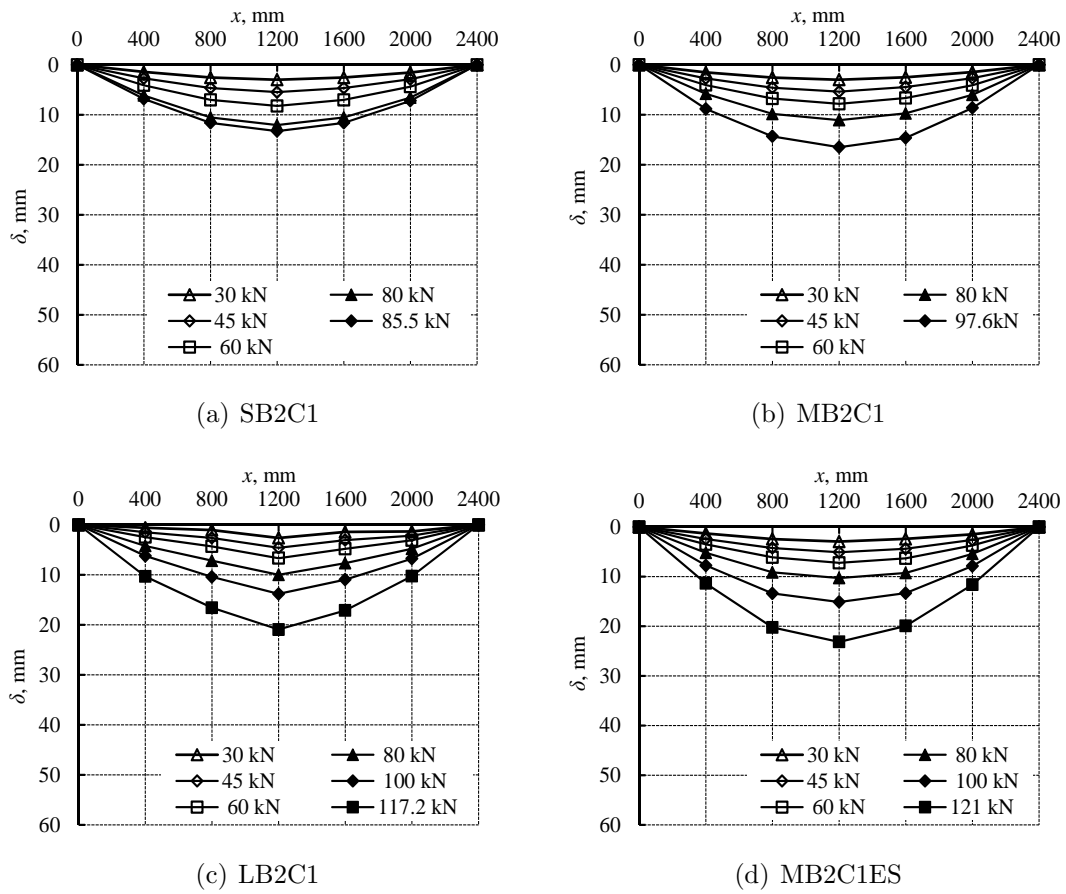


Figure 7.43: Deflection of beams strengthened with NSM CFRP bars.

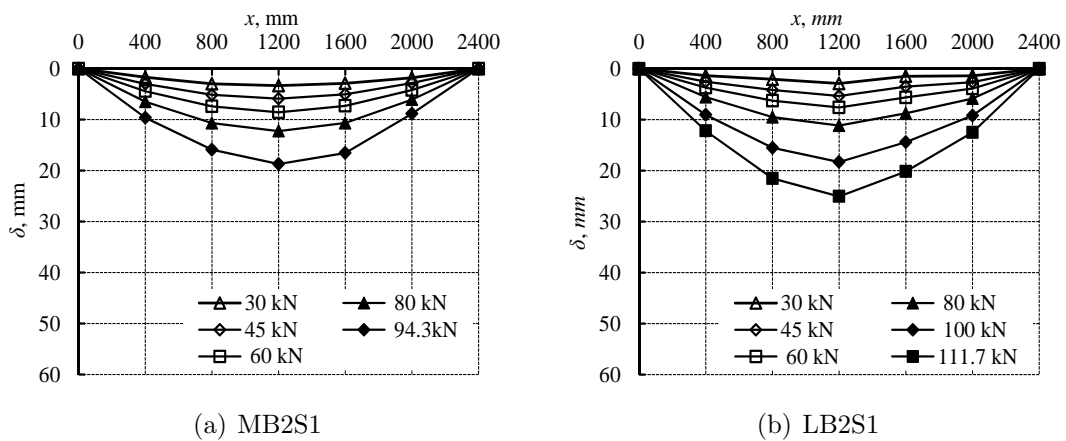


Figure 7.44: Deflection of beams strengthened with NSM CFRP strips.

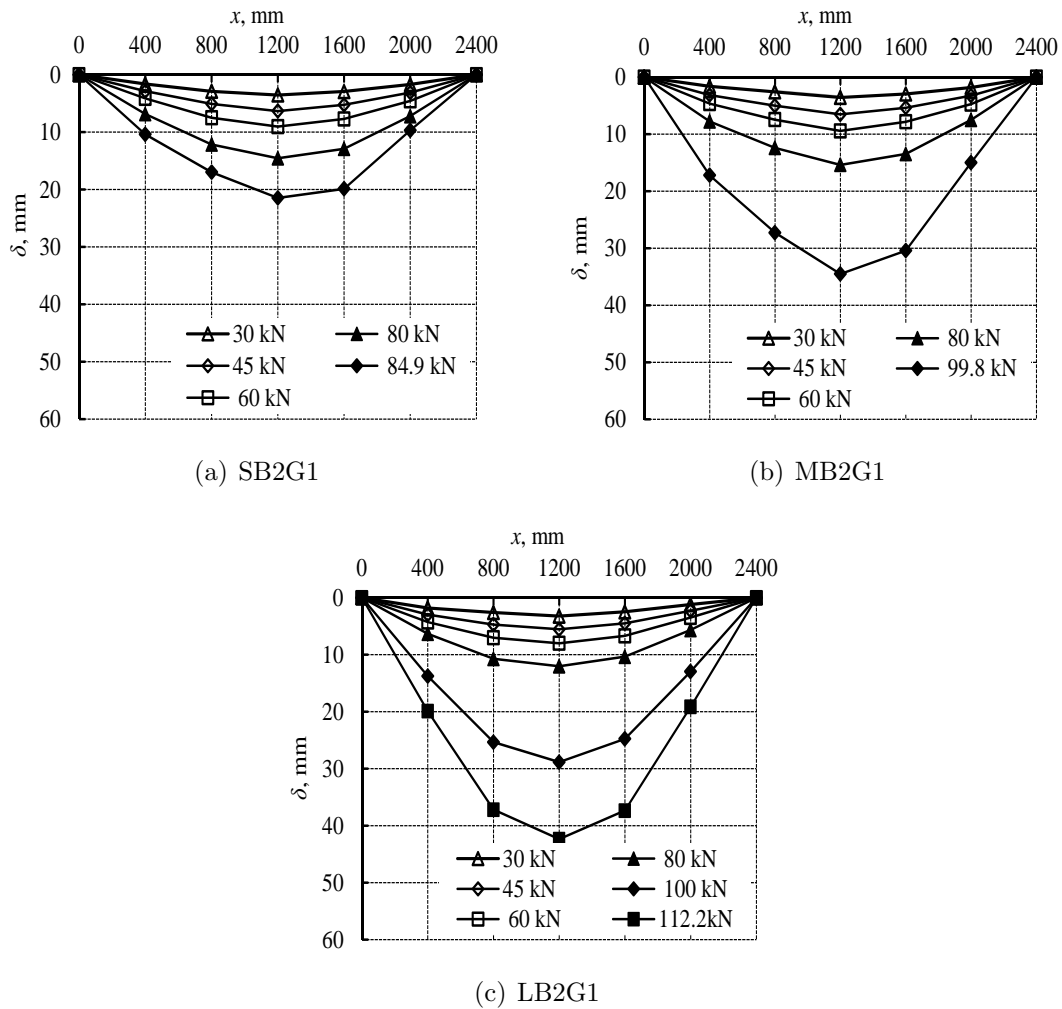


Figure 7.45: Deflection of beams strengthened with NSM GFRP G1 bars.

7.4.5 Global comparison

In this section, the effect of bond length, NSM area, end supporting and transverse wrapping (T and ES) and NSM properties on the yield load and maximum load efficiencies reported and discussed (see Fig. 7.47) . As shown in Fig. 7.47a, the yield load efficiency increased as E_f increased or applying the ES to the bar ends. Increasing the bond length from 480 mm to 1000 mm (limited bond = 2000 mm) increased the yield load efficiency with different percentages ranging from 4.6 % to 26.5 %, in contrast, there was no increase in the yield load efficiency when the bond length increased from 384 to 480 mm.

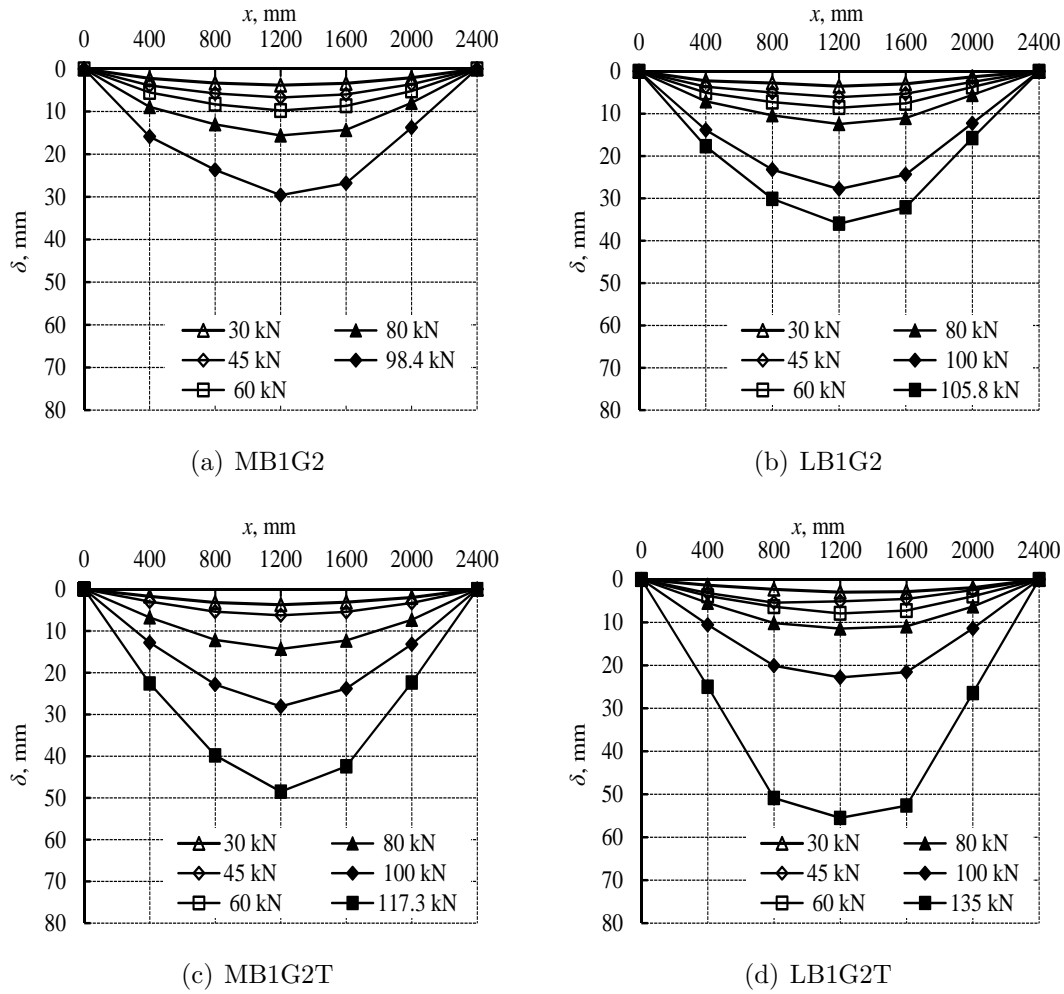


Figure 7.46: Deflection of beams strengthened with NSM GFRP G2 bars.

Fig. 7.47b shows that the maximum load efficiency increased as the bond length and E_f increased or by using ES and T modifications. For beams strengthened with partially bond length equal to 480 mm, the maximum load efficiency increased by 73.1 % over the CB when the ES was applied to the beams with NSM CFRP bars while the maximum load efficiency increased by 66.6 % when T was applied to the beam with GFRP bar (see Fig. 7.47b).

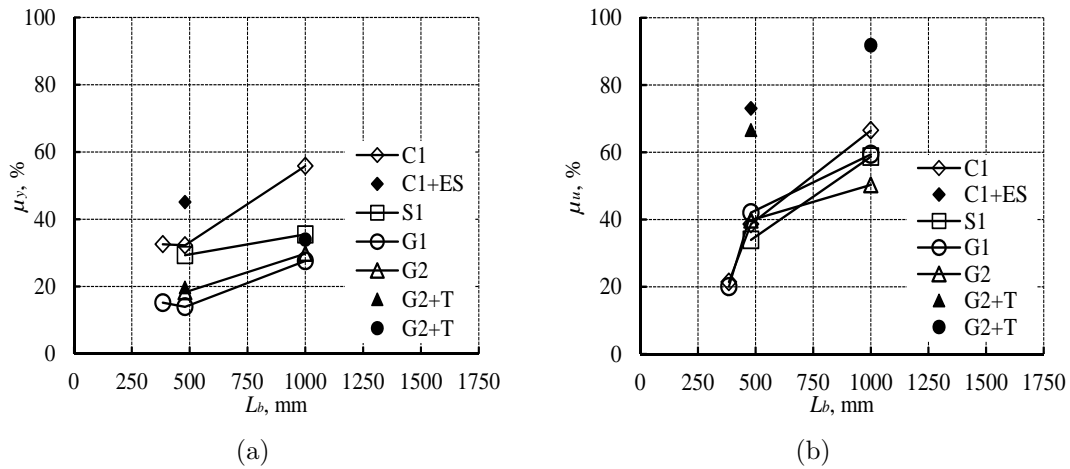


Figure 7.47: Effect of NSM reinforcement on the load efficiency of the strengthened RC beams: (a) at yield load and (b) at ultimate load.

7.4.6 Conclusions

In this series eight strengthened RC beams were prepared and tested in addition to un-strengthened beam (CB). The beams were strengthened with partially bonded NSM reinforcement to study the effect of construction details and FRP characteristics on the flexural performance. The result of the tested beams in this series were compared to the result of the beams tested in the first and the second series. From the above results the following conclusions were obtained:

- For all the strengthened beams, as the bond length increased the stiffness and the maximum capacity increased while the deflection decreased. The failure of the beams strengthened with NSM CFRP reinforcement was concrete cover separation that started at the cutoff except for beams with CFRP strips which failed at strip- epoxy interface. Moreover, the failure of the RC beams strengthened with GFRP bars was concrete cover separation except for the beam L1G2 that failed by concrete-epoxy interface failure.
- Increasing the bond length from 480 mm to 1000 mm increased the yield load efficiency with different percentages ranging from 4.6 % to 26.5 %; in contrast, there was no increase in the yield load efficiency when the bond length increased from 384 to 480 mm.

- The recorded strains increased as the area and modulus of elasticity of the NSM reinforcement decreased. Beyond the yielding load, the slope of load strain curves of the beams with GFRP bars was higher than that of the beams with CFRP bars.
- The recorded compressive strain decreased as the bond length increased, especially after steel yielding. The effect of NSM area and shape had slight effect on the compressive strain recorded before the internal steel yielded. After yielding, the values of recorded strain for beams strengthened with GFRP bars with lower E_f , increased with a higher rate than those strengthened with CFRP bars.
- The deflection of the strengthened beams decreased as the bond length increased or when end anchorage (ES) was applied, since the effect of composite action increased. Moreover, the deflection of the beams strengthened with GFRP bars decreased when the transverse wrapping was applied to the beams confining the NSM system (FRP bars and epoxy).
- For beams strengthened with partially bond length equal to 480 mm, the maximum load efficiency increased by 73.1 % over the CB when the end anchorage (ES) was applied to the beams with CFRP bars, while the maximum load efficiency increased by 66.6 % when transverse confinement (T) was applied to the beam with GFRP bar.

Part III

Conclusions and Future Work

Chapter 8

Conclusions and future work

8.1 Summary

The use of fibre reinforced polymer (FRP) bars and strips as near surface mounted (NSM) reinforcement has become an emerging technique for the strengthening of reinforced concrete (RC) members. The bond behaviour of the NSM system depends on the interaction in the two existing interfaces and the response, in terms of load slip and load capacity may be strongly affected by different parameters. As a consequence of the variety of factors affecting the bond, different studies on the behaviour of NSM FRP reinforcement have been carried out in recent years. The present work is a contribution to a better knowledge of the behaviour of concrete structures strengthened with NSM FRP reinforcement. The study carried out is composed of two main parts: bond behaviour and flexural behaviour of NSM FRP strengthened flexural elements. An extensive experimental programme was performed on both aspects, which was complemented by a numerical study of the bond behaviour. The main conclusions obtained from this work are indicated in the following.

8.2 Bond behaviour

8.2.1 Experimental research

An experimental programme using a modified pullout test was carried out to study the effect of different factors on the bond behaviour of NSM FRP bars in

concrete. Three series of specimens were tested to study the effect of groove surface (pre-formed and saw cut), groove geometry (dimensions and shapes), bar size, FRP bar type (material and surface treatment), bond length, adhesive properties, concrete properties and also of the incorporation, in the groove-concrete system, of different construction details that modify the NSM-concrete interaction (transverse interlocking with or without shear connectors, covering plate with shear connectors and confinement of surrounding concrete) on the bond behaviour of NSM FRP bars in concrete. Two epoxy resins from different suppliers were used; one of them was modified by adding two different percentages (1.88 %, 3.76 %) of a special additive in order to obtain resins with different properties, so that finally four types of adhesive (A, B, C and D) were used. The material properties of the FRP bars and the variables introduced had different effects on the bond behaviour of the specimens that were tested. From the test results, the following conclusions are obtained:

- The adhesive type had a great effect on the behaviour of NSM FRP bars in longitudinal and transverse directions. This effect varied according to the bond length and FRP properties. With the same bond length and groove dimensions, the failure load of specimens increased with the modulus of elasticity and tensile strength of epoxy. This was shown in the load slip responses, as well as in the analysis of the transverse strains.
- For specimens with NSM carbon fibre reinforced polymer (CFRP) bars (those with a smoother surface), bar-epoxy interface failure due to bar was the critical failure mechanism. Epoxy type B distributed the stresses along the bond length evenly, preventing sudden failures and allowing advantage to be taken of longer bond lengths.
- In specimens with CFRP bars, changing the adhesive type from A to B increased the failure load of the joint by approximately 44.27 %, 20.38 % and 16.73 % for bond lengths $12d_b$, $24d_b$ and $30d_b$ respectively. For specimens with glass fibre reinforced polymer (GFRP) bars, changing the adhesive type from A to B increased the failure load of the joint by approximately 21.47 % and 32.45 % for bond lengths $12d_b$ and $24d_b$ respectively.
- Increasing groove width, bar size and bond length increased the failure load of the NSM FRP bars regardless of FRP properties and surface treatment. On

the other hand, groove shape and transverse interlocking had no effect on the failure mode and capacity as a result of epoxy splitting.

- The use of mechanical interlocking in the epoxy-concrete interface with or without shear connectors, stepped grooves and covering plate enhanced the concrete-epoxy bond and slightly increased the failure loads. Moreover, the use of stepped grooves, mechanical interlocking with and without shear connectors, and covering plate with shear connectors may be a solution for the epoxy concrete failure in the case of smooth grooved surfaces.
- An analysis of these results taken jointly with those reported by other researches indicates that the main factors affecting bond behaviour, failure load and the mode of failure of NSM FRP bars are bond length, bar size and adhesive properties. When epoxy resin is used, the failure load increases as the groove size increases. For this reason the groove size seems to be a secondary factor affecting the failure load, which depends mainly on the adhesive properties.

8.2.2 Numerical analysis

The material and geometric properties of the FRP bars or strips, the characteristics of the adhesive and the concrete quality greatly affect the strengthening effectiveness of the NSM FRP technique. Constitutive models able to adequately simulate the interface between NSM FRP elements and concrete are decisive for the correct prediction of the load capacity and cracking process of concrete structures strengthened according to this technique. The assessment of the influence of the relevant factors that affect the NSM FRP bond behaviour, on the values of the parameters that define these constitutive models is also crucial for reliable numerical simulations of this type of structures by using the finite element method (FEM). The FEM-based modelling of NSM FRP bond behaviour was used to perform an inverse analysis to derive the local bond stress slip law from the experimental results obtained in direct pullout tests. The methodology was found to be suitable to analyze and compare the bond behaviour of various types of NSM FRP bars, as well as to assess the influence of the relevant parameters. From the analysis performed in this study, the following conclusions can be drawn:

- The obtained local bond slip, $\tau - s$, equations were found to be capable of simulating the global behaviour of all the tested specimens with various types of NSM bars, epoxy properties, concrete strengths and bond lengths.
- The larger the elasticity modulus of the adhesive, the higher the axial stiffness of the compressive micro-struts formed into the adhesive, which leads to a stiffer and strong bond connexion.
- The strength and stiffness of the local bond law (given through the values of τ_{max} and s_{max}) increase with the tensile strength and modulus of elasticity of the adhesive, while parameters α and α' defining the shape of the pre- and post-peak branches are not significantly affected.
- As the concrete strength increases, the values of the parameters α and α' , decrease, due to the smaller deformability and higher confinement provided by the concrete surrounding the bond zone. Due to the same reason, by increasing the concrete strength s_{max} has tendency to slightly decrease, while in the CFRP specimens the τ_{max} tends to increase moderately.
- The local bond stress slip law of NSM GFRP bars is characterized by higher values of s_{max} and lower values of α and α' than those of NSM CFRP bars, while τ_{max} is similar. The more ductile response of the specimens reinforced with GFRP bars can be attributable to the smaller axial stiffness. The ribs composing the surface of the GFRP bars might have contributed to the formation of micro-compressive struts in the adhesive, which increased the FRP confinement during the pullout process, resulting a more ductile pullout response for the specimens strengthened with GFRP bars.

8.3 flexural behaviour

An experimental programme on of twenty three RC beams strengthened in flexure with NSM FRP bars and strips with partially and limited bond lengths and one additional un-strengthened control beam was performed. The test variables consisted of the FRP material, bond length, the number of NSM bars and their

area, epoxy properties, and the strengthening arrangement. Two types of FRP bars, carbon and glass, were used: one size of carbon bars, C1, and two sizes for the glass bars, G1 and G2. Two types of epoxy MBRACE (BASF) and POLYFIXER EP (ROBERLO) denoted as A and B were used to install the bars in the concrete grooves. The load capacity, deflection, mode of failure, FRP strain, concrete strain, free end slip and transverse strain in epoxy and concrete of the tested beams were compared. From the test results the following conclusions are obtained:

- Doubling the area of NSM FRP bars increased the yield load of the beam with a slight effect on the maximum load capacity due to concrete cover separation failure. On the other hand, with the same mechanical properties and area, the shape and dimensions of the NSM FRP reinforcement had slight effect on the load capacity of the strengthened beams.
- For all the strengthened beams, as the bond length increased the stiffness and the maximum capacity increased while the deflection decreased. The failure of the beams strengthened with NSM CFRP reinforcement was concrete cover separation that started at the cutoff except for beams with CFRP strips failed at strip- epoxy interface. By the way, the failure of the beams strengthened with partially bonded GFRP G2 bars was concrete cover separation while that strengthened with a limited bond length failed due to concrete-epoxy interface failure.
- Use of transverse wrapping (T) and mechanical interlocking with shear connectors (IS) confined the beam, delayed the concrete cover separation and increased the stiffness, yield load and maximum load capacity. The percentage of increase in the maximum load capacity of beams strengthened with NSM CFRP bars was 95.9 % and 121.6 % over the CB when the IS and T applied respectively, while yield load was not affected. On the other hand, when the IS and T was applied on the beams strengthened with GFRP bars, the failure load increased by 85.2 % and 91.8 % over the control beam respectively, with a slight increase in the yield load.
- Increasing the bond length from 480 mm to 1000 mm increased the yield load efficiency with different percentage ranging between 4.6 % to 26.5 %; in

contrast there was no increased in the yield load efficiency when the bond length increase from 384 to 480 mm. Moreover, the maximum load efficiency increased as the bond length and E_f increased or by using end anchorage (ES) and T. For beams strengthened with partially bond length equal to 480 mm, the maximum load increased by 73.1 % over the CB when the ES was applied to the beams with CFRP bars, while the maximum load increased by 66.6 % when T was applied to the beam with GFRP bar.

- The recorded compressive strain decreased as the bond length increased especially after steel yielding. The effect of NSM FRP area and shape had slight effect on the compressive strain recorded before the internal steel yielded. After yielding, the values of recorded strain for beams strengthened with GFRP bars, with lower modulus of elasticity, increased with a higher rate than those strengthened with CFRP bars.
- The deflection of the strengthened beams decreased as the bond length increased or ES as it increased the effect of composite action. Moreover, the deflection of the beams strengthened with GFRP bars decreased when the transverse wrapping was applied to the beams confining the NSM system (FRP bars and epoxy).
- The recorded transverse strains confirmed that the behaviour of the NSM bars under direct pullout is dissimilar to the behaviour in bending. In direct pullout test, in contrast to bending tests, the NSM bar exerted the stresses on epoxy that transferred through the epoxy paste to the surrounding concrete.
- From all the above conclusion it is observed that, the NSM technique is effective technique in increasing the load capacity and stiffness of the concrete RC beams. The load efficiency in this technique is depended mainly on the area of FRP bars, bond length and the mode of failure while the stiffness enhancement is depended mainly on the modulus of elasticity of FRP bars and the bond length. Controlling the mode of failure occurred by the concrete cover separation using especial construction details enhanced the load efficiency of the strengthened beams. Finally, the use of IS, ES and T increased also the stiffness and the maximum load capacity of the strengthened beams.

8.4 Future work

Based on the results of this research, the following topics are suggested for future work:

- To further study on the bond behaviour of the NSM FRP strengthening systems are needed including additional possible influencing parameters and combinations of them.
- To study the behaviour of elements strengthened in flexure with NSM FRP reinforcement under sustained and fatigue loading considering also the influence of previous cracking.
- To study the behaviour of concrete structures in flexure internally reinforced with FRP bars and strengthened with NSM FRP reinforcement.
- To use the available experimental data concerning to the NSM FRP strengthening technique to arrive at design equations able to predict the failure load of the strengthened beams.
- To perform a detailed numerical analysis for NSM FRP strengthened structural elements taking into account the main geometrical and mechanical properties involved.

Bibliography

- [1] ACI Committee 440. Guide for the design and construction of externally bonded FRP systems for strengthening concrete structures (ACI 440.2R-02). Technical report, American Concrete Institute, Farmington Hills, Michigan, 2002.
- [2] R. Capozucca. Damage to reinforced concrete due to reinforcement corrosion. *Construction and building materials*, 9:295–303, 1995.
- [3] S. Yang, K. Park, and W. Neale. Flexural behaviour of reinforced concrete beams strengthened with prestressed carbon composites. *Composite Structures*, 88:497–508, 2009.
- [4] M. Baena. Study of bond behaviour between FRP reinforcement and concrete. *PhD thesis, University of Girona*, page 292, 2010.
- [5] M. Tavakkolizadeh and H. Saadatmanesh. Flexural behaviour of reinforced concrete beams strengthened with prestressed carbon composites. *Journal of Structural Engineering*, 129:30–40, 2003.
- [6] M. Tavakkolizadeh. Strengthening and repair of steel \bar{U} concrete composite girders using CFRP laminates. *PhD thesis, University of Arizona*, 2001.
- [7] R. Sen, L. Liby, and Mullins G. Strengthening steel bridge sections using CFRP laminates. *Composites Part B: Engineering*, 32(4):309–322, 2001.
- [8] S. O. Asplund. Strengthening bridge slabs with grouted reinforcement. *Journal of the American Concrete Institute*, 20(2):397–406, 1949.

- [9] J. F. Chen and J. G. Teng. Anchorage strength models for FRP and steel plates bonded to concrete. *Journal of Structural Engineering*, 127(7):784–791, 2001.
- [10] S Rankovic, R. Folic, and M. Mijalkovic. Effect of RC beams reinforcement using near surface mounted reinforcement FRP composites. *Architecture and Civil Engineering*, 8:177–185, 2010.
- [11] S.J.E. Dias and J.A.O. Barros. NSM shear strengthening technique with CFRP laminates applied in high-strength concrete beams with or without pre-cracking. *Composite Structures*, 43(2):290–301, 2012.
- [12] S.J.E. Dias and J.A.O. Barros. Shear strengthening of RC beams with NSM CFRP laminates: Experimental research and analytical formulation. *Composite Structures*, 99:477–490, 2013.
- [13] S.J.E. Dias and J.A.O. Barros. Shear strengthening of RC T-section beams with low strength concrete using NSM CFRP laminates. *Cement and Concrete Composites*, 33(2):334–345, 2011.
- [14] T. Hassan and S.H. Rizkalla. Investigation of bond in concrete structures strengthened with near surface mounted carbon fiber reinforced polymer strips. *Journal of Composites for Construction*, 7(3):248–257, 2003.
- [15] L. De Lorenzis. Anchorage length of near surface mounted fibre-reinforced polymer rods for concrete strengthening - analytical modelling. *ACI Structural Journal*, 101(3):375–386, 2004.
- [16] L. De Lorenzis and A. Nanni. Shear strengthening of reinforced concrete beams with near surface mounted fibre-reinforced polymer rods. *ACI Structural Journal*, 98(1):60–68, 2001.
- [17] A. Nanni. North american design guidelines for concrete reinforcement and strengthening using FRP: principles, applications and unresolved issues. *Construction and Building Materials*, 17:439–446, 2003.

- [18] R. El-Hacha and S.H. Rizkalla. Near surface mounted fibre reinforced polymer reinforcements for flexural strengthening of concrete structures. *ACI Structural Journal*, 101(5):717–726, 2004.
- [19] T Hassan and S.H. Rizkalla. Bond mechanism of near surface mounted fibre reinforced polymer bars for flexural strengthening of concrete structures. *ACI Structural Journal*, 101(6):830–839, 2004.
- [20] R. Parretti and A. Nanni. Strengthening of RC members using near surface mounted FRP composites: Design overview. *Advances in Structural Engineering*, 7(6):469–483, 2004.
- [21] J. A. O. Barros and A. S. Fortes. Flexural strengthening of concrete beams with CFRP laminates bonded into slits. *Cement and Concrete Composites*, 27(4):471–480, 2005.
- [22] J. A. O. Barros and S. J. E. Dias. Near surface mounted CFRP laminates for shear strengthening of concrete beams. *Cement and Concrete Composites*, 28(3):276–292, 2006.
- [23] J. A. O. Barros, S. J. E. Dias, and J. L. T. Lima. Efficacy of CFRP-based techniques for the flexural and shear strengthening of concrete beams. *Cement and Concrete Composites*, 29(3):203–217, 2007.
- [24] G.J. Ha, Y.Y. Kim, and C.G. Cho. Groove and embedding techniques using CFRP trapezoidal bars for strengthening of concrete structures. *Engineering Structures*, 30(4):1067–1078, 2008.
- [25] M. Badawi and K. Soudki. Flexural strengthening of RC beams with prestressed NSM CFRP rods - experimental and analytical investigation. *Construction and Building Materials*, 23(10):3292–3300, 2009.
- [26] R. Capozucca. Static and dynamic response of damaged RC beams strengthened with NSMCFRP rods. *Composite Structures*, 91(3):237–248, 12 2009.
- [27] F. Al Mahmoud, A. Castel, R. François, and C. Tourneur. Strengthening of RC members with near surface mounted CFRP rods. *Composite Structures*, 91(2):138–147, 11 2009.

- [28] F. Al Mahmoud, A. Castel, R. François, and C. Tourneur. Rc beams strengthened with NSM CFRP rods and modelling of peeling-off failure. *Composite Structures*, 92(8):1920–1930, 7 2010.
- [29] S.J.E. Dias and J.A.O. Barros. Performance of reinforced concrete T-beams strengthened in shear with NSM CFRP laminates. *Engineering Structures*, 32(2):373–384, 2010.
- [30] I.G. Costa and J.A.O. Barros. Flexural and shear strengthening of RC beams with composite materials - the influence of cutting steel stirrups to install CFRP strips. *Cement and Concrete Composites*, 32(7):544–553, 2010.
- [31] S.M. Soliman, E. El Salakawy, and B. Benmokrane. Flexural behaviour of concrete beams strengthened with near surface mounted fibre reinforced polymer bars. *Canadian Journal of Civil Engineering*, 37(10):1371–1382, 2010.
- [32] A.S. Kalayci, B. Yalim, and A. Mirmiran. Construction tolerances and design parameters for NSM FRP reinforcement in concrete beams. *Construction and Building Materials*, 24(10):1821–1829, 2010.
- [33] H.T. Choi, J.S. West, and K.A. Soudki. Partially bonded near surface mounted CFRP bars for strengthened concrete T-beams. *Construction and Building Materials*, 25(5):2441–2449, 5 2011.
- [34] J. A. O. Barros, I. G. Costa, and A. Ventura-Gouveia. CFRP flexural and shear strengthening technique for RC beams: Experimental and numerical research. *Advances in Structural Engineering*, 14(3):551–571, 2011.
- [35] H.Y. Omran and R. El-Hacha. Nonlinear 3D finite element modelling of RC beams strengthened with prestressed NSM CFRP strips. *Construction and Building Materials*, 31:74–85, 2012.
- [36] A.H. Rami. Nonlinear finite element modelling of RC beams strengthened with NSM FRP rods. *Construction and Building Materials*, 27(1):461–471, 2012.
- [37] R. Capozucca. Overview of testing to failure program of a highway bridge strengthened with FRP composites. *International Symposium on FRP for*

- Reinforcement of Concrete Structures (FRPRCS4)*, Baltimore, pages 69–80, 1999.
- [38] L. De Lorenzis and J.G. Teng. Near surface mounted FRP reinforcement: An emerging technique for strengthening structures. *Composites Part B: Engineering*, 38(2):119–143, 2007.
- [39] D. Foti. Preliminary analysis of concrete reinforced with waste bottles PET fibers. *Construction and Building Materials*, 25, 2011.
- [40] D. Foti. Use of recycled waste pet bottles fibers for the reinforcement of concrete. *Composite Structures*, 96, 2011.
- [41] D. Foti and S. Vacca. Comportamiento mecánico de columnas de hormigón armado reforzadas con mortero reoplástico./ mechanical behaviour of concrete columns reinforced with rheoplastic mortar. *Materiales de Construcción*, 63 (310):267–282, 2012.
- [42] FIB Bulletin 10. Bond of reinforcement in concrete. State-of-the-art report, Tech. Rep., 2000.
- [43] American Concrete Institute Technical Committee 440. Guide for the design and construction of concrete reinforced with FRP bars. ACI 440.1R-03t, 2003.
- [44] K. Pilakoutas, Z. Achillides, and P. Waldron. Non-ferrous reinforcement in concrete structures. In *Edinburgh: Civil-Comp Ltd; 1997*, p. 47-58. PT: J; CT: Mouchel Centenary Conference on Innovation in Civil and Structural Engineering; CY: AUG 19-21, 1997; CL: CAMBRIDGE, ENGLAND; TC: 0; UT: ISIP:000071363500005.
- [45] M.S. Mohamed Ali, D.J. Oehlers, M.C. Griffith, and R. Seracino. Interfacial stress transfer of near surface mounted FRP-to-concrete joints. *Engineering Structures*, 30(7):1861–1868, 2008.
- [46] S.T. Smith and J.G. Teng. FRP-strengthened rc. 2002.
- [47] X.J. Lu, J.G. Teng, L.P. Ye, and J.J. Jiang. Bond slip models for FRP sheets /plates bonded to concrete. *Engineering Structures*, 27:920–937, 2005.

- [48] S.K. Sharma, M.S. Mohamed Ali, D. Goldar, and P.K. Sikdar. Plate-concrete interfacial bond strength of FRP and metallic plated concrete specimens. *Composites Part-B: Engineering*, 37(1):54–63, 2006.
- [49] J.F. Chen, H. Yuan, and J.G. Teng. Debonding failure along a softening FRP to concrete interface between two adjacent cracks in concrete members. *Engineering Structures*, 29(2):259–270, 2007.
- [50] X.Z. Lu, L.P. Ye, J.G. Teng, and J.J. Jiang. Meso-scale finite element model for FRP sheets / plates bonded to concrete. *Engineering Structures*, 27(4):564–575, 2005.
- [51] J.G. Teng and J. Yao. Plate end debonding in FRP-plated RC beams-II: Strength model. *Engineering Structures*, 29, 2007.
- [52] J. Yao and J.G. Teng. Plate end debonding in FRP-plated RC beams-I: Experiments. *Engineering Structures*, 29(10):2457–2471, 2007.
- [53] H. Yuan, J.G. Teng, R. Seracino, Z.S Wu, and Yao J. Full-range behaviour of FRP to concrete bonded joints. *Engineering Structures*, 26(6):553–565, 2007.
- [54] U. Ebead and H. Saeed. Hybrid shear strengthening system for reinforced concrete beams: An experimental study. *Engineering Structures*, 49:421–433, 2013.
- [55] K.C. Panda, S.K. Bhattacharyya, and S.V. Barai. Strengthening of RC T-beams with shear deficiencies using GFRP strips. *Journal of Civil Engineering and Architecture*, 5(1):56–67, 2011.
- [56] A.S. Nadeem. Experimental investigation of RC beams strengthened with externally bonded FRP composites reinforcement. *Latin American Journal of Solids and Structures*, 6:343–362, 2009.
- [57] T. Alkhrdaji, A. Nanni, G. Chen, and M. Barker. Upgrading the transportation infrastructure: solid RC decks strengthened with FRP. *Concrete International, American Concrete Institute*, 21(10):37–41, 1999.

- [58] B. Täljsten, A. Carolin, and H. Nordin. Concrete beams strengthened with near surface mounted CFRP laminates. In *Proceedings of CFRPCS-5, C.Burgoyne (ed.) Cambridge, UK*, pages 107–116, 2001.
- [59] B. Täljsten, A. Carolin, and H. Nordin. Concrete structures strengthened with near surface mounted reinforcement of CFRP. *Advances in Structural Engineering*, 6(3):201–21, 2003.
- [60] G.E. Warren. Pier upgrade advanced technology demonstration site no. 3: Bravo 25, naval station pearl harbor, hawaii. Site specific report ssr-2567-shr, Naval Facilities Engineering Service Center, Port Hueneme, California, 2000.
- [61] P. Emmons, J. Thomas, and G.M. Sabnis. New strengthening technology for blue circle cement silo repair and upgrade. In *Proceedings of FRP Workshop US-AID, Cairo, Egypt*, 2001.
- [62] W.C. Tang, R.V. Balendran, A. Nadeem, and H.Y. Leung. Flexural strengthening of reinforced lightweight polystyrene aggregate concrete beams with near surface mounted GFRP bars. *Building and Environment*, 41(10):1381–1393, 2006.
- [63] I.S.T. Liu, D.J.O. ehlers, and R. Seracino. Tests on the ductility of reinforced concrete beams retrofitted with FRP and steel near surface mounted plates. *Journal of Composites for Construction*, 10(2):106–114, 2006.
- [64] A. Pridmore and Vistasp M. Structural response of near surface mounted CFRP strengthened reinforced concrete bridge deck overhang. Technical report, Final Report submitted to the California Department of Transportation, 2008.
- [65] D.H. Lim. flexural behaviour of concrete structures strengthened with NSM and EB CFRP strips. In *The 3rd ACF International Conference-ACF / VCA*, 2008.
- [66] H. Nordin, B. Täljsten, and A. Carolin. Concrete beams strengthened with prestressed near surface mounted reinforcement (NSFR). In *Proceedings of the International Conference on FRP Composites in Civil Engineering. Elsevier*, pages 1067–1075, 2001.

- [67] L. De Lorenzis, K. Lundgren, and A. Rizzo. Anchorage length of near surface mounted fibre reinforced polymer bars for concrete strengthening - experimental investigation and numerical modelling. *ACI Structural Journal*, 101(2):269–278, 2004.
- [68] L. De Lorenzis, A. Rizzo, and A. La Tegola. A modified pullout test for bond of near surface mounted FRP rods in concrete. *Composites Part B: Engineering*, 33(8):589–603, 2002.
- [69] D Galati and L. De Lorenzis. Effect of construction details on the bond performance of NSM FRP bars in concrete. *Advances in Structural Engineering*, 12:683–700, 2009.
- [70] S.M. Soliman, E. El Salakawy, and B. Benmokrane. Bond performance of near surface mounted FRP bars. *Journal of Composites for Construction*, 15(1):103–111, 2011.
- [71] A. Bilotta, F. Ceroni, M. Di Ludovico, E. Nigro, M. Pecce, and G. Manfredi. Bond efficiency of EBR and NSM FRP systems for strengthening concrete members. *Journal of composite for construction*, 15(7):757–72, 2011.
- [72] D. Novidis, S.J. Pantazopoulou, and E. Tentolouris. Experimental study of bond of NSM-FRP reinforcement. *Construction and Building Materials*, 21(8):1760–1770, 8 2007.
- [73] X. Yan, B. Miller, A. Nanni, and C.E. Bakis. Characterization of cfrp bars used as near surface mounted reinforcement. In *In: Forde MC, editor. Proceedings of the Eighth International Structural Faults and Repair Conference. Edinburgh, Scotland: Engineering Technics Press; 1999. p. 10. CD-ROM version.*, 1999.
- [74] F. Al Mahmoud, A. Castel, R. François, and C. Tourneur. Anchorage and tension-stiffening effect between near surface mounted CFRP rods and concrete. *Cement and Concrete Composites*, 33(2):346–352, 2 2011.
- [75] J. Sena Cruz, J. Branco, M. Jorge, J.A.O. Barros, C. Silva, and V. Cunha. Bond behaviour between glulam and GFRP’s by pullout tests. *Composites Part B: Engineering*, 43(3):1045–55, 2012.

- [76] R. Seracino, N.M. Jones, M.S. Mohamed Ali, M.W. Page, and D.J. Oehlers. Bond strength of near surface mounted CFRP strip-to-concrete joints. *Journal of Composites for Construction*, 11(4):401–409, 2007.
- [77] L. De Lorenzis. Strengthening of RC structures with near surface mounted FRP rods. *PhD Thesis*, University of Lecce(Italy), 2002.
- [78] S.J. Cruz and J.A.O. Barros. Modelling of bond between near surface mounted CFRP laminate strips and concrete. *Computers and Structures*, 82(17-19): 1513–1521, 7 2004.
- [79] H. Nordin and B. Täljsten. Concrete beams strengthened with CFRP. a study of anchor lengths. In *Proceedings 10th conference on structural faults and repair, London (UK)*, 2003.
- [80] J.G. Teng, L. De Lorenzis, B. Wang, R. Li, T.N. Wong, and L. Lam. Debonding failures of RC beams strengthened with near surface mounted CFRP strips. *Journal of Composites for Construction*, 10(2):92–105, 2006.
- [81] M. Blaschko. Zum tragverhalten von betonbauteilen mit in schlitze eingeklebten CFK-lamellen. *Bericht 8/2001 aus dem Konstruktiven Ingenieurbau*, TU München(147 pages=[in German],), 3 2001.
- [82] R. Eligehausen, E.P. Popov, and V.V. Bertero. Local bond stress slip relationships of deformed bars under generalized excitations. Technical report, Report No. 83/23, EERC, Berkeley, CA: University of California; P.162, 1983.
- [83] M. Blaschko. Bond behaviour of CFRP strips glued into slits. In *Proceedings of Sixth International Symposium on FRP Reinforcement for Concrete Structures (FRPCS-6)*, World Scientific, Singapore, July 8-10, pages 205–214, 2003.
- [84] R.A. Tepfers. A theory of bond applied to overlapped tensile reinforcement splices for deformed bars. Technical report, Gothenburg, Sweden:Division of Concrete Structures, Chalmers University of Technology; Publication 73:2, p. 328., 1973.

- [85] L. De Lorenzis, A. Nanni, and A. La Tegola. Flexural and shear strengthening of reinforced concrete structures with near surface mounted FRP rods. *Proc., 3rd Inter.Conf. on Advanced Composite Materials in Bridges and Structures, Ottawa, Canada*, pages 521–528, 2000.
- [86] L. De Lorenzis, F. Micelli, and A. La Tegola. Passive and active near surface mounted FRP rods for flexural strengthening of RC beams. In *In: Proceedings ICCI-02, San Francisco (CA), CD-ROM version*, 2002.
- [87] L. De Lorenzis and A. Nanni. Characterization of FRP rods as near surface mounted reinforcement. *Journal of Composites for Construction*, 5(2):114–121, 2001.
- [88] L. De Lorenzis. Strengthening of RC structures with near surface mounted FRP rods. MSc. thesis, Department of Civil Engineering, University of Missouri-Rolla, Rolla, MO, 2000.
- [89] N. Kishi, H. Mikami, Y. Kurihashi, and S. Sawada. Flexural behaviour of RC beams reinforced with NSM AFRP rods. In *Proceedings of the International Symposium of Bond Behaviour of FRP in Structures (BBFS 2005), Hong Kong, China, December 7-9*, pages 345–350, 2005.
- [90] W.T. Jung, Y.H. Park, J.S. Park, J.Y. Kang, and Y.J. You. Experimental investigation on flexural behaviour of RC beams strengthened by NSM CFRP reinforcements. In *In 7th International Symposium: Fibre Reinforced Polymer FRP Reinforcement for Concrete Structures*, eds. Carol K. Shield, John P. Busel, Stephanie L. Walkup, and Doug D. Gremel. Farmington Hills, Michigan: American Concrete Institute, pages 795–806, 2005.
- [91] B. Taljsten and H. Nordin. Concrete beams strengthened with external prestressing using external tendons and near surface mounted reinforcement (NSMR). In *In SP-245CD Case Histories and Use of FRP for Prestressing Applications*, eds. Raafat El-Hacha and Sami H. Rizkalla. Farmington Hills, Michigan: American Concrete Institute, CD-ROM, pages 143–164, 2007.
- [92] N. Wahab, K.A. Soudki, and T. Topper. Mechanism of bond behaviour of con-

- crete beams strengthened with near surface mounted CFRP bars for strengthened concrete T-beams. *J. Compos. for Constr.*, 15(1):85–92, 2011.
- [93] A. Crasto, R. Kim, and W. Ragland. Private communication. In *University of Dayton Research Institute*, 1999.
- [94] M. Arduini, M. Romagnolo, G. Camomilla, and A. Nanni. Influence of concrete tensile softening on the performance of NSM strengthened RC beams: experiments. In *Proceedings ACMBS-IV, Calgary (Canada)*, CD-ROM, July, 2004.
- [95] J.R. Yost, Gross S.P., Dinehart D.W., and Mildenberg J. Near surface mounted cfrp reinforcement for the structural retrofit of concrete flexural members. In *Proceedings ACMBS-IV, Calgary (Canada)*, CD-ROM, July, 2004.
- [96] L. De Lorenzis and A. Nanni. Bond between near surface mounted fibre reinforced polymer rods and concrete in structural strengthening. *ACI Structural Journal*, 99:123–132, 2002.
- [97] I. A. Sharaky, L. Torres, and I. Baena, M. and Vilanova. Effect of different material and construction details on the bond behaviour of NSM FRP bars in concrete. *Construction and Building Materials*, 38, 2012.
- [98] I. A. Sharaky, L. Torres, and C. Baena, M. and Miàs. An experimental study of different factors affecting the bond of NSM FRP bars in concrete. *Composite Structures*, 99, 2012.
- [99] A. Ventura-Gouveia. Constitutive models for the material nonlinear analysis of concrete structures including time dependent effects. Technical report, textscPh.D. Thesis, University of Minho, Portugal, 2011.
- [100] J.M. Sena-Cruz and J.A.O. Barros. Bond between near surface mounted carbon fibre reinforced polymer laminate strips and concrete. *ASCE Composites for Construction Journal*, 8(6):519–527, 2004.
- [101] F. Ceroni, J. A.O. Barros, M. Pecce, and M. Ianniciello. Assessment of nonlinear bond laws for near surface mounted systems in concrete elements. *Composites: Part B*, 45(1):666–681, 9 2013.

- [102] J.M. Sena-Cruz. Strengthening of concrete structures with near surface mounted CFRP laminate strips. Technical report, textscPh.D. Thesis, Dept. of Civil Engineering, University of Minho, Portugal, July , 198 pp.
- [103] A. Scanlon and P.H. Bischoff. Shrinkage restraint and loading history effects on deflections of flexural member. *ACI Structural Journal*, 105(4):498–506, 2008.
- [104] CEB-FIP. Model code 1990, design code. Technical report, Comité Euro-International Du Béton, Thomas Telford Services Ltd, London, 1990.
- [105] D. Schnerch and S. Rizkalla. Flexural strengthening of steel bridges with high modulus CFRP strips. *Journal of Bridge Engineering, ASCE*, 2008.
- [106] Lenwari A, Thepchatri T, and Albrecht P. Flexural response of steel beams strengthened with partial length CFRP plates. *J Compos Construct, ASCE*, 9(4):296–303, 2005.

Part IV

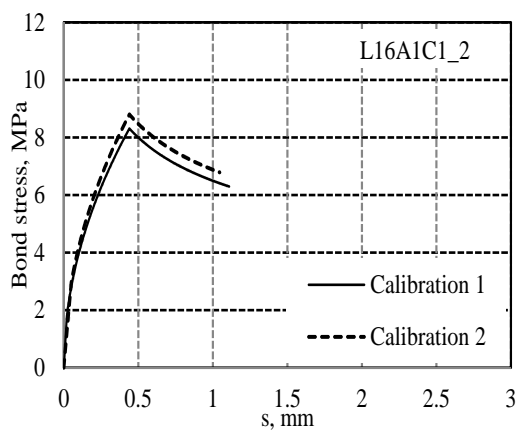
Appendix

Appendix A

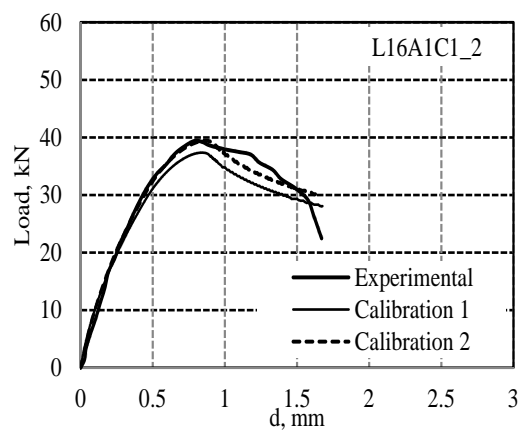
EMPIRICAL CALIBRATIONS FOR INVERSE ANALYSIS

In Chapter 5 a finite element analysis is performed using the programme FEMIX v4. A finite element method (FEM) based smeared crack model is used to assess, by inverse analysis, the influence of various parameters on the bond behaviour of the FRP NSM systems by simulating a series of pullout tests. The numerical calibrations on bond slip and force displacement curves are included in this appendix.

The numerical curves named Calibration 1 refer to τ - s analytical curve results from the first trial, while the Calibration 2 curves are obtained using the values of the parameters that define the τ - s law that fit, as much as possible, the experimental F - d curve up the peak point. The parameters of τ - s law of Calibration 2 are used for the study and comparisons. Furthermore the F - d curve is the curve obtained from Calibration 2.

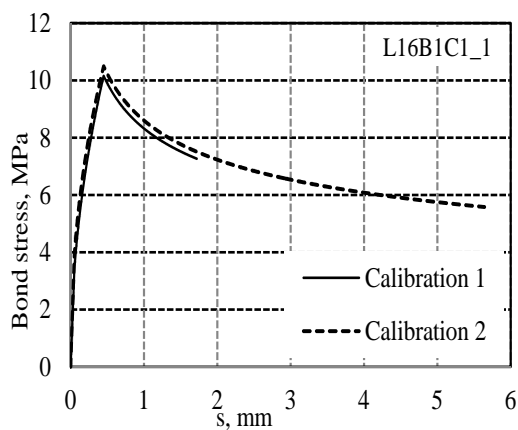


(a) The numerical τ - s curves

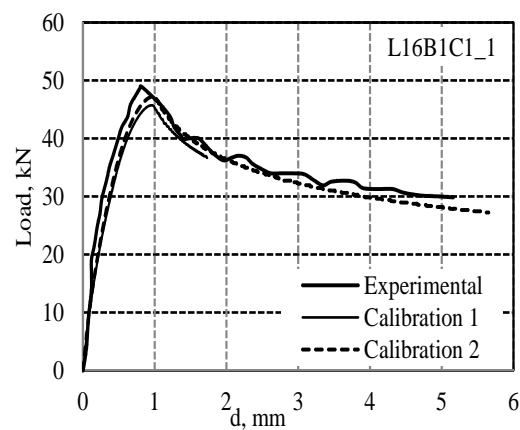


(b) The numerical and experimental F - d curves

Figure A.1: Calibration curves for specimen L16A1C1-2.



(a) The numerical τ - s curves



(b) The numerical and experimental F - d curves

Figure A.2: Calibration curves for specimen L16B1C1-1.

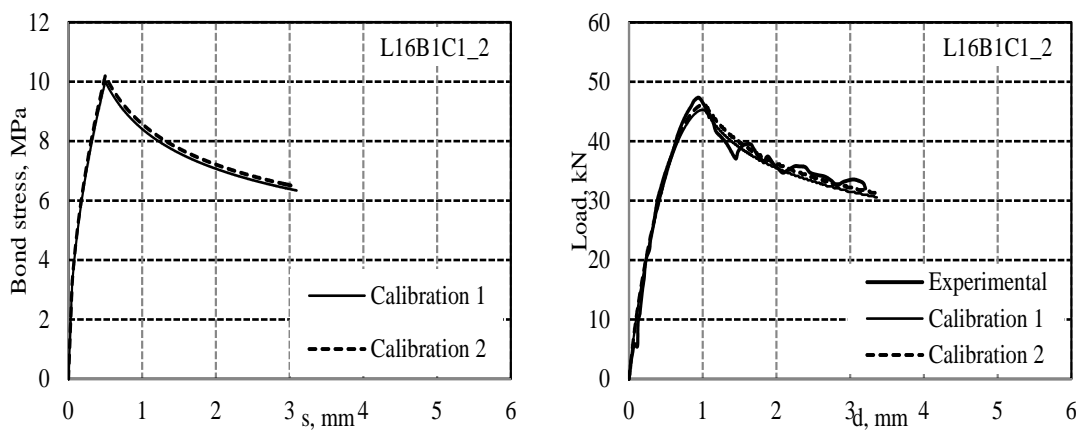
(a) The numerical τ - s curves(b) The numerical and experimental F - d curves

Figure A.3: Calibration curves for specimen L16B1C1-2.

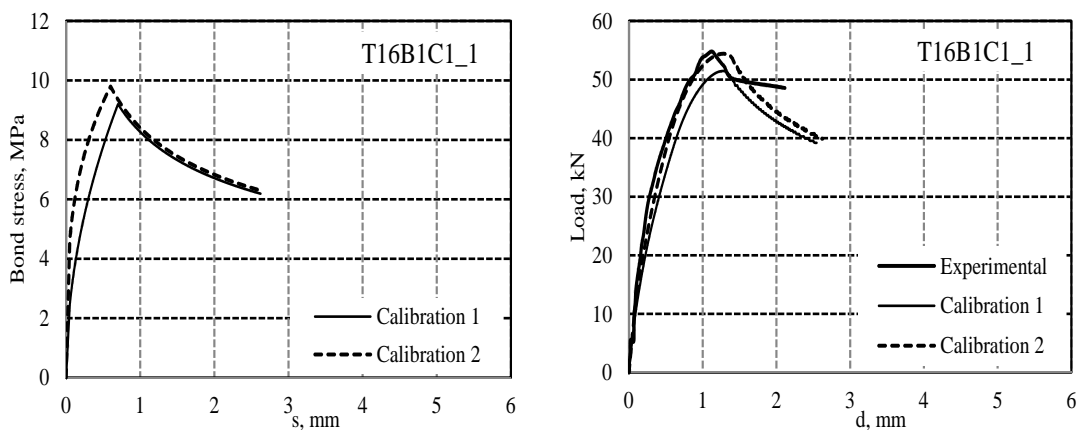
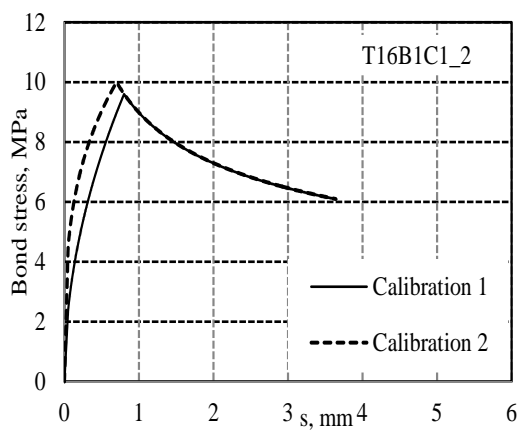
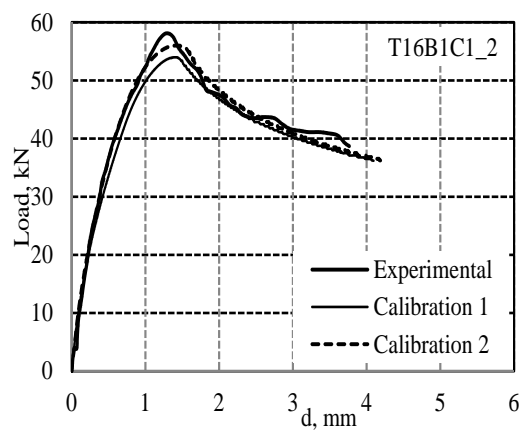
(a) The numerical τ - s curves(b) The numerical and experimental F - d curves

Figure A.4: Calibration curves for specimen T16B1C1-1.

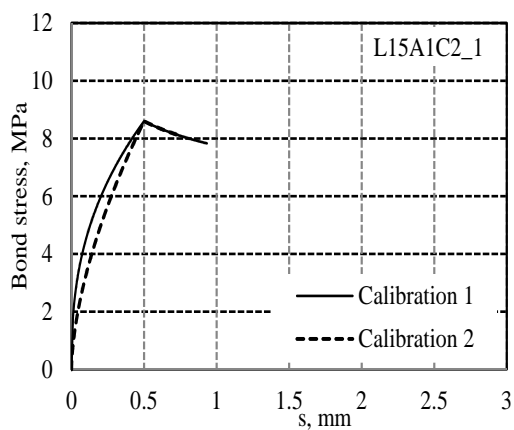


(a) The numerical τ - s curves

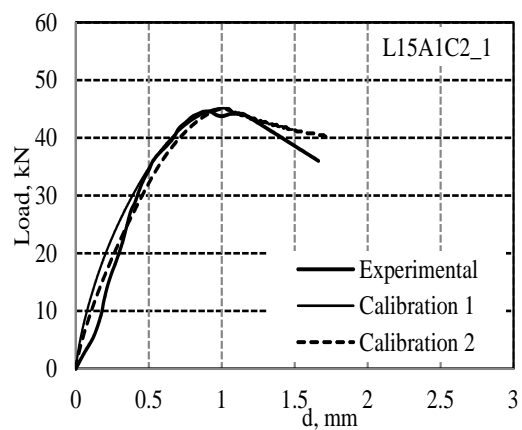


(b) The numerical and experimental F - d curves

Figure A.5: Calibration curves for specimen T16B1C1-2.



(a) The numerical τ - s curves



(b) The numerical and experimental F - d curves

Figure A.6: Calibration curves for specimen L15A1C2-1.

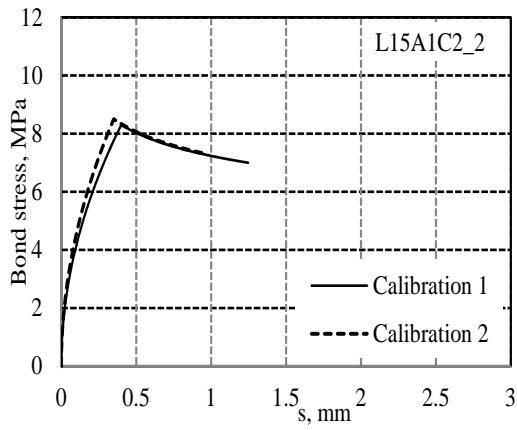
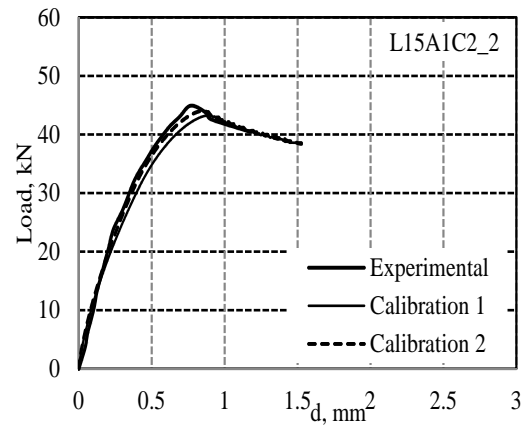
(a) The numerical τ - s curves(b) The numerical and experimental F - d curves

Figure A.7: Calibration curves for specimen L15A1C2-2.

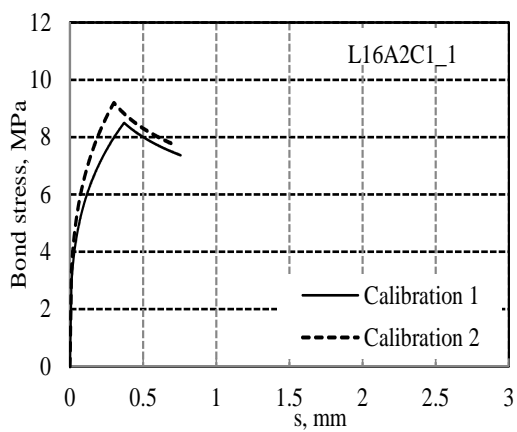
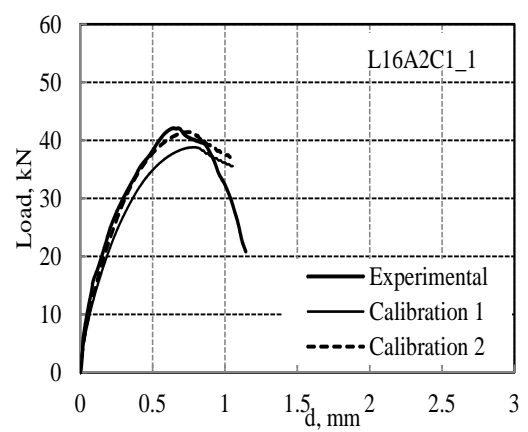
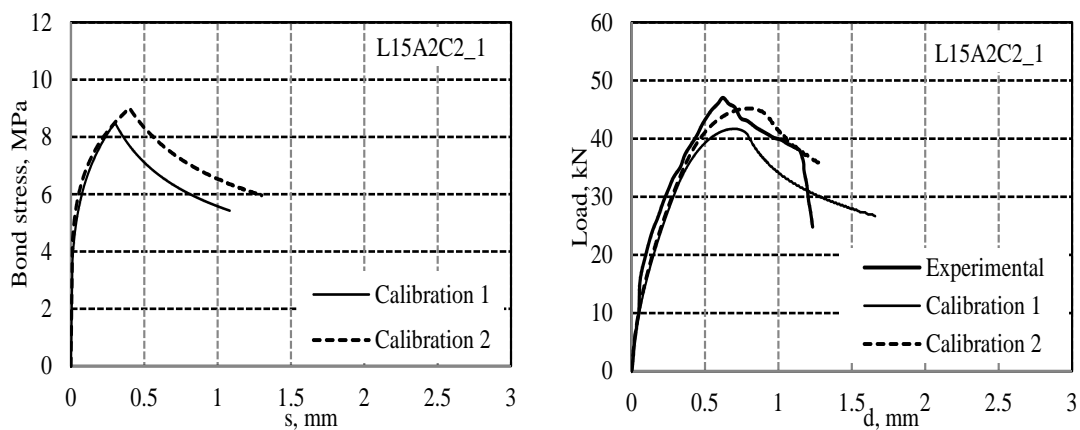
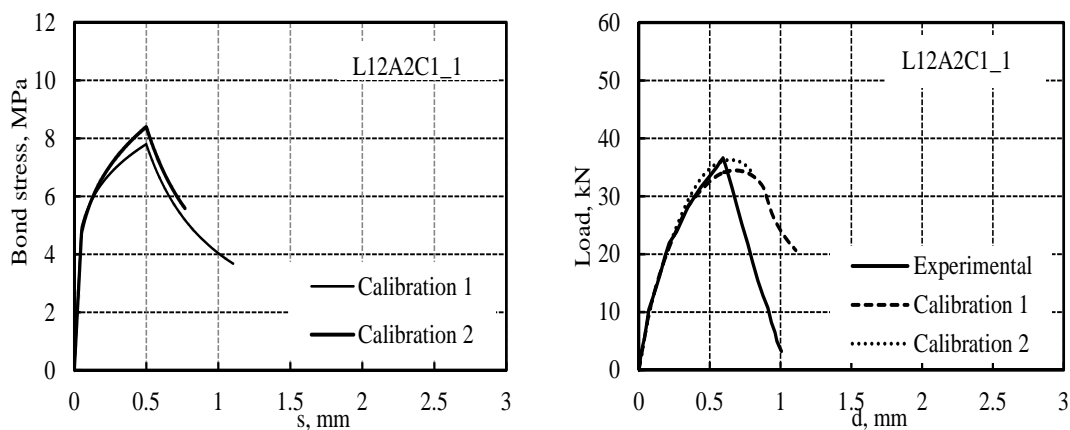
(a) The numerical τ - s curves(b) The numerical and experimental F - d curves

Figure A.8: Calibration curves for specimen L16A2C1-1.



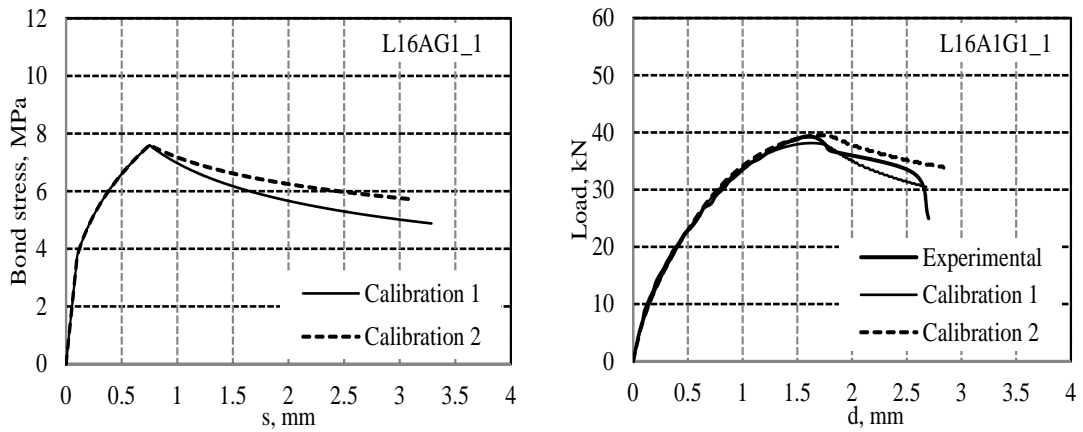
(a) The numerical τ - s curves (b) The numerical and experimental F - d curves

Figure A.9: Calibration curves for specimen L15A2C2-1.



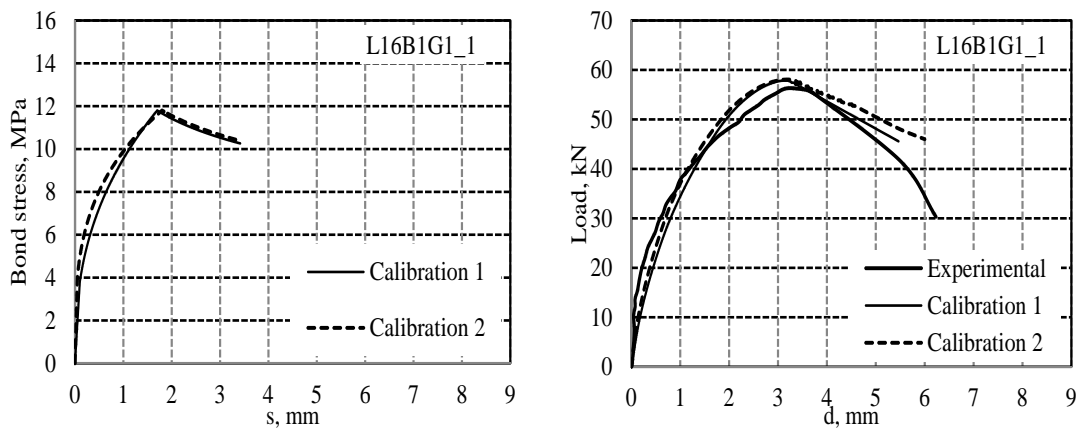
(a) The numerical τ - s curves (b) The numerical and experimental F - d curves

Figure A.10: Calibration curves for specimen L12A2C1-1.



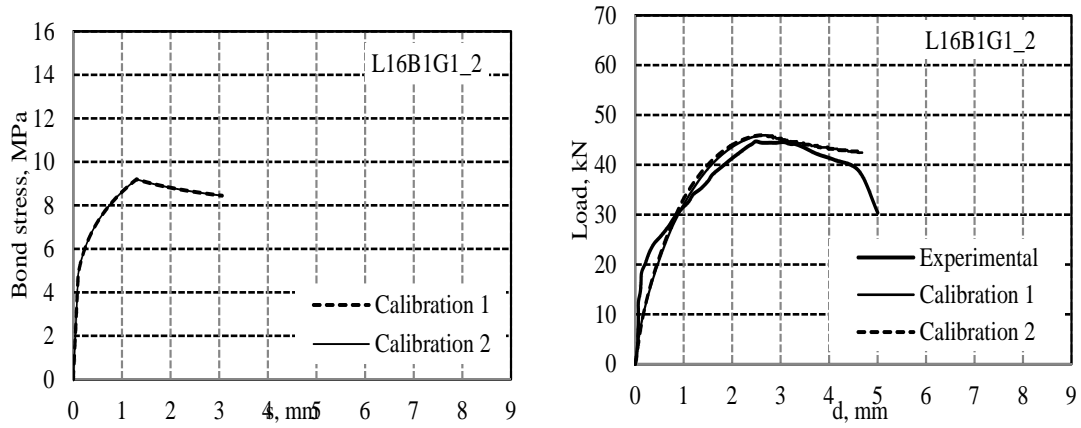
(a) The numerical τ - s curves (b) The numerical and experimental F - d curves

Figure A.11: Calibration curves for specimen L16A1G1-1.



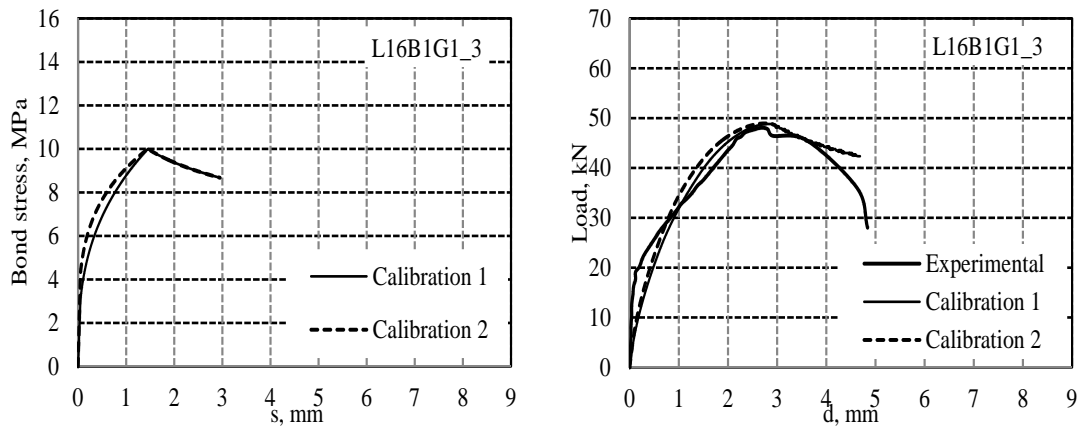
(a) The numerical τ - s curves (b) The numerical and experimental F - d curves

Figure A.12: Calibration curves for specimen L16B1G1-1.



(a) The numerical τ - s curves (b) The numerical and experimental F - d curves

Figure A.13: Calibration curves for specimen L16B1G1-2.



(a) The numerical τ - s curves (b) The numerical and experimental F - d curves

Figure A.14: Calibration curves for specimen L16B1G1-3.

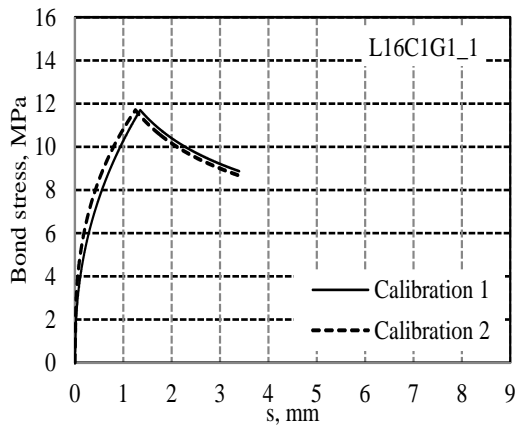
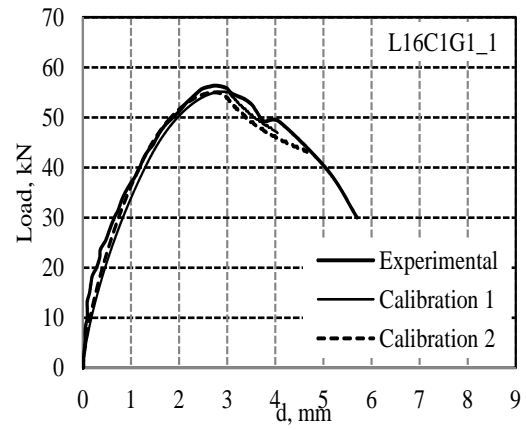
(a) The numerical τ - s curves(b) The numerical and experimental F - d curves

Figure A.15: Calibration curves for specimen L16C1G1-1.

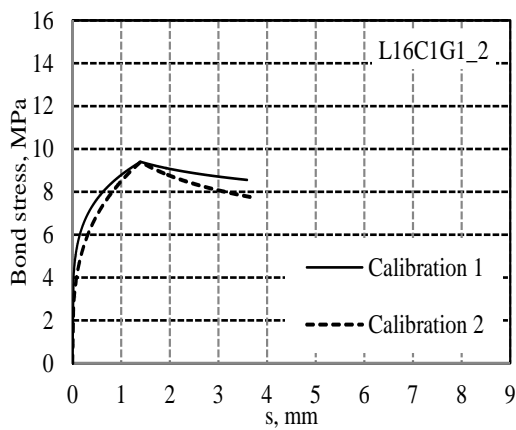
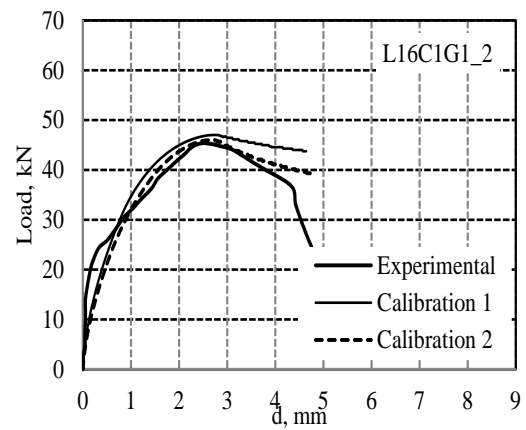
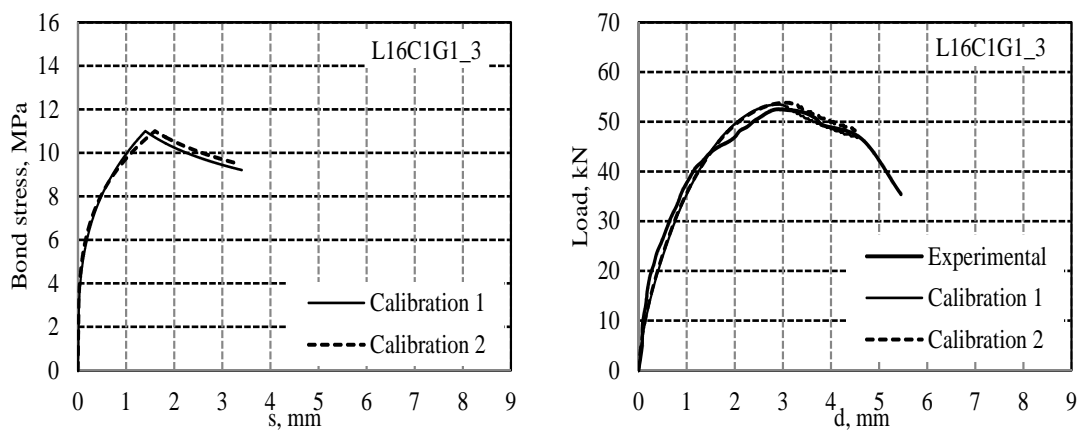
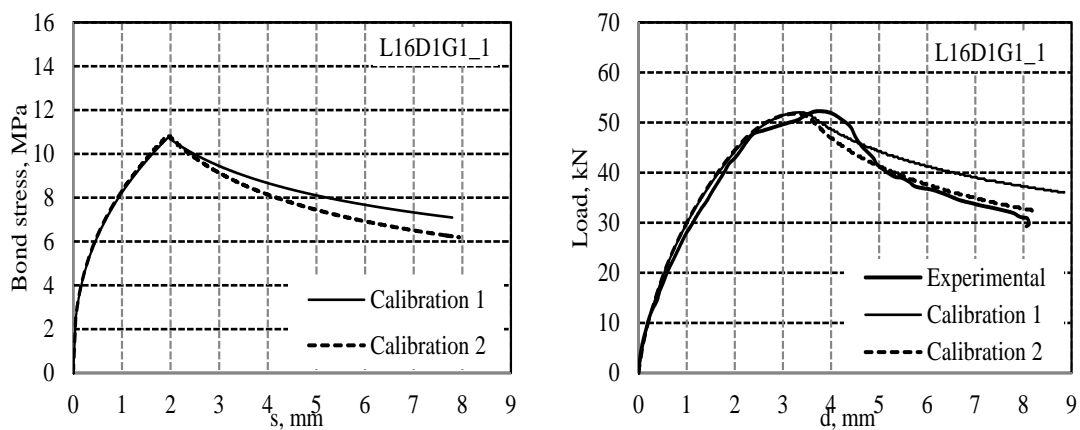
(a) The numerical τ - s curves(b) The numerical and experimental F - d curves

Figure A.16: Calibration curves for specimen L16C1G1-2.



(a) The numerical τ - s curves (b) The numerical and experimental F - d curves

Figure A.17: Calibration curves for specimen L16C1G1-3.



(a) The numerical τ - s curves (b) The numerical and experimental F - d curves

Figure A.18: Calibration curves for specimen L16D1G1-1.